TRACTION FORCE OPTICAL COHERENCE MICROSCOPY: A NEW METHOD TO STUDY THE DYNAMIC MECHANICAL BEHAVIOR OF CELLS AND MULTICELLULAR COLLECTIVES WITHIN SCATTERING MEDIA

A Dissertation

Presented to the Faculty of the Graduate School

of Cornell University

in Partial Fulfillment of the Requirements for the Degree of

Doctor of Philosophy

by

Jeffrey Alesh Mulligan

May 2020

TRACTION FORCE OPTICAL COHERENCE MICROSCOPY: A NEW METHOD TO STUDY THE DYNAMIC MECHANICAL BEHAVIOR OF CELLS AND MULTICELLULAR COLLECTIVES WITHIN SCATTERING MEDIA

Jeffrey Alesh Mulligan, Ph.D.

Cornell University 2020

Mechanobiology is a prominent research field which seeks to elucidate the role of physical forces and mechanical interactions throughout various biological processes, including morphogenesis, wound healing, and cancer metastasis, among others. Traction force microscopy (TFM) is an important family of experimental techniques used by mechanobiologists to study and quantify the forces that cells exert upon their surroundings. Recent years have seen a growing demand for TFM methods capable of studying the dynamic, 3D, and collective behaviors of cells embedded within optically scattering media. However, traditional imaging modalities for TFM (e.g., confocal microscopy) do not currently allow researchers to satisfy these demands.

In this dissertation, I present traction force optical coherence microscopy (TF-OCM), a TFM platform based on optical coherence tomography (OCT), to address the as yet unmet imaging needs of mechanobiology researchers and study the dynamic mechanical behavior of cells and multicellular collectives within scattering media. In the first half of this dissertation, I summarize current methods and emerging needs of the TFM field and provide detailed derivations and discussions regarding signal processing methods for OCT imaging. In the latter half, I present the key experimental findings of my research.

A pilot study was first performed to demonstrate the ability of OCT imaging to capture substrate deformations induced by cellular traction forces (CTFs). This was followed by a proof-of-concept study which enabled the quantitative reconstruction of time-varying CTFs exerted by isolated cells, resulting in the realization of TF-OCM as a full-fledged experimental technique. The critical image reconstruction procedures developed along the way have since proven useful in the context of other OCT imaging applications as well. Finally, a collaborative application-focused study was performed, which demonstrated the ability of TF-OCM to study the dynamics of large multicellular collectives embedded within scattering collagen substrates. Although much work remains to be done in order to enable quantitative TF-OCM in such complex settings, these findings show that TF-OCM offers a promising avenue to pursue new and valuable research endeavors in mechanobiology.

BIOGRAPHICAL SKETCH

Jeffrey Alesh Mulligan grew up on a walnut farm near the city of Lakeport in Lake County, California. There, Jeffrey was raised by his parents, Steve and Linda, alongside his sister Kelly. Throughout his childhood, Jeffrey developed a broad interest in science, math, and the natural world. He was also fortunate enough to partake in the increasingly rare educational experience of an agricultural life: raising animals, planting orchards, tending gardens, and generally wandering about outdoors when nothing else piqued his interest.

Jeffrey graduated from Clear Lake High School in 2010, after which he enrolled at Harvard College in Cambridge, Massachusetts to study engineering. He was never a big fan of the weather out there, but he was grateful to meet many wonderful and extraordinary people. After spending his first year cleaning bathrooms in the dorms of upperclassmen, Jeffrey began working as a tutor for fellow undergraduates in mathematics and engineering, which further cultivated his love for teaching and helping others. Although Jeffrey specialized in biomechanics and materials on paper, he picked up an interest in signal processing along the way, which was bolstered by extra coursework on the subject and a summer research internship in image processing with the Harvard Center for Systems Biology. Jeffrey was awarded his S.B. in Engineering Sciences in 2014.

In order to continue pursuing his interest in signal processing, Jeffrey enrolled as a PhD student in the School of Electrical and Computer Engineering at Cornell University in Ithaca, New York. Through an unexpected sequence of events, Jeffrey joined the research lab of Professor Steve Adie in the spring of 2015 to pursue optics research, despite lacking any former coursework in the subject. He nevertheless adapted quickly and soon took on the roll of teaching and training new members to the lab in the theory and practice of optical

coherence tomography (OCT) systems. Soon after, Jeffrey refined his research focus toward the development of an OCT-based platform for traction force microscopy, which he hoped would provide useful new research capabilities to the numerous mechanobiology researchers who toiled away in the labs above his subterranean optics lair.

You will find many of the end products of Jeffrey's research in this dissertation. What you will not find are his endeavors to become a better educator and communicator, which were sponsored by the U.S. Department of Education, the School of Biomedical Engineering, and the Cornell University Center for Teaching Innovation. Nor will you find records which chronicle the countless hours that he spent learning, joking, complaining, laughing, and stumbling through his research alongside his numerous intelligent, hilarious, and hard-working peers. You will also find no transcripts of the weeks worth of phone calls that he shared with his family and friends, who provided the critical support that kept him merely on the *brink* of utter madness during stressful times. And finally, you will find no accounts of how much he cherished peaceful walks through the Cornell Botanic Gardens and other natural areas surrounding Cornell.

Jeffrey was awarded his M.S. in Electrical and Computer Engineering in the fall of 2017. As of this writing, Jeffrey is on track to earn his PhD in Electrical and Computer Engineering in May 2020. Upon completion, he plans to return to California, where he hopes to continue learning, grow a garden, and enjoy good times with family and friends.

To my family,

Thank you for everything you have taught me

and for everything that you gave to give me a good life.

ACKNOWLEDGEMENTS

I owe my gratitude to more people than I could ever detail here.

Firstly, I would like to thank my advisor, Professor Steve Adie, for his guidance, support, and enthusiasm throughout my program. I had many interesting experiences through my work in this lab, be they in research, teaching, or professional development, and I am grateful to have had the opportunity to pursue them. The lab provided a challenging yet entertaining environment for me to learn and explore, and I am more than pleased with how much I was able to grow in this setting.

I would also like to thank the Minor Members of my Special Committee: Professor Clifford Pollock, for his calm perspective and earnest interest in my research throughout our numerous conversations over the years, and Professor Claudia Fischbach for her pragmatic approach and eagerness to help me transform my work into methods that provide practical benefits to other researchers.

I would like to give a huge shout-out to all of the Weill Hall basement dwellers who helped to make life and science in a sunless, white-walled basement fun. I would like to give special thanks in particular to Yu-Ting Cheng, Dr. John Foo, Dr. Mohammad Haft-Javaherian, Dr. Jason Jones, Dr. Michael (Mike) Lamont, and Dr. David Small. This esteemed crowd gave me endless laughs, long conversations, and valuable perspectives on life. And of course, I must include honorary basement dweller Lu Ling. I could not have asked for a better collaboration partner and friend to count on amid the insanity of months upon months of imaging experiments and data processing.

And to my remaining collaborators, Dr. Xinzeng Feng, Professor François (Frank) Bordeleau, and Professor Cynthia (Cindy) Reinhart-King, thank you for our times together and your hard work to help make my research possible.

I would be nowhere if not for the company and efforts of my fellow Adie Lab members. Their hard work and perseverance have astounded me to no end. PhD students Nichaluk (Nikki) Leartprapun, Siyang Liu, and Meiqi Wu. Postdocs Dr. Yuechuan Lin and Dr. Justin Luo. Undergraduate-turned-Masters student Colin Mackey. It was an absolute pleasure to spend so much time with you all and finish this long journey with all of you there. I would also like to extend a special thanks to alumni Gavrielle (Gav) Untracht, Rishyashring (Rishee) Iyer, and Asher Novick, who all helped shape my experience here and were a blast to work with. And lastly, a thank you to my undergraduate researchers for their work and dedication. I hope I managed to teach you something valuable!

More broadly, thanks to all the staff at the Cornell Center for Teaching Innovation and the Fellows I met through their programs (who helped teach me to teach and learn how to learn), the Dilmun Hill student farm (for many seasons of delicious produce), Scott Coldren (the GFA for ECE, for his endless hard work, patience, and calm demeanor), and my long-time roommate Alex Loiben (for being a good friend when I needed one and for providing limitless puns at all the times when I did not need them). People like you are what define Cornell–to me, anyway.

To my friends, who are off living their own lives all over the country and the world. Thank you for the frequent calls or occasional check-ins, whichever we shared. You were always there when I needed you.

Finally, I would like to thank my family, to whom I owe more than I could possibly recount. To my dad, Steve, I cannot thank you enough for the years worth of phone calls, support, jokes, trivia, rants, and the occasional kick in the pants that helped me get through this program. To my mom, Linda, I wish I could consider myself even one-tenth as strong you. Thank you for your un-

ending interest in learning from me and doing your best to teach me new perspectives, even when times are stressful. And to my sister, Kelly, your unfailing enthusiasm and tenacity are a beacon in my life. Thank you for teaching me how to be a big brother. You may not realize it, but I would not be the sort of scientist I am today if not for you.

TABLE OF CONTENTS

LIST OF TABLES

LIST OF FIGURES

CHAPTER 1

INTRODUCTION

1.1 Background

Mechanics play a key role in biological form, function, and behavior across spatial scales–from organs and tissues all the way down to sub-cellular phenomena. Physical forces, mechanical properties, geometric features, and the like have been shown to influence and direct biological processes such as wound healing, angiogenesis, morphogenesis, cell migration, and cancer progression. As a consequence, 'mechanobiology' has emerged as a diverse and growing research field which seeks to elucidate how mechanical interactions govern physiology and disease [71, 93]. As new lines of inquiry have been adopted, new techniques and technologies have been developed to meet the growing needs of researchers and their experiments alike.

Traction force microscopy (TFM) is a diverse family of techniques which quantify the mechanical forces that cells exert on their surroundings. Since cellular traction forces (CTFs) are involved in numerous biological processes, TFM has become an important tool for mechanobiology research [111, 141, 152]. TFM consists of two primary stages: imaging and force reconstruction. When cells exert forces on a substrate, the substrate becomes deformed in response. Optical imaging is used to record these deformations. Post-processing methods are then used to both quantify the deformations and reconstruct the forces that would be required to induce them, given the mechanical properties of the substrate.

TFM has a long history of application to the study of cells cultured on the

surface of flat substrates [36, 152]. However, since cell behavior/phenotype can differ substantially in 2D versus 3D environments [71, 117, 157, 180, 186], there has been a growing demand for the development of TFM techniques which can be used to study the behavior of cells embedded in physiologically relevant 3D environments. The first instance of '3D TFM' was reported in 2010 [89], and related techniques have emerged since [54, 61, 112]. In the meantime, the demand for studies of large cellular *collectives* (in 2D and 3D) has grown substantially [86, 116, 174]. (After all, animal cells rarely live or act in isolation.) However, the standard imaging tools used for TFM have begun to confine experimental capabilities in this area (especially for studies of 3D collective behavior).

Confocal fluorescence microscopy is the current standard method for generating the 3D image data required for 3D TFM. As a consequence, the range of experiments and biological model systems which are readily compatible with standard 3D TFM methods is limited. In particular, 3D image acquisition with confocal fluorescence microscopes can be time-consuming (up to several minutes and longer). This limits the rate at which new data may be acquired and may result in samples being exposed to laser light for long periods of time. Photobleaching and phototoxicity due to such extended exposures can reduce image quality and alter cell behavior. This impedes the ability of standard 3D TFM methods to perform extended time-lapse studies of dynamic systems [47, 89]. Finally, confocal fluorescence microscopy has a limited penetration depth which typically extends only a few hundred micrometers into optically scattering media. This limits the ability of TFM to study large cell collectives (such as spheroids or organoids, which can be hundreds of micrometers in size) within physiologically relevant scattering media such as collagen.

This dissertation presents a new method to circumvent the traditional imaging limitations of 3D TFM by employing a *nontraditional* imaging modality: optical coherence tomography.

Optical coherence tomography (OCT) is an interferometric imaging modality that enables non-invasive, label-free imaging of scattering contrast in biological samples. Operating on principles similar to broadband radar, ultrasound, and related techniques, OCT records the *magnitude* and *phase* of backscattered light in the visible-to-near-infrared spectrum. As a result, OCT is capable of imaging in scattering media with a volumetric field-of-view (FOV) up to $1 \times 1 \times 1$ mm^3 or larger,[1] making it well-suited for volumetric imaging of extended cell collectives. These volumes can be acquired in only seconds to minutes, since modern OCT microscopes perform spatially multiplexed data acquisition.[2] This rapid acquisition speed (in combination with the near-infrared illumination, low incident beam power,[3] and label-free contrast of OCT) makes OCT well-suited for both high-speed and extended time-lapse studies, since photobleaching and phototoxicity are of little to no concern. Finally, by combining high numerical aperture optics with numerical image formation algorithms inspired by synthetic aperture radar [3, 137], OCT can provide micrometer-scale isotropic spatial resolution throughout the entire volumetric FOV. Considering all of these factors together, OCT provides a convenient means to capture short-to-long-term cellular behavior spanning micrometer-to-millimeter spatial scales

---

[1]This is due to a combination of the relatively long wavelength of red-to-near-infrared light (in comparison to the ultraviolet-to-visible light typical to confocal microscopes) with enhanced rejection of multiply-scattered light (due to the fact that OCT can distinguish multiply-scattered light from singly-scattered light via the different amounts of *time* that each type of light spends propagating throughout the microscope).

[2]A typical confocal microscope acquires 3D data via time-consuming 3D raster scanning of an optical beam focus throughout the imaged volume. In comparison, OCT microscopes typically perform parallelized acquisition along one or more spatial dimensions, and thus require scanning along only 2 or fewer dimensions in order to acquire an entire 3D image.

[3]Typically <5 mW.

within scattering media.

Since the imaging capabilities of OCT are well-matched to the capabilities required to meet the growing demand for TFM of 3D and/or multicellular constructs, we proposed traction force optical coherence microscopy (TF-OCM) as a new method to study the dynamic mechanical behavior of cells and multicellular collectives within scattering media [110]. Although OCT (and its high-resolution counterpart: optical coherence *microscopy*, or OCM) have previously been used to study dynamic cell behaviors [98, 139, 170], TF-OCM would *additionally* provide quantitative measurements of substrate deformations and cellular traction forces, which are necessary for advancing research in mechanobiology. Accompanying the development of TF-OCM, new image reconstruction and image processing routines were devised [94, 112], and new opportunities emerged which might pave the way to the creation of an OCT-based mechanobiology research platform that can characterize *both* cellular traction forces and the mechanical properties of surrounding substrates [87, 113].

1.2 Outline, scope, and objectives of this dissertation

This dissertation records key concepts, theory, methods, algorithms, and findings which contributed to the development of traction force optical coherence microscopy as a new experimental technique for conducting mechanobiology research. Like all TFM techniques, TF-OCM relies upon the union of a broad range of interdisciplinary knowledge and skills. It is crucial that future researchers be provided with a strong foundation from which they may develop new experimental capabilities and make new findings. It is my hope that this

dissertation will serve as a useful educational document, and that new opportunities might be found among the limitations of current methods. Toward this end, the remaining chapters have been organized as follows:

Chapter 2 summarizes current standard approaches in TFM and reviews recent innovations in the field. The goal of this chapter is to provide readers with a basic understanding of TFM, and to serve as a starting point from which new literature searches might begin and/or new methods might be pursued and developed. Note that this chapter is a lightly edited version of a previously published work (Ref. [111]) which was written during the summer of 2017 and published in 2018.

Chapter 3 provides detailed derivations and discussions regarding the theory of (spectral domain) OCT image acquisition and signal processing. The goal of this chapter is to provide readers with the basic knowledge and skills required to perform fundamental research in OCT imaging (and by extension, TF-OCM). Of course, similar knowledge may be obtained from literature searches and experience within the OCT field. However, it is my hope that this particular digest of the basics will help beginners to better 'hit the ground running' (and/or give a new perspective to more established researchers).

Chapter 4 provides detailed derivations and discussions regarding computational image formation for OCT. Specifically, this chapter details methods for the computational mitigation of defocus and optical aberrations (via computational adaptive optics and related techniques). This chapter also details additional image formation routines which were developed and used to compensate for non-ideal imaging conditions. These latter routines were critical components of TF-OCM workflows, and have found use in other OCT imaging stud-

ies. Thus, the contents of this chapter serve as the current baseline which readers must understand in order to replicate TF-OCM methods 'from the ground up'.

Chapter 5 summarizes the methods and findings of a pilot study which demonstrated the ability of computed OCT imaging to capture and measure the action of cell forces upon a surrounding 3D substrate. This study paved the way for follow-up research which used substantially more advanced methods and provided enhanced imaging capabilities. The findings shown in this chapter were previously published in early 2017 (Ref. [110]).

Chapter 6 summarizes the methods and findings of a proof-of-concept study which resulted in the first complete realization of TF-OCM. TF-OCM was demonstrated to enable the quantitative measurement of dynamic cell traction forces exerted by isolated cells embedded in a 3D Matrigel substrate. The critical image formation routines outlined in Chapter 4.4 were first developed and/or used for TF-OCM in this study. The findings shown in this chapter were previously published in early 2019 (Ref. [112]).

Chapter 7 summarizes methods and findings from an application-focused study which adapted the TF-OCM methods of Chapter 6 in order to enable multi-day time-lapse studies of multicellular spheroids embedded in collagen substrates. The resulting imaging capabilities enabled experiments that contributed key findings to a broader biological study which was published in 2020 (Ref. [94]). The image reconstruction routines detailed in this chapter are the most recent and recommended methods for performing TF-OCM (as of this writing). Notable challenges to quantitative TF-OCM in multicellular settings are discussed and future potential investigations are proposed.

Chapter 8 concludes this dissertation and summarizes the overall contributions of this work. A summary of possible areas for follow-up investigations is also provided for future researchers to consider.

CHAPTER 2

TRACTION FORCE MICROSCOPY: A REVIEW OF STANDARD APPROACHES, ONGOING CHALLENGES, AND RECENT INNOVATIONS

Content reuse disclosure   The contents (text, figures, etc.) of this chapter have been reprinted from a previously published book chapter of which I was the first author.[1] Minor alterations to the original work have been made for this adaptation. These include minor grammatical edits (for clarity) and the omission of Figs. 15.1 and 15.6-15.10 from the original work (to avoid permissions conflicts with other publishers). To view the full contents of the original chapter, please see Ref. [111].

Author contributions statement   The original book chapter on which this dissertation chapter is based (Ref. [111]) was primarily written by me (J.A. Mulligan), with guidance, editing, and minor text passages contributed by the co-authors of the original book chapter. Figure 2.4 (Fig. 15.5, in the original publication) was contributed by co-authors F. Bordeleau and C.A. Reinhart-King.

---

[1]Reprinted with permission from Springer Nature Customer Service Centre GmbH: J.A. Mulligan, F. Bordeleau, C.A. Reinhart-King, S.G. Adie. Traction Force Microscopy for Noninvasive Imaging of Cell Forces. In: C. Dong, N. Zahir, K. Konstantopoulos (eds) Biomechanics in Oncology. Advances in Experimental Medicine and Biology, vol 1092. `https://doi.org/10.1007/978-3-319-95294-9_15` © Springer, Cham (2018)

2.1 Abstract

The forces exerted by cells on their surroundings play an integral role in both physiological processes and disease progression. Traction force microscopy is a noninvasive technique that enables the *in vitro* imaging and quantification of cell forces. Utilizing expertise from a variety of disciplines, recent developments in traction force microscopy are enhancing the study of cell forces in physiologically relevant model systems, and hold promise for further advancing knowledge in mechanobiology. In this chapter, we discuss the methods, capabilities, and limitations of modern approaches for traction force microscopy, and highlight ongoing efforts and challenges underlying future innovations.

2.2 Introduction

The growing field of mechanobiology has resulted in a heightened understanding of how cells both shape and respond to mechanical properties and forces in their environment. Driving this understanding is a growing body of evidence, which has revealed that the biophysical interactions of cells with both the extracellular matrix (ECM) and neighboring cells play an integral role in the progression of many physiological and pathological processes [180, 122, 18, 40, 186, 20, 145, 157]. In tumor progression, for example, the ECM progressively stiffens due to increased cell-mediated collagen deposition and cross-linking [134, 91]. In turn, the increased stiffness influences cancer cell growth, angiogenesis, and metastasis [122, 91, 14]. Cells sense and respond to extracellular biophysical cues through molecular mechanotransduction mechanisms, such as integrin-based focal adhesion complex signaling and actin-myosin reorga-

nization [51, 99, 149]. These biophysical interactions play a key role in the on-set and progression of cancer [122, 18, 186, 20, 91, 49], stem cell differentiation [58, 30, 53, 187, 38], morphogenesis [101], and wound healing [187].

A central feature shared among these biophysical phenomena is cell force. Cell forces are well known to play critical roles in such processes as metasta-sis [80], angiogenesis [70, 85], and dynamic self-organization of cell aggregates [160]. It should therefore come as no surprise that the forces exerted by cells on their environment, and how cells respond to mechanical stress and strain, are of significant interest to researchers in the area of biophysics. As a result, there is an ongoing demand in the field of mechanobiology to be able to quantify cell forces and their impact on biological systems and phenomena.

Among the techniques that have been developed to enable the study of cell forces, this chapter will focus on the methods that have collectively come to be known as traction force microscopy (TFM). TFM encompasses a family of tech-niques which enable the quantitative measurement of cell traction forces via noninvasive optical imaging of deformations induced within continuous elastic substrates. The term 'traction force' initially referred to the shearing forces ex-erted by adherent cells cultured on flat 2D surfaces. However, TFM has since grown to enable the measurement of general forces in three dimensions, ex-erted by cells grown either on the surface of, or embedded within, a substrate. In brief, TFM enables the indirect assessment of cell traction forces by first imag-ing the deformations that traction forces induce in the ECM or other substrates. Cell forces are then computationally reconstructed using a suitable model that relates forces, deformations, and known substrate mechanical properties.

The origins of TFM lie in the experiments of Harris et al., who reported in

1980 that cells cultured on a thin membrane of silicone rubber exerted contractile forces which caused the membrane to buckle and wrinkle [65]. The amount of wrinkling could then be used to estimate the magnitude of cell traction forces. Although these experiments laid the initial foundations for the optical measurement of cell forces, they did not enable robust force quantification due to the highly nonlinear and chaotic nature of membrane wrinkling. In 1999, Dembo and Wang presented the seminal work which marked the beginning of true TFM, as it is known today [36]. Silicone membranes were replaced with slabs of polyacrylamide hydrogel, coated with ECM proteins. This change in material and geometry eliminated wrinkling behavior, necessitating the addition of fluorescent beads embedded in the substrate to be used as fiducial markers for measuring deformations. As the substrate underwent transverse deformations in response to cell traction forces, the embedded beads were dragged along with it. This enabled the measurement of local substrate deformations by imaging displacements of the beads. Traction forces were then computed from these displacements using a mechanical model of the substrate.

Since then, further developments have drawn upon various tools and advances in biology, materials science, imaging, signal processing, and computing, to make TFM the diverse and powerful tool that it is today. Alongside TFM, other technologies for measuring cell forces have emerged [141]. For example, to alleviate the difficulties of force reconstruction and substrate preparation in TFM, a new kind of substrate was developed, consisting of microfabricated arrays of silicone posts [169]. In response to cell forces, these posts act like deformable springs, with behavior that is both well-characterized and tunable by controlling post geometry. However, as cells may only adhere to the top surfaces of posts, such systems present a geometrical constraint that is not observed

in typical flat, continuous substrates, raising concerns about physiological relevance. Another method has enabled the measurement of molecular stretching under tension by making use of fluorescence resonance energy transfer (FRET) [57]. However, the difficulty of obtaining quantitative force measurements that account for cell environmental conditions currently limit this technology such that it may only be used to complement, rather than serve as a substitute for, TFM [152]. As a result, TFM remains at the leading edge for the quantitative measurement of forces exerted by single cells and cell collectives on their environment.

As a tool for research in mechanobiology, TFM is frequently applied to investigate the relationships between biochemical/biomechanical cues, signaling pathways, ECM mechanics, mechanotransduction, and subsequent cell behaviors [8, 109, 129, 176, 105, 165]. Despite its broad use, there are limitations to common incarnations of TFM, and many opportunities exist for further innovation and application to novel biological questions. To address this issue, ongoing developments are enabling application of TFM to *in vitro* systems of ever greater complexity and physiological relevance.

The remainder of this chapter has been written with a focus on the principles and techniques behind these recent developments in TFM. We review the common methods and considerations which constitute the core of modern TFM techniques, with the intent of fostering an awareness and appreciation for the capabilities and limitations of common TFM methods. We also discuss potential areas of growth and innovation for TFM research in the near future. In doing so, we highlight various research achievements which have made critical steps toward developing TFM into a more powerful tool for the study of cell forces in

physiologically relevant systems and for making contributions to the growing field of mechanobiology.

2.3 From engineered systems to cell forces

Although modern implementations of TFM are quite diverse, all methods follow the same basic workflow (Fig. 2.1). Depending on the biological question at hand and the system under study, a substrate material is chosen. This material will deform when exposed to cell traction forces, and therefore must be mechanically characterized to enable the reconstruction of forces later on in the process. Fiducial markers (typically, fluorescent microbeads) are added to the surface of, or embedded within, the substrate. This adds optical contrast to the substrate, and allows traction force-induced deformations to be measured via the imaging of marker displacements.

Two or more images of the substrate are required. One image captures the non-deformed reference state, when there are no traction forces and the substrate is fully relaxed. The additional image/s capture the deformed state (at a single or multiple points in time), when adherent or embedded cells exert traction forces, causing marker agents to displace from their reference positions. The reference and deformed images are then used to generate measurements of the substrate deformations.

Once the traction force-induced substrate deformations are determined, this data is combined with the known (measured) mechanical properties of the substrate to reconstruct cell traction forces. Many force reconstruction methods exist to choose from, with the selection depending on the choice of mechanical
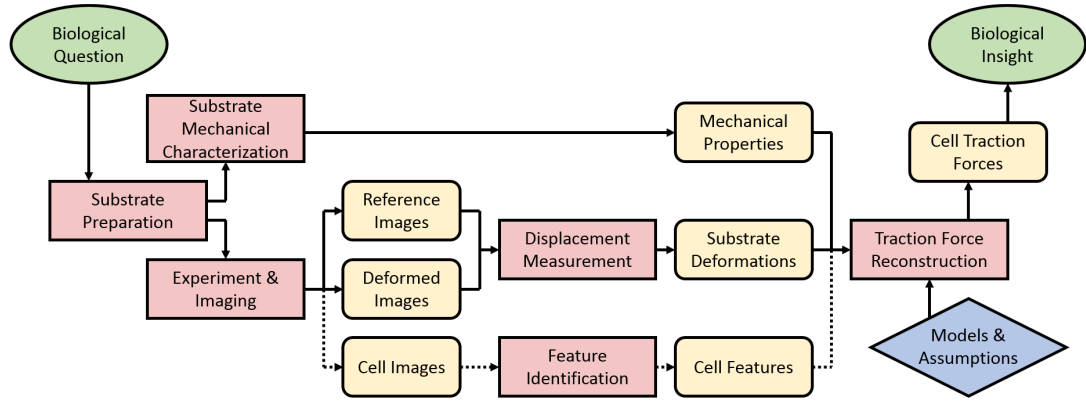
Figure 2.1: High-level overview of the basic TFM workflow. Red (sharp rectangle) and yellow (rounded rectangle) panels indicate procedures and their output data, respectively. The models and assumptions used in TFM (depicted by the blue diamond) have direct bearing on the type of traction force reconstruction methods that may be used. Dashed lines indicate experimental steps that may not be necessary, depending on the specific TFM methods chosen. For full details of the TFM workflow, please refer to the text. Reprinted with permission from Ref. [111]. © Springer, Cham (2018)

model and any other relevant assumptions made for the study. Typical force reconstruction methods rely on the assumption that the substrate material is linear, elastic, isotropic, and homogeneous and undergoes only small deformations/strains due to cell traction forces. However, as discussed in Section 2.4, recent advancements are beginning to reduce the need to rely on such assumptions [161, 173, 159, 54, 172]. Certain traction force reconstruction methods also rely on additional imaging data, typically in the form of cell structural information, such as a cell membrane outline, or the location of focal adhesion sites [36, 158, 19, 150]. (The fact that this information is only required by some TFM methods is indicated by the dashed lines in Fig. 2.1.) Once traction forces have been reconstructed, they may be used to yield insights which address the original biological question, or may even result in new unexpected discoveries.

Although the description above is sufficient to understand the general prin-

ciples behind TFM, further detail is required to appreciate the common experimental considerations, practical implementations, and limitations of TFM. The remainder of this section discusses the individual steps of TFM in greater detail. That said, the information provided below is still a very general overview. Many useful and extensive reviews exist on these topics, which the reader is encouraged to explore if seeking additional perspectives and discussion beyond that found here [152, 81, 62, 130, 128].

2.3.1 Substrate selection and mechanical characterization

Substrate selection is a critical choice in any TFM study. This is because substrate composition and geometry are fundamentally linked to what types of systems can be modeled, what behaviors cells will exhibit, what kinds of forces can be exerted, what imaging and data processing methods are required, and finally, how traction force reconstruction may be performed. The founding works of TFM provide an illustrative example of the importance of substrate design. The transition from silicone membranes to polyacrylamide slabs played a crucial role in enabling the first incarnation of modern quantitative TFM [36, 124]. The new polyacrylamide platform provided flexibility and convenience for the repeatable fabrication of substrates that could be tuned to match the stiffness observed in a variety of *in vivo* tissues [124]. ECM proteins covalently bonded to the substrate surface (to enable cell adhesion) provided cells with binding domains that more closely resembled those of native ECM/tissue and provided an extra degree of freedom in experimental design. (Collagen and fibronectin, which are among the most abundant ECM components found in tumors [41, 183, 100], are often used for this purpose.) Finally, the geometry of the

substrate, in combination with its linear elastic, homogeneous, and isotropic properties, allowed the traction force reconstruction problem to be vastly simplified, making quantitative and reliable TFM feasible to implement. The development of these systems was so successful that cell culture experiments performed on the surface of polyacrylamide hydrogels have since become the gold standard for measuring cell forces with TFM.

With advancements in imaging, data processing, and computation, this classic platform has expanded capabilities. While 2D cell culture on the surface of polyacrylamide hydrogels has been traditionally used to study purely transverse deformations and forces, it has been shown that even cells grown on flat surfaces can exert three-dimensional forces, causing out-of-plane deformations of the hydrogel substrate [188, 103, 47]. The measurement of 3D cell forces exerted in 2D cultures gave rise to what is referred to in the literature as either 2.5D- or 3D-TFM [188, 47]. (We will adopt the '2.5D' naming convention here to distinguish this method from 3D-TFM methods that quantify the 3D forces exerted by cells embedded within 3D environments.) These 2.5D-TFM methods can help to provide a more complete picture of traction force-mediated cellular activity than is offered by 2D-TFM methods [188]. Despite these advances, the polyacrylamide platform is limited in that it does not enable the measurement of 3D forces exerted by cells residing within fully 3D environments. Since cell behavior can greatly differ in 2D versus 3D environments [180, 186, 157, 117], there is a need for substrate systems that enable TFM in 3D cell culture.

Approaches to obtain platforms compatible with 3D-TFM rely on either engineered polymers or the use of native ECM scaffold materials. Legant et al. performed 3D-TFM by making use of polyethylene glycol (PEG) hydrogels, in-

corporating domains that allowed for both adhesion (fibronectin RGD binding domain) and degradation (matrix metalloproteinase susceptible linkers) by embedded cells [89, 107]. Other studies in 3D settings have chosen to make use of materials that more closely approximate natural 3D tissue environments, such as fibrin [70], Matrigel [110, 112], and collagen [54, 78]. As will be discussed in Section 2.4, the use of these biopolymer substrates enables TFM in fully 3D environments, but can introduce complications such as nonlinearity, heterogeneity, and anisotropy. These factors complicate the characterization and modeling techniques required to accurately reconstruct traction forces. Nevertheless, the application of TFM to such systems that more closely approximate physiological environments is expected to be a major theme in future TFM research.

Once a substrate is constructed, its mechanical properties must be characterized, since these properties will inform how traction forces relate to observable deformations. As most TFM substrates are chosen/assumed to be linear, elastic, isotropic, and homogeneous, it is typical that only macroscopic mechanical properties, like the Young's (elastic) modulus and Poisson's ratio, are sought [150]. As a result, mechanical characterization methods have historically been fairly simple. The most common techniques include bulk rheometry [161], indentation testing (such as by depressing a steel ball) [81], and atomic force microscopy (AFM) [173]. However, when biopolymers are used for constructing TFM substrates, the (typically heterogeneous) mechanical properties on the micro/nanoscale throughout the substrate volume are unknown/inaccessible to these methods. Possible future methods of characterization will be discussed in Section 2.4.8.

2.3.2 Obtaining a reference state

In order to quantify the impact of cell traction forces on the environment, TFM requires measurements of the substrate in both reference (relaxed) and deformed (loaded) states. While the method for obtaining a reference state is rarely discussed at length in the literature, it is an important experimental design consideration. Some 2D culture-based methods image the substrate before the addition of any adherent cells to the sample [135]. This allows for a truly relaxed state to be obtained, with no risk of substrate alteration due to cellular activity. However, this arrangement can be problematic, as the act of adding cells to the sample may inadvertently disrupt the sample position and orientation relative to the imaging system. If not prevented or accounted for by hardware in the imaging setup, such misalignments complicate the measurement of traction force-induced deformations [135]. Specific experimental constraints such as long culture times, or the possibility that cells will migrate into/out of the field of view, can make obtaining the reference state first infeasible in some cases. This method is not used for 3D-TFM with embedded cultures, due to the fact that cells are added at the time of substrate fabrication, eliminating the opportunity to obtain a truly cell-free reference state. As one potential solution, samples may be imaged immediately after substrate polymerization, before cells have had ample time to apply significant forces in the substrate [21]. However, other factors, such as swelling of the substrate over time when immersed in culture media, may hinder this approach.

Alternatively, the deformed state may be imaged first, after cells have been added to the system and have begun exerting traction forces. Cell forces may then be removed *in situ* via chemical treatment. The compounds applied may

cause cell death, detachment, or inhibition of cell contractility. (In the last case, the effectiveness of traction force inhibition must be established to ensure complete relaxation is achieved.) Under the assumption that the substrate undergoes purely elastic (reversible) deformation, the removal of cell traction forces is sufficient to allow the substrate to return to its original relaxed state. However, this assumption is not necessarily valid when cells are capable of remodeling the substrate (such as in the case of 3D degradable ECM/hydrogels). In this scenario, measurements taken over a long period of time (several hours and longer) can be susceptible to alteration of the substrate geometry and mechanical properties by cell-induced remodeling. This would then have to be accounted for in the force reconstruction process [54]. Therefore, it is recommended that substrate recoverability is tested to ensure reliable traction force reconstructions when not using TFM models that account for remodeling.

Finally, fabrication techniques can assist in obtaining a reference state. For example, Polio et al. used an indirect micropatterning approach to bond fluorescently labeled fibronectin to the surface of a polyacrylamide gel [132]. The fibronectin was deposited in discrete dots, forming a rectangular grid with 5 μm spacing. These fibronectin dots were then used as fiducial markers to track substrate deformations resulting from cell traction forces. Since the fabricated pattern of markers was known *a priori*, deformations could be determined without imaging a reference state. As a result, a single prepared substrate could be used to image many separate cells across multiple fields of view, enabling high-throughput imaging for 2D-TFM experiments. As an added benefit, the fibronectin dots served as the only sites where cells could exert forces on the polyacrylamide gel. Constraining the locations of cell tractions allows for simplified and robust traction force reconstruction procedures, as will be discussed

in Sections 2.3.5 and 2.4.1 [158, 150, 132, 163]. However, the artificial constraint on cell force locations imposed by this method may impact physiological relevance, similar to the micropillar arrays mentioned previously. In spite of this limitation, it should be noted that methods using micropatterned adhesion sites/markers do enable novel studies on the effects of different patterns and choices/combinations of ECM proteins on cell traction forces [131].

2.3.3 Noninvasive imaging of cell force-induced deformations

TFM may be considered a noninvasive technique in that the measurements of substrate deformations are obtained through optical imaging, without disturbing the experimental system. Since TFM frequently relies on the use of embedded fluorescent marker beads to track displacements within the substrate, widefield fluorescence and confocal fluorescence imaging are commonplace in many TFM procedures. When images of cellular structure are required for force reconstruction or visualization, phase-contrast imaging is also commonly used in 2D- and 2.5D-TFM settings. While these standard microscopy techniques have been in use for years, increasing demands for 3D imaging, speed, reduced photobleaching/phototoxicity, and higher resolution, among other factors, are driving the emergence of TFM conducted with alternative imaging methods, which will be discussed in Section 2.4.9. Regardless of the imaging technique used, there are three major factors that must be considered for imaging systems in TFM: field of view, acquisition speed, and resolution.

An imaging system must have a large field of view to make reliable measurements for TFM. In the context of cells cultured on a flat substrate, the field

of view must be wide enough to capture regions far away from the cell/s under study. If this is not achieved, cells outside the field of view, but close to the cell/s of interest, may alter the substrate deformations within the field of view. This can prevent the accurate reconstruction of traction forces exerted by the cell/s of interest. Moreover, if cell migration is expected, the field of view must be large enough to prevent the cell/s from exiting the field of view before the conclusion of the experiment. In the case of cells cultured in 3D environments, these field of view requirements must be extended to three dimensions. Therefore, the imaging system must also be able to capture images over a large depth range for the same reasons described above for the case of 2D systems.

Imaging speed is an important consideration when dynamic systems or photobleaching/phototoxicity are of concern. Cells can exert dynamic forces on timescales as short as minutes [110, 112, 21]. Therefore, imaging speeds must be faster than these dynamic processes, or cell forces may change during acquisition. For 2D imaging systems, this is rarely an issue. However, it can become a major concern for 3D imaging systems, which can take several minutes to acquire a single volume. Moreover, longer imaging times can risk causing photodamage to cells (potentially altering cell behavior) and may result in photobleaching of fluorescent markers or labels (disabling them for use in measuring substrate deformations or cell structure).

Finally, imaging resolution is a vital component for TFM. As many TFM techniques rely on obtaining information about cell structure, the imaging resolution must be sufficient to capture these features. Failure to do so may result in inaccurate traction force reconstructions. Imaging resolution must also be high enough to distinguish fiducial markers and capture their displacements within

the substrate. This is a concern particularly when dense marker concentrations are employed, a scenario which is discussed below in Section 2.3.4.

2.3.4   Measuring cell force-induced deformations

Substrate deformations are measured by tracking the displacement of attached/embedded markers between the reference and deformed states of the sample. Each marker provides a unique measurement in space of the underlying deformations of the substrate. Therefore, the density of the markers (markers per volume) limits the spatial sampling frequency at which deformation data may be acquired. It is therefore crucial that marker densities are high enough to capture the spatial variations of the displacement field (i.e., to capture the variations with high enough resolution), while ensuring that the markers are small enough and the density is low enough that the presence of the markers does not appreciably alter the behavior of the system. Marker bead diameters typically lie within the range of tens of nanometers to micrometers [152], and typical mean particle spacings are in the range of one to tens of micrometers [62]. As a general rule-of-thumb, bead spacings for high-resolution TFM applications are typically found to be on the order of ten times the bead diameter [89, 126, 61]. Those seeking very high resolution displacement field measurements often turn to novel methods, such as the use of beads of different colors and multiple imaging channels [128, 89, 144], or even super-resolution microscopy [28], to capture useful images in samples with very high bead concentrations. The tracking of markers is commonly performed using either of two paradigms: single-particle tracking or cross-correlation-based tracking.

Single-particle tracking involves tracking the position of individual markers. The primary challenge lies in uniquely identifying the same markers in both the reference and deformed state images [43]. Images must therefore be of high enough signal quality and imaging resolution that marker beads may be reliably tracked with minimal errors and noise artifacts. The resulting displacement field typically consists of measurements acquired at randomly distributed locations in space (resulting from the random positions of marker beads). When force reconstruction is performed, these random sampling locations may either be used directly, or may be interpolated onto a grid, depending on the force reconstruction method chosen.

Cross-correlation-based tracking does not identify the motion of individual markers. Instead, it captures the motion of local groups of markers. This is commonly done via digital image correlation (DIC) for two-dimensional systems or digital volume correlation (DVC) for three-dimensional systems. DIC and DVC track the bulk motion of windowed regions of the sample containing multiple markers. As displacements are computed wherever a window is constructed, correlation-based tracking allows for the measurement of the displacement field to take place on a rectangular grid, which can be convenient for later processing steps (such as Fourier transforms) during force reconstruction.

When implementing cross-correlation-based tracking, cross-correlation window design plays a critical role in computing the displacement field. Large window sizes help reduce noise in the displacement field measurements, but come at the cost of poorer resolution, degrading displacement features on the order of and smaller than the window size. In other words, the window acts as a low-pass filter over the displacement data. Window profiles modify the inten-

sity across space within the windowed region and impact the spatial frequency response of the cross-correlation. Consequently, an improperly designed window may amplify or attenuate displacement features of differing sizes in a biased manner [10]. Correlation methods in TFM typically rely on the assumption of purely translational motion of marker clusters over small distances. Recent efforts in TFM have sought to mitigate this issue, enabling efficient correlation-based tracking of large deformations [10], as well as deformations which exhibit dilation/stretching [46].

Although various implementations of particle tracking and cross-correlation-based tracking are the most common tools employed by TFM researchers, it is worth noting that measuring deformations between images is a problem of ongoing interest and research in the field of computer vision. As such, a wide variety of algorithms are available for adaptation to specific TFM experimental settings and applications [167]. Optical flow algorithms are one example that has been explored for use in TFM [67]. Ultimately, the choice of tracking algorithm for a particular study will be influenced by many factors, including experimental conditions, traction force reconstruction method, desired accuracy, and available time and computing resources.

2.3.5 Force reconstruction

Of all the elements of TFM, the final reconstruction of cell traction forces is perhaps the most diverse. Various models and techniques have been introduced, with great potential for both refinement and innovation. Because force reconstruction is closely tied to both experimental design and ongoing developments

24

Common force reconstruction methods in TFM

Themes to consider:
- Sensitivity to noise
- Compatibility with complex systems/models
- Computational complexity

Direct methods
- Computes stress from strain using constitutive relations
- Cell tractions reconstructed from stress field
- Requires high resolution + low noise in displacement measurements

Inverse methods
- Inverts elasticity equations to generate hypothesized traction forces from measured displacements
- Often features an iterative process
- Sensitive to noise (typically mitigated with regularization)
- Very common, and has been applied to many diverse models

Finite element methods (FEM)
- Extremely powerful and well-suited for both simple and complex geometries/models
- Computationally expensive/time-consuming

Green's function methods (GFM)
- Limited scope of suitable geometries/models
- Vastly simplified + rapid computation
- May be hybridized with FEM for advanced methods

Boundary element method (BEM)
- Origin of modern TFM
- Reconstruction performed in space domain (similar in form to FEM)
- Relatively slow for GFM procedures (Inverts dense system of linear equations)

Fourier transform traction cytometry (FTTC)
- Commonly used method
- Reconstruction performed in Fourier domain
- Very fast, as the Fourier domain converts numerical convolution to multiplication (i.e., results in a very sparse system of linear equations)
- Requires uniform grid of displacement data

Traction reconstruction with point forces (TRPF)
- Constrains forces to focal adhesion sites
- Reconstruction performed in space domain
- Precursor to more advanced methods that incorporate cell mechanical models
- Potential to be more robust to noise, due to the constraints imposed on force distribution

Figure 2.2: Common traction force reconstruction methods in TFM, at a glance. Further details and discussion for each method can be found in the text. Reprinted with permission from Ref. [111]. © Springer, Cham (2018)

in TFM, it is important to be aware of its various forms, requirements, capabilities, and limitations. What follows is an overview of common methods, with large inspiration drawn from the review by Schwarz and Soiné [152], which the reader is encouraged to explore for further detail. A summary of the traction force reconstruction methods discussed here may be found illustrated in Fig. 2.2, with notable features outlined in Table 2.1.

Table 2.1: Features of standard TFM reconstruction methods

TFM method	Noise sensitivity	Typical noise mitigation	Computational cost	Compatible with complex geometries & materials?	Dimensionality
Direct TFM	High	Data smoothing	Low	Yes[a]	2D, 2.5D, 3D
FEM-TFM	High	Regularization	High	Yes	2D, 2.5D, 3D
BEM	High	Regularization	Medium	No	2D, 2.5D
FTTC	High	Data smoothing & regularization[b]	Very Low	No	2D, 2.5D
TRPF	Low[c]	Regularization	Low[d]	No	2D, 2.5D

[a]Assuming a suitable stress-strain constitutive relation is available
[b]Typically uses cross-correlation-based tracking, which smooths data. Force reconstruction is often regularized.
[c]Extra information used by this technique helps stabilize force reconstruction
[d]Determined by number of focal adhesion sites
Reprinted with permission from Ref. [111]. © Springer, Cham (2018)

Direct and inverse methods

One intuitive method available for the reconstruction of cell traction forces is what has been referred to as the 'direct' TFM method [152]. By making use of measurements of the strain field within the substrate, stress can be computed 'directly' via the stress-strain constitutive relation which characterizes the substrate material (such as Hooke's law for linear elastic solids) [172, 62, 47, 63]. As a result, the stress field can be determined throughout the deformed substrate by plugging the measured strain field into the constitutive relation. Cellular

traction forces located at the cell membrane can then be computed from the stress field. This method relies on obtaining a reasonably accurate approximation of the strain field. In practice, the strain field is obtained by taking the spatial gradient of the measured displacement field data. As a consequence, the displacement field must be measured with high enough resolution to sufficiently capture its variability over small regions. Moreover, the measurements must have low noise, because gradient operations amplify noise artifacts, especially over short spatial scales. In the presence of sufficiently high noise, the gradient operation must often be accompanied by some form of filtering or regularization operation [47]. Direct TFM is a younger member in the family of traction force reconstruction methods. Used primarily in 2.5D-TFM settings, its emergence has been enabled by the growing availability of high-quality 3D imaging [152]. Though it is currently less prevalent than older methods, direct TFM has demonstrated promise for application in substrates that exhibit large deformations [172] or viscoelasticity [173], which many of the more common methods (e.g., Green's function methods, which will be discussed shortly) are not compatible with.

An alternative framework is the family of 'inverse' TFM methods, which constitute the majority of methods reported in TFM studies. Inverse TFM does not compute stresses and tractions directly from the measured displacement/strain data, as is done in direct TFM. Instead, a hypothesis is made about what distribution of cellular traction forces would be most likely to produce the measured displacement field, given the constraints of a suitable mechanical model. Depending on the specific technique chosen, this estimate may be arrived at either through direct computation or via iterative methods (although iteration is the dominant approach) [152, 19]. Iterative methods are constructed

to minimize (typically in the least squares sense) the discrepancy between the measured displacements and the displacements that would result from the reconstructed (hypothesized) traction field. To mitigate the impact of noise and address the ill-posed nature of the inverse problem, this minimization procedure is often regularized [152, 150, 144]. That is, the possible traction reconstructions are constrained by the imposition of additional information and/or constraints beyond those directly underlying the mechanical model [158, 150]. Regularization for inverse TFM will be addressed in greater detail at the end of this section.

Finite element and Green's function methods

In order to implement inverse TFM methods, one must be able to generate predictions of displacement fields that would result from hypothesized cell traction forces. There are two major approaches in the inverse TFM family for making such predictions: finite element methods (FEM) and Green's function methods (GFM).

The details underlying finite element analysis are beyond the scope of this chapter. However, in brief, finite element methods operate by partitioning a model of the sample into a set of discrete subunits, or elements. The behavior of each element is governed by the fundamental (elasticity) equations of the system, with constraints imposed on each element by its neighbors and/or the boundary conditions of the substrate. This allows for the construction of a system of equations that may be solved through various methods. FEM has the advantage that it can be adapted to model complex geometries and governing equations. For this reason, FEM has found significant use in the area of

3D-TFM, where complex cell boundaries prevent the use of analytical solutions to the elasticity equations in the traction force reconstruction process [54, 89]. FEM is also suited to nonlinear material models and geometric nonlinearities resulting from large deformations [152, 161]. As a result of its broad capabilities, FEM has played a key role in many TFM studies and will likely continue to do so in emerging methods and future studies (although applications of FEM to biopolymer substrates will likely rely increasingly on novel mechanical characterization techniques in order to take advantage of more advanced mechanical models). Despite its clear advantages and future prospects, the power and flexibility of FEM come at substantial computational cost, which motivates the use of simpler models and computing methods to accelerate the process of traction force reconstruction.

One family of alternatives to FEM is Green's function methods. GFM models make use of several assumptions to enable efficient computation of traction forces. These include the ubiquitous assumptions which constrain the substrate to be composed of a linear, elastic, isotropic, homogeneous material (although these assumptions often do not apply in tissues). In addition, GFM models rely on the assumption of small strains (to avoid geometric nonlinearities from large deformations) and are often confined, in practice, to simple substrate geometries with traction forces applied on a planar surface (although this is not always the case, as discussed in Section 2.4.1).

Although using these assumptions and constraints can limit the accuracy and physiological relevance of TFM studies, they vastly simplify the computation required for traction force reconstruction. For GFM in particular, these assumptions allow for the substrate to be regarded as a linear space-invariant (LSI)

system which takes cellular traction forces as the input and yields substrate deformations as the output. The response of such a system to a point-like cell traction force (as might approximately occur at a focal adhesion site [158, 150, 132]) is described by a Green's function, which is determined by the properties and geometry of the system. Due to the linearity of the substrate, the solution to the elasticity equations that relate traction forces to substrate displacements may be written as a weighted sum of these Green's functions. Specifically, the relationship between the substrate deformations and the applied traction forces is described by a convolution relation [144]:

$$\mathbf{u}(\mathbf{r}) = \int \mathbf{G}(\mathbf{r} - \mathbf{r}')\mathbf{f}(\mathbf{r}') \, d\mathbf{r}' \tag{2.1}$$

where $\mathbf{u}(\mathbf{r})$ denotes displacement of the substrate at the location $\mathbf{r} = (x, y, z)$, $\mathbf{f}(\mathbf{r}')$ denotes the cell traction force applied at the location $\mathbf{r}' = (x', y', z')$, and $\mathbf{G}(\mathbf{r} - \mathbf{r}')$ denotes the (spatially invariant) Green's function of the system. The integration over $\mathbf{r}'$ signifies a summation of contributions from all the traction forces exerted throughout the sample. In other words, the substrate displacement at any one location is a net effect of all traction forces exerted throughout the sample. The dimensionality of the system under study will determine the number of components/elements in $\mathbf{u}(\mathbf{r})$, $\mathbf{f}(\mathbf{r}')$, and $\mathbf{G}(\mathbf{r} - \mathbf{r}')$. As a simple example of how Green's functions relate traction forces to substrate displacements, consider a 2D-TFM system which assumes only transverse forces and displacements (as is common throughout early and many modern TFM works). The displacement of the substrate $\mathbf{u}$ (at $\mathbf{r}$) in response to a single point-force $\mathbf{f}$ (at $\mathbf{r}'$) can be expressed using Cartesian coordinates (x, y) by:

$$\begin{bmatrix} u_x \\ u_y \end{bmatrix} = \begin{bmatrix} G_{xx} & G_{xy} \\ G_{yx} & G_{yy} \end{bmatrix} \begin{bmatrix} f_x \\ f_y \end{bmatrix} \tag{2.2}$$
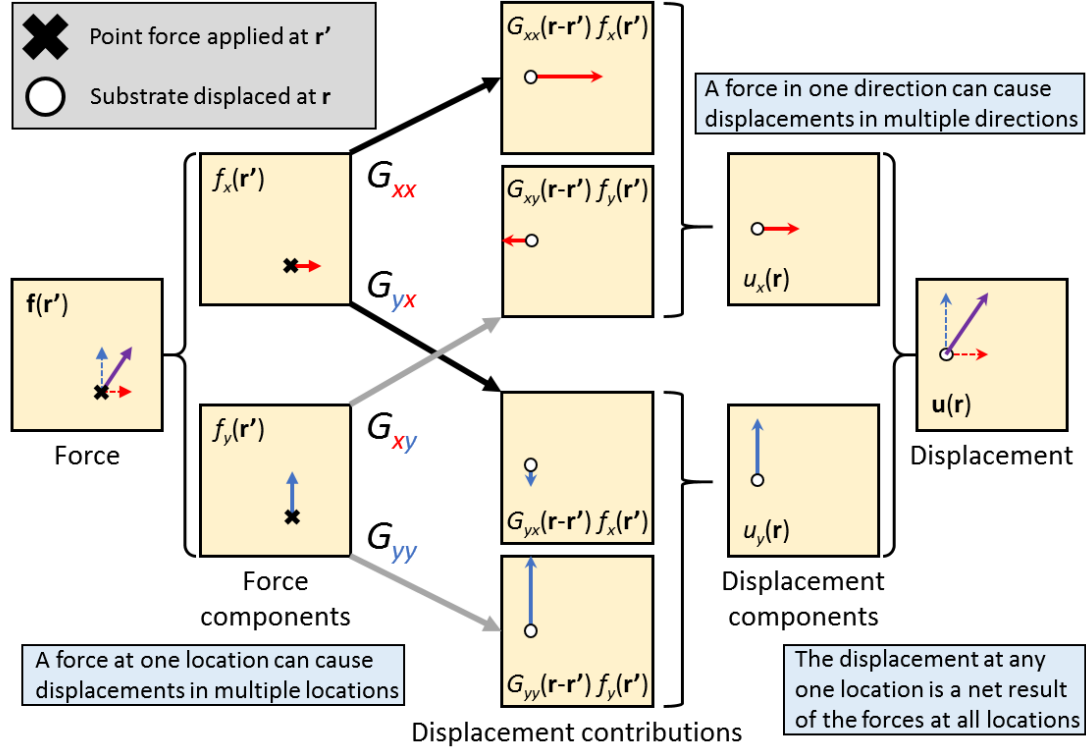
Figure 2.3: How Green's functions relate traction forces to substrate displacements. The above diagram serves as a depiction of how a 2D system governed by Eqns. (2.1) and (2.2) responds to localized traction forces. In principle, Eqn. (2.1) allows displacements throughout the substrate to be computed from any general distribution of cell traction forces, so long as a Green's function for the system can be determined. The goal of GFM-based force reconstruction is to invert the above process (i.e., to generate a distribution of traction forces from the known Green's function and measured substrate displacement data). Reprinted with permission from Ref. [111]. © Springer, Cham (2018)

where u_i and f_j denote the components of displacement and force, respectively, and G_{ij} denotes an element of the system's Green's function, which describes the contribution of the j-component of force (at $\mathbf{r}'$) to the i-component of displacement (at $\mathbf{r}$). Figure 2.3 provides an illustration of this example. As can be seen with this notation, it is important to note that a force in one direction can contribute to displacements in any direction.

As the relation of force to displacement is given by a convolution, the objec-

tive of GFM is then to perform deconvolution, using the known Green's function and displacement data to invert the relation in Eqn. (2.1) and reconstruct the cell traction forces. There are various methods by which this deconvolution is achieved in the field of TFM, which will be detailed below. Currently, GFM has been applied to 2D- and 2.5D-TFM systems [36, 19, 150, 106, 35], with cells adhered to an elastic substrate with a flat surface geometry. Green's functions have been determined and used for models of the substrate as an elastic half-space [19] and as a slab of finite thickness [63]. A variation of GFM hybridized with FEM has also been applied to 3D-TFM (detailed in Section 2.4.1).

One major theme to keep in mind throughout the following sections is the issue of experimental noise. Green's functions in TFM act as low-pass filters, attenuating features that span short spatial scales. Upon measurement of substrate displacements, noise corrupts the true displacement signal. As traction force reconstruction involves inverting the low-pass effects of Green's functions, noise artifacts are amplified over short spatial scales and can have a severe impact on the quality and accuracy of reconstructed traction forces [144]. This motivates the use of regularization, which is detailed at the end of this section.

Common variations of Green's function methods

There are three primary techniques used in TFM to reconstruct forces using Green's functions. These are the boundary element method (BEM) [36], Fourier transform traction cytometry (FTTC) [19], and traction reconstruction with point forces (TRPF) [150]. Application and implementation of these methods involves several important considerations, which are discussed in the primary literature. The basic concepts are outlined below.

BEM was the first method to emerge among modern TFM techniques that enable accurate quantitative traction force reconstructions [36]. BEM requires, in addition to the displacement data, a tracing of the cell boundary. Once this boundary is established, the surface region of the cell that is in contact with the substrate is approximated by a discretized mesh. It is assumed that traction forces may originate only from within this surface (Fig. 2.4, panel 3). The discrete set of locations where cell tractions may originate is combined with the discrete displacement data to convert Eqn. (2.1) into a linear system of equations, which may be solved using standard methods. (This makes BEM similar in form to FEM but performed with simplified equations and without generating a mesh representation of the surrounding substrate.) In practice, due to noise constraints, the system is usually inverted with a variation of regularized least squares. In summary, this method solves the inverse problem in the space domain but depends upon reliable cell tracing and can be sensitive to the chosen meshing procedure [36, 144]. Because the linear systems of equations solved by BEM are often very large and dense/non-sparse, BEM can take longer to execute than other GFM techniques.

In contrast, FTTC solves the inverse problem in the Fourier domain, where the relation described in Eqn. (2.1) takes the form:

$$\tilde{\mathbf{u}}(\mathbf{k}) = \tilde{\mathbf{G}}(\mathbf{k})\tilde{\mathbf{f}}(\mathbf{k}) \tag{2.3}$$

where $\tilde{\mathbf{u}}(\mathbf{k})$, $\tilde{\mathbf{G}}(\mathbf{k})$, $\tilde{\mathbf{f}}(\mathbf{k})$ denote the Fourier transforms of the displacement field, Green's function, and traction field, respectively, and $\mathbf{k}$ denotes the spatial frequency coordinate [152, 19, 144]. Since convolution (Eqn. (2.1)) is converted to multiplication in the Fourier domain (Eqn. (2.3)), the reconstruction of traction forces is reduced to $\tilde{\mathbf{f}}(\mathbf{k}) = \tilde{\mathbf{G}}(\mathbf{k})^{-1}\tilde{\mathbf{u}}(\mathbf{k})$, which is simply a multiplication of the Fourier domain displacement data with the inverse of the Fourier domain
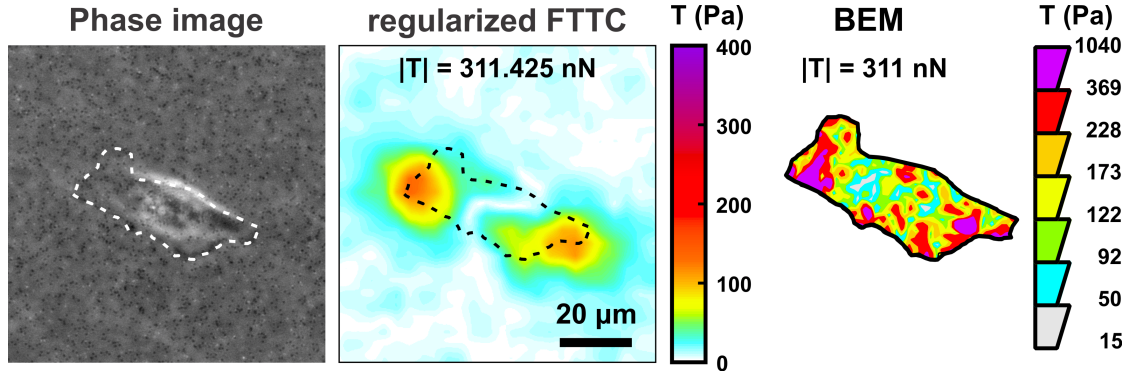
Figure 2.4: Comparison of traction force reconstruction with FTTC versus BEM. Phase contrast image of an MDA-MB-231 cell (left) and associated traction force reconstructions using FTTC (middle) and BEM (right). The substrate consisted of a collagen-coated polyacrylamide gel with Young's modulus of 5 kPa, with embedded Alexa fluor 488 polystyrene beads (diameter 0.5 μm). FTTC was regularized with Tikhonov regularization. Note that the tractions reconstructed using FTTC do not necessarily correspond to the true cell surface. The reconstructed traction forces are also very smooth, due to a combination of regularization and low fluorescent bead density. The tractions reconstructed with BEM, on the other hand, are confined exclusively to the cell surface but possess a more irregular distribution of forces. This feature is likely to be an artifact of noise and insufficient regularization. Reprinted with permission from Ref. [111]. © Springer, Cham (2018)

Green's function. However, this procedure is sensitive to the presence of noise or other errors in the displacement data, and therefore is typically modified with a regularization procedure (which will be discussed in the next subsection). Following the inversion process, the reconstructed traction forces are obtained by taking the inverse Fourier transform of $\tilde{\mathbf{f}}(\mathbf{k})$. Note that in order to make efficient use of Fourier transforms (i.e., via the fast Fourier transform), displacement data must be provided at locations on a uniform rectangular grid (either through interpolation or the use of correlation-based displacement tracking). In general, FTTC is very fast compared to space domain methods, since the Fourier transforms and element-wise multiplications used by FTTC have lesser computational complexity than space domain operations like convolution and matrix inversion. As a result, FTTC methods are very common in the literature due

to both their simplicity and efficiency. One drawback of FTTC is that it does not make use of any information about the cell structure and as a result is vulnerable to predicting the presence of traction forces originating outside the cell boundary (Fig. 2.4, panel 2). FTTC may be modified to mitigate this concern. However, such procedures are not frequently reported in the literature [19].

TRPF, as its name suggests, seeks to reconstruct a force distribution consisting of point-like forces, unlike the smoother/continuous distributions generated by BEM and FTTC [150]. TRPF assumes that cell traction forces are localized to focal adhesion sites. By imaging the locations of these sites in any given cell with appropriate fluorescent labeling (assuming these additional imaging capabilities are available), a set of acceptable locations where traction forces may originate is established. Similar to BEM, this set of locations is used in conjunction with the displacement data to allow Eqn. (2.1) to be converted into a linear system of equations. Due to the sparsity of locations where traction forces may be reconstructed, TRPF can mitigate the effects of noise (and the associated need for regularization) by constraining the possible traction force solutions, although this potential benefit degrades with increasing numbers/density of point forces [150, 144].

Regularization

The reconstruction of cell traction forces from measured displacements via inverse methods is an ill-posed problem. That is, when the true substrate displacements are not precisely known due to uncertainties from noise or errors in the data, cell traction forces cannot be precisely reconstructed (i.e., the reconstruction process does not produce unique solutions). In addition, small changes in

the displacement data can result in large changes in the reconstructed traction field (i.e., the reconstruction process is sensitive to noise) [150]. As a result, the presence of noise can have a severe impact on the accuracy and quality of traction force reconstructions. To address this issue, the inverse problem may be regularized.

Regularization incorporates additional *a priori* information into the inverse problem, beyond that which is already contained in the displacement data and mechanical model used during force reconstruction. This information helps constrain and stabilize the possible traction force solutions to the ill-posed inverse problem presented by TFM [150]. In other words, regularization assumes that certain types of reconstructed force distributions are not valid solutions to the inverse problem. The specific regularization procedure determines what types of solutions are suppressed and what trade-offs may result. Although regularization can be formulated to impose many types of constraints, most forms of regularization employed in TFM are specifically designed to suppress the effects of noise artifacts in the reconstruction process.

FTTC can provide some intuition as to why noise is such a prevalent concern. Following from Eqn. (2.3), unregularized FTTC reconstructs traction forces as a product of the inverse Green's function and the displacement data: $\tilde{\mathbf{f}}(\mathbf{k}) = \tilde{\mathbf{G}}(\mathbf{k})^{-1}\tilde{\mathbf{u}}(\mathbf{k})$. However, Green's functions in TFM typically act as low-pass filters. In other words, the Green's function may have singular values that approach zero at higher spatial frequencies (i.e., when the magnitude of $\mathbf{k}$ is large). When singular values are small, multiplying the displacement data by $\tilde{\mathbf{G}}(\mathbf{k})^{-1}$ is akin to performing division by very small numbers. When this occurs, values in the displacement data are strongly amplified during force reconstruction. This is

a problem because any noise in the displacement data is also subject to these amplification effects. Regularization in TFM seeks to mitigate this effect.

The most common form of regularization in TFM for mitigating noise is zero-order Tikhonov regularization, which penalizes large values in the reconstructed traction force data [152, 144]. That is, force reconstructions that contain very large forces are assumed to be undesirable solutions to the inverse problem. Regularization suppresses these solutions by modifying the functions that relate traction forces and displacement data. For example, zero-order Tikhonov regularization applied to FTTC modifies the inversion process to take the form [152, 144]:

$$\tilde{\mathbf{f}}(\mathbf{k}) = \left(\tilde{\mathbf{G}}(\mathbf{k})^{\mathrm{T}} \tilde{\mathbf{G}}(\mathbf{k}) + \lambda^2 \mathbf{I} \right)^{-1} \tilde{\mathbf{G}}(\mathbf{k})^{\mathrm{T}} \tilde{\mathbf{u}}(\mathbf{k}) \tag{2.4}$$

where $\mathbf{I}$ denotes the identity matrix and λ is a scalar value, which determines the strength of the regularization procedure. In the case where $\lambda = 0$, Eqn. (2.4) is equivalent to the original unregularized FTTC formulation, $\tilde{\mathbf{f}}(\mathbf{k}) = \tilde{\mathbf{G}}(\mathbf{k})^{-1}\tilde{\mathbf{u}}(\mathbf{k})$. The effect of this new formulation is to alter the Fourier domain Green's function such that singular values close to zero have their magnitudes increased, while large singular values are left relatively unchanged. Specifically, a singular value with magnitude σ is modified by the regularization procedure to obtain a new magnitude $(\sigma^2 + \lambda^2)/\sigma$. This reduces the amplification of noise where the inversion process is most vulnerable (i.e., when the values of σ are close to zero). The trade-off of this regularization procedure in TFM is that reconstructed traction fields may be smoother than the true traction field and may underestimate the maximum traction values. Although FTTC was highlighted in the above example, the same principles apply to zero-order Tikhonov regularization in other force reconstruction techniques.

Selection of the regularization parameter λ involves making a trade-off between suppressing noise artifacts and over-smoothing the reconstructed traction field and must be taken into account when interpreting results. Selection of a parameter often involves solving the inverse problem several times until an optimal value can be determined. Because the optimal value may vary between datasets, this iterative optimization procedure must often be repeated between datasets, meaning that regularization parameter selection can add significant computational cost.

Although zero-order Tikhonov regularization is prevalent in TFM, its inherent suppression of large forces and tendency to smooth out the reconstructed traction field may be undesirable for a given study. Alternative regularization schemes may be sought to better meet experimental demands. For example, first-order Tikhonov regularization suppresses rapid spatial fluctuations in the traction field (by penalizing the gradient of the traction field, instead of the traction field itself). Although this regularization scheme would not directly suppress large forces, it would still act to smooth out the final reconstructed traction field, in exchange for suppressing noise artifacts [144]. In applications where cells exhibit strong localized forces, such as those seen at focal adhesion sites in 2D/2.5D settings, L_1-regularization may be an appropriate choice [9, 166]. This scheme imposes the assumption that the true traction field is sparse and so attempts to reconstruct a small number of regions containing strong localized tractions. In this manner, the mechanism by which L_1-regularization constrains the inverse problem is reminiscent of the TRPF method. However, this method requires longer computation times than other common forms of regularization. In general, this is because the solution to the L_1-regularized problem cannot be expressed in closed form and must be determined through an iterative process.

From another perspective, unlike TRPF, which takes focal adhesion sites as an input and reconstructs force, L_1-regularization must determine both the location and strength of cell traction forces simultaneously. Further discussion and details regarding other possible methods for regularization may be found in the literature of inverse problems [39].

It should be noted that regularization is not strictly necessary to address sensitivity to noise. For example, the use of cross-correlation-based displacement tracking (as is often done for FTTC) reduces noise artifacts through the filtering effects of the cross-correlation windowing functions. Noise is therefore reduced in the displacement data before it is input into the inverse problem. Of course, accurate reconstructions rely on raw images and correlation windows that support the spatial resolution (and corresponding spatial bandwidth) necessary to preserve all the relevant displacement data across the filtering operation. If this condition is not met, noise may be suppressed, but the reconstructed traction field may also become over-smoothed, similar to what happens in the case of over-regularized traction reconstructions.

2.4   The future of TFM

Much remains to be achieved in order to extend TFM to the study of more complex, physiologically relevant, biological systems. In addition, expanding the use of TFM within mechanobiology will require advances that make new methods more accessible to researchers from diverse areas of study. This will be important to enable discoveries made through fundamental mechanobiology and biomechanics research that may be later translated into new clinical diagnosis

and treatment paradigms. Future improvements, such as addressing nonlinearity, heterogeneity, ECM remodeling, etc., have often been relegated to a few cursory statements in the discussion sections of primary literature. This is not unreasonable, as the work involved to experimentally address these concerns is far from simple. However, ongoing research efforts have nevertheless persisted and sought to advance TFM to address new levels of system complexity. In this section, we review the motivations and recent advancements made to address several factors that may be critical to future research efforts in TFM and cell mechanics.

2.4.1   Advanced force reconstruction methods

The development of novel force reconstruction methods largely relies on two primary resources. First is the development of new mechanical models that incorporate additional information about the mechanical properties and features of both substrates and cells. Second is the development of reconstruction methods that minimize computational complexity, in order to make efficient use of available time and computing resources. New methods that help better address these needs hold strong promise for advancing TFM and mechanobiology at large. For example, the incorporation of additional cell structural data may enable the development of more robust and useful TFM models and results. Soiné et al. presented what has been termed 'model-based TFM' (MB-TFM) [158]. MB-TFM uses images of both focal adhesion sites and stress fibers to construct an approximate mechanical model of the cell under study. Presently demonstrated in a 2D setting, MB-TFM models stress fibers and the actin network together as a cable network that distributes internal cellular tension and uses focal adhesion

sites as anchor points that exert traction forces on the substrate. An FEM-based algorithm determines what distribution of fiber tensions will produce the necessary forces at the focal adhesion sites to generate the measured displacement field. This method has been shown to be robust to measurement noise, without the need for regularization. In essence, the constraints imposed by the cable network mechanical model provide the necessary stabilizing information that would otherwise be provided by regularization in other TFM methods. The reason for this becomes clear when observing that the traction forces at individual focal adhesions are related to one another, as mediated by the communication of forces over the stress fiber + actin cable network. MB-TFM is thus more strongly constraining than the TRPF method discussed previously, which did not assume a mechanical correlation between forces at different focal adhesion sites. Finally, in addition to the reconstructed traction forces, the network tensions yield information about the internal distribution of forces within the cell, offering potential insight into the mechanisms of force transmission and mechanosensing beyond what could be achieved with prior TFM methods. MB-TFM still has its limitations, however. As described in the original work, MB-TFM cannot be universally applied to all cell types/scenarios. In addition, MB-TFM relies on high-quality imaging of cellular features, which is not always readily available, and can be negatively impacted by chemical reagents that modulate cell contractility behavior [158].

Other advances have led to progress in the area of computation time. Although GFM-based traction force reconstructions have allowed for the accelerated development of TFM as a tool for studying cell mechanics, future advances will likely rely on more computationally expensive methods like FEM to analyze increasingly complex models of cells and surrounding environments.

As such, novel computing methods that maximize the ability of researchers to study complex systems while minimizing computational cost/time are of high value to the field of TFM. One prime example is the method presented by Legant et al. for 3D-TFM [89]. In brief, the complicated 3D geometry of the cell-substrate interface made standard GFM impossible, since the system's Green's function was no longer spatially invariant (a fundamental characteristic leveraged by standard GFM models). In other words, the function $\mathbf{G}(\mathbf{r} - \mathbf{r}')$ in Eqn. (2.1) became a more general $\mathbf{G}(\mathbf{r}, \mathbf{r}')$. In addition, an analytical formula to describe the new spatially varying Green's function would be incredibly complex, which implies that FEM would be a superior computing option. However, iterative execution of FEM solvers to reconstruct the traction field would be extremely computationally expensive. A hybrid solution was therefore developed. First, the cell-substrate interface was approximated with a discretized mesh. FEM was then used to compute the displacements induced by a unit traction applied at a single facet of the discretized mesh. By repeating this process for each facet, the spatially varying Green's function was computed. This numerically derived Green's function was then used to accelerate the reconstruction of traction forces beyond what could be achieved with FEM alone. This method and future hybridized methods like it, which use FEM to do the 'hard work' of faster algorithms, may pave the way to making TFM a more efficient and readily accessible tool in the arsenal of cell mechanics researchers working on difficult and computationally intensive problems like 3D-TFM.

2.4.2 3D forces and environments

It has been established that cell behavior can greatly differ in 2D versus 3D environments [180, 186, 157, 117]. Although 2D cell culture is convenient to study, many cell systems of interest natively develop and interact with 3D tissue environments, where they are influenced by ECM mechanical properties and 3D forces [14]. As such, the measurement of cellular forces in 3D settings may be critical to future research in morphogenesis, cancer, and other processes. For years, TFM was largely restricted to 2D environments and 2D cell traction reconstructions. However, even cells cultured on 2D surfaces can exhibit significant forces with components in all three dimensions [188, 47, 35], motivating the development of '2.5D-TFM' techniques that capture these 3D forces. In recent years, 3D-TFM research has expanded the field to the study of 3D forces exerted by cells cultured within fully 3D environments. As discussed in the previous section, the methods presented by Legant et al. [89], which made use of a hybridized FEM-GFM approach for traction force reconstruction, are a predominant work in the growing collection of 3D-TFM research [54, 62, 110, 78, 112]. Although 3D-TFM is not necessarily a 'new' technique and has already been the subject of substantial research efforts, many outstanding challenges remain to be addressed in order to realize its full potential for revealing the roles of cell forces in 3D environments and behaviors.

Major challenges to 3D-TFM span the full spectrum of stages in the TFM workflow, including sample fabrication, imaging, mechanical characterization, modeling, and traction force reconstruction. Fabricated 3D substrates must present a physiologically relevant environment that enables normal cellular activity (and therefore requires the use of engineered polymers or natural biopoly-

mers). The 3D imaging required to capture cell features and substrate displacements can be time-consuming (a problem if cell behaviors and forces are dynamic) and can be impeded by optical challenges like scattering, absorption, and photobleaching/phototoxicity. Many 3D substrate materials (such as ECM proteins) can be highly nonlinear, heterogeneous, and anisotropic and are difficult or impossible to characterize on the micro- to nanoscale with conventional methods. Finally, modeling and force reconstruction (implemented using FEM) can be difficult to implement and incur substantial computational costs. Despite these challenges, the need to understand the role of forces in 3D tissue models will promote a continued growth of 3D-TFM methods in the future.

2.4.3 Collective behaviors

Many questions of interest in the field of mechanobiology involve not just single cells, but entire cell collectives which contribute to emergent features and behaviors [145, 135, 116, 23, 59, 168, 120, 37, 69, 192, 177, 175, 174, 123, 48, 86]. An increasing interest in the collective mechanical behavior of cells has arisen from experimental evidence in both normal organism development [193] and pathological data [59]. Collective cell behaviors have already been the subject of extensive study in 2D settings, and recent research has begun to yield insights into collective behaviors in 3D environments. These investigations have enabled the observation of such phenomena as cell jamming [145, 59, 123], collective polarization and migration [116], wave-like propagation of cell velocities and tractions [154], emergent compressive stresses in the ECM, and mechanical interaction of separated cell clusters [54]. TFM has contributed to several studies of traction forces exerted by cellular collectives in both 2D and 3D set-

tings [54, 135, 116, 175, 154], with expanded application likely in the future. Measuring the traction forces of cell collectives presents several imaging challenges. Observation of collectives requires a large imaging field-of-view (in two or three dimensions) while maintaining a sufficiently high resolution to capture cell features and substrate deformation data at length scales appropriate to the phenomena being studied. Moreover, imaging may need to take place over a wide range of time scales, from minutes, to hours, to several days for standard model systems, or even weeks in future studies of tumor formation or development. Finally, as cell collectives can substantially modify the ECM and exert strong forces, TFM with cell collectives will likely have to address several of the other challenges discussed in the rest of this section, such as heterogeneity, remodeling, and nonlinearity.

2.4.4   Beyond linear elasticity

Although linear elastic environments are easy to fabricate and study, they do not capture many of the complex properties of biological tissue, such as viscoelasticity or nonlinearity, which may be crucial for understanding cell behavior. For example, it has been shown that stem cell differentiation and behavior are altered by the viscous/relaxation properties of their surroundings [25, 24]. However, whether viscoelasticity has a corresponding effect on cell traction forces remains to be characterized. Studying cell traction forces in such environments requires new models to connect traction forces to substrate deformations. Toyjanova et al. have demonstrated one framework for TFM which incorporates viscoelastic properties, opening new avenues for studying systems beyond what current quasi-static/purely elastic models can accommodate [173].

Nonlinearity is a potentially rich area for exploration with TFM. Indeed, most biological materials in which cells reside exhibit nonlinear mechanical behavior. It is therefore not surprising that cells are able to respond to these nonlinear properties. For example, fibrous networks such as collagen support long-range force transmission over small collections of fibers, a highly nonlinear process that can enable long-range mechanical communication between cells [70, 161, 61, 143, 138]. Steinwachs et al. recently demonstrated 3D-TFM of cells cultured in a collagen environment, making use of a nonlinear model [161]. In that work, collagen was modeled as having three regimes of mechanical behavior, corresponding to the buckling, straightening, and stretching of collagen fibers. The FEM-based nonlinear 3D-TFM framework was used to study cell traction forces and migration dynamics, as well as responses to varying collagen concentrations. Hall et al. used another approach [61], wherein the 3D collagen network surrounding the cell was modeled as containing both regions of isotropically oriented fibers and regions of (anisotropically) aligned fibers. A fiber network model was used to study how cell-induced strain may create regions of aligned collagen fibers from initially isotropic orientations and how such alignment alters the local ECM mechanical properties [182]. This network model was then used to yield a nonlinear continuum model for FEM-based cell force reconstruction, allowing insight into mechanical feedback interactions between cells and the surrounding collagen ECM [61, 182]. Future TFM studies incorporating nonlinearity will likely face significant challenges in achieving reliable mechanical characterization of samples. Inverse TFM methods will also face a need for computationally intensive FEM-based models to enable traction force reconstruction in nonlinear systems. Nevertheless, progress will continue, as further extensions of TFM for nonlinear systems stand to greatly enhance un-

derstanding of the diverse physical interactions of cells with physiological ECM environments.

2.4.5 Heterogeneity

Although homogeneity has been a convenient assumption for the field of TFM, the environments presented by tissues are often highly heterogeneous. Notably, as revealed by *in situ* observations, the stroma becomes increasingly heterogeneous as collagen is deposited during tumor progression [134]. Heterogeneities in tissue can take many forms, including changes in density, stiffness, architecture, pore size, and levels of cross-linking, all of which can have bearing on cellular behaviors [14, 22, 104]. It is therefore likely that future TFM studies will need to address the effects of heterogeneities on cell force. For example, cells cultured on micropillar arrays with spatially varying stiffness have been shown to exhibit a preference for stiffer substrates, where they exert greater force [17, 179, 146]. Some initial work of TFM in the area of heterogeneity has investigated the effects of stiffness gradients [179], barriers to cell migration [77], and cell-induced mechanical heterogeneities [54]. Heterogeneities not only affect cell behavior, but cell activity induces heterogeneity on many length scales [54, 21, 74]. Cell-induced heterogeneity can also negatively impact cell traction force reconstruction, if not properly accounted for [54]. Future work will require both novel substrate fabrication techniques as well as new mechanical characterization methods and improved computational models to better understand the impact of heterogeneity on cell forces and behavior.

2.4.6 Anisotropy

It has been demonstrated that anisotropy significantly impacts cell behavior [21, 9]. For example, substrates with oriented nano/microtopographies have been shown to influence cell alignment [6] and the differentiation of adult neural stem cells [136]. Cells will also preferentially align and migrate in the direction of greatest rigidity [146]. In addition, remodeling of the ECM by both single cells [21] and cell collectives [45] tends to result in anisotropic fiber alignments. That is, cells not only react to anisotropic environments, but they actively create them as well. Anisotropy is therefore a potentially rich area of application for future TFM research. Though uncommon, some work has been done to apply TFM to anisotropic settings. For example, FEM-based TFM has been conducted to reconstruct the 3D forces exerted by cells grown on a non-planar, 'wavy' surface (i.e., with topographical, as opposed to mechanical, anisotropy) [159]. Anisotropic systems pose challenges for both mechanical characterization and computational reconstruction of traction forces. In tissues, anisotropy is often accompanied by heterogeneity and nonlinearity, adding further complications to traction force reconstruction. Depending on the system under study, anisotropic samples may result in imaging consequences, such as a spatially varying optical point spread function, which can impact the tracking of embedded bead displacements [159]. Future TFM methods that address anisotropy and its associated challenges will likely be crucial to the future study of accurate tissue models and cell forces.

2.4.7 Remodeling and dynamics

ECM remodeling and dynamics are essential features of many cellular processes and behaviors [34]. For example, the migration of highly invasive cancer cells is facilitated through remodeling of the ECM, resulting in the formation of tumor-associated collagen signatures (TACS), such as increased collagen density, the presence of straightened (taut) collagen fibers, and radially aligned collagen fibers that facilitate invasion [134]. Radially aligned fibers oriented away from a tumor, sometimes referred to as 'collagen highways', are associated with the most invasive phenotypes of cancer and have been observed *in vitro* [23], in animal models [134], and in clinical cases [31]. Cells can modulate the mechanical properties of the ECM with traction forces via strain-hardening, and through degradation of the ECM with matrix metalloproteinases [74]. Moreover, cells can exert forces on the timescale of minutes [21] and can induce significant ECM remodeling on the timescale of hours [54, 23]. Not only are dynamics and ECM remodeling of interest to biomechanics research, but their effects can severely impact traction force reconstructions (such as through the formation of heterogeneities, anisotropy, and nonlinear effects) [161, 54]. As a result, TFM techniques that capture and accommodate ECM remodeling and cell dynamics are crucial to generating a complete picture of biophysical phenomena.

Some works in TFM have already begun to investigate the relationship of remodeling and dynamics with cell traction forces. Gjorevski and Nelson investigated the forces exerted by microfabricated mouse mammary epithelial tissues embedded in collagen gels [54]. It was determined through imaging and AFM that cellular activity introduced significant mechanical heterogeneity into the collagen ECM. Incorporating this heterogeneity into the traction force recon-

struction process suggested that failing to account for these cell-induced ECM modifications may result in severe underestimation of cellular traction forces. Other works in TFM have explored the role of traction forces in many scenarios involving 2D collective cell migration and dynamics. For example, Notbohm et al. investigated the traction forces and migration dynamics of confined monolayers of canine kidney cells. The monolayers exhibited collective traction forces and motions that oscillated in time. Serra-Picamal et al. reported the presence of 'waves' of traction forces, intercellular stresses, and cell velocities propagating through a cell monolayer [154]. These waves are not the result of passive phenomena (as are everyday waves like sound, light, or vibrations). Instead, these waves are hypothesized to be an active spatiotemporal phenomenon governed by dynamic cellular responses to mechanical communication from neighboring cells. Future works that explore cellular remodeling and dynamics with TFM may lead to further novel observations of cellular behaviors and their effects on the ECM environment.

2.4.8 Mechanical characterization of substrates

The use of synthetic substrates with established fabrication protocols has made the task of substrate mechanical characterization a relatively simple one, when compared to the biological and computational components of typical TFM experiments. Mechanical characterization has often been performed using bulk rheometry, indentation testing, or atomic force microscopy. However, as TFM applications move increasingly toward the use of natural biopolymers which exhibit complex mechanical behaviors, these established methods will become less applicable. The study of three-dimensional systems and ECM remodel-

ing will further compound this problem. As a result, future TFM efforts will rely on the use of novel techniques for mechanical characterization in 3D ECM and tissue environments. Several emerging techniques have made significant strides toward addressing these needs. These include Brillouin microscopy (BM) [4, 148, 190, 147], optical coherence elastography (OCE) [75, 184, 113, 87], and optical tweezers-based active microrheology (AMR) [74, 79]. These emerging methods enable the noninvasive measurement of mechanical properties in 3D substrates. Although the ability of these methods to provide reliable quantitative mechanical properties relevant to TFM are currently limited, future research into these and related techniques may enable the development of novel imaging platforms capable of noninvasively capturing the 3D distributions and dynamics of cell structures, traction forces, and ECM properties, an ambitious endeavor with great potential for accelerating cell biophysics research.

2.4.9 Novel imaging platforms

To date, the imaging platforms of choice for TFM have been fluorescence microscopy and confocal fluorescence microscopy. However, with a growing diversity of TFM methods and application spaces, TFM research stands to benefit from the use of novel imaging platforms to expand its capabilities. For example, TFM has been recently performed using stimulated emission depletion (STED) microscopy [28]. STED and other super-resolution methods may allow substrate deformations to be imaged with higher resolution (by allowing for higher bead concentrations) and can provide detailed information about protein structures in and around cells. Confocal reflectance microscopy was recently employed for 3D-TFM [76], eliminating the need for either fluorescent labels or

marker beads. Instead, deformations were measured by directly tracking the motion of collagen fibers. Optical coherence microscopy (OCM) has recently been demonstrated as a means to enable 3D-TFM in highly scattering media with rapid volume acquisition speeds [110, 112, 94] (see Chapters 5–7). Another advantage of an OCM-based system would be the opportunity to merge TFM and optical coherence elastography in a single imaging system, enabling measurement of both substrate deformations and changes in substrate mechanical properties due to remodeling and/or strain-hardening. Other rapid volumetric imaging modalities, such as light sheet microscopy or swept confocally aligned planar excitation (SCAPE) microscopy [16], may be well-suited for volumetric TFM studies in substrates with lower optical scattering.

2.4.10 Advancing mechanobiology

Although great strides have been made in TFM to increase resolution, accuracy, and compatibility with new environments, the fact remains that implementing TFM–from experimental design, to imaging, to data processing and force reconstruction–is not a trivial task. This is because the development and implementation of new techniques relies on expertise from across a wide range of academic disciplines. Ultimately, researchers in the field must often make trade-offs. For example, incorrect assumptions or approximations can severely corrupt traction force reconstructions. However, the data obtained may still yield insight toward answering the biological questions at hand, and the 'inaccurate' method may turn out to be less time-consuming or easier to implement. The question that must be answered is, what TFM protocols and performance levels are sufficient for a given experiment? Alternatively, in the context of Fig. 2.1,

what methods are sufficient to provide the necessary insights that address the biological question? In some contexts, forces may not even be strictly necessary, so long as information related to forces and cell energy expenditure are available. Koch et al. presented methods for quantifying ECM strain energy, circumventing the reconstruction of traction forces exerted by cells embedded in 3D environments [78]. Similarly, Stout et al. devised the use of 'mean deformation mechanics' as a substitute for cell force reconstructions when the mechanical properties of the substrate are not well-characterized [162]. As TFM methods advance, those who wish to make use of TFM as a tool for mechanobiology research will have to carefully consider the quantitative needs of their research questions and what the various TFM methods have to offer.

As new techniques in TFM migrate from development to widespread application, methods to make the new tools compatible with the high-throughput needs of biophysics and mechanobiology researchers will be a necessity. Even if a method is imperfect, its ability to perform rapid and repeated experimentation will be crucial to moving research efforts forward. As one example, Park et al. have presented a high-throughput cell traction force screening platform based on FTTC to enable rapid testing of how drug compounds impact cell forces [119]. With the development of such platforms, TFM can begin to make broader impacts and help further transform biophysics and mechanobiology research into a standard practice in biomedicine.

2.5 Conclusion

We have reviewed the central techniques and principles of traction force microscopy, including substrate choice, mechanical characterization, imaging, measurement of substrate deformations, and traction force reconstruction. Building on and moving beyond these principles, we have highlighted several areas of active research and potential future innovation, which may fuel the growth of TFM toward applications in the study of more realistic/physiological engineered tissue and tumor-like microenvironments which manifest traits such as nonlinearity, heterogeneity, and temporal variations due to cell-induced remodeling. TFM relies on a strong foundation of carefully engineered techniques, as demonstrated by ongoing research efforts taking place at every step of the process.

Underlying many of the ongoing technical innovations in TFM are two major themes: (1) the utilization of new constraints and information to form more complete mechanical models of cell biophysics and behavior and (2) the creation of novel force reconstruction methods that address both the challenges of speed and compatibility with physiologically relevant sample properties and geometries. Accompanying both of these themes are a few critical challenges. The development of high-throughput experimental methods and the minimization of computational complexity will play key roles in accelerating the investigation of new biological questions with TFM. And in order to make effective use of new models that are compatible with physiologically relevant environments, TFM will rely on the continued development of technologies that enable high-resolution mechanical characterization of tissue and ECM environments. Although advances made in TFM and other fields will enable research under in-

creasingly diverse conditions, managing trade-offs in accuracy versus through-put will likely remain a common theme in the near future.

Overall, TFM is more than a rapidly growing tool for the noninvasive measurement of cell forces. TFM has already played a leading role in many seminal works of mechanobiology, revealing the influence of physical properties and forces on cell behavior and exposing intrinsic differences between normal and cancerous cells [122, 80, 127, 121]. As an area of research, TFM has merged expertise from a wide range of academic disciplines and is fostering close collaborations between physical scientists, biological scientists, and clinicians. With future application in more physiologically relevant environments, TFM holds the potential to offer insights into the biophysical behaviors of both single cells and collectives over multiple length scales, spanning processes over minutes to days. Whether used to investigate the processes of how cancer develops and progresses, how wounds heal, or how cells go about their 'normal everyday functions' such as growth and morphogenesis, TFM remains and will continue to be a central tool to help understand cellular forces and their role in mechanobiology.

CHAPTER 3

FUNDAMENTALS OF SIGNAL COLLECTION AND IMAGE RECONSTRUCTION FOR SPECTRAL DOMAIN OPTICAL COHERENCE TOMOGRAPHY

3.1 Introduction

One of the most important things I have learned in my research program is the value of building a strong foundation. Innovation, just like learning, requires researchers to make new connections between many initially separate concepts, methods, and observations. The more tools, skills, and ways of thinking you have available, the easier it becomes to build those connections.

Although prior literature is rich in information and provides a good starting point, I found that doing the math, writing the code, and playing around with the concepts for myself was critical to developing a useful understanding and intuition about my field of study. I owe most of my own research achievements to long days and nights spent contemplating what might otherwise be considered trivial, mundane, or 'solved'. Such is the luxury of a doctoral program!

I found teaching to be an excellent way to identify holes in my own knowledge and to get asked just the right kinds of 'strange questions' that would ultimately lead to new ideas. Between the Fall of 2015 and the writing of this dissertation during the 2019-2020 academic year, I trained new lab members in the fundamentals of OCT imaging and signal processing. These 'OCT-101' lessons have been a fun tradition for me, and I will miss teaching them. I cannot understate how valuable they were to me (and hopefully, to the lab).

This chapter is my attempt to record and share these lessons with you.

Although OCT systems are simple to construct and use,[1] a strong understanding of the mathematics underlying OCT imaging is critical to the development of new methods, system designs, and algorithms. The sections that follow provide derivations and explanations of the equations underlying signal collection and image reconstruction for spectral domain OCT (SD-OCT). If you are not already familiar with these concepts, I strongly advise that this text be used as a guide *while you perform independent derivations for yourself*. If you *are* already familiar, I always recommend revisiting the derivations anyway. You never know what you will learn! Good luck, and most importantly, have fun!

3.2   Principles of OCT imaging

OCT microscopes record the position and contrast of scattering interfaces within an object via low coherence interferometry. In general, broadband light is made to propagate along two distinct optical paths following a free-space or fiber-based splitter. Along one path (hereafter referred to as the 'sample arm'), the light illuminates a 3D scattering object (the 'sample') whose structure is to be recorded. Along the other path (hereafter referred to as the 'reference arm'), the light propagates freely until it strikes a mirror (the 'reference mirror'). Light scattered by the sample is recombined with light reflected by the reference mirror, and the interference pattern generated by the two superimposed fields is recorded by a detector. This interferometric process generates images which record both the magnitude and phase of the scattered optical field collected from

---

[1] ;)

the sample. As a consequence, OCT can leverage unique advantages over more conventional intensity-based microscopes for performing high-throughput and high-resolution imaging.

The key information encoded in the optical field is the time taken for light to propagate into the sample and back out to the detector. This 'time of flight' (TOF) is proportional to the 'optical path length' (OPL) traveled by the light via the relation OPL $= c \times$ TOF, where c is the speed of light in a vacuum. If light propagates within a vacuum, OPL corresponds to the physical distance traveled by the light. However, for a homogeneous medium with a refractive index of n, the physical distance traveled will instead be OPL/n.[2] Therefore, it is important to note that a measurement of OPL does *not* always provide a direct measurement of the physical distance traveled by light. However, a physical distance may be determined if the refractive index is known *everywhere* along the light's optical path. In OCT images, OPL dictates *where* (specifically, *how deep*) a signal appears in the image, and the amount of light measured at a given OPL dictates *how bright* that location appears.

In this manner, OCT generates 3D images via measurements of the time delay and strength with which waves 'echo' back from scattering objects, analogous to related technologies such as ultrasound, sonar, and radar. However, although these related techniques can typically measure TOF directly, OCT cannot. The speed of light is simply too fast for standard electronics to directly mea-

---

[2]If this concept is unclear, here is one way to think about OPL: Say you have monochromatic light (i.e., light consisting of a single precise temporal/angular frequency) that is propagating along a given path. Now, freeze time! Count the number of wavelengths (peak-to-peak, trough-to-trough, etc.) between two selected points along the optical path. The physical length of a given wavelength may vary as a function of the local refractive index (i.e., the light waves compress/stretch when entering a medium with a higher/lower refractive index). The OPL of your selected path segment is given by the number of wavelengths counted times the *free-space/vacuum wavelength* for that angular/temporal frequency of light.

sure TOF at the scales required for microscopy (micrometer-scale spatial resolution in OPL requires TOF measurements with femtosecond-scale temporal resolution). Instead, TOF measurements are made indirectly via the interference of the fields collected from the sample and reference arms. Consequently, OCT measures the *difference* between the TOF of the scattered sample arm light and the TOF of the reflected reference arm light (which is typically held constant). Sample structure is preserved in this process, since this indirect measurement only differs from the true sample arm TOF by an additive constant.

3.3   Beam-scanning SD-OCT

Although interferometer designs, data acquisition methods, and signal processing techniques differ among the various 'species' of OCT, the core underlying mathematical concepts are conserved. However, since the original research reported throughout this dissertation was performed using beam-scanning spectral domain OCT (SD-OCT), all discussions pertaining to system design, data acquisition, and algorithm design will focus specifically on this class of OCT microscopes. Should you wish to explore these principles in the context of other types of OCT systems, deriving the basic imaging equations is always highly encouraged. If the derivations in the next section are not directly applicable, they still ought to serve as a decent guide for setting up the proper equations.

Beam-scanning OCT microscopes assemble 3D images from a sequence of independently acquired 'A-scans'. Each A-scan consists of a 1D array of data, acquired when the scanned imaging beam is centered at a particular lateral position (x, y), and encodes signals acquired across a (large) range of depths (z). In

SD-OCT, all of the depths encoded in an A-scan are acquired in parallel by the 1D pixel array of a spectrometer camera. This eliminates the need to perform physical scanning of the beam focus, sample, or reference mirror along the axial (depth) dimension. Consequently, a full 3D image may be obtained by performing a single 2D raster scan of the imaging beam across the set of desired lateral (x, y) positions. (Compare this to confocal microscopes, which must perform 3D raster scanning of the focal spot of the imaging beam through every single desired (x, y, z) position in the sample.) This enables SD-OCT systems to acquire 3D images with a millimeter-scale field-of-view (FOV), micrometer-scale spatial sampling, and acquisition times on the order of seconds to minutes. This makes SD-OCT an attractive option for performing rapid volumetric imaging of scattering biological samples.

However, the speed benefit provided by SD-OCT via its parallelized acquisition of data along z is not without trade-offs. Due to the lack of axial scanning when acquiring 3D data, the optical focus of the imaging beam will remain at a single fixed depth within the sample. Data acquired at positions away from this depth will be imaged while out-of-focus. For very low numerical aperture systems (with a lateral resolution on the order of $10\,\mu$m or larger at focus), this typically does not impose a significant penalty to image quality across the axial FOV of the system. For higher numerical aperture systems (with a lateral resolution on the order of $10\,\mu$m or smaller at focus), defocus severely degrades image quality outside the focal plane. This is the classic trade-off between focal plane resolution and depth-of-field (DOF) of an imaging system. Fortunately, due to the interferometric nature of OCT image acquisition, numerical image formation methods are available to combat this trade-off. One such method is computational adaptive optics (CAO), which enables the mitigation of defocus

and optical aberrations in OCT images during post-processing [3]. Under the right conditions, this can synthesize/restore focal plane resolution throughout the imaged volume. For SD-OCT, this enables cellular resolution imaging over depths ranging from hundreds of micrometers to millimeters while still leveraging the speed benefits of parallelized acquisition along depth. CAO is discussed in detail in Chapter 4, and so the derivations of this chapter will present only a simplified picture of the full imaging process that takes place.

3.4 The SD-OCT spectral signal

3.4.1 System model

Beam-scanning SD-OCT systems typically take the form of a Michelson interferometer, such as that shown in Fig. 3.1. Although the system shown in the figure consists entirely of free-space optics, SD-OCT systems are typically constructed from a mixture of free-space and fiber optics. Other standard components (such as scanning mirrors, polarization controllers, etc.) have been omitted from the model for simplicity. In order to construct a model for OCT signal acquisition, we must describe the path that light takes through the system, and define pertinent variables along the way which can impact the optical field.

To begin, broadband light is emitted by the source (e.g., a pulsed-mode laser, superluminescent diode, or supercontinuum laser) and propagates a distance z_0 to the splitter. A fraction a_t of the incident power transmits through the splitter (and enters the reference arm) while a remaining fraction a_r reflects (and enters the sample arm).
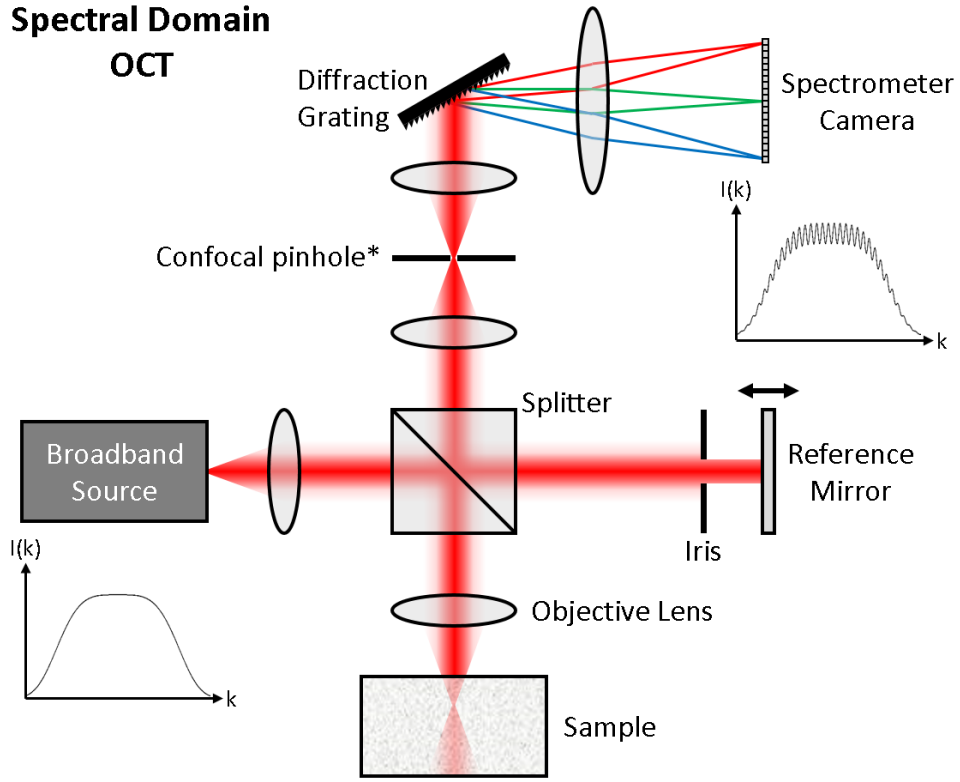
Figure 3.1: Diagram of a basic SD-OCT imaging system based upon a Michelson interferometer. Some common components (scanning mirrors, polarization controllers, optical fibers, etc.) have been omitted for simplicity.

In the reference arm, the light propagates a distance z_r until it strikes the reference mirror, upon which the light reflects and propagates a distance z_r back to the splitter. Only a fraction R of the total optical power within reference arm returns to the splitter, as determined by the reflectivity of the reference mirror and the size of the (adjustable) iris. Finally, a fraction a_r of the returning reference arm power reflects off of the splitter and enters the detection arm.

In the sample arm, a similar process takes place. The sample arm light propagates a distance z_s and strikes a scattering interface in the sample. A fraction $\eta(z_s)$ of the incident optical field then scatters and propagates a distance z_s back to the splitter. (Note that $\eta(z)$ defines a depth-dependent 'scattering potential',

which is what the final OCT image will encode.) Finally, a fraction a_t of the returning sample arm power transmits through the splitter and enters the detection arm.

The two superimposed fields (returning from the reference arm and sample arm, respectively) propagate a distance z_d through the detection arm until they are measured at the 1D pixel array of a spectrometer camera. Along this path, a diffraction grating is used to cause the various wavelengths of light within the beam to split apart in space and travel to different camera pixels. As a result, each pixel of the camera corresponds to a particular wavenumber k of light. The wavenumber-dependent interference pattern formed by the combination of the reference and sample arm fields forms the raw SD-OCT spectral signal, from which an OCT image may be reconstructed.

Although Fig. 3.1 depicts focused beams at various locations, the math that follows throughout this chapter will assume the use of optics with a *very* low numerical aperture (i.e., extremely long focal lengths) such that the lateral and angular dependence of the optical signal may be ignored. In other words, we will focus entirely on one-dimensional signals with respect to k and z. Dependence on x and y will be addressed in Chapter 4.

Armed with this simple model, we may now proceed to derive a formula for the SD-OCT spectral signal.

3.4.2 Derivation of the SD-OCT spectral signal

The optical field incident on the spectrometer camera is a superposition of the reflected reference arm field E_r and the scattered sample arm field E_s. The total field E_{tot} for a particular wavenumber of light k is then given by:

$$E_{tot}(k) = E_r(k) + E_s(k) \tag{3.1}$$

However, the spectrometer camera cannot measure this field directly, and instead can only measure the time-averaged intensity I_{tot} of the total field. This intensity measurement corresponds to the raw 'SD-OCT spectral signal', which must undergo further processing in order to generate an OCT image.

$$I_{tot}(k) \propto |E_{tot}(k)|^2 \tag{3.2a}$$

$$= |E_r(k) + E_s(k)|^2 \tag{3.2b}$$

$$= (E_r(k) + E_s(k)) (E_r(k) + E_s(k))^* \tag{3.2c}$$

$$= E_r(k)E_r^*(k) + E_s(k)E_s^*(k) + E_s(k)E_r^*(k) + E_s^*(k)E_r(k) \tag{3.2d}$$

$$= |E_r(k)|^2 + |E_s(k)|^2 + E_s(k)E_r^*(k) + (E_s(k)E_r^*(k))^* \tag{3.2e}$$

The first two terms of Eqn. (3.2e) correspond to the intensities of the reference arm and sample arm fields, respectively. The *sum* of the latter two terms corresponds to the (real-valued) interference pattern formed by the superposition of E_r and E_s at the detector. It will be shown that the third term encodes the data required to reconstruct the desired (complex-valued) OCT image signal.

First, expressions for E_r and E_s must be obtained by accounting for all optical 'operations' that take place between the light source and detector along each arm of the microscope. For simplicity, propagation along a small distance dz will be modeled as an operation which advances the phase of the optical field by

$n(k, z) \times k \times dz$, where $n(k, z)$ is the wavenumber- and location-varying refractive index along the optical path of the light. For now, we will assume propagation through a vacuum, such that $n(k, z) = 1$. All other optical operations will be assumed to modify only the magnitude of the optical field.[3]

We begin by deriving an expression for E_r. Starting with an initial field *amplitude* spectrum $A(k)$ emitted by the source, we traverse the reference arm optical path shown in Fig. 3.1, and accumulate the effects of each optical operation encountered along the way. The resultant reference arm field is given by:

$$E_r(k) = A(k) \times e^{jkz_0} \times \sqrt{a_t} \times e^{jkz_r} \times \sqrt{R} \times e^{jkz_r} \times \sqrt{a_r} \times e^{jkz_d} \qquad (3.3a)$$

$$= A(k) \sqrt{a_r a_t R} \, e^{jk(2z_r + z_0 + z_d)} \qquad (3.3b)$$

Deriving an expression for E_s requires more detail. First, we define the 'scattering potential' $\eta(z)$ of the sample, where z is a distance along the sample arm optical path with respect to the location of the splitter. This scattering potential is defined as the ratio of the magnitude of the scattered field to that of the incident field (typically, $\eta(z) \ll 1$). If the sample arm contains a scattering interface at a *single* location z_s (i.e., $\eta(z) = \eta(z_s)\delta(z - z_s)$, for $\delta(\cdot)$ the Dirac delta function):

$$E_s(k; z_s) = A(k) \times e^{jkz_0} \times \sqrt{a_r} \times e^{jkz_s} \times \eta(z_s) \times e^{jkz_s} \times \sqrt{a_t} \times e^{jkz_d} \qquad (3.4a)$$

$$= A(k) \sqrt{a_r a_t} \, \eta(z_s) e^{jk(2z_s + z_0 + z_d)} \qquad (3.4b)$$

Equation (3.4b) bears a close resemblance to Eqn. (3.3b) because we have assumed that the sample is effectively a very weak mirror. However, when the sample contains scattering interfaces at many different depths, Eqn. (3.4b)

---

[3]For example, although operations such as transmission versus reflection at the splitter impact the phase of the optical field, these effects will not substantially affect our derivations and conclusions, and so will be ignored.

must be revised to be a summation of scattered field contributions from *every* depth within the sample. Under the first Born approximation (i.e., that the incident/illumination field is not appreciably altered by the sample[4]), we obtain:

$$E_s(k) = \int_{-\infty}^{\infty} A(k) \sqrt{a_r a_t}\, \eta(z_s)e^{jk(2z_s+z_0+z_d)}\, dz_s \tag{3.5a}$$

$$= A(k) \sqrt{a_r a_t}\, e^{jk(z_0+z_d)} \int_{-\infty}^{\infty} \eta(z_s)e^{j(2k)z_s}\, dz_s \tag{3.5b}$$

Note that although the above integrals have a lower bound of $-\infty$, $\eta(z_s)$ will be assumed to be zero for $z < 0$ since, given our system model, we should not be obtaining scattering signals from any location except those which appear *after* the splitter (which was defined to be located at $z = 0$). The lower bound of $-\infty$ (instead of $z = 0$) is retained for mathematical convenience. With that in mind, the integral component of Eqn. (3.5b) may appear familiar. It is merely the Fourier transform of the scattering potential $\eta(z)$ with respect to the family of basis functions: $\exp(-j2kz)$. For brevity, we will designate this Fourier transform of $\eta(z)$ by the function $\tilde{\eta}(k')$ via the relation:

$$\tilde{\eta}(k') = \int_{-\infty}^{\infty} \eta(z)e^{-jk'z}\, dz, \tag{3.6}$$

where $k' = -2k$. In order to minimize the number of variables which appear in our equations, we will also define $\tilde{h}(k') = |A(k)|^2$. Using these relations, and substituting Eqns. (3.3b) and (3.5b) into Eqn. (3.2e), we obtain:

$$I_{tot}(k') \propto (a_r a_t)\tilde{h}(k')\left[R + |\tilde{\eta}(k')|^2 + \sqrt{R}\, e^{jk'z_r}\tilde{\eta}(k') + \left(\sqrt{R}\, e^{jk'z_r}\tilde{\eta}(k')\right)^*\right] \tag{3.7a}$$

$$= I_r(k') + I_s(k') + \tilde{S}(k') + \tilde{S}^*(k') \tag{3.7b}$$

Each term/expression in Eqns. (3.7a) and (3.7b) is discussed below.

---

[4]Failure of the first Born approximation results in a variety of artifacts, including shadows, 'phase shadowing' (a common problem in OCT angiography and optical coherence elastography), sample-induced dispersion and optical aberrations, and reduced signal-to-background ratio due to multiple scattering.

3.4.3 Interpretation of the SD-OCT spectral signal

Interferometer collection efficiency: $(a_r a_t)$

This scaling term is defined solely by the properties of the splitter used to separate the sample and reference arms. Following conservation of energy, $a_t + a_r \leq 1$. Therefore, the maximum possible value of this coefficient (given our system model) is 0.25, attained when $a_t = a_r = 0.5$.[5] Any deviation from this maximal uniform splitting ratio will decrease the total signal collection efficiency of the system. However, practical considerations for microscope design often result in the use of non-uniform ratios. The microscopes used to perform the studies detailed in this dissertation used ratios of $a_t : a_r = 90\!:\!10$. Such a skewed splitting ratio reduces the incident power on the sample, which can be important for minimizing thermal damage or other optical disturbances to biological systems.

Illumination power spectrum: $\tilde{h}(k') = |A(k)|^2$

This term corresponds to the power spectrum of the light source, and acts as a wavenumber-dependent scaling factor across the entire spectral signal. Since light sources always exhibit a finite bandwidth, this term acts as a bandpass filter on the spectral signal, and therefore limits the axial resolution that can be achieved in reconstructed OCT images. Note that the axial and lateral resolutions of OCT microscopes are typically decoupled.[6] The illumination power spectrum limits the best possible axial resolution, whereas the numerical aperture of the sample arm optics limits the best possible lateral resolution.

---

[5]Note that different *types* of interferometers and/or OCT systems have been shown to be able to exceed this efficiency value [142, 7].

[6]This is the trend for *most* OCT systems (which have small numerical apertures by typical microscopy standards). However, higher numerical aperture OCT systems can break this trend.

Reference arm reflectivity: R

This term is simply the (power) reflectivity of the reference arm. It serves to modify the strength of the signals $I_r(k') \propto R$, $\tilde{S}(k') \propto \sqrt{R}$, and $\tilde{S}^*(k') \propto \sqrt{R}$. Typically, the reflectivity ($0 \leq R \leq 1$) is adjusted with a tunable aperture/iris placed within the reference arm to ensure that all four components of the spectral signal will be recorded within the dynamic range of the spectrometer camera.[7]

Background spectrum: $I_r(k') = a_r a_t \tilde{h}(k') R$

This signal is a scaled version of the illumination power spectrum. Since $I_r(k')$ contains no information about sample structure, it can be considered a constant 'background' term within the full spectral signal, hence the name 'background spectrum'. Under typical imaging conditions, the background spectrum will always possess the greatest power among all four terms in Eqn. (3.7b). As a consequence, a large fraction of the spectrometer camera's dynamic range will be occupied by this signal, instead of the desired image spectrum.

Self-interference/auto-correlation spectrum: $I_s(k') = a_r a_t \tilde{h}(k') |\tilde{\eta}(k')|^2$

This signal corresponds to the power spectrum of the light collected from the sample arm. Since the expression for $I_s(k')$ contains no information about the reference arm field, this is the only component of the spectral signal which remains constant under changes to both the reflectivity and position of the reference arm mirror. Often referred to as the 'self-interference' or 'auto-correlation' signal of the sample arm, $I_s(k')$ is not *typically* of use for reconstructing OCT images. Since it is typical that $\eta(z) \ll \sqrt{R}$, it often follows that $|\tilde{\eta}(k')|^2 \lll R$. In fact, $I_s(k')$ is typically the smallest component of the spectral signal, and is so weak

---

[7]The dynamic range is the range of collected energy which is both above the detector noise floor and below the maximum/saturation level.

that standard OCT reconstruction algorithms completely ignore its existence. However, when this assumption fails (i.e., the sample scatters or reflects a large quantity of light back to the detector), this signal can create artifacts that corrupt the reconstructed OCT image. For an extended discussion regarding such artifacts, see Appendix A.

OCT image spectrum: $\tilde{S}(k') = a_r a_t \tilde{h}(k') \sqrt{R} \, e^{jk'z_r} \tilde{\eta}(k')$

This signal is the first of two components in the spectral signal generated by the interference of $E_r(k)$ and $E_s(k)$ at the detector. As a result, this signal encodes a mixture of information from both the reference and sample arms of the microscope, and will be referred to as the 'OCT image spectrum' $\tilde{S}(k')$. This mixture of information is precisely what allows OCT to measure TOF and OPL (up to an additive constant), and by extension, the structure of the sample. The process by which an image is generated from this image spectrum will be explored in the next section.

Conjugate image spectrum: $\tilde{S}^*(k') = \left(a_r a_t \tilde{h}(k') \sqrt{R} \, e^{jk'z_r} \tilde{\eta}(k') \right)^*$

As its name implies, this term is the complex conjugate of the OCT image spectrum $\tilde{S}(k')$. As a result of this relationship, $\tilde{S}^*(k')$ must encode a variation of the OCT image signal, which will be referred to as the 'conjugate image signal'. The impact of this second image signal will be explored in the next section.

3.5 SD-OCT image reconstruction

Now that we have a model for the raw spectral signal captured by an SD-OCT system, we can define methods to reconstruct an OCT image. In particular, we desire a process to isolate and reconstruct a depiction of the scattering potential $\eta(z)$, which corresponds to the position and strength of scattering interfaces within the sample.

3.5.1 Image reconstruction under ideal conditions

In order to derive the process by which an OCT image is reconstructed from its spectral signal, we first assign our initial raw spectral signal (with equality) to the function I_0:

$$I_0(k') = I_r(k') + I_s(k') + \tilde{S}(k') + \tilde{S}^*(k') \tag{3.8}$$

Observing the standard assumption that the self-interference spectrum is negligibly small yields:

$$I_0(k') \approx I_1(k') = I_r(k') + \tilde{S}(k') + \tilde{S}^*(k') \tag{3.9}$$

Next comes the first 'official' step in a standard OCT image reconstruction routine. We must remove the background spectrum, which does not encode any information about the sample, but nevertheless occupies a large fraction of the total energy of the spectral signal. If we have characterized our background spectrum (see Appendix B), we simply perform 'background subtraction':

$$I_2(k') = I_1(k') - I_r(k') = \tilde{S}(k') + \tilde{S}^*(k') \tag{3.10}$$

We now arrive at what appears to be an impasse. The spectral signal is acquired by a camera, which can only return real-valued (intensity) measurements. How-

ever, $\tilde{S}(k')$ and $\tilde{S}^*(k')$ are complex-valued functions. Since the two spectral signals are conjugates, their sum remains real-valued, as we would expect of our measurements. Unfortunately, this also means that the imaginary parts of the two spectra completely annihilate each other such that:

$$I_2(k') = 2\mathcal{R}[\tilde{S}(k')] = 2\mathcal{R}[\tilde{S}^*(k')] \tag{3.11}$$

where $\mathcal{R}[\cdot]$ denotes the 'real part' operator. It is clear that the two signals are not separable, in the general case, without the assistance of additional explicit knowledge or optical 'tricks'. We will return to this problem momentarily. For now, we substitute in the expressions for the remaining terms in Eqn. (3.10):

$$I_2(k') = \left(a_r a_t \tilde{h}(k')\sqrt{R}\right)\left(e^{jk'z_r}\tilde{\eta}(k') + e^{-jk'z_r}\tilde{\eta}^*(k')\right) \tag{3.12}$$

We drop the constant terms (for simplicity), yielding:

$$I_3(k) = \tilde{h}(k')\left(e^{jk'z_r}\tilde{\eta}(k') + e^{-jk'z_r}\tilde{\eta}^*(k')\right) \tag{3.13}$$

Since we wish to reconstruct a space-domain image signal, we must take an inverse Fourier transform to obtain $\eta(z)$ from $\tilde{\eta}(k')$. (This inverse Fourier transform is the 'final step' in a standard OCT image reconstruction routine.) In the fashion of Eqn. (3.6), we define the inverse Fourier transform relation:

$$\eta(z) = \int_{-\infty}^{\infty} \tilde{\eta}(k')e^{jk'z}\,dk' \tag{3.14}$$

Note that any scalar coefficients that emerge from the use of this unnormalized transform will be ignored for simplicity (and because they do not appreciably affect the interpretation of image data anyway). Leveraging the convolution theorem (i.e., frequency-domain multiplication corresponds to space-domain convolution), we obtain the inverse Fourer transform of the first term

in Eqn. (3.13) to define the 'OCT image signal':

$$S(z) = h(z) \star \delta(z + z_r) \star \eta(z) \qquad (3.15a)$$

$$= h(z) \star \eta(z + z_r) \qquad (3.15b)$$

where $h(z)$ denotes the inverse Fourier transform of $\tilde{h}(k')$, and '$\star$' denotes the convolution operator. From Eqn. (3.15b), we observe that the sample structure/scattering potential $\eta(z)$ has been shifted such that any structures *physically* located at a distance of approximately z_r downstream from the splitter appear near the origin ($z = 0$) in the reconstructed OCT image. That is, the reference arm length directly determines which part of the sample will appear centered in the reconstructed image. $h(z)$ corresponds to the axial point spread function (PSF) of the imaging system and is determined solely by the illumination power spectrum.[8] Since $\tilde{h}(k')$ is a real-valued function, it follows that $h(z)$ is conjugate symmetric (i.e., $h(z) = h^*(-z)$). We can now take the inverse Fourier transform of the second term in Eqn. (3.13) to yield the 'conjugate image signal':

$$S_c(z) = h(z) \star \delta(z - z_r) \star \eta^*(-z) \qquad (3.16a)$$

$$= h(z) \star \eta^*(-(z - z_r)) \qquad (3.16b)$$

$$= h^*(-z) \star \eta^*(-z + z_r) \qquad (3.16c)$$

$$= S^*(-z) \qquad (3.16d)$$

Eqn. (3.16d), shows that the conjugate image signal is merely a conjugated and space-reversed version of the OCT image signal from Eqn. (3.15b), with the reversal taking place about the origin of the reconstructed image. The 'total image signal' remains a superposition of the two image signals:

$$S_{tot}(z) = S(z) + S^*(-z) \qquad (3.17)$$

---

[8]If a_r, a_t, and R were not constants, and were instead functions of k, then they too would modify the axial point spread function.

Recall that the OCT image spectrum and conjugate image spectrum terms in Eqn. (3.10) were not directly separable, in the general case, due to their identical real parts and mutually annihilated imaginary parts. However, from Eqn. (3.17), we can now define a condition under which the image signals *can* be separated. If the OCT image signal obeys the condition: $S(z) = 0$ for $z \leq 0$, then $S_c(z) = 0$ for $z \geq 0$, and the two image signals are separable, since their non-zero regions do not overlap in space. This can be achieved by adjusting the sample location and/or the reference mirror position[9] such that the sample surface is located at a position $z_{\text{surf}} > z_r$.[10] Note that if these conditions are satisfied, then the two spectra in Eqn. (3.10) actually *are* separable in the spectral domain via a Hilbert transform, since the Hilbert transform relies on these exact same assumptions/conditions in order to be valid.

In summary, given an ideal imaging process, the OCT image signal is obtained from the raw OCT spectral signal via the following procedure:

1. Ignore the self-interference spectrum term (assuming this is appropriate)

2. Background subtraction (assuming $I_r(k')$ is properly characterized)

3. Inverse Fourier transform

4. Retain the image signal only in the region $z > 0$ (assuming the sample was appropriately placed to allow for separation of the OCT image signal from the conjugate image signal)

---

[9]It is recommended that adjusting the reference mirror position takes priority, especially if the focal plane of the imaging beam is already located at a 'good spot' within the sample.

[10]This statement assumes $h(z)$ is a delta function. In practice, since $h(z)$ has a finite non-zero width, the sample surface must be placed at a slightly greater depth (i.e., at least one-half of the width of $h(z)$ further away from the splitter in comparison to the reference mirror) than this condition specifies.

3.5.2 A simple example

Consider a sample that consists of a weak mirror located at a position $z = z_s$ with respect to the splitter. Assuming that this mirror is very thin and has a scattering potential of η_s, we define the sample scattering potential as:

$$\eta(z) = \eta_s \delta(z - z_s) \tag{3.18}$$

It follows that $\tilde{\eta}(k') = \eta_s e^{-jk'z_s}$, and we obtain our spectral signal:

$$I_{tot}(k') \propto (a_r a_t)\tilde{h}(k')\left[R + |\tilde{\eta}(k')|^2 + \sqrt{R}\,e^{jk'z_r}\tilde{\eta}(k') + \left(\sqrt{R}\,e^{jk'z_r}\tilde{\eta}(k')\right)^*\right] \tag{3.19a}$$

$$= (a_r a_t)\tilde{h}(k')\left[R + \eta_s^2 + \sqrt{R}e^{jk'z_r}\eta_s e^{-jk'z_s} + \left(\sqrt{R}e^{jk'z_r}\eta_s e^{-jk'z_s}\right)^*\right] \tag{3.19b}$$

$$\propto \tilde{h}(k')\left[R + \eta_s^2 + \eta_s\sqrt{R}e^{-jk'(z_s-z_r)} + \left(\eta_s\sqrt{R}e^{-jk'(z_s-z_r)}\right)^*\right] \tag{3.19c}$$

$$= \tilde{h}(k')\left[R + \eta_s^2 + 2\eta_s\sqrt{R}\cos(k'(z_s - z_r))\right] \tag{3.19d}$$

$$= \tilde{h}(k')\left[R + \eta_s^2 + 2\eta_s\sqrt{R}\cos(k'\Delta z)\right], \Delta z = z_s - z_r \tag{3.19e}$$

The three terms in Eqn. (3.19e) correspond to the background spectrum, the self-interference spectrum, and the (real-valued) superposition of the OCT image spectrum and conjugate image spectrum, respectively. For this simple example, the superposition term clearly demonstrates how the SD-OCT spectral signal encodes the brightness and position of scattering interfaces. For now, we ignore the $\tilde{h}(k')$ term by assuming that $\tilde{h}(k') = 1$. What remains of the superposition term is merely a cosine wave defined by two degrees of freedom: its amplitude (which is proportional to η_s) and its frequency in the *spectral* domain (given by Δz). Of course, η_s determines how much light our sample scatters and therefore controls the 'brightness' of the object in our reconstructed image. Likewise, Δz encodes the difference between the OPL of the sample arm light and the OPL of the reference arm light, and therefore encodes a position for our sample to appear at in the reconstructed OCT image.

In order to reconstruct our example OCT image, we first assume that $\eta_s^2 \ll R$ and $\eta_s^2 \ll 2\eta_s \sqrt{R}$, yielding:

$$I_1(k') = \tilde{h}(k')\left[R + 2\eta_s \sqrt{R}\cos(k'(z_s - z_r))\right] \tag{3.20}$$

Next we perform background subtraction:

$$I_2(k') = I_1(k') - \tilde{h}(k')R = \tilde{h}(k')2\eta_s \sqrt{R}\cos(k'(z_s - z_r)) \tag{3.21}$$

For demonstration purposes, we break our real-valued signal into its complex-valued constituents (the OCT image spectrum and conjugate image spectrum):

$$I_3(k') = \tilde{h}(k')\eta_s \sqrt{R}\left(e^{-jk'(z_s-z_r)} + e^{jk'(z_s-z_r)}\right) \tag{3.22}$$

and take an inverse Fourier transform:

$$S_{tot}(z) = \left(\eta_s \sqrt{R}\right)h(z) \star (\delta(z - (z_s - z_r)) + \delta(z + (z_s - z_r))) \tag{3.23a}$$

$$= \left(\eta_s \sqrt{R}\right)(h(z - (z_s - z_r)) + h(z + (z_s - z_r))) \tag{3.23b}$$

Consistent with our previous derivations, this image signal is conjugate-symmetric about its origin. Here, we have two bandwidth-limited pulses appearing at $z = z_s - z_r$ and $z = -(z_s - z_r)$, corresponding to the OCT image signal and conjugate image signal, respectively. We can define this correspondence only because we have 'cheated' by having access to the full complex-valued signals in our derivations. In practice, if we were presented with only the total image signal (and possessed no knowledge about the value of z_s), we would have no way of knowing which of the two pulses corresponds to the OCT image signal.[11] This ambiguity is readily resolved if the sample and reference mirror are set up such that the condition $z_s > z_r$ (or alternatively, $z_s < z_r$) is guaranteed.

---

[11] The reader is invited to derive the total image signal for a sample with a scattering potential of $\eta(z) = \eta_s\delta(z - z'_s)$, where $z'_s = 2z_r - z_s$. This will cause the positions of the OCT image signal and conjugate image signal in Eqn. (3.23b) to be swapped, but the total image signal (along with its associated ambiguity) will remain unchanged. Given only the total image signal, we would not be able to determine whether the sample was located at z_s or z'_s.

3.5.3 Dispersion

The derivations and procedures we have discussed so far relied upon the assumption that imaging was performed in a vacuum (i.e., that the refractive index $n(k,z) = 1$). However, this assumption is far from reality for everyday OCT imaging. Optical fibers, optical elements, and samples all have refractive indices which differ drastically from that of a vacuum. By itself, a refractive index $\neq 1$ is not a problem. (We will see in the derivations below that imaging inside a medium with a constant refractive index merely scales the reconstructed OCT image along the axial dimension.) Challenges *do* arise, however, from the fact that glass and other optical materials are *dispersive* (i.e., the refractive index varies as a function of wavenumber). To understand the consequences of dispersion, we will have to perform a new round of derivations.

We return to the optical 'operations' used to define Eqns. (3.3b), (3.4b), and (3.5b). Light propagation through a dielectric medium advances the phase of the optical field according to:

$$\phi(k) = \int_\Omega n(k,z)k\,dz \tag{3.24}$$

where Ω denotes a specific optical path along z. Now, we must define the appropriate phase changes induced by propagation through each arm of the OCT system in Fig. 3.1 (from source to splitter, splitter to reference mirror, splitter to

a location $z = z_s$ in the sample arm, and splitter to detector, respectively):

$$\phi_0(k) = \int_0^{z_0} n_0(k, z)k\, dz \tag{3.25a}$$

$$\phi_r(k) = \int_0^{z_r} n_r(k, z)k\, dz \tag{3.25b}$$

$$\phi_s(k, z_s) = \int_0^{z_s} n_s(k, z)k\, dz \tag{3.25c}$$

$$\phi_d(k) = \int_0^{z_d} n_d(k, z)k\, dz \tag{3.25d}$$

where n_0, n_r, n_s, and n_d are the space- and wavenumber-dependent refractive index profiles along each branch of the microscope. We will neglect any scattering that emerges from sharp changes in these refractive index profiles (such as the air-glass interface of a lens). As a result, we will assume that the only light returning to the microscope comes from either the sample (described by $\eta(z)$) or the reference arm mirror. Although this assumption is not true, it is practically relevant (as will be noted later in the discussion on discretely-sampled signals). We next obtain our revised reference arm field:

$$E_r(k) = A(k) \times e^{j\phi_0(k)} \times \sqrt{a_t} \times e^{j\phi_r(k)} \times \sqrt{R} \times e^{j\phi_r(k)} \times \sqrt{a_r} \times e^{j\phi_d(k)} \tag{3.26a}$$

$$= A(k)\sqrt{a_r a_t R}\, e^{j(2\phi_r(k)+\phi_0(k)+\phi_d(k))} \tag{3.26b}$$

We also obtain our revised sample arm field (for an isolated scattering interface):

$$E_s(k; z_s) = A(k) \times e^{j\phi_0(k)} \times \sqrt{a_r} \times e^{j\phi_s(k,z_s)} \times \eta(z_s) \times e^{j\phi_s(k,z_s)} \times \sqrt{a_t} \times e^{j\phi_d(k)} \tag{3.27a}$$

$$= A(k)\sqrt{a_r a_t}\, \eta(z_s)e^{j(2\phi_s(k,z_s)+\phi_0(k)+\phi_d(k))} \tag{3.27b}$$

And finally, we obtain the total sample arm field by accounting for scattering from all valid depths[12] within the sample:

$$E_s(k) = A(k)\sqrt{a_r a_t}\, e^{j(\phi_0(k)+\phi_d(k))} \int_{-\infty}^{\infty} \eta(z_s)e^{j2\phi_s(k,z_s)}\, dz_s \tag{3.28}$$

---

[12]Recall the assumption that $\eta(z) = 0$ for $z < 0$.

Recall that the integral term in Eqn. (3.5b) was a Fourier transform. However, the integral term in Eqn. (3.28) can no longer be considered a Fourier transform, even though its form does remain similar to one. Instead of a projection onto a basis of complex (sinusoidal) exponential functions, we now have a projection onto a basis of functions which are 'chirped' by the refractive index profile within the sample arm. By itself, this equation will not be terribly enlightening. We will have to apply (reasonable) assumptions to gain intuition.

However, we will first continue with our derivation to obtain expressions for the four terms of our spectral signal. As a reminder, we are plugging our revised reference and sample arm fields into the expression:

$$I_{tot}(k) = |E_r(k)|^2 + |E_s(k)|^2 + E_s(k)E_r^*(k) + (E_s(k)E_r^*(k))^* \qquad (3.29)$$

By inspection, we determine that the background spectrum will remain unchanged from the previous derivation. Likewise, although the expression for the self-interference spectrum does change, it will not be shown here, since we will still assume this term to be negligibly small for the purposes of performing image reconstruction. The OCT image spectrum $\tilde{S}(k')$ will be given by:

$$\tilde{S}(k') = a_r a_t \tilde{h}(k') \sqrt{R} e^{-j2\phi_r(k)} \int_{-\infty}^{\infty} \eta(z_s) e^{j2\phi_s(k,z_s)} \, dz_s \qquad (3.30)$$

where $\tilde{h}(k')$ and $k' = -2k$ are defined as before. At this stage, assumptions must be leveraged to advance further. First, we will 'split' the sample arm into two regions. The first region (immediately after the splitter) encompasses all of the optical components used for directing light to–and collecting light from–the sample. The second region begins at the sample surface (located at $z = z_{\mathrm{surf}}$) and extends to infinity. This second region will be assumed to have a depth- and wavenumber-invariant refractive index n. This approximation is usually

78

acceptable for standard OCT imaging in homogeneous biological and/or polymer samples to depths on the order of 1-2 mm.[13] If $\eta(z) = 0$ for $z < z_{\text{surf}}$, then:

$$\tilde{S}(k') = a_r a_t \tilde{h}(k') \sqrt{R} e^{-j2\phi_r(k)} \int_{-\infty}^{\infty} \eta(z_s) e^{j2\phi_{s,1}(k)} e^{j2kn(z_s - z_{\text{surf}})} \, dz_s \tag{3.31a}$$

$$\phi_{s,1}(k) = \int_0^{z_{\text{surf}}} n_s(k,z) k \, dz \tag{3.31b}$$

Simplifying further (and dropping constant terms for simplicity), we obtain:

$$\tilde{S}(k') = \tilde{h}(k') e^{j\Delta\phi(k')} \int_{-\infty}^{\infty} \eta(z_s) e^{-jk'nz_s} \, dz_s \tag{3.32a}$$

$$\Delta\phi(k) = 2(\phi_{s,1}(k) - \phi_r(k) - knz_{\text{surf}}) \tag{3.32b}$$

$$\Delta\phi(k') = 2(\phi_{s,1}(-k'/2) - \phi_r(-k'/2) - (-k'/2)nz_{\text{surf}}) \tag{3.32c}$$

(Note that the casting of $\Delta\phi$ as a function of k' is done to keep in line with our previous conventions and avoid mixing the variables k and k' in our equations below.) Our assumptions have allowed us to arrive at a 'proper' Fourier transform relation in the integral term. However, due to the introduction of the sample refractive index n, the integral now evaluates to $\tilde{\eta}(nk')$ (instead of the previously defined function $\tilde{\eta}(k')$). If we assume our image reconstruction algorithm is 'blind' to the the value of n, then the OCT image signal is still obtained by taking the inverse Fourier transform defined in Eqn. (3.14), yielding:

$$S(z) = h(z) \star h_\phi(z) \star \eta(z/n) \tag{3.33}$$

where $h_\phi(z)$ denotes the inverse Fourier transform of $e^{j\Delta\phi(k')}$. Note that the reconstructed scattering potential $\eta(z/n)$ is an axially scaled version of $\eta(z)$.[14] In

---

[13]Numerical mitigation strategies can be employed when this assumption fails (such as when acquiring data over a large depth range within strongly dispersive media). Details may be found in Appendix E.

[14]If $n > 1$, $\eta(z/n)$ is 'stretched' compared to $\eta(z)$ by a factor of n. This is a manifestation of the fact that OCT measures OPL and *not* physical distance. As stated at the beginning of this chapter, if an object has an *optical path length* of d_{OPL} in the reconstructed image, its physical length d will be given by d_{OPL}/n. The division by n cancels out the 'stretching' present in $\eta(z/n)$.

Eqn. (3.15a), $h_\phi(z)$ was equal to $\delta(z + z_r)$, and was responsible for shifting the reconstructed image data such that the origin of the image signal was centered about the *physical* location $z = z_r$ in the sample arm. However, the more generalized formulation for $h_\phi(z)$ that we have just derived may not be so benign.

To better understand the nature of $h_\phi(z)$, we first perform a Taylor series expansion of $\Delta\phi(k')$ about the point $k' = k'_c = -2k_c$, for k_c the central wavenumber of the bandwidth of the light source:

$$\Delta\phi(k') = \alpha_0 + \alpha_1(k' - k'_c) + \alpha_2(k' - k'_c)^2 + \alpha_3(k' - k'_c)^3 + O\left((k' - k'_c)^4\right) \qquad (3.34)$$

Assuming the high-order terms are negligible, we can rewrite Eqn. (3.32a) as:

$$\tilde{S}(k') \approx \tilde{h}(k')e^{j\alpha_0}e^{j\alpha_1(k'-k'_c)}e^{j\left(\alpha_2(k'-k'_c)^2+\alpha_3(k'-k'_c)^3\right)}\tilde{\eta}(nk') \qquad (3.35)$$

The OCT image signal is then given by:

$$S(z) = h(z) \star e^{j\left(\alpha_0-\alpha_1 k'_c\right)}\delta(z + \alpha_1) \star h_\alpha(z; \alpha_2, \alpha_3) \star \eta(z/n) \qquad (3.36a)$$

$$\propto h(z) \star h_\alpha(z; \alpha_2, \alpha_3) \star \eta((z + \alpha_1)/n) \qquad (3.36b)$$

where $h_\alpha(z; \alpha_2, \alpha_3)$ is the inverse Fourier transform of $e^{j\left(\alpha_2(k'-k'_c)^2+\alpha_3(k'-k'_c)^3\right)}$. With this refined formulation of Eqn. (3.33), we can develop a clearer picture regarding the impact of $h_\phi(z) \approx e^{j\left(\alpha_0-\alpha_1 k'_c\right)}\delta(z+\alpha_1)\star h_\alpha(z; \alpha_2, \alpha_3)$. The constant scaling term $e^{j\left(\alpha_0-\alpha_1 k'_c\right)}$ is inconsequential for image analysis, and can be discarded (alongside the numerous other scaling factors we have dropped throughout these derivations). The $\delta(z + \alpha_1)$ term will merely shift the origin of the reconstructed image within the sample (analogous to the $\delta(z + z_r)$ term in Eqn. (3.15a)). If the coefficient α_1 shifts the image origin to an undesired location in the sample arm, its value can always be tuned by adjusting the reference arm mirror position z_r. Therefore, the $\delta(z + \alpha_1)$ term is also inconsequential. This leaves $h_\alpha(z; \alpha_2, \alpha_3)$ as the only remaining source of potential trouble. Since h_α is the only term to

be a function of α_2, α_3, and any higher-order terms (if relevant), h_α encodes the consequences of using dispersive optical materials in an OCT system.

It turns out (see Appendix C) that $h_\alpha(z; \alpha_2, \alpha_3)$ causes image blurring along the axial dimension when $(\alpha_2, \alpha_3) \neq (0,0)$. For standard microscopes, image blurring can be difficult to mitigate, especially in samples with dense internal structure. Thankfully, there are multiple simple ways to address this issue in OCT imaging. If axial blurring is significant (i.e., if the length of the blurred PSF is hundreds of micrometers or greater), extra optical components can be introduced to mitigate the blurring (see Appendix D). This hardware-based compensation of dispersion merely requires that the reference arm and sample arm contain the *same total amount of dispersion* (such that the quadratic and higher-order terms of $\phi_{s,1}$ and ϕ_r from Eqn. (3.32b) cancel out). If an OCT system contains only one type of material besides air (e.g., a single type of glass for all optical components), then the impact of dispersion will be minimal when the sample and reference arms contain the *same total amount* of glass. Alternatively, if the 'dispersion mismatch' between the sample and reference arms is relatively small (resulting in a blurred PSF whose length is only a few hundred micrometers or smaller), computational compensation is a very simple option for canceling out dispersion coefficients. If α_2 and α_3 are characterized (via empirical measurement or a suitable optimization procedure), computational dispersion compensation is performed via:

$$\tilde{S}_\alpha(k') = \tilde{S}(k')e^{-j\left(\alpha_2(k'-k'_c)^2 + \alpha_3(k'-k'_c)^3\right)} \tag{3.37a}$$

$$= \tilde{h}(k')e^{j\alpha_0}e^{j\alpha_1(k'-k'_c)}\tilde{\eta}(nk') \tag{3.37b}$$

yielding:

$$S_\alpha(z) \propto h(z) \star \eta((z + \alpha_1)/n) \tag{3.38}$$

81

and the original (unblurred) axial PSF $h(z)$ is restored. However, we must not forget that this computational dispersion compensation will not only be applied to the OCT image spectrum, but to the conjugate image spectrum as well.

$$\tilde{S}_{tot,\alpha}(k') = \left(\tilde{S}(k') + \tilde{S}^*(k')\right)e^{-j\left(\alpha_2(k'-k'_c)^2+\alpha_3(k'-k'_c)^3\right)} \tag{3.39a}$$

$$= \tilde{h}(k')[e^{j\alpha_0}e^{j\alpha_1(k'-k'_c)}\tilde{\eta}(nk') + \dots$$
$$e^{-j\alpha_0}e^{-j\alpha_1(k'-k'_c)}e^{-j2\left(\alpha_2(k'-k'_c)^2+\alpha_3(k'-k'_c)^3\right)}\tilde{\eta}^*(nk')] \tag{3.39b}$$

As a result, the total image signal is:

$$S_{tot,\alpha}(z) = h(z) \star [A_\alpha\eta((z+\alpha_1)/n) + \dots$$
$$A_\alpha^*\left(\eta^*((-z+\alpha_1)/n) \star h_\alpha^*(-z; 2\alpha_2, 2\alpha_3)\right)] \tag{3.40}$$

for $A_\alpha = e^{j(\alpha_0-\alpha_1k'_c)}$. Although the blurring of the OCT image signal is mitigated, the axial blurring of the conjugate image signal is *doubled* in the dispersion-compensated total image signal. If hardware-based compensation were employed instead, both the OCT image signal and conjugate image signal would have been corrected in equal amounts.[15]

In summary, given the presence of artifacts introduced by dispersion mismatch between the sample and reference arms, the OCT image signal is obtained from the raw spectral signal via the following procedure:

1. Ignore the self-interference spectrum term (assuming this is appropriate)

2. Background subtraction (assuming $I_r(k')$ is properly characterized)

3. Computational dispersion compensation (using α_2 and α_3 at minimum)

4. Inverse Fourier transform

---

[15]This is a common theme in OCT. Measuring the complex-valued optical field enables the use of computational methods which mimic physical optical processes. However, despite their convenience, computational methods often exhibit limitations which may not exist for their hardware-based analogs. The 'no free lunch' principle continues to hold.

5. Retain the image signal only in the region $z > 0$ (assuming the sample was appropriately placed to allow for separation of the OCT image signal from the conjugate image signal). Do not forget to account for axial 'stretching' of the image signal by a factor of n when interpreting the output image.

3.5.4 Discretely sampled spectra

Thus far, we have performed derivations using infinite and continuous domains in wavenumber and space. However, OCT image data is always acquired in a finite and discretized fashion. The spectrometer camera used to capture $I_{tot}(k)$ contains a 1D array of N pixels, corresponding to a finite set of wavenumbers $k_i \in \{k_0, k_1, \ldots, k_{N-1}\}$, yielding the discrete OCT spectral signal $I_{tot}[k_i]$. Although the mathematics for OCT image reconstruction remain largely unchanged, a few important practical considerations do emerge.

Assume that the spectrometer acquires $I_{tot}[k_i]$ with uniform sampling (i.e., $k_{i+1} - k_i$ is a constant Δk for $i \in \{0, 1, \ldots, N-2\}$). Assuming there are no dispersive elements in our microscope, the discrete OCT spectral signal will be given by:

$$\tilde{S}[k_i] = \left(a_r a_t \sqrt{R}\right) \tilde{h}[k_i] e^{-j2k_i z_r} \int_{-\infty}^{\infty} \eta(z_s) e^{j2k_i z_s} \, dz_s \tag{3.41}$$

where $\tilde{h}[k_i] = |A[k_i]|^2$. We have kept all functions in terms of k_i (instead of $k'_i = -2k_i$) to minimize complications in our derivations downstream. The OCT image signal can be obtained from an inverse *discrete* Fourier transform (DFT)[16]:

$$S[z_m] = \sum_{i=0}^{N-1} \tilde{S}[k_i] e^{-j2k_i z_m} \tag{3.42}$$

---

[16]Recall that we previously defined our OCT spectral signal to be a Fourier transform of the sample structure $\eta(z)$ with respect to a set of basis functions of the form e^{-j2kz}.

for m an integer (usually, *but not necessarily*, constrained to the set $\{0, 1, \ldots, N-1\}$).

Eqn. (3.42) is the discrete analog to the continuous inverse Fourier transform that we defined previously[17]:

$$S(z) = \int_{-\infty}^{\infty} \tilde{S}(k)e^{-j2kz}\, dk \tag{3.43}$$

Although Eqn. (3.42) is easy enough to understand, it must be noted that the standard formulation of the DFT (and its inverse) are computationally inefficient, and are typically replaced with a fast Fourier transform (FFT) algorithm. However, using the FFT presents a problem. Most programmers will leverage highly optimized FFT routines obtained from a pre-made library. These routines do not allow us to explicitly encode physical values of k_i and z_m into the transform. Instead, the FFT[18] computes the signal:

$$S[z_m] = \sum_{i=0}^{N-1} \tilde{S}[k_i]e^{-j\frac{2\pi m}{N}i} \text{ for } m \in \{0, 1, \ldots, N-1\} \tag{3.44}$$

In order to understand the consequences of this transformation, we return to our previous simple example of a sample consisting of a single weak scatterer: $\eta(z) = \eta_s\delta(z - z_s)$. Our discrete OCT spectral signal would then be given by:

$$\tilde{S}[k_i] = \left(a_r a_t \sqrt{R}\right)\tilde{h}[k_i]e^{-j2k_iz_r}\eta_s e^{j2k_iz_s} \tag{3.45}$$

Dropping scaling factors and plugging into Eqn. (3.44) yields:

$$S[z_m] = \sum_{i=0}^{N-1} \tilde{h}[k_i]e^{j2k_i(z_s-z_r)}e^{-j\frac{2\pi m}{N}i} \text{ for } m \in \{0, 1, \ldots, N-1\} \tag{3.46a}$$

$$= h[z_m] \star \sum_{i=0}^{N-1} e^{-j\left(\frac{2\pi m}{N}i - 2k_i(z_s-z_r)\right)} \text{ for } m \in \{0, 1, \ldots, N-1\} \tag{3.46b}$$

---

[17]Now in terms of k instead of k'.

[18]A *forward* FFT was used here to utilize the same sign convention in the phase term as our *inverse* DFT defined in Eqn. (3.42). Note that both the forward and inverse FFT can be used for OCT image reconstruction. Both transforms will yield the desired OCT image signal–except one of the transforms will return the OCT image signal upside-down compared to the other.

This begs the question: what *are* the discrete values of z_m at which our OCT image signal is ('perfectly') reconstructed? The DFT and FFT both assume data is uniformly spaced in both the space and spectral domains. We will assume that $k_i = k_0 + i\Delta k$ and $z_m = m\Delta z$. We can obtain Δk from the full bandwidth of our spectrometer: $\Delta k = (k_{N-1} - k_0)/(N - 1)$. But what will be the value of Δz? Assume the scatterer is located at a position $z = z_r + \hat{m}\Delta z$, for $\hat{m}$ an integer. Eqn. (3.46b) then becomes:

$$S[z_m] = h[z_m] \star \sum_{i=0}^{N-1} e^{-j\left(\frac{2\pi m}{N}i - 2k_i\hat{m}\Delta z\right)} \text{ for } m \in \{0, 1, \ldots, N-1\} \qquad (3.47)$$

Given that the sample structure takes the form of a delta function at $z = z_r + z_{\hat{m}}$, the reconstructed OCT image signal should yield a pulse centered at $z_m = z_{\hat{m}}$. This is achieved when the phase term in Eqn. (3.47) satisfies the condition:

$$\frac{2\pi m}{N}i - 2k_i\hat{m}\Delta z = 0, \text{ for } i \in \{0, 1, \ldots, N-1\} \text{ and } m = \hat{m} \qquad (3.48)$$

Applying this condition for $i = i_0$ and $i = i_1$, we infer:

$$\frac{2\pi\hat{m}}{N}i_0 - 2k_{i_0}\hat{m}\Delta z = \frac{2\pi\hat{m}}{N}i_1 - 2k_{i_1}\hat{m}\Delta z \qquad (3.49a)$$

$$\frac{2\pi\hat{m}}{N}(i_0 - i_1) = 2((k_0 + i_0\Delta k) - (k_0 + i_1\Delta k))\hat{m}\Delta z \qquad (3.49b)$$

$$\frac{2\pi\hat{m}}{N}(i_0 - i_1) = 2(i_0 - i_1)\Delta k\hat{m}\Delta z \qquad (3.49c)$$

$$\Delta z = \frac{\pi}{N\Delta k} \qquad (3.49d)$$

So, for FFT-based OCT image reconstruction, the height of each pixel along z (in terms of OPL[19]) will be given by Eqn. (3.49d). At first glance, this would appear to imply that the full axial range available to the reconstructed image signal will be $[0, (N-1)\Delta z]$. However, the OCT image signal must typically lie within only the first *half* of this 'full range' (i.e., $z_m \in [0, (\lceil N/2\rceil - 1)\Delta z]$). Understanding why

---

[19]Inside a medium of refractive index n, the physical value of Δz is $\pi/(nN\Delta k)$.

this is the case requires an understanding of the conjugate image signal, a background in the basic theory of discrete signals and Fourier transforms (which will not be detailed here), and knowledge of the optics underlying spectrometer design. In brief:

1. **The conjugate image signal appears as a mirror image of the OCT image signal about the origin of the reconstructed OCT image.** This should be apparent if you have followed the derivations of this chapter so far. Given our previous discussions on how to place the sample in order to keep the OCT image signal and conjugate image signal separable, we also know that our imaging system should be set up so that the OCT image signal appears in the region where $z > 0$, and the conjugate image signal appears where $z < 0$. Note that the standard DFT/FFT equations above (which are 'blind' to the details of our system) perform reconstructions for $z_m \in [0, (N-1)\Delta z]$. This might appear to imply that the conjugate image signal should not be present in the reconstruction. However, that brings us to the next point.

2. **Finite-length discrete signals and their Fourier transforms are 'periodic'.** This means that if the DFT/FFT were extended to perform reconstructions across all possible locations in space, they would produce a periodic signal with period $N\Delta z$. Therefore, a conjugate image signal that is 'truly' located in the region $-(N/2)\Delta z < z < 0$ (a region that our equations above *did not* reconstruct) will *also* appear in the region $(N/2)\Delta z < z < N\Delta z$ (a region that our equations above *did* reconstruct). So in practice, our OCT image signal can only extend to a depth of $(N/2)\Delta z$ before it begins to experience overlap with the conjugate image signal. Therefore, for the case of discretely sampled signals, the only way to guarantee that the OCT image signal

and conjugate image signal do not overlap is to ensure that $\eta(z) = 0$, for $z < z_r$ and for $z > z_r + (N/2)\Delta z$. Thick samples often fail the latter criterion. However, image signal overlap may be mitigated by our final point.

3. **SD-OCT signals get weaker as the OPL mismatch between the sample and reference arm increases.** This is called the spectrometer 'roll-off' or 'fall-off' effect. For a scattering surface located at a fixed position $z = z_s$, the amplitude of the *measured* interference signal formed between the sample and reference arms decays as the difference between z_s and z_r grows. This is a result of spatial averaging that takes place within the spectrometer. Due to a combination optical limitations and the size of camera pixels, a given pixel within the spectrometer will collect light over a *range* of wavenumbers. (A good spectrometer design will attempt to minimize this range, but will never be able to decrease the range to zero.) As a result, the pixel can only measure the *average* intensity of the spectral signal about its corresponding central wavenumber k_i. When interference fringes (such as the cosine wave in Eqn. (3.19e)) vary rapidly as a function of k, the local average intensity of the spectral signal about k_i can vary drastically from the true intensity of the spectral signal at *precisely* k_i. The consequence is that the origin of reconstructed OCT images will exhibit the greatest signal strength, while signals from other depths will decline with distance from the origin. Signals which originate from an OPL that differs drastically from z_r (e.g., those beyond our $(N/2)\Delta z$ cut-off discussed above) can be significantly attenuated, and will eventually fall below detectable levels. This is why reflections off of optical surfaces (such as lenses) in our sample arm do not typically cause problems during image reconstruction. The OPL mismatch between those optical surfaces and the reference mir-

ror is typically so great that the interference fringe signal between them is obliterated by spatial averaging within the spectrometer.[20]

In summary, given a discretely sampled SD-OCT spectral signal of length N (with uniform sampling period Δk in the spectral domain), the OCT image signal is obtained from the raw spectral signal via the following procedure:

1. Ignore the self-interference spectrum term (assuming this is appropriate)

2. Background subtraction (assuming $I_r[k_i]$ is properly characterized)

3. Computational dispersion compensation (using α_2 and α_3 at minimum)

4. Discrete Fourier transform or fast Fourier transform (forward and inverse transforms are acceptable)

5. Retain the image signal only in the valid region (of size $(N/2)\Delta z$ where $\Delta z = \pi/(N\Delta k)$ in terms of OPL). Do not forget to account for axial 'stretching' of the image signal by a factor of n.

3.5.5 Non-uniformly sampled spectra

Before we can discuss how to actually implement an OCT image reconstruction algorithm, we must address one final (and critical) point. Our derivations above for discretely sampled signals assumed that the SD-OCT spectral signal was sampled at uniform intervals along k (i.e., $k_{i+1} - k_i$ is a constant Δk for $i \in \{0, 1, \ldots, N - 2\}$). However, designing a spectrometer that achieves

---

[20]However, the average energy from those far-away surfaces does still get captured, resulting in an anomalous increase in the apparent value of the background spectrum. In general, the use of anti-reflection coatings is recommended to minimize this effect and maximize the available dynamic range of the camera.

uniform sampling can be difficult...and expensive! In practice, most SD-OCT spectrometers sample the spectral signal along a non-uniformly spaced set of wavenumbers $\hat{k}_i \in \{\hat{k}_0, \hat{k}_1, \ldots, \hat{k}_{N-1}\}$ (for which $\hat{k}_{i+1} - \hat{k}_i$ is *not* constant with respect to $i \in \{0, 1, \ldots, N-2\}$). In order to properly reconstruct an OCT image, the image reconstruction procedure *must* be modified to correct for non-uniform sampling. The standard way to do this is to incorporate a resampling step that numerically estimates the values of the spectral data across a uniformly spaced set of locations (the values of k_i defined previously) from the original data (obtained at each value of $\hat{k}_i$). Implementations of this spectrum resampling step will not be discussed here.[21] However, a few recommendations will be made:

1. It is recommended that the uniformly spaced set of query points k_i be defined to cover the same range as the original non-uniformly spaced set of points $\hat{k}_i$. That is, if $\hat{k}_0$ and $\hat{k}_{N-1}$ correspond to the extremal values of the total range spanned by all $\hat{k}_i$, then define $k_i = \hat{k}_0 + i\Delta k$ for $i \in \{0, 1, \ldots, N-1\}$ and $\Delta k = (\hat{k}_{N-1} - \hat{k}_0)/(N-1)$. This will allow you to avoid problems with extrapolation, truncation, and insufficient or redundant interpolation.

2. High-order interpolation is typically needed to perform spectrum resampling. Sinc, spline, and cubic polynomial interpolators (or approximations thereof) may be a good choice. Low-order interpolators (e.g., nearest-neighbor or linear interpolators) are almost universally bad choices. The errors introduced by low-order schemes can severely corrupt the image signal, especially at depths far from the image origin (i.e., for large discrepancies between z_s and z_r, as detailed in our prior discussions).

3. Since resampling is one of the most computationally expensive steps in

---

[21]For instruction purposes, however, you can find a tutorial on the construction of cubic spline interpolators in Appendix F.

FFT-based OCT image reconstruction algorithms, the algorithm must be chosen to balance accuracy and speed. I would personally suggest that you beware of 'nested' interpolators (such as up-sampling procedures followed by additional interpolation). With a little effort, such procedures can usually be combined into a single step (see Section 3.7).

4. OCT literature is full of algorithms which get passed along from user to user, and paper to paper. Not all of these algorithms are efficient. Although it is best not to reinvent the wheel, it can be beneficial to obtain a better wheel. If you will be developing an OCT reconstruction algorithm, make sure you know enough math to identify the right wheel for the job.

If spectrum resampling is neglected (or is performed improperly), the axial resolution of the reconstructed OCT image will be degraded in a depth-dependent fashion. This consequence can be readily inferred if we consider the reconstruction of a point scatterer. To begin, we redefine Eqn. (3.45) to apply to the case of non-uniformly sampled data:

$$\tilde{S}[\hat{k}_i] = \left(a_r a_t \sqrt{R}\right) \tilde{h}[\hat{k}_i] e^{-j2\hat{k}_i z_r} \eta_s e^{j2\hat{k}_i z_s} \tag{3.50}$$

Assuming our OCT image reconstruction algorithm fails to account for this non-uniform sampling, we (incorrectly) attempt to reconstruct the image signal via:

$$S[z_m] = \sum_{i=0}^{N-1} \tilde{S}[\hat{k}_i] e^{-j2k_i z_m} \tag{3.51a}$$

$$= \sum_{i=0}^{N-1} \left(a_r a_t \sqrt{R}\right) \tilde{h}[\hat{k}_i] e^{-j2\hat{k}_i z_r} \eta_s e^{j2\hat{k}_i z_s} e^{-j2k_i z_m} \tag{3.51b}$$

where $z_m = m\Delta z$, for $m \in \{0, 1, \ldots, N-1\}$, $\Delta z = \pi/(N\Delta k)$, $\Delta k = (\hat{k}_{N-1} - \hat{k}_0)/(N-1)$, and $k_i = \hat{k}_0 + i\Delta k$, for $i \in \{0, 1, \ldots, N-1\}$. For simplicity, we drop all constant

scaling terms and assume a uniform power spectrum ($\tilde{h}[k_i] = \tilde{h}[\hat{k}_i] = 1$):

$$S[z_m] = \sum_{i=0}^{N-1} e^{-j2\hat{k}_i z_r} e^{j2\hat{k}_i z_s} e^{-j2k_i z_m} \tag{3.52a}$$

$$= \sum_{i=0}^{N-1} e^{j2(\hat{k}_i(z_s - z_r) - k_i z_m)} \tag{3.52b}$$

At this stage, the subtleties of discrete-domain signals start to become a distraction to building intuition. However, it should be clear that the mismatch between the non-uniformly spaced $\hat{k}_i$ and the uniformly spaced k_i in Eqn. (3.52b) may cause some strange and undesirable effects. We convert the equation into a continuous domain analog:

$$S(z) = \int_{-\infty}^{\infty} e^{j2(\hat{k}(z_s - z_r) - kz)} \, dk \tag{3.53}$$

Since our sample is a point scatterer, and since we have assumed a uniform (and infinite) laser spectrum, our reconstructed image ought to be a delta function (under ideal image reconstruction conditions). Realizing this scenario would require that the phase term in the equation above be linear with respect to k. But what *actually* happens? We define a Taylor series expansion relating $\hat{k}$ to k:

$$\hat{k}(k) = \beta_0 + \beta_1(k - k_c) + \beta_2(k - k_c)^2 + \beta_3(k - k_c)^3 + O\left((k - k_c)^4\right) \tag{3.54}$$

for k_c the central wavenumber of light acquired by the spectrometer. If we choose to ignore higher-order terms, Eqn. (3.53) becomes:

$$S(z) = \int_{-\infty}^{\infty} e^{j2\left((\beta_0 + \beta_1(k - k_c) + \beta_2(k - k_c)^2 + \beta_3(k - k_c)^3)(z_s - z_r) - kz\right)} \, dk \tag{3.55}$$

Without any further derivations, it should be clear that the phase term in the above expression is decidedly *nonlinear* with respect to k, given values of β_2, β_3, etc. $\neq 0$. This nonlinearity in the phase term will cause the reconstructed image of the scatterer to deviate from an ideal delta function and become 'blurred' (see

Appendix C). Moreover, observe that the nonlinearity increases proportionally to the value of $z_s - z_r$. This means that scatterers imaged near the origin of the reconstructed image will suffer only a small degree of nonlinearity, and thus will only be blurred along z to a small degree. Scatterers imaged far from the origin will suffer a large degree of nonlinearity and will be blurred substantially.

In summary, given a discretely sampled SD-OCT spectral signal of length N (with non-uniform sampling in the spectral domain), the OCT image signal is obtained from the raw spectral signal via the following procedure:

1. Ignore the self-interference spectrum term (assuming this is appropriate)

2. Background subtraction (assuming $I_r[\hat{k}_i]$ is properly characterized)

3. Spectrum resampling (mapping from $\hat{k}_i$ to k_i)

4. Computational dispersion compensation (using α_2 and α_3 at minimum)

5. Discrete Fourier transform or fast Fourier transform (forward and inverse transforms are acceptable)

6. Retain the image signal only in the valid region (of size $(N/2)\Delta z$ where $\Delta z = \pi/(N\Delta k)$ in terms of OPL). Do not forget to account for axial 'stretching' of the image signal by a factor of n.

3.6 FFT-based reconstruction

Given our previous derivations, we can construct a minimal MATLAB script for reconstructing 3D OCT images. It is inefficient and it needlessly generates several intermediate copies of the data,[22] but it should still be instructional.

---

[22]Do not use it with large data sets!

```
%%----------------------------------------------%%
% VARIABLES ASSUMED TO EXIST                     %
% raw : Raw spectral data. Dims->(k,x,y)         %
% c   : Spectrometer calibration coeffs; maps    %
%       camera pix -> wavelength (nm), see code  %
%%----------------------------------------------%%

%% SET UP ---------------------------------------%%
[N,X,Y] = size(raw);
lambda  = zeros(N,1);
for i   = 1:length(c)
    lambda = lambda + c(i)*((1:N).^(i-1))'; %(nm)
end
kraw = 1000*(2*pi./lambda); %(rad/um), non-uniform

%% BACKGROUND SUBTRACTION ----------------------%%
% Frame-by-frame *estimate* of power spectrum
bkgnd          = median(raw,2);
d_nonuniform   = bsxfun(@minus,raw,bkgnd);

%% SPECTRUM RESAMPLING -------------------------%%
k         = linspace(kraw(1),kraw(end),N)';
d_uniform = interp1(kraw,d_nonuniform,k,'spline');

%% DISPERSION COMPENSATION ---------------------%%
alpha2 = 0; % Tune as necessary,  symmetric blur
alpha3 = 0; % Tune as necessary, asymmetric blur
kc       = 0.5*(k(1) + k(end));
phi_disp = alpha2*(k-kc).^2 + alpha3*(k-kc).^3;
d_corr=bsxfun(@times,d_uniform,exp(-1i*phi_disp));

%% INVERSE FOURIER TRANSFORM + DISPLAY----------%%
img   = ifft(d_corr,[],1);
frame = 1; % Tune to scroll through volume
imagesc(abs(squeeze(img(:,:,frame))));
```

3.7   Matrix-based reconstruction

3.7.1   A tale from the lab

In the Fall of 2016, I encountered a problem. I had a large collection of time-
lapse OCT images to reconstruct and analyze. With only one week remaining

until a paper submission deadline, I realized that I did not have enough time left to reconstruct my images on our lab computer using my (then current) reconstruction routine (let alone analyze the images and complete a manuscript). It was frustrating, especially since there was only a narrow range of depths that I needed to analyze. My raw spectral data consisted of 4096 pixels/A-scan. Since I was using an FFT-based algorithm, each A-scan in my reconstructed 3D images contained 4096 distinct depths. However, 2048 of those had to be reserved for the conjugate image signal (in order to keep it separable from the OCT image signal). And among the 2048 depths that remained, the portion of my sample that I cared about occupied less than 500 of those depths. So in the end, more than 85% of the depths my routine was reconstructing were 'useless' to me.

One afternoon, I was working in the lab. By working, of course, I mean that I was complaining about my plight to one of my fellow researchers: Gavrielle Untracht. I do not recall the precise details of our exchange, but I said something to the effect of "I wish there was a way to reconstruct only the regions I cared about, and stop wasting resources on those I don't need." Gav's response was something along the lines of "Well, maybe there *is* a way." And I realized she was right.

The reconstruction method that is detailed below is what emerged from that interaction. In brief, several key steps (spectrum resampling, dispersion compensation, the Fourier transform, and windowing out my desired depths) were combined into a single operation: a matrix multiplication. (Unfortunately, this did not turn out to be an original discovery. Examples of matrix-based OCT reconstruction in the literature include complex master-slave OCT [140] and compressive sensing OCT [97].) Of course, matrix multiplication is extremely

inefficient compared to operations like the FFT. However, matrix-based OCT image reconstruction did help to drastically speed up my own image reconstruction routine, given that particular lab computer, and given the constraint of a MATLAB-based programming environment. I did not meet my deadline, in the end, but I *did* manage to get by with a one-week extension. I would not have managed it without finding this method. I cannot guarantee that this formalism will be helpful to you for a given application, but it is a tool that may be worth keeping in mind nevertheless.

3.7.2 Vector-matrix formulation of OCT image reconstruction

Let $\mathbf{v} \in \mathbb{R}^{N \times 1}$ denote a single A-scan of raw SD-OCT spectral data. Each entry v_i for $i \in \{0, 1, \ldots, N - 1\}$ records the SD-OCT spectral signal corresponding to a particular wavenumber $\hat{k}_i$ from a non-uniformly spaced set of wavenumbers $\{\hat{k}_0, \hat{k}_1, \ldots, \hat{k}_{N-1}\}$.

Background subtraction

Let $\mathbf{b} \in \mathbb{R}^{N \times 1}$ denote the background spectrum. Each entry b_i records the background spectrum at the corresponding wavenumber $\hat{k}_i$. (See Appendix B for characterization methods.) Background subtraction is then performed via:

$$\mathbf{v} - \mathbf{b} \tag{3.56}$$

Spectrum resampling

Define a uniformly spaced set of wavenumbers $\{k_0, k_1, \ldots, k_{N-1}\}$ which obey the relation $k_i = k_0 + i\Delta k$ for $i \in \{0, 1, \ldots, N-1\}$, where $k_0 = \hat{k}_0$ and $\Delta k = (\hat{k}_{N-1} - \hat{k}_0)/(N-1)$. Spectrum resampling interpolates the spectral data in order to *estimate* the value of the spectral signal at each query value k_i. Many common interpolation methods (e.g., nearest neighbor, linear, polynomial, spline, sinc, and combinations thereof) compute interpolated values via weighted sums of the original data (see Appendix F for a discussion on cubic splines). That is, a re-sampling/interpolation operation that maps a vector $\mathbf{f} \in \mathbb{R}^{B \times 1}$ to another vector $\mathbf{g} \in \mathbb{R}^{A \times 1}$ can be described as:

$$g_a = \sum_{b=0}^{B-1} W_{a,b} f_b \tag{3.57a}$$

$$\mathbf{g} = \mathbf{W}\mathbf{f} \tag{3.57b}$$

where $\mathbf{W} \in \mathbb{R}^{A \times B}$ denotes a 'resampling matrix' whose entries $W_{a,b}$ are the 'resampling weights'. For spectrum resampling, $\mathbf{W} \in \mathbb{R}^{N \times N}$, and the specific values of each $W_{a,b}$ are determined by the set of all $\hat{k}_i$, k_i, and the chosen resampling scheme. In general, $\mathbf{W}$ is a sparse matrix (most entries are equal to, or very nearly, zero). As a result, Eqn. (3.57a) can be computed very efficiently (and is the standard method for performing spectrum resampling). Equation (3.57b), by comparison, is computationally inefficient, but will be useful to us. We can perform spectrum resampling on our spectral signal (after performing background subtraction) via:

$$\mathbf{W}(\mathbf{v} - \mathbf{b}) \tag{3.58}$$

Dispersion compensation

Dispersion mismatch causes axial blurring in the OCT image signal by inducing a curved phase profile (see Appendix C) across the spectral signal. If this curved phase profile can be well approximated by the function $\phi[k_i] = \alpha_2(k_i - k_c)^2 + \alpha_3(k_i - k_c)^3$, where $k_c = (k_0 + k_{N-1})/2$, then dispersion compensation can be performed on our resampled spectral data via:

$$\mathbf{A}\mathbf{W}(\mathbf{v} - \mathbf{b}) \tag{3.59}$$

where $\mathbf{A} \in \mathbb{C}^{N \times N} = \mathrm{diag}\left(e^{-j\phi[k_i]}\right)$.

Fourier transform

Define the discrete Fourier transform matrix $\mathbf{F} \in \mathbb{C}^{N \times N}$ with entries:

$$F_{a,b} = e^{-j\frac{2\pi a}{N}b} \tag{3.60}$$

Then, we can obtain our complex-valued OCT image signal $\mathbf{s} \in \mathbb{C}^{N \times 1}$ from our resampled and dispersion-compensated spectral signal via:

$$\mathbf{s} = \mathbf{F}\mathbf{A}\mathbf{W}(\mathbf{v} - \mathbf{b}) \tag{3.61}$$

Depth-selective reconstruction

Although matrix multiplications are computationally inefficient, the advantage of Eqn. (3.61) is that the individual matrices (which encode distinct steps of OCT image reconstruction) can be combined into a single linear operator $\mathbf{\Theta} = \mathbf{F}\mathbf{A}\mathbf{W}$, allowing OCT image reconstruction to be performed with a single matrix multiplication. Moreover, this single operator allows for the selective reconstruction

of individual depths in the image by discarding rows which would otherwise reconstruct depths outside the region of interest. Any single row of the OCT image can be individually reconstructed via:

$$s_a = \sum_{i=0}^{N-1} \Theta_{a,i}(v_i - b_i) \tag{3.62}$$

Other linear operations

The 'OCT reconstruction matrix' defined in Eqn. (3.61) can be considered as a linear mapping operator $\mathbf{\Theta} : \hat{k} \rightarrow z$ over a finite and discrete set of locations within its input and output domains. Many other useful operations can be formulated as linear mappings, including magnitude/phase filters, up-/down-sampling, and space/frequency-varying filters (such as depth-dependent dispersion compensation–see Appendix E). Incorporating these additional operations does not add to the computational complexity of the final combined mapping encoded by the OCT reconstruction matrix.

3.7.3 Computational complexity

Of course, most of the linear operations which comprise the OCT image reconstruction process are sparse, making their execution via matrix multiplication a poor choice from the standpoint of computational efficiency. Even the Fourier transform (a 'dense' linear mapping) can be computed with the FFT algorithm, which has only $N \log_2 N$ complexity compared to the N^2 complexity of the full matrix-based DFT. Even when only reconstructing $M < N$ depths in the image (by discarding rows of the reconstruction matrix), the reduced complexity (MN)

of the OCT reconstruction matrix may still exceed the complexity of the sparse operations and FFT.

That being said, depending on external constraints such as application, available computing hardware, programming environment, and data read/write considerations, matrix-based OCT image reconstruction may be a useful alternative to more conventional OCT image reconstruction algorithms. Moreover, the matrix formalism is easy to modify for making optimizations. For example, the various steps preceding the Fourier transform can be combined into a single sparse operation using the matrix formalism as a guide. Thus, OCT reconstruction can be split into a single sparse operation followed by a Fourier transform. Again, the utility of such methods will depend on your settings and application.

3.7.4   Matched filter formulation

There is another method to formulate OCT reconstruction matrices: matched filters. Given an OCT image signal containing a single scattering interface located precisely at the position $z = m\Delta z$ (in terms of OPL), we can ask ourselves: what would be the corresponding (complex-valued) OCT *spectral* signal that we would expect to observe in our raw spectral data (ignoring the background, self-interference, and conjugate terms)? Assuming a uniform laser power spectrum (and ignoring scaling factors) the OCT spectral signal $\Psi \in \mathbb{C}^{N \times 1}$ which we would

expect to observe would be:

$$\Psi_i^m = e^{j(2\hat{k}_i m \Delta z + \phi[\hat{k}_i])} \tag{3.63a}$$

$$\Delta z = \frac{\pi}{N \Delta k} = \frac{\pi(N-1)}{N(\hat{k}_{N-1} - \hat{k}_0)} \tag{3.63b}$$

$$\phi[\hat{k}_i] = \alpha_2(\hat{k}_i - k_c)^2 + \alpha_3(\hat{k}_i - k_c)^3 \tag{3.63c}$$

$$k_c = (\hat{k}_0 + \hat{k}_{N-1})/2 \tag{3.63d}$$

This signal model accounts for both non-uniform sampling and dispersion in the signal phase.[23] Note that Δz is given in terms of OPL instead of physical distance (since we do not necessarily know the refractive index of our sample). We can concatenate a collection of such signals to define a 'signal prediction matrix'. If we wish to reconstruct an (origin-centered, length N) set of depths $m\Delta z$ for $m \in \{-\lfloor N/2 \rfloor, \ldots, \lceil N/2 \rceil - 1\}$, then

$$\boldsymbol{\Psi} \in \mathbb{C}^{N \times N} = \begin{bmatrix} \Psi^{m=-\lfloor N/2 \rfloor} & \cdots & \Psi^{m=0} & \cdots & \Psi^{m=\lceil N/2 \rceil - 1} \end{bmatrix} \tag{3.64}$$

We can now define an OCT reconstruction matrix as $\boldsymbol{\Theta} = \boldsymbol{\Psi}^\dagger$, where '$\dagger$' denotes the Hermitian (conjugate transpose) operator. This OCT reconstruction matrix is a depth-dependent, phase-only matched filter which reconstructs OCT images without the need to define a resampling procedure. If we wish to define a 'true' matched filter, then we could incorporate the laser spectrum $\tilde{\mathbf{h}} \in \mathbb{R}^{N \times 1}$ via $\boldsymbol{\Theta} = \left(\tilde{\mathbf{H}}\boldsymbol{\Psi}\right)^\dagger$, where $\tilde{\mathbf{H}} = \text{diag}\left(\tilde{\mathbf{h}}\right)$. As before, other linear mapping operations may be incorporated into this matrix as well.

The signal prediction matrix $\boldsymbol{\Psi}$ has additional uses. It can be used as a forward model for compressive sensing/sparse signal processing applications. It can also be used as a test bed for comparing OCT reconstruction procedures. If a reconstruction procedure (matrix-based or otherwise) is 'perfect', then using

---

[23]Depth-dependent dispersion can be accounted for by modifying the phase term of Eqn. (3.63a). See Appendix E for further details.

Ψ as the input will yield an identity matrix at the output. In practice, there will tend to be cross-talk between distinct depths (e.g., the 'ideal' identity matrix output will instead be blurred along depth).

3.7.5   Phase-only matched filter implementation

```
%%------------------------------------------------%%
% VARIABLES ASSUMED TO EXIST                      %
% raw : Raw spectral data. Dims->(k,x,y)          %
% c   : Spectrometer calibration coeffs; maps     %
%       camera pix -> wavelength (nm), see code   %
%%------------------------------------------------%%

%% SET UP ----------------------------------------%%
[N,X,Y] = size(raw);
lambda  = zeros(N,1);
for i   = 1:length(c)
    lambda = lambda + c(i)*((1:N).^(i-1))'; %(nm)
end
kraw = 1000*(2*pi./lambda); %(rad/um), non-uniform

%% BACKGROUND SUBTRACTION ------------------------%%
% Frame-by-frame *estimate* of power spectrum
bkgnd = median(raw,2);
data  = bsxfun(@minus,raw,bkgnd);

%% DISPERSION COMPENSATION PARAMETERS ------------%%
alpha2 = 0; % Tune as necessary,  symmetric blur
alpha3 = 0; % Tune as necessary, asymmetric blur

kc       = 0.5*(kraw(1) + kraw(end));
phi_disp = alpha2*(kraw-kc).^2 + ...
           alpha3*(kraw-kc).^3;

%% PHASE-ONLY MATCHED FILTER ---------------------%%
m  = (-floor(N/2):ceil(N/2)-1);
dz = pi*(N-1)/(N*abs(kraw(end) - kraw(1)));
Psi= exp(1i*bsxfun(@plus,2*dz*(kraw*m),phi_disp));
O  = Psi';

%% IMAGE RECONSTRUCTION --------------------------%%
img = reshape(O*reshape(data,[N X*Y]),[N X Y]);
frame = 1; % Tune to scroll through volume
imagesc(abs(squeeze(img(:,:,frame))));
```

COMPUTATIONAL IMAGE FORMATION METHODS FOR VOLUMETRIC OPTICAL COHERENCE MICROSCOPY

4.1 Introduction

In the previous chapter, we performed extensive derivations and analyses of SD-OCT signal collection and image reconstruction methods. However, those derivations relied on the assumption of an optical system which used *very* low numerical aperture optics. This allowed the SD-OCT spectral and image signals to be approximated as 1D functions of k and z, respectively. Such a model will be insufficient for the analysis of high resolution 3D OCT imaging systems.

In this chapter, a focused Gaussian beam with a non-negligible numerical aperture will be incorporated into our models. This will require accounting for the lateral dimensions (x, y) and their corresponding spatial frequencies (q_x, q_y). The focused beam will introduce a depth-dependent lateral resolution, which may be further impacted by optical aberrations. Additional image formation routines (computational adaptive optics (CAO), in particular) are therefore required to optimize the resolution of reconstructed 3D OCT images. Further modifications to these routines were developed to mitigate distortions which emerge from the interaction of CAO with non-idealities in the optical system.

Similar to the prior chapter, I advise you to perform your own derivations and to work with real data and code to develop your understanding and intuition about the contents of this chapter. The best tip that I can offer is to ensure that you have developed a strong background in Fourier analysis for 1D signals.

Higher-dimensional Fourier analysis will rely on the same principles, but will have more variables at play. Thankfully, examining 1D components of higher-dimensional functions will often be sufficient for understanding the principles at play in 2D/3D signals and systems.[1]

4.2   The 3D SD-OCT point spread function

In order to understand and manipulate the 3D SD-OCT image signal, we must determine the OCT *spectral* signal which will be acquired from a point scatterer (i.e., we must determine the 3D point spread function). Previously, we derived this signal as a function of k only. Here, we will derive this signal as *both* a function of wavenumber k and lateral position of the scanning beam (x, y).[2]

4.2.1   Effective PSF of beam-scanning systems

The sample arm of beam-scanning SD-OCT imaging systems share a common imaging geometry, which is illustrated in Fig. (4.1). For now, follow the beam path denoted by the black rays, which are aligned to the optical axis of the imaging system. Light is emitted from a pinhole (usually, the tip of an optical fiber) into the illumination path of the system. Within this path, the beam of light is collimated and transported to an objective lens, which focuses the beam into the sample. A scattering particle (the green dot) which lies within the beam

---

[1]In fact, you will find that 3D image formation routines are strongly analogous to the 1D routines outlined in the previous chapter. For example, interferometric synthetic aperture microscopy (ISAM) is analogous to spectrum resampling, and computational adaptive optics (CAO) is analogous to (depth-dependent) dispersion compensation.

[2]We will assume that the beam does not shift along z.
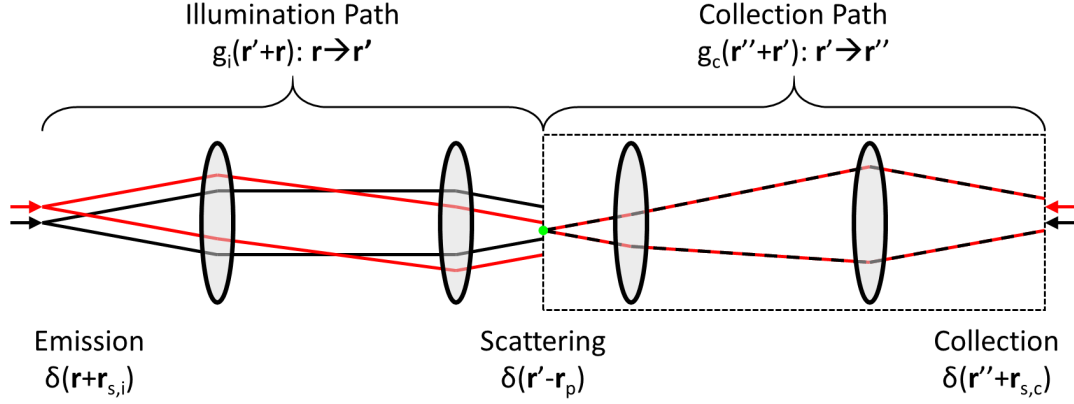
Figure 4.1: Illustration of optical paths within the sample arm of a typical beam-scanning SD-OCT imaging system. See text for details.

path scatters the incident optical field, and acts as a point source which supplies light to the collection path of the system. Note that the particle need not lie at the focus of the illumination beam in order to generate a scattering signal.

The light traverses the collection path of the system, and is eventually focused onto another pinhole (again, this is usually the tip of an optical fiber). Note that this focusing may not be perfect and is determined by the location of the scattering particle with respect to the collection path optics. Another way to think about this is to visualize a *virtual* 'collection beam' which is emitted from the collection pinhole and focuses within the sample via the collection optics. If the scattering particle does not lie at the focus of the collection beam, then the light scattered by the particle will not be perfectly focused upon the collection pinhole. Scattered light which successfully traverses the collection pinhole is recombined with light from the reference arm and sent to the spectrometer camera for interferometric signal acquisition.

Lateral scanning of the illumination and collection beams is usually performed with a set of scanning mirrors located within the illumination and col-

lection paths. However, in Fig. (4.1), scanning is performed via lateral translation of the illumination and collection pinholes. For an ideal optical system, pinhole-based scanning is equivalent to mirror-based scanning and is easier to illustrate and use for constructing a mathematical model. To visualize the effect of scanning upon the optical signal, follow the red rays in Fig. (4.1).

Lateral position within the planes of the illumination pinhole, scatterer, and collection pinhole are denoted by the vectors $\mathbf{r}$, $\mathbf{r'}$, and $\mathbf{r''}$, respectively. Assume that the emitted field takes the form of a delta function, which is translated to a position $\mathbf{r} = -\mathbf{r}_{s,i}$ in order to shift the beam. That is, our initial field in the $\mathbf{r}$-plane is given by $\delta(\mathbf{r} + \mathbf{r}_{s,i})$.

We next assume that a field originating at a position $\mathbf{r}$ in the $\mathbf{r}$-plane is mapped to the field distribution $g_i(\mathbf{r'} + \mathbf{r})$ in the $\mathbf{r'}$-plane. Note that this assumes that the optical system is linear, space-invariant in the lateral dimensions, and has a magnification factor of -1. In order to compute the illumination field within the $\mathbf{r'}$-plane, we integrate the field contributions from across the $\mathbf{r}$-plane:

$$\int_{\mathbf{r} \in \mathbb{R}^2} g_i(\mathbf{r'} + \mathbf{r})\delta(\mathbf{r} + \mathbf{r}_{s,i}) \, dr^2 = g_i(\mathbf{r'} - \mathbf{r}_{s,i}) \tag{4.1}$$

Assuming that the sample contains a single small scattering particle at a position $\mathbf{r'} = \mathbf{r}_p$ such that the scattering potential is given by $\eta(\mathbf{r'}) = \delta(\mathbf{r'} - \mathbf{r}_p)$, then the scattered field within the $\mathbf{r'}$-plane will be given by the product of the illumination field and the scattering potential: $g_i(\mathbf{r'} - \mathbf{r}_{s,i})\delta(\mathbf{r'} - \mathbf{r}_p)$.

Similarly to the illumination path, let the collection path be described by a linear, laterally space-invariant, and -1 magnification function $g_c(\mathbf{r''} + \mathbf{r'})$, which maps a point source at a position $\mathbf{r'}$ in the $\mathbf{r'}$-plane to a field distribution in the $\mathbf{r''}$-plane. Integrating the scattered field contributions from across the $\mathbf{r'}$-plane

to obtain the total scattered field in the $\mathbf{r}''$-plane yields:

$$\int_{\mathbf{r}'\in\mathbb{R}^2} g_i(\mathbf{r}'-\mathbf{r}_{s,i})\delta(\mathbf{r}'-\mathbf{r}_p)g_c(\mathbf{r}''+\mathbf{r}')\,dr'^2 = g_i(\mathbf{r}_p-\mathbf{r}_{s,i})g_c(\mathbf{r}''+\mathbf{r}_p) \qquad (4.2)$$

Finally, we assume that the collection pinhole takes the form of a delta function centered at a position $\mathbf{r}'' = -\mathbf{r}_{s,c}$ in the $\mathbf{r}''$-plane. Integrating the scattered field in the $\mathbf{r}''$-plane over the collection pinhole yields the total field which will be collected by the optical system:

$$\int_{\mathbf{r}''\in\mathbb{R}^2} g_i(\mathbf{r}_p-\mathbf{r}_{s,i})g_c(\mathbf{r}''+\mathbf{r}_p)\delta(\mathbf{r}''+\mathbf{r}_{s,c})\,dr''^2 = g_i(\mathbf{r}_p-\mathbf{r}_{s,i})g_c(\mathbf{r}_p-\mathbf{r}_{s,c}) \qquad (4.3)$$

From this relationship, we observe that the total point spread function of the imaging system will be a product of an illumination PSF g_i with a collection PSF g_c. For standard beam-scanning SD-OCT systems, the illumination and collection paths are one and the same. Backscattered light simply traverses the illumination path in reverse until it is collected by the original illumination pinhole. This will be referred to as a 'double-pass' imaging geometry.[3] Under these conditions $\mathbf{r}_{s,i} = \mathbf{r}_{s,c}$, and both terms may be replaced by a single term $\mathbf{r}_s$. Furthermore, if we assume that the optical system is reciprocal, then $g_i = g_c$, and we obtain a final field measurement of $g_i^2(\mathbf{r}_p-\mathbf{r}_s)$, corresponding to a net PSF of:

$$g_i^2(-\mathbf{r_s}) \qquad (4.4)$$

All together, we conclude that a model of the 3D SD-OCT point spread function may be obtained from a model of the illumination beam.

---

[3]OCT systems with distinct or 'forked' illumination and collection paths do exist. The differing paths allow for greater control of optical system properties. However, such systems are uncommon due to their increased complexity and difficulty of construction.

4.2.2 Spectral domain propagation kernel

In order to model the illumination beam, we need to be able describe the propagation of light through 3D space.[4] For 3D propagation of planar wavefronts, the scalar wavenumber is replaced by a 3D wave vector $\mathbf{k} = \langle k_x, k_y, k_z \rangle = k\hat{\mathbf{r}}$, where $\hat{\mathbf{r}}$ is a unit vector which points in the direction of propagation. As a result, the total phase change observed between two locations $\mathbf{r}_0$ and $\mathbf{r}_1$ will be given by $\Delta\phi_{01} = n\mathbf{k} \cdot (\mathbf{r}_1 - \mathbf{r}_0)$.

Given a beam propagating along the z-axis, assume that we know the optical field distribution $E(x, y, z, k)$ within the xy-plane at a particular depth z and wavenumber k. This 2D field can be decomposed into its lateral spatial frequency spectrum via:

$$\tilde{E}(q_x, q_y, z, k) = \int_{-\infty}^{\infty} \int_{-\infty}^{\infty} E(x, y, z, k) e^{-j(q_x x + q_y y)} \, dx \, dy \tag{4.5}$$

In a vacuum, there is a direct correspondence between the spatial frequency vector $\mathbf{q} = \langle q_x, q_y, q_z \rangle$ and wave vector $\mathbf{k} = \langle k_x, k_y, k_z \rangle$. However, in a homogeneous medium with refractive index n, $\mathbf{q} = n\mathbf{k}$.[5] We can always perform lateral Fourier transforms with respect to (q_x, q_y) so long as we know the discrete set of (x, y) points that we scan our beam through. However, taking a Fourier transform with respect to $\mathbf{k}$ also requires knowledge of n. Given this distinction, we will have be careful to not confuse $\mathbf{q}$ and $\mathbf{k}$ when performing our derivations.

In order to determine how the beam evolves along z we need only modify the phase of $\tilde{E}(q_x, q_y, z, k)$. Specifically, we need to change the phase by $n\mathbf{k} \cdot \langle 0, 0, \Delta z \rangle = nk_z \Delta z$, where Δz is the physical distance traveled along z. Using the relations

---

[4]Recall from the previous chapter that for 1D light propagation, the phase was assumed to evolve as $d\phi / dz = nk$. We need to expand upon this.

[5]Note that this relationship only holds for modeling beam propagation. It will not necessarily hold for Fourier transforms of the OCT image signal!

$k_x^2 + k_y^2 + k_z^2 = k^2$, $q_x^2 + q_y^2 + q_z^2 = q^2$, and $\mathbf{q} = n\mathbf{k}$, we conclude that:

$$\tilde{E}(q_x, q_y, z + \Delta z, k) = \tilde{E}(q_x, q_y, z, k)e^{jnk_z\Delta z} \tag{4.6a}$$

$$= \tilde{E}(q_x, q_y, z, k)e^{j\Delta z\sqrt{(nk)^2-(nk_x)^2-(nk_y)^2}} \tag{4.6b}$$

$$= \tilde{E}(q_x, q_y, z, k)e^{j\Delta z\sqrt{(nk)^2-q_x^2-q_y^2}} \tag{4.6c}$$

We will define $e^{j\Delta z\sqrt{(nk)^2-q_x^2-q_y^2}}$ as the 'spectral domain propagation kernel', which we can use to perform beam propagation operations to signals defined within the spatial frequency domain.

4.2.3 Paraxial Gaussian beam model

Now that we have a general model for the (space-varying) 3D OCT PSF as a function of the illumination beam, and can predict how such a beam evolves along depth, we can plug in an appropriate beam model to derive useful formulas for the 3D OCT spectral and image signals. Since most beam-scanning SD-OCT systems use single-mode optical fibers to introduce light to (and collect light from) the sample arm, the Gaussian beam makes for an appropriate and analytically tractable model.

Assume that the illumination beam of our SD-OCT system is a Gaussian beam with waist ($1/e$ radius) w, focal plane depth of $z = z_f$, and uniform power spectrum ($|A(k)|^2 = 1$). Let the (scalar, at focus) illumination field take the form:

$$E_i(x, y, z_f, k) = e^{-(x^2+y^2)/w^2} \tag{4.7}$$

Applying a 2D lateral Fourier transform yields[6] (see Appendix G):

$$\tilde{E}_i(q_x, q_y, z_f, k) = w^2 e^{-(w^2/4)(q_x^2 + q_y^2)} \tag{4.8}$$

In order to determine the optical field at depths outside the focal plane, we advance the phase of $\tilde{E}_i(q_x, q_y, z_f, k)$ via multiplication with the spectral domain propagation kernel from Eqn. (4.6c), yielding:

$$\tilde{E}_i(q_x, q_y, z - z_f, k) = w^2 e^{-(w^2/4)(q_x^2 + q_y^2)} e^{j(z - z_f)\sqrt{(nk)^2 - q_x^2 - q_y^2}} \tag{4.9}$$

Applying the paraxial approximation, we obtain:

$$\tilde{E}_i(q_x, q_y, z - z_f, k) = w^2 e^{-(w^2/4)(q_x^2 + q_y^2)} e^{j(z - z_f)\sqrt{(nk)^2 - q_x^2 - q_y^2}} \tag{4.10a}$$

$$\approx w^2 e^{-(w^2/4)(q_x^2 + q_y^2)} e^{j(z - z_f)\left(nk - (q_x^2 + q_y^2)/2nk\right)} \tag{4.10b}$$

$$= w^2 e^{-(w^2/4)(q_x^2 + q_y^2)} e^{jnk(z - z_f)} e^{-j\left((z - z_f)/2nk\right)(q_x^2 + q_y^2)} \tag{4.10c}$$

$$= w^2 e^{-\left(w^2/4 + j(z - z_f)/2nk\right)(q_x^2 + q_y^2)} e^{jnk(z - z_f)} \tag{4.10d}$$

Returning to the space domain along the lateral dimensions yields:

$$E_i(x, y, z - z_f, k) = \mathcal{F}^{-1}_{(x,y) \to (q_x, q_y)}\left[w^2 e^{-\left(w^2/4 + j(z - z_f)/2nk\right)(q_x^2 + q_y^2)} e^{jnk(z - z_f)} \right] \tag{4.11a}$$

$$= e^{jnk(z - z_f)} \mathcal{F}^{-1}_{(x,y) \to (q_x, q_y)}\left[w^2 e^{-\left(w^2/4 + j(z - z_f)/2nk\right)(q_x^2 + q_y^2)} \right] \tag{4.11b}$$

$$= e^{jnk(z - z_f)}\left(\frac{w^2}{w^2/4 + j(z - z_f)/2nk} e^{-(x^2 + y^2)/4\left(w^2/4 + j(z - z_f)/2nk\right)} \right) \tag{4.11c}$$

$$\propto e^{jnk(z - z_f)}\left(\frac{w^2}{w^2 + j2(z - z_f)/nk} e^{-(x^2 + y^2)/\left(w^2 + j2(z - z_f)/nk\right)} \right) \tag{4.11d}$$

$$= aw^2 e^{jnk(z - z_f)} e^{-a(x^2 + y^2)}, \quad a = 1/\left(w^2 + j2(z - z_f)/nk \right) \tag{4.11e}$$

---

[6]All Fourier transforms of Gaussian functions shown in this chapter will be denoted with equality, even though constant factors not related to w or z will be dropped. These dropped factors do not impact our analyses here.

4.2.4 Measured field from a point scatterer

For an SD-OCT imaging system that obeys the PSF model which culminated in Eqn. (4.4), the SD-OCT image spectrum that would be measured (after interferometric detection) from a scatterer located at a position $\mathbf{r}' = \langle x', y', z' \rangle$ will be:

$$\tilde{S}(x, y, k; \mathbf{r}', z_f) = E_i^2(x' - x, y' - y, z' - z_f, k)e^{j2k(z_{f,OPL} - z_{r,OPL})} \tag{4.12a}$$

$$= a^2 w^4 e^{j2nk(z' - z_f)} e^{-2a((x' - x)^2 + (y' - y)^2)} e^{j2k(z_{f,OPL} - z_{r,OPL})} \tag{4.12b}$$

$$= a^2 w^4 e^{j2nk(z' - z_f)} e^{-2a((x - x')^2 + (y - y')^2)} e^{j2k(z_{f,OPL} - z_{r,OPL})} \tag{4.12c}$$

where $z_{f,OPL}$ is the OPL between the splitter and the focal plane of the beam and $z_{r,OPL}$ is the OPL of the reference arm. For brevity, we will hereafter define $z_{fr} = z_{f,OPL} - z_{r,OPL}$.[7] We will assume that background subtraction, spectrum resampling, and dispersion compensation have already been performed in order to obtain $\tilde{S}(x, y, k; \mathbf{r}', z_f)$ from the raw SD-OCT spectral data. We once more return to the spatial frequency domain:

$$\tilde{S}(q_x, q_y, k; \mathbf{r}', z_f) = \mathcal{F}_{(x,y) \to (q_x, q_y)} \left[a^2 w^4 e^{j2nk(z' - z_f)} e^{-2a((x - x')^2 + (y - y')^2)} e^{j2kz_{fr}} \right] \tag{4.13a}$$

$$\propto a w^4 e^{j2nk(z' - z_f)} e^{-(q_x^2 + q_y^2)/8a} e^{-j(q_x x' + q_y y')} e^{j2kz_{fr}} \tag{4.13b}$$

$$= a w^4 e^{j2nk(z' - z_f)} e^{-(q_x^2 + q_y^2)(w^2 + j2(z' - z_f)/nk)/8} e^{-j(q_x x' + q_y y')} e^{j2kz_{fr}} \tag{4.13c}$$

$$= a w^4 e^{-(w^2/8)(q_x^2 + q_y^2)} e^{-j(q_x x' + q_y y')} e^{j2kz_{fr}} e^{j2nk(z' - z_f)} e^{-j(z' - z_f)(q_x^2 + q_y^2)/(4nk)} \tag{4.13d}$$

$$= a w^4 e^{-(w^2/8)(q_x^2 + q_y^2)} e^{-j(q_x x' + q_y y')} e^{j2kz_{fr}} e^{j(z' - z_f)(2nk - (q_x^2 + q_y^2)/(4nk))} \tag{4.13e}$$

$$\approx a w^4 e^{-(w^2/8)(q_x^2 + q_y^2)} e^{-j(q_x x' + q_y y')} e^{j2kz_{fr}} e^{j(z' - z_f)\sqrt{(2nk)^2 - q_x^2 - q_y^2}} \tag{4.13f}$$

Let's analyze the terms of Eqn. (4.13f):

---

[7]Not coincidentally, z_{fr} is the depth (in terms of OPL) at which the focal plane will appear in reconstructed OCT images.

- The leading term $a = \left(w^2 + j2(z' - z_f)/nk \right)^{-1}$ encodes depth-dependent changes in signal magnitude and phase. If $z_R = nkw^2/2$ denotes the Rayleigh range of our illumination beam, then $a = e^{j\psi(z'-z_f)}/(wW(z' - z_f))$, where $\psi(z' - z_f) = -\arctan((z' - z_f)/z_R)$ corresponds to the Gouy phase shift and $W(z' - z_f) = w\sqrt{1 + ((z' - z_f)/z_R)^2}$ is the $1/e$ radius of the illumination beam as a function of depth. Although the Gouy phase induces phase curvature along the k-axis, this term is negligible for our analysis of defocus.

- The first exponential term is a real-valued function corresponding to a Gaussian magnitude profile along the lateral spatial frequencies. The width of this function in the spatial frequency domain increases as the focal plane beam waist decreases. This is consistent with the principle that attaining smaller focal spots requires larger spatial frequency bandwidths.

- The second exponential term is a phase-only function which is modulated by the lateral position (x', y') of the scattering particle. Since these phase profiles are linear, they do not cause any distortions or image degradation. They merely shift the PSF along x and y such that the function is centered on the location of the scattering particle.

- The third exponential term is a phase-only function which, similarly to the second term, encodes a spatial position. In this case, the term encodes the position of the focal plane with respect to the origin of the reconstructed OCT image (in terms of OPL).

- The fourth (and final) exponential term is yet another phase-only function. However, we encounter a problem. The phase profile is *curved* along all three of our spectral variables, q_x, q_y, and k. As discussed in Appendix C, these curved profiles will cause blurring of the space-domain OCT image signal (along x, y, and z, respectively). This blurring scales proportionally

111

to $(z' - z_f)$, causing an increase in image degradation with increasing distance from the focal plane. Note that if we apply the assumptions of the previous chapter (i.e., we assume a *very* low numerical aperture such that a signal is present only for very small values of q_x and q_y), then this term is well-approximated by $e^{j2nk(z'-z_f)}$. In this form, the term would merely encode the depth of the scattering particle with respect to the focal plane. However, for systems with a non-zero numerical aperture, the term takes its present form in Eqn. (4.13f) and induces degradation of the image.

In general, we will have to manipulate our signal $\tilde{S}(q_x, q_y, k)$ in order mitigate the blurring caused by the final exponential term in Eqn. (4.13f) (which will hereafter be referred to as the 'defocus kernel'). Doing so will allow us to restore an optimal focal plane resolution throughout our imaged volume (regardless of axial position with respect to the focal plane).

4.3   Defocus mitigation

Defocus mitigation techniques seek to remove depth-dependent blurring in OCT images by reducing or removing the phase curvature introduced by the defocus kernel. Unlike refocusing techniques for intensity-based imaging, defocus mitigation techniques for OCT can be formulated as direct, non-interative methods so long as the location of the focal plane is known, and the spectral-domain variables can be determined from the operating characteristics of the system (e.g., spatial sampling rates in (x, y), a mapping from spectrometer pixel to wavenumber, and the refractive index of the sample[8]). This is thanks to the

---

[8]Typically, the refractive index of water is used to describe biological samples.

fact that OCT measures the phase of the scattered optical field through inter-ferometric detection. Here we will review methods for defocus mitigation, in order of increasing computational efficiency.

4.3.1 3D phase correction

The first, perhaps obvious, method for defocus mitigation is to perform a 3D phase correction which cancels out the phase of the defocus kernel:

$$\phi(q_x, q_y, k; z - z_f) = \left(z - z_f\right) \sqrt{(2nk)^2 - q_x^2 - q_y^2} \tag{4.14}$$

In order to refocus our scattering particle (located at a depth of $z = z'$), we need to apply a phase of $-\phi(q_x, q_y, k; z' - z_f)$. Applying such an operation to our signal from Eqn. (4.13f) yields:

$$\tilde{S}(q_x, q_y, k; \mathbf{r}', z_f) e^{-j\phi(q_x, q_y, k; z' - z_f)} = aw^4 e^{-(w^2/8)(q_x^2 + q_y^2)} e^{-j(q_x x' + q_y y')} e^{j2kz_{fr}} \tag{4.15}$$

Ignoring the Gouy phase term encoded in a, we find that the phase of our 'cor-rected' signal no longer has curvature with respect to q_x, q_y, or k. However, we also appear to have destroyed information about the axial location of our scattering particle, since the variable z' has been canceled out. In fact, the axial location of the image of the scattering particle has been shifted such that it is co-localized with the focal plane at the OPL position $z_f - z_r$ in the reconstructed OCT image. So, not only has the particle been 'refocused', the image of the particle has been shifted into the focal plane of our image. This has the unin-tended consequence that any other scatterers which were originally imaged *at* the focal plane have now been shifted *out* of the focal plane, and have become defocused in the process. This means that, even though 3D phase correction

113

can bring different depths into focus, each depth in the image requires its own unique 3D multiplication operation in order to be refocused by the procedure. This makes 3D phase correction extremely computationally expensive, and so this technique is not employed for OCT, as far as I am aware. However, for instructional purposes, here is the most efficient formulation that I know of:

Assuming we have identified the location of the focal plane in the defocus-corrupted OCT image, then we have also determined z_{fr} (which corresponds to the axial location of the focal plane in the OCT image, in terms of OPL). We compute the function:

$$\tilde{S}_{z_f=0}(q_x, q_y, k) = \tilde{S}(q_x, q_y, k)e^{-j2kz_{fr}} \tag{4.16}$$

which has the effect of axially shifting the space-domain image data such that the focal plane is located at the origin ($z = 0$) of the image. We then perform depth-dependent refocusing *and* extraction of the refocused plane $S(x, y; z)$ via:

$$S(x, y; z) = \mathcal{F}^{-1}_{(x,y)\to(q_x,q_y)}\left[\int_{-\infty}^{-\infty} \tilde{S}_{z_f=0}(q_x, q_y, k)e^{-j\phi(q_x,q_y,k;z)}\, dk\right] \tag{4.17}$$

Note that the $(z - z_f) = (z - 0)$ term used for computing $\phi(q_x, q_y, k; z)$ must be given in terms of the *physical* length (not OPL)!

4.3.2   Interferometric synthetic aperture microscopy

Interferometric synthetic aperture microscopy (ISAM) is a vastly more efficient method for performing defocus mitigation. First reported in 2007 [137], ISAM leverages techniques which were originally developed to optimize the resolution of synthetic aperture radar images. In order to understand the operating

principles underlying ISAM, we first return to the phase of our defocus kernel:

$$\phi(q_x, q_y, k; z - z_f) = \left(z - z_f\right) \sqrt{(2nk)^2 - q_x^2 - q_y^2} \tag{4.18}$$

This curved phase profile causes blurring which increases proportionally to distance from the focal plane. We have encountered depth-dependent blurring before. Specifically, we encountered depth-dependent axial blurring when our OCT image reconstruction procedure failed to account for non-uniform sampling of the spectral data (Section 3.5.5). Recall that SD-OCT data is typically acquired with non-uniform sampling with respect to k. Instead, spectral data is sampled uniformly with respect to a distorted variable $\hat{k}$, which was defined as:

$$\hat{k}(k) = \beta_0 + \beta_1(k - k_c) + \beta_2(k - k_c)^2 + \beta_3(k - k_c)^3 + O\left((k - k_c)^4\right) \tag{4.19}$$

for k_c the central wavenumber acquired by the spectrometer. When we *failed* to resample the data from being uniformly sampled in $\hat{k}$ to being uniformly sampled in k, a residual curved phase profile emerged whose magnitude was proportional to the distance of the scattering particle from the origin of the reconstructed image (i.e., the resulting axial blurring grew proportionally to distance from the image origin). Just as a resampling procedure is used to prevent/mitigate depth-dependent axial blurring, ISAM uses a resampling procedure to mitigate depth-dependent beam defocus.

Define the variable:

$$q_z(q_x, q_y, k) = \sqrt{(2nk)^2 - q_x^2 - q_y^2} \tag{4.20}$$

ISAM resamples the spectral signal $\tilde{S}(q_x, q_y, k)$ (which is uniformly sampled with respect to k) to be uniformly sampled with respect to q_z, yielding $\tilde{S}(q_x, q_y, q_z)$.[9]

---

[9]If spectrum resampling was not performed, $\tilde{S}(q_x, q_y, \hat{k})$ can also be mapped to $\tilde{S}(q_x, q_y, q_z)$.

Performing this resampling operation results in a new phase profile:

$$\phi(q_x, q_y, q_z; z - z_f) = \left(z - z_f\right) q_z \tag{4.21}$$

This profile has no curvature with respect to q_x, q_y, or q_z. The lack of any phase curvature in the new profile means that blurring due to defocus has been eliminated entirely. The resampled phase profile now merely encodes axial position with respect to the focal plane. In order to correctly apply our resampling procedure, however, a few more details are required.

Since *all* the terms defining our signal will be subjected to resampling, we must ensure that the resampling procedure which mitigates the phase curvature of the defocus kernel will not *induce* blurring by warping the phase of other terms. We restate our signal from Eqn. (4.13f):

$$\tilde{S}(q_x, q_y, k; \mathbf{r}', z_f) = aw^4 e^{-(w^2/8)(q_x^2 + q_y^2)} e^{-j(q_x x' + q_y y')} e^{j2kz_{fr}} e^{j(z' - z_f)\sqrt{(2nk)^2 - q_x^2 - q_y^2}} \tag{4.22}$$

Given that the Gouy phase shift contained in a is negligible (such that we can assume $a \approx |a|$), the third exponential term ($e^{j2kz_{fr}}$) is the only other term besides the defocus kernel which is a function of k. Unfortunately, since this term is linear with respect to k, applying the ISAM resampling procedure will induce curvature in this component of the signal. Thankfully, there is a simple solution to this. Since the term contains no explicit information about individual scatterers, we can simply remove this term before performing resampling, and restore

the term afterward:

$$\tilde{S}_{\text{ISAM}}(q_x, q_y, q_z; \mathbf{r}', z_f) = \text{ISAM}\left[\tilde{S}(q_x, q_y, k; \mathbf{r}', z_f)e^{-j2kz_{fr}}\right]e^{j(z_{fr}/n)q_z} \tag{4.23a}$$

$$\propto \text{ISAM}\left[ae^{-(w^2/8)(q_x^2+q_y^2)}e^{-j(q_x x'+q_y y')}e^{j2kz_{fr}}e^{j(z'-z_f)\sqrt{(2nk)^2-q_x^2-q_y^2}}e^{-j2kz_{fr}}\right]e^{j(z_{fr}/n)q_z} \tag{4.23b}$$

$$\approx |a|\,e^{-(w^2/8)(q_x^2+q_y^2)}e^{-j(q_x x'+q_y y')}\text{ISAM}\left[e^{j2kz_{fr}}e^{j(z'-z_f)\sqrt{(2nk)^2-q_x^2-q_y^2}}e^{-j2kz_{fr}}\right]e^{j(z_{fr}/n)q_z} \tag{4.23c}$$

$$\propto \left(1/W(z'-z_f)\right)e^{-(w^2/8)(q_x^2+q_y^2)}e^{-j(q_x x'+q_y y')}\text{ISAM}\left[e^{j(z'-z_f)\sqrt{(2nk)^2-q_x^2-q_y^2}}\right]e^{j(z_{fr}/n)q_z} \tag{4.23d}$$

$$= \left(1/W(z'-z_f)\right)e^{-(w^2/8)(q_x^2+q_y^2)}e^{-j(q_x x'+q_y y')}e^{j(z'-z_f)q_z}e^{j(z_{fr}/n)q_z} \tag{4.23e}$$

where $\text{ISAM}[\cdot]$ denotes the ISAM resampling operation which maps $k \to q_z$. The pre-multiplication by $e^{-j2kz_{fr}}$ has the effect of axially shifting the OCT image signal such that the focal plane is located at the origin of the reconstructed image.[10] The post-multiplication by $e^{j(z_{fr}/n)q_z}$ (although not strictly necessary) shifts the focal plane back to its original depth in the image after ISAM is performed.

Restoring the space domain signal is achieved via a 3D Fourier transform:

$$S_{\text{ISAM}}(x, y, z; \mathbf{r}', z_f) = \int_{-\infty}^{\infty}\int_{-\infty}^{\infty}\int_{-\infty}^{\infty}\tilde{S}_{\text{ISAM}}(q_x, q_y, q_z; \mathbf{r}', z_f)e^{j(q_x+q_y-q_z)}\,dq_x\,dq_y\,dq_z \tag{4.24a}$$

$$\propto \left(1/W(z'-z_f)\right)e^{-(2/w^2)\left((x-x')^2+(y-y')^2\right)}\delta(z-(z'-z_f)-z_{fr}/n) \tag{4.24b}$$

The phase of the signal in Eqn. (4.23e) is linear with respect to q_x, q_y, and q_z. This means that the resolution of the image is no longer a function of position, and is limited only by the lateral bandwidth (defined by the first exponential term $e^{-(w^2/8)(q_x^2+q_y^2)}$) and the axial bandwidth (defined by the resampled laser spectrum $|A(q_z)|^2$, which we did not include in our derivations above). Interestingly,

---

[10]This is identical to the operation performed in Eqn. (4.16). As was described for that scenario, z_{fr} may be calibrated based solely on the OCT image itself (rather than requiring explicit knowledge about the actual position of the focal plane and reference mirror).

ISAM is able to mitigate defocus within 3D data using only a 1D resampling operation.[11] This allows ISAM to be very computationally efficient compared to depth-dependent 3D phase correction. However, under the right conditions, defocus mitigation can be performed even faster, and with greater flexibility.

4.3.3   Computational adaptive optics

Computational adaptive optics (CAO) is a method which assumes that the curvature of the defocus kernel is negligible along the *k*-axis [3]. In doing so, CAO is able to replace the depth-dependent 3D operations of the 3D phase correction method with depth-dependent 2D operations, resulting in vastly improved computational speeds which can even surpass that of ISAM. Furthermore, the speed of CAO can be leveraged to enable the measurement and mitigation of optical aberrations (within certain limits, of course). One last time, we return to the phase profile of our defocus kernel:

$$\phi(q_x, q_y, k; z - z_f) = \left(z - z_f\right) \sqrt{(2nk)^2 - q_x^2 - q_y^2} \tag{4.25}$$

As we discussed previously, this phase profile exhibits curvature along all three spectral variables q_x, q_y, and k. But what are the relative amounts of curvature

---

[11]Granted, the resampling operation *does* change as a function of (q_x, q_y). However, this is not a major concern, especially if a look-up table can be used to define each resampling operation.

along each dimension? Under the paraxial approximation ($q_x, q_y \ll 2kn$):

$$\frac{\partial \phi}{\partial k} = \frac{2nk\left(z - z_f\right)}{\sqrt{(2nk)^2 - q_x^2 - q_y^2}} \approx \frac{2nk}{\sqrt{(2nk)^2}}\left(z - z_f\right) = 1\left(z - z_f\right) \tag{4.26a}$$

$$\frac{\partial \phi}{\partial q_x} = \frac{-q_x\left(z - z_f\right)}{\sqrt{(2nk)^2 - q_x^2 - q_y^2}} \approx \frac{-q_x}{\sqrt{(2nk)^2}}\left(z - z_f\right) = \frac{-q_x}{2nk}\left(z - z_f\right) \tag{4.26b}$$

$$\frac{\partial \phi}{\partial q_y} = \frac{-q_y\left(z - z_f\right)}{\sqrt{(2nk)^2 - q_x^2 - q_y^2}} \approx \frac{-q_y}{\sqrt{(2nk)^2}}\left(z - z_f\right) = \frac{-q_y}{2nk}\left(z - z_f\right) \tag{4.26c}$$

In the absence of curvature, we would expect the derivatives above to be constant with respect to the spectral variables. Since $\partial \phi / \partial k$ satisfies this condition (under the paraxial approximation), we conclude that the defocus kernel exhibits negligible curvature along the k-axis, meaning that defocus is due almost entirely to curvature along the q_x- and q_y-axes[12]. As a result, we can approximate the phase of our defocus kernel by:

$$\phi(q_x, q_y, k; z - z_f) \approx \phi(q_x, q_y; k_c, z - z_f) = \left(z - z_f\right)\sqrt{(2nk_c)^2 - q_x^2 - q_y^2} \tag{4.27}$$

where k_c is the central wavenumber that we have previously defined throughout our derivations. Since we have lost dependence on k, we no longer require the signal to be in the 3D spectral domain (q_x, q_y, k) in order to cancel out the phase profile of the defocus kernel. Instead we need only be in the spectral domain along the lateral dimensions (q_x, q_y).

---

[12]Of course, if we use a very high numerical aperture system, this conclusion breaks down, as do our paraxial beam model and associated derivations. Thankfully, even 'high resolution' OCM systems tend to obey the paraxial approximation 'well enough'. If you want to investigate this subject with a little more rigor (while still being able to apply the paraxial approximation), examine the second-order derivatives of ϕ: $\partial^2 \phi / \partial k^2$, $\partial^2 \phi / \partial q_x^2$, $\partial^2 \phi / \partial q_y^2$, $\partial^2 \phi / \partial k \partial q_x$, $\partial^2 \phi / \partial k \partial q_y$, and $\partial^2 \phi / \partial q_x \partial q_y$. You may predict/observe some interesting phase curvature (and consequent spatial blurring) properties of defocus for high numerical aperture OCT systems and/or for low numerical aperture OCT systems at large distances from the focal plane! For example, for large amounts of defocus/blurring, the PSF of the OCT system will start to become 'bowl-shaped', as opposed to flat, like our analysis above predicts. 3D phase correction and ISAM account for this, while CAO does not!

Starting with a reconstructed 3D OCT image $S(x, y, z)$ (which is corrupted by beam defocus), we take a 2D lateral Fourier transform to obtain $\tilde{S}(q_x, q_y, z)$. If we recast z_f as the depth of the focal plane with respect to $z = 0$ in the OCT image, the defocus-corrected image can be obtained via:

$$\mathcal{F}^{-1}_{(x,y)\to(q_x,q_y)}\left[\mathcal{F}_{(x,y)\to(q_x,q_y)}\left[S(x,y,z)\right]e^{-j(z-z_f)\sqrt{(2nk_c)^2-q_x^2-q_y^2}}\right] \tag{4.28}$$

(Note that $z - z_f$ must be given in terms of physical length, not OPL!) If there are phase aberrations (e.g., astigmatism, coma, spherical aberration, etc.) present in addition to defocus, CAO can compensate for these aberrations as well. If the total phase aberrations of the optical system are well approximated by the function $\phi_a(q_x, q_y)$, then the aberration-corrected image will be given by:

$$S_{ac}(x,y,z) = \mathcal{F}^{-1}_{(x,y)\to(q_x,q_y)}\left[\mathcal{F}_{(x,y)\to(q_x,q_y)}\left[S(x,y,z)\right]e^{-j(z-z_f)\sqrt{(2nk_c)^2-q_x^2-q_y^2}}e^{-j\phi_a(q_x,q_y)}\right] \tag{4.29}$$

Of course, optical aberrations are not typically known *a priori*. Instead, $\phi_a(q_x, q_y)$ is often formulated as a weighted sum of Zernike polynomials[13] across a user-defined aperture. If we define $q_{r,\max} = 4/w$ as the $1/e^2$ radius of the Gaussian magnitude term in Eqn. (4.13f), then $\phi_a(q_x, q_y)$ may be approximated as:

$$\phi_a(q_x, q_y) \approx \sum_{i=1}^{\infty} a_i Z_i(q_x/q_{r,\max}, q_y/q_{r,\max}) \tag{4.30}$$

where a_i is a scalar weighting coefficient and Z_i is the ith Noll-indexed Zernike polynomial.[14] Appropriate values of a_i can be computed via an optimization procedure which maximizes/minimizes a suitable metric function of the CAO-processed image.[15] Although analogous methods for aberration correction are

---

[13] Any number of basis function families could be used. The Zernike basis is just the standard, and is particularly well-suited for efficiently describing common optical aberrations.

[14] Typically, going beyond $i = 15$ becomes impractical.

[15] L_p-norms of $S_{ac}(x, y, z)$ are common choices for metric functions. (The only exception is the L_2-norm, which cannot be optimized, as a consequence of Parseval's theorem.) Entropy-based metrics and metrics of the spatial frequency content of the Fourier transform of $|S_{ac}(x, y, z)|$ are also common choices.

also possible for the 3D phase correction and ISAM methods detailed previously, the formulations become cumbersome and computationally expensive. The simple formulations and computational efficiency enabled by the 2D nature of CAO make optimization routines that sense defocus and aberrations feasible.

There is a lot of room for further discussion about the intuition, theory, properties, and implementation of CAO for higher-order aberration correction. However, such topics did not play a significant role in the research of this dissertation. Therefore, I will defer to my colleagues in the lab and in the field at large to provide these discussions in their own publications and dissertations! From this point on, we will work exclusively with the defocus-mitigation implementation of CAO from Eqn. (4.28). In spite of this, the optimizations and discussions outlined in the remainder of this chapter do have relevance to higher-order implementations of CAO.

4.3.4 Limitations of computational image formation methods

Of course, the capabilities of CAO (and the related techniques we have discussed) to optimize resolution are limited. If aberrations are very large, they can contribute to irreversible signal loss. In the case of pure defocus, the magnitude of the OCT image signal degrades with distance from the focal plane, as governed by $1/W(z' - z_f)$. This signal reduction implies that, despite our defocus mitigation efforts, the SNR of the OCT image will eventually drop below the noise floor at depths far from the focal plane. This signal degradation will take place over especially short distances for high numerical aperture systems. Higher-order aberrations can have more complicated effects, such as contribut-

ing additional depth-dependent effects to the image SNR and modifying the depth-dependent modulation transfer function of the optical system (which can degrade resolution, even when CAO corrections are optimal). Moreover, these degradations can make the metric functions of aberration-sensing optimization procedures non-convex, and therefore difficult to solve in an efficient manner.

4.3.5 Basic CAO implementation

```
%%------------------------------------------------%%
% VARIABLES ASSUMED TO EXIST                      %
% data : Defocused OCT image S(z,x,y)             %
%          Size = [Z,X,Y]                         %
% k    : Uniformly spaced wavenumber axis         %
%          Size = [N,1]                           %
% dx,dy: Pixel size in beam-scanning grid         %
% n    : Refractive index of medium               %
% zf   : Location of focal plane (physical units) %
%          with respect to first pixel in 'data'  %
%%------------------------------------------------%%

%% SET UP ----------------------------------------%%
[Z,X,Y] = size(data);
[N]     = length(k);
kc      = mean(k);

dk = abs(k(end)-k(1))/(N-1);
dz = abs(pi/(n*N*dk));

qx = (2*pi/dx)*(1/X)*(0:1:X-1)';
qx = qx - qx(ceil((X+1)/2));

qy = (2*pi/dy)*(1/Y)*(0:1:Y-1)';
qy = qy - qy(ceil((Y+1)/2));

[qx,qy] = ndgrid(qx,qy);
qr      = sqrt(qx.^2 + qy.^2);
qr      = ifftshift(qr); % Optimize out fftshifts

% Aperture to prevent imaginary #'s. Can shrink to
% perform low-pass filtering of signal as well.
aperture = (qr <= 2*n*kc);

% Defocus kernel
phase = aperture .* sqrt((2*n*kc)^2 - qr.^2);
```

```
%% PERFORM CAO--------------------------------%%
output = data;
for i = 1:Z
        planeFD    = fft2(squeeze(data(i,:,:)));
        correction = aperture.*exp(-1i*(dz*i-zf)*phase);
        plane      = ifft2(planeFD .* correction);

        output(i,:,:) = plane;
end
```

4.4   Mitigation of system non-idealities

Although standard image formation techniques ('basic' SD-OCT image recon-
struction combined with CAO) readily generate high-resolution 3D OCT im-
ages, those images are not guaranteed to be suitable for applications which re-
quire the quantitative analysis of sample structure. For example, traction force
optical coherence microscopy (TF-OCM, which will be detailed in Chapters 5-7)
was developed to quantify the forces exerted by cells embedded in a 3D extra-
cellular matrix (ECM). A key step in TF-OCM is the measurement of 3D sub-
strate deformations induced by the action of cell forces upon the surrounding
environment. As a consequence, TF-OCM is sensitive to non-idealities in the
imaging process which cause images to become spatially warped and distorted.
Therefore, the development of TF-OCM required the development of multiple
modifications to the standard SD-OCT image formation procedure in order to
compensate for non-ideal imaging conditions [112]. The sections that follow
detail both common system non-idealities and methods that can be used to mit-
igate them (with the goal of minimizing the emergence of distortions across
time-lapse image data). Detailed equations and diagrams regarding the current
recommended implementation of these methods may be found in Chapter 7.6.

4.4.1 Bulk modulation

Beam misalignment and/or sample tilt can cause the detected OCT signal to become modulated (i.e., the lateral bandwidth of the OCT signal shifts from being centered at $(q_x, q_y) = (0, 0)$ to being centered at $(q_x, q_y) = (q'_x, q'_y)$. Applying a naive CAO procedure which fails to account for signal modulation results in an interesting interaction. Starting with an ideal (i.e., free of defocus) image signal $S(x, y, z)$ which has been modulated by the function $e^{j(q'_x x + q'_y y)}$, we approximate the *original* defocus-corrupted signal in the spatial frequency domain as:

$$\tilde{S}(q_x - q'_x, q_y - q'_y, z)e^{j(z-z_f)\sqrt{(2nk_c)^2-(q_x-q'_x)^2-(q_y-q'_y)^2}} \tag{4.31}$$

Note that the modulation affects *both* the desired signal and the defocus kernel. If we apply a CAO algorithm which fails to account for modulation, we obtain:

$$\tilde{S}(q_x - q'_x, q_y - q'_y, z)e^{j(z-z_f)\sqrt{(2nk_c)^2-(q_x-q'_x)^2-(q_y-q'_y)^2}}e^{-j(z-z_f)\sqrt{(2nk_c)^2-q_x^2-q_y^2}} \tag{4.32}$$

The defocus kernel and the correction that we have applied do not match. As a consequence, the residual phase term will induce distortions in the output image signal. Under the paraxial approximation and the assumption that $q'_x, q'_y \ll 2nk_c$, we approximate the above expression with:

$$\tilde{S}(q_x - q'_x, q_y - q'_y, z)e^{j(z-z_f)\left(2nk_c - \left((q_x-q'_x)^2+(q_y-q'_y)^2\right)/4nk_c\right)}e^{-j(z-z_f)\left(2nk_c-(q_x^2+q_y^2)/4nk_c\right)} \tag{4.33a}$$

$$= \tilde{S}(q_x - q'_x, q_y - q'_y, z)e^{j(z-z_f)\left((q'_x q_x + q'_y q_y)/2nk_c - (q'^2_x + q'^2_y)/4nk_c\right)} \tag{4.33b}$$

$$= \tilde{S}(q_x - q'_x, q_y - q'_y, z)e^{j(z-z_f)(q'_x q_x + q'_y q_y)/2nk_c}e^{-j(z-z_f)(q'^2_x + q'^2_y)/4nk_c} \tag{4.33c}$$

Returning to the space domain yields a corrupted image signal:

$$S(x - x_0(z), y - y_0(z), z)e^{j\left(q'_x(x-x_0(z))+q'_y(y-y_0(z))\right)}e^{-j(z-z_f)(q'^2_x + q'^2_y)/4nk_c} \tag{4.34}$$

where

$$(x_0(z), y_0(z)) = \left(-\frac{q'_x}{2nk_c}(z - z_f), -\frac{q'_y}{2nk_c}(z - z_f)\right) \tag{4.35}$$

124

We observe that the ideal image signal $S(x, y, z)$ has undergone a lateral shearing operation (akin to pushing against the side of a deck of cards).[16] This shearing increases proportionally to distance from the focal plane, and is directly proportional to the strength of the initial signal modulation.

Ideally, this artifact would be mitigated by optimizing system alignment. However, if the optical system lacks the necessary degrees of freedom or fine-tuning capabilities, performing computational mitigation *prior* to CAO is a viable option. First, the amount of modulation along the *x*- and *y*-dimensions must be determined. The heuristic that I have used is, given an OCT image signal $S(x, y, z)$ (not to be confused with the $S(x, y, z)$ used above), compute:

$$\hat{S}(q_x, q_y) = \int_{-\infty}^{\infty} \left| \mathcal{F}_{(x,y,z) \to (q_x,q_y,q_z)} [S(x, y, z)] \right| dq_z \tag{4.36}$$

For a system which uses Gaussian beams, this (real-valued) function will have an approximately Gaussian profile. There may be some local noise or sharp peaks, which can be removed with a 2D median filter. Local quadratic curve fitting can then be used to locate the peak of the Gaussian profile. The coordinates of the peak correspond to the modulation parameters (q_x', q_y'). Bulk demodulation is then be performed via:

$$S(x, y, z)e^{-j(q_x'x + q_y'y)} \tag{4.37}$$

This will mitigate the modulation of the signal and the consequent formation of shearing artifacts when performing CAO. An alternative formulation for mitigating signal modulation is to shift the phase correction function applied during CAO such that it is centered at (q_x', q_y') in the spatial frequency domain. This latter method has been used as a key step to combat distortion artifacts which emerged when applying CAO algorithms to astigmatic OCT systems [95].

---

[16]Since we typically visualize only the *magnitude* of OCT images, we can safely ignore the phase terms in Eqn. (4.34).

4.4.2 Phase instability

There is extensive literature on the phase stability requirements of CAO and related methods. References [155, 156] provide useful information on this topic. In brief, any phenomena which cause the phase of the OCT signal to evolve in complex and unexpected ways during signal acquisition can degrade or completely eliminate the benefits of computational image formation methods. Sources of instability include sample motion, OPL fluctuations in the optical system due to vibrations, temperature changes, etc., and laser source instability, among others. Since phase instability is often induced by random processes, it can be difficult to mitigate its effects. To gain a more intuitive understanding of the effects of phase instability, we can work through a simple thought experiment.

Assume that an SD-OCT imaging system acquires A-scans over a set of (x, y) locations following a lateral raster scanning pattern. Let the x-axis correspond to the 'fast axis' of this scanning pattern, while the y-axis corresponds to the 'slow axis'. Let the phase of the 'true' (defocused) OCT image signal $S(x, y, z)$ be corrupted by some time-varying phase function $\phi_s(t)$ throughout the acquisition process due to phase instability. The raster scanning pattern used to acquire the image can be described by a time-varying set of lateral beam positions: $(x(t), y(t))$. This scanning patterns maps $\phi_s(t)$ to a space-domain function $\phi_s(x(t), y(t))$, such that the acquired image signal can be described by:

$$S_s(x, y, z) = S(x(t), y(t), z)e^{j\phi_s(x(t),y(t))} = S(x, y, z)e^{j\phi_s(x,y)} \tag{4.38}$$

Assuming that $\phi_s(t)$ fluctuates about some constant mean, we can think about $\phi_s(t)$ in terms of its amplitude and its frequency content. These properties control the *local rate* at which $\phi_s(t)$ evolves over *time*. The relative speed of the raster scanning pattern versus the rate of phase fluctuations determines how severely

$\phi_s(x, y)$ changes with respect to *position*. The faster $\phi_s(t)$ evolves compared to the speed of scanning beam, the steeper the *local slope* of $\phi_s(x, y)$ will be (i.e., in units of radians per unit length). The slow axis in particular will be especially vulnerable to phase instability, since the slow axis is typically traversed 2-3 orders of magnitude slower than the fast axis of the raster scanning pattern.

If we zoom in on a particular lateral patch (centered at $(\hat{x}, \hat{y})$) of our image data, we can approximate the local signal of that patch by:

$$S(x - \hat{x}, y - \hat{y}, z)e^{j\phi_s(x-\hat{x}, y-\hat{y})} \approx S(x - \hat{x}, y - \hat{y}, z)e^{j\phi(\hat{x},\hat{y})}e^{j\left(\phi_{s,x}(\hat{x},\hat{y})(x-\hat{x})+\phi_{s,y}(\hat{x},\hat{y})(y-\hat{y})\right)} \quad (4.39)$$

where $\phi_{s,x}$ and $\phi_{s,y}$ denote the gradient of ϕ_s with respect to x and y, respectively. This bears a close resemblance to the bulk modulation problem discussed previously, but now we have a *local* signal modulation, meaning that any distortions which emerge from CAO will vary as a function of (initial) lateral position (in addition to growing in strength with distance from the focal plane). From this, we can infer the general effect of different levels of phase instability:

- **Very slow** fluctuations, such that the phase is approximately constant throughout image acquisition, will have a negligible effect.

- **Slow** fluctuations, such that the phase evolves approximately linearly across the entire FOV, will appear equivalent to a bulk modulation.

- **Moderate** fluctuations, such that there are several 'hills' and 'valleys' of phase fluctuations across the FOV (which are much wider than the local uncorrected/pre-CAO PSF width), will result in local image distortions (especially along the slow axis) after CAO.

- **Rapid** fluctuations, which are not well-approximated by 1st-order polynomials (linear functions) over length scales on the order of the local

uncorrected/pre-CAO PSF width, will prevent CAO from functioning properly. Images will still 'refocus', but some of the signal energy will no longer localize properly, such that images of point scatterers will appear to be corrupted by local, space-varying aberrations.

- **Very rapid** fluctuations, such that the phase evolves substantially over length scales smaller than the local uncorrected PSF width, will significantly impair or completely eliminate the ability of CAO to refocus signals. Images of point scatterers will be surrounded by a 'haze' of signals that cannot be localized to a single point using even high-order aberration corrections. In the worst case, a 'corrected' PSF may appear no better than the original uncorrected PSF.

Note that these principles have been inferred in the context of small phase fluctuations (which tend to emerge from axial OPL fluctuations that are smaller than the axial resolution of the system). Large vibrations in the sample or imaging system (along any dimension) can cause our assumptions that the image signal exists on a rectangular grid of points in (x, y, z) to fail, and we will lose our ability to perform Fourier analysis, in the general case, and our formulation of (and ability to perform) FFT-based CAO algorithms will fall apart.

In the course of my research, I encountered 'moderate' phase instability, which caused local depth-dependent shearing distortions in my images. For an example, see Supplementary Movie 1 in Ref. [112]. Thankfully, these distortions can be mitigated with 'phase registration' procedures that are commonly available for *in vitro* imaging applications.

First, assume we have acquired an image of a sample which includes a glass coverslip. The coverslip has two surfaces: one which contacts the sample, and

the other which is exposed to the open environment (typically, the immersion fluid of the objective lens, be it air, water, oil, etc.). The latter coverslip surface serves as a strong and isolated reflector. If phase instability is due primarily to axial OPL fluctuations, then the signal from the glass surface provides a good measurement of the corrupting phase function, and can be used to mitigate the effects of phase instability.[17]

Phase registration method 1

If the surface of the coverslip is flat and level in the image (i.e., the surface exists along a single depth z_c), then we extract the phase of the image signal at this depth:

$$\phi_c(x, y) = \angle S_s(x, y, z_c) \tag{4.40}$$

and use this phase to cancel out the corrupting phase:

$$\left(S(x, y, z)e^{j\phi_s(x,y)}\right)e^{-j\phi_c(x,y)} \approx S(x, y, z) \tag{4.41}$$

Since imaging a glass surface that is perfectly flat and level is unlikely to occur, this method often needs to be supplemented with other procedures (e.g., coherence gate curvature correction, which is described in the next section).

Phase registration method 2 (preferred)

Given the limitations and dependencies of method 1, I recommend using this method instead. Given a coverslip surface that is *approximately* flat and level,

---

[17]Note that the coverslip surface needs to be *clean*! Do not get the surface of your sample dirty or scratched, or you will be out of luck for performing high-resolution imaging beneath the sites of contamination/damage.

centered about a position $z = z_c$, identify a minimal axial range $[z_c - \Delta z_c, z_c + \Delta z_c]$ which fully contains the image of the glass surface (axial PSF and all) yet *does not contain any other scattering interfaces/surfaces*. Create a copy of the original dataset $S_s(x, y, z)$ and apply a window:

$$S_c(x, y, z) = S_s(x, y, z)W(z - z_c; \Delta z_c) \tag{4.42}$$

where

$$W(z; \Delta z_c) = \begin{cases} 1 & |z| \leq \Delta z_c \\ 0 & \text{otherwise} \end{cases} \tag{4.43}$$

Next, compute:

$$\phi_c(x, y, q_z) = \angle \mathcal{F}_{z \to q_z} [S_c(x, y, z)] \tag{4.44}$$

This phase function encodes the position of the glass surface (including any corrupting phase shifts as well as residual dispersion that our previous routines may have failed to compensate). Finally, phase registration is achieved via:

$$\mathcal{F}^{-1}_{z \to q_z} \left[\mathcal{F}_{z \to q_z} [S_s(x, y, z)] e^{-\phi_c(x,y,q_z)} e^{-jq_z z_c} \right] \tag{4.45}$$

Analogous to our previously described dispersion compensation and CAO procedures, this function cancels out any phase shifts and residual dispersion in the image signal. It also has the side effect of axially shifting each A-scan until the glass appears flat and level in the output image.[18] The factor of $e^{-jq_z z_c}$ ensures that the glass appears at its original depth of z_c in the output image.

---

[18]This is actually a useful effect, as discussed in the section on coherence gate curvature.

4.4.3 Coherence gate curvature

Coherence gate curvature (CGC) is a phenomenon which results from the use of non-ideal optical systems and manifests as space-varying distortions in reconstructed OCT image data [55]. Detailed derivations and explanations regarding CGC may be found in Appendix H. In brief, a major feature of CGC is to cause planar surfaces in the sample to appear as curved surfaces in the OCT image. In particular, this curvature results from axial shifting of the OCT image signal, where the amount of axial shifting varies as a quadratic function of the lateral beam position. Although it is relatively easy to derive an idealized model of CGC, deriving the exact form of CGC for a real system (which may have many non-ideal optical elements) is not always feasible. Such was the case for the imaging systems used for this dissertation. As a consequence, heuristics were used for establishing acceptable computational CGC mitigation techniques.[19]

Coordinate system heuristics

In practice, planar surfaces tend to appear both tilted *and* curved in OCT images due to a combination of non-idealities in optical design (e.g., CGC, beam misalignment, etc.) and sample positioning. Determining how much tilt and/or curvature is a real feature of the sample versus an artifact of the optical system can be difficult. Therefore, the following heuristics were applied throughout the research of this dissertation.

1. Assume the presence of a flat reflective surface in the sample (such as a

---

[19]Although these heuristics were sufficient for my purposes in developing TF-OCM (detailed in later chapters), there is still room to improve CGC mitigation techniques. Some possible avenues for exploration are discussed in Appendix H.

glass coverslip for *in vitro* biological experiments).[20]

2. Assume that the 'ideal' or 'correct' coordinate system for image analysis is one in which this surface appears both flat and level in the OCT image.[21]

3. Assume that a coordinate transformation which consists solely of lateral position-dependent axial shifting/translations will suffice to arrive at a decent approximation of the 'ideal' coordinate system.

4. This approximate coordinate transformation will not result in sufficient residual distortions that substantially harm experimental capabilities which rely upon subsequent processing of the OCT image data.

These heuristics were chosen in order to prioritize an approximate method (which is both simple and consistent) over a more accurate method (which could be both complicated to calibrate and computationally expensive to apply). A consequence of using this heuristic is that residual image distortions may be present which can neither be corrected nor readily accounted for. However, the method is easy to implement and apply across numerous systems without time-consuming calibration procedures or other analyses. As with any computational method, improved system designs that minimize the initial problem (via hardware) will make residual errors in post-processing a vanishing concern. For an example of such a system, see Appendix I.

CGC mitigation method 1

Recall that phase registration method 2 has a 'side effect' of making the windowed glass surface appear flat and level in the output OCT image. This corre-

---

[20]We require such a surface for performing phase registration anyway.

[21]The 'level' condition is not necessary, but is useful in practice.

sponds exactly to the desired output image established by our heuristics. There-fore, the easiest way to perform CGC mitigation is to apply phase registration method 2! Such a technique was first reported in Ref. [55].

CGC mitigation method 2

The problem with CGC method 1 is that the (tilted and curved) glass sur-face could span an axial range of up to 50-100 μm for images exhibiting large amounts of CGC and/or using a very large lateral FOV. In such extreme cases, the windowed signal $S_c(x, y, z)$ from phase registration method 2 will contain a lot of 'empty space' and so may incorporate a large quantity of background noise which degrades the resulting output image. Even worse, it may not be possible to window out the entire surface without including other surfaces within the windowed axial range. As a result I developed an alternative method specifically for applications to time-lapse data (which leverage the same or sim-ilar corrections repeatedly).

First, the glass surface is approximated by a quadratic function:

$$z_c(x, y) = a_{xx}x^2 + a_{xy}xy + a_{yy}y^2 + a_x x + a_y y + a_0 \tag{4.46}$$

Then, this curvature is removed using the Fourier shift theorem:

$$S_{\text{flat}}(x, y, z) = \mathcal{F}_{z \to q_z}^{-1} \left[\mathcal{F}_{z \to q_z} \left[S(x, y, z) \right] e^{jq_z(z_c(x,y)-z_{c,0})} \right] \tag{4.47}$$

where c_0 is a constant (e.g., $z_{c,0} = a_0$). For time-lapse data, $z_{c,0}$ should be chosen to be constant across all processed images. This will cause the images to be axially registered following CGC mitigation.

CGC mitigation method 3

Since CGC mitigation method 2 relies on a curve-fitting procedure, it is not guaranteed to completely mitigate CGC. Therefore, I recommend a third method: Perform CGC mitigation method 2 for 'coarse' corrections and follow up with CGC mitigation method 1 for 'fine' corrections. This method yields the best results since the first step will make the glass surface used by all methods appear *nearly* flat and level. Step two can then be performed using a very narrow axial window, thus minimizing noise or other artifacts which would otherwise corrupt the procedure. (The resulting image will also be phase-registered!) You can find equations and diagrams outlining this procedure in Chapter 7.6.

CGC mitigation method 4

The very last method that I developed in my research was a hybrid of hardware-based and computation-based methods. My optical system was redesigned to physically minimize CGC artifacts in my image data (see Appendix I). Data was then processed using CGC mitigation method 3.

4.4.4   Focal plane curvature

The focal plane of an imaging system is often assumed to be flat and level. However, as a consequence of using non-ideal optical systems, the focal 'plane' of an imaging system may instead take the form of a curved surface. To complicate matters, this focal plane curvature (FPC) may be different from the CGC of the optical system. This means that even after performing CGC mitigation, the focal

plane may still appear titled and/or curved in the OCT image. (For an example of how this can happen, see Appendix J.)

This creates a problem for typical CAO algorithms like that defined in Eqn. (4.28). Such algorithms rely upon the assumption of a laterally-invariant PSF. However, when the focal 'plane' is curved due to FPC, the lateral PSF varies as a function of lateral position. CAO algorithms which can accommodate for a laterally varying PSF do exist [84], however, such algorithms can be difficult to calibrate and/or computationally expensive to perform. In order to address this problem, I devised a simple method to temporally 'remove' FPC, perform CAO, and then 'restore' FPC back to its original state (and thus restore the image to a state where CGC is minimal). Specifically, starting with a CGC-mitigated image, the focal 'plane' is approximated with a quadratic function:

$$z_f(x, y) = b_{xx}x^2 + b_{xy}xy + b_{yy}y^2 + b_x x + b_y y + b_0 \tag{4.48}$$

Then, FPC is removed in a similar fashion to CGC mitigation method 2:

$$\mathcal{F}_{z \to q_z}^{-1} \left[\mathcal{F}_{z \to q_z} \left[S(x, y, z) \right] e^{jq_z \left(z_f(x,y) - z_{f,0} \right)} \right] \tag{4.49}$$

where $z_{f,0}$ is a constant (such as b_0 or the mean value of $z_f(x, y)$ across the FOV). Unlike the constant $z_{c,0}$ from CGC mitigation method 2, the value of $z_{f,0}$ may be allowed to vary between time-points in a time-lapse dataset. The resulting image exhibits a 'flat' focal plane and thus a lateral PSF which is approximately invariant with lateral position. CAO is then performed to optimize the depth-dependent lateral resolution of the image, and FPC is then restored via the inverse operation to Eqn. (4.49):

$$\mathcal{F}_{z \to q_z}^{-1} \left[\mathcal{F}_{z \to q_z} \left[S(x, y, z) \right] e^{-jq_z \left(z_f(x,y) - z_{f,0} \right)} \right] \tag{4.50}$$

The resulting 3D image thus exhibits an optimal lateral resolution at all (x, y, z) positions. An example illustrating the effects of this procedure is shown in

Chapter 6 and Ref. [112]. Different methods for performing the initial quadratic fitting step may be found in Chapters 6 and 7.

4.4.5   Order of operations

It is important that corrections for bulk modulation, phase instability, coherence gate curvature, and focal plane curvature be done in the correct order. In brief, CGC removal, phase registration, and FPC removal should be performed prior to calibrating and removing bulk modulation. This is because the bulk modulation calibration can be corrupted by curvature artifacts and/or phase instabilities (which warp, distort, and/or smear the lateral spatial frequency content of the image). Once these steps are completed, CAO can be performed and followed by FPC restoration and any subsequent image processing/analysis.

CHAPTER 5

MEASUREMENT OF DYNAMIC CELL-INDUCED 3D DISPLACEMENTS FOR TRACTION FORCE OPTICAL COHERENCE MICROSCOPY: A PILOT STUDY

Content reuse disclosure The contents (text, figures, etc.) of this chapter have been reprinted/adapted from a previously published journal paper of which I was the first author.[1] Some sections/passages of the original work have been replaced with updated/alternative content (e.g., the Introduction). Other sections have been omitted to avoid redundancy with other content present elsewhere in this dissertation (e.g., the Abstract, portions of the Discussion, etc.). The contents of this chapter which have been reprinted/adapted will be indicated, as appropriate. To view the full contents of the original paper, please see Ref. [110].

Author contributions statement All experiments/data/results were performed/obtained/generated by me (J.A. Mulligan) in their entirety. The original journal paper on which this chapter is based (Ref. [110]) was primarily written by me, with guidance and editing contributed by the co-authors of the original study.

---

[1]Reprinted/adapted with permission from The Optical Society: J.A. Mulligan, F. Bordeleau, C.A. Reinhart-King, S.G. Adie. Measurement of dynamic cell-induced 3D displacement fields in vitro for traction force optical coherence microscopy. *Biomed. Opt. Express* **8**(2), 1152-1171 (2017). https://doi.org/10.1364/BOE.8.001152 © The Optical Society (2017)

5.1 Introduction

This chapter highlights the methods and findings of a pilot study which we performed in 2016. The objective was to determine and demonstrate whether we could use OCT imaging to record 3D deformation fields induced by the traction forces of cells embedded in a 3D hydrogel substrate. Such capabilities are vital to performing traction force optical coherence microscopy (TF-OCM). This study was originally published in *Biomedical Optics Express* in 2017 (Ref. [110]).

Please note that at the time of this study, many key image formation routines (detailed in Chapter 4.4) and hardware developments (see Appendix I) had not yet been developed. As such, this chapter should be used primarily for historical context, and for its discussions of important factors related to the development of TF-OCM. I have also included occasional footnotes containing new thoughts that have emerged in hindsight.

Since this is the first instance of TF-OCM methods that appear in this dissertation, the Methods will be detailed prior to discussing the results. In later chapters, this will be reversed.

All remaining passages and figures in this chapter (below) have been reprinted/adapted with permission from Ref. [110] © The Optical Society (2017)

5.2 Methods

5.2.1 Cell culture and 3D sample preparation

NIH-3T3 fibroblasts (ATCC, CRL-1658) were maintained in media consisting of a 100:10:1 solution of Dulbecco's Modified Eagle Medium (Life Technologies), bovine calf serum (Life Technologies), and penicillin-streptomycin (Life Technologies). 3D cell cultures were prepared for imaging by first suspending fibroblasts in chilled (4°C) media at a density of 2×10^5 cells/mL. To provided scattering contrast for use in deformation tracking, 0.5 μm diameter polystyrene beads in aqueous solution (Sigma-Aldrich) were added to the cell suspension to achieve a concentration of approximately 1×10^9 beads/mL. This suspension was then combined in a 1:1 ratio (by volume) with Matrigel (Corning). The resulting mixture was deposited in 100 μL aliquots onto the surface of glass-bottomed petri dishes with a 10 mm diameter circular microwell (MatTek) and left to gel/solidify for 30 minutes in an incubator. Samples were then covered with culture media, left overnight in an incubator (~12 hours), and imaged the following day. In addition to these 3D cell cultures, imaging phantoms for displacement tracking validation were prepared using an identical protocol, excluding the addition of cells.

5.2.2 OCM system and data acquisition

Samples were imaged using a custom-built spectral-domain optical coherence microscopy (SD-OCM) system. The illumination source was a Ti:Sapphire laser (Femtolasers, INTEGRAL Element) with a central wavelength of 800 nm and a

full-width-at-half-maximum bandwidth of 160 nm. A-scans were acquired using a spectrometer (Wasatch Photonics) with a 300 nm full bandwidth, coupled to a 4096 pixel 12-bit CMOS line scan camera (Teledyne Dalsa, Piranha4). This yielded an axial sampling period of 0.75 μm per pixel (physical length in aqueous media) after image reconstruction. The system exhibited a sensitivity of 85 dB at 350 μm optical path delay from the zero optical path delay position,[2] and a sensitivity fall-off of -10 dB/mm of optical path length. We believe that the sensitivity was limited by the alignment of the line scan camera, which had square 10.56 μm pixels, rather than 'tall' rectangular pixels which provide superior tolerance to misalignment. The objective lens used in this study was an Olympus XLUMPlanFl 20$\times$/0.95 W / ∞/0. Samples were imaged in an inverted configuration, with illumination and collection occurring through the bottom surface of the glass-bottomed petri dishes. In this configuration, the axial and transverse resolutions of the system were approximately 2.4 μm and 1.5 μm, respectively.

Volumes acquired under the time-lapse imaging protocol consisted of 1024×1024 A-scans, acquired at a line scan rate of 30 kHz with an exposure time of 12 μs. The dimensions ($z \times x \times y$) of each full reconstructed volume were $1536 \times 420 \times 420$ μm^3 in aqueous media ($2048 \times 1024 \times 1024$ voxels). However, due to constraints imposed by the limited depth-of-field of the objective lens, only a $225 \times 420 \times 420$ μm^3 ($300 \times 1024 \times 1024$ voxels) volume surrounding the imaged cell/s was reconstructed and saved for further analysis using a high-speed SD-OCM processing method for depth-selective reconstruction (see Chapter 3.7) [27]. To achieve this, the imaged cells and the focal plane of the sys-

---

[2]For any who are unfamiliar with the term, zero optical path delay (OPD) denotes the position in the OCT image where the OPL of light collected from the sample arm exactly matches the OPL of light collected from the reference arm. In other words, it is the axial origin ($z = 0$ position) of the reconstructed OCT image.

tem were co-localized prior to image acquisition at a position of 1 mm below the zero optical path delay position, enabled by custom-built acquisition software with a real-time live display and computational adaptive optics (CAO) enabled [171]. Using these volume dimensions enabled the use of a high transverse spatial sampling frequency (at 410 nm/pixel, to accommodate the high transverse resolution) while maintaining a field-of-view which captured a large volume surrounding each imaged cell, all while maintaining a manageable data set size for analysis in MATLAB with limited computer memory (128 GB RAM on our system). Approximately 150 GB of raw SD-OCM data was acquired for each time-lapse imaging experiment.

5.2.3 Experimental design and time-lapse imaging protocol

Physiological temperature, humidity, and pH were maintained throughout imaging using an incubation stage (Okolab, UNO-PLUS). To demonstrate the viability of using OCM imaging to quantify the dynamics of 3D cell-induced extracellular matrix (ECM) deformations, cells in the previously described 3D culture were exposed to either cytochalasin D (a well-characterized actin cytoskeleton destabilizing agent that inhibits cell contractility [181]) dissolved in dimethyl sulfoxide (DMSO) at a concentration of 0.5 mM for the experimental group, or pure DMSO for the control group. The imaging and exposure protocol was as described below.

To identify and select a fibroblast cell for imaging, the sample was translated until a cell (which appears as a ~30-100 μm scattering structure embedded in the optically clear Matrigel) became visible in the live display. Since we sought

to image cells that were actively interacting with the ECM, the candidate cell was inspected for the presence of filopodia protruding into the ECM, and for a generally elongated morphology, as is typical for healthy NIH-3T3 cells in 3D culture [60]. If these features were not present (i.e., the cell lacked protrusions or had a roughly spherical morphology), the cell was rejected and the searching process continued. After identifying what appeared to be a suitable cell or cell pair, the sample and imaging FOV were fixed in place for the remainder of the experiment.

Each sample was imaged every 5 minutes for a total time of 90 minutes. Baseline cell activity (i.e., without reagent exposure) was recorded during the first 30 minutes. After 30 minutes, samples were exposed to the appropriate reagent (cytochalasin D solution or pure DMSO). For the experimental group, cytochalasin D solution was added to the culture media in which the sample was immersed, resulting in a final cytochalasin D concentration of 1 μM, and a final DMSO concentration of 0.2 vol%. For the control group, pure DMSO was added to the culture media to achieve a final DMSO concentration of 0.2 vol%. Cell activity was then monitored for an additional 60 minutes following the introduction of these compounds, yielding a final total of 19 time-points per sample.

5.2.4 Reconstruction of volumetric OCM data sets and image sequences for displacement tracking

Volumetric data sets were reconstructed in MATLAB R2014b using the standard operations of background spectrum subtraction, spectrum resampling, disper-

sion compensation, and the Fourier transform (see Chapter 3) [102]. The high

resolution objective resulted in defocus artifacts which increased rapidly with

distance from the focal plane. Therefore, defocus was compensated using com-

putational adaptive optics (CAO, see Chapter 4) [3]. The technique used con-

sisted of a plane-by-plane 2D deconvolution, which was performed in the spa-

tial frequency domain using multiplication with a phase-only correction kernel

[3, 171]. The kernel parameters were determined via maximization of a peak

image intensity metric. This metric was used to obtain an initial estimate of

the proper defocus correction at each depth in a given volumetric data set.[3]

The final applied kernel parameters were obtained from a linear fit of the ini-

tial estimates, since the severity of the defocus phase aberration increases ap-

proximately linearly with distance from the focal plane.[4] This fitting operation

helped to reduce noise in the metric-driven correction kernel calibration. The

underlying assumption is that phase aberrations vary slowly with depth, such

that adjacent or nearby depths must undergo similar corrections. The linear re-

lationship of the defocus phase aberration in depth is an assumption used in

prior work, and is based upon axial beam propagation (see Chapter 4) [171].

To study local average ECM deformations in the transverse and vertical di-

mensions of the sample, maximum intensity projections were obtained from the

reconstructed volumes. This operation collapses the 3D displacement tracking

---

[3]This was not explained well in the original publication. In brief, defocus was cor-
rected via the application of a phase-only function in the form of a 2D paraboloid with
a particular scalar weight $a \in \mathbb{R}$. An initial estimate for a at a particular depth z
was obtained via $\hat{a}(z) = \text{argmax}\,[f(\alpha; z)]$, where $f(\alpha; z)$ is the metric function: $f(\alpha; z) =$
$L_\infty\left[\mathcal{F}^{-1}_{(x,y)\to(q_x,q_y)}\left[\mathcal{F}_{(x,y)\to(q_x,q_y)}\left[S(z,x,y)\right]\exp\left(j\alpha\left(q_x^2 + q_y^2\right)\right)\right]\right]$, where L_∞ denotes the 'L-infinity norm',
$\mathcal{F}_{(x,y)\to(q_x,q_y)}$ and $\mathcal{F}^{-1}_{(x,y)\to(q_x,q_y)}$ denote the forward and inverse 2D Fourier transform across the lat-
eral dimensions, and $S(z,x,y)$ is the 3D complex-valued OCT image signal. I consider this an
outdated method for defocus correction. See Chapter 4 for an alternative formulation.
[4]That is, the final applied correction coefficient $a(z)$ was given by the best-fit linear polyno-
mial for the coefficient estimates $\hat{a}(z)$.

problem into multiple 2D tracking problems, which may be performed indepen-
dently within cross-sectional slices of the imaged volume along both the trans-
verse and vertical orientations. Projections in the transverse orientation were
obtained from the full $225 \times 420 \times 420\ \mu\mathrm{m}^3$ volumes previously described (form-
ing a $420 \times 420\ \mu\mathrm{m}^2$ projection in the xy-plane). Vertically-oriented projections
were obtained by projecting along a $40\ \mu$m thick vertical slice intersecting the
imaged cell body/bodies (forming a $225 \times 420\ \mu\mathrm{m}^2$ projection in the zx-plane).

Over the 90-minute imaging span, some bulk sample drift was present be-
tween acquisitions. This bulk drift between time-points was removed using 2D
cross-correlation performed over the full FOV of the maximum intensity pro-
jection image sequences. This operation acts as a high-pass spatial filter on the
computed cell-induced ECM displacement fields, and assumes that the imaged
cell does not cause a bulk displacement of the substrate it is embedded in. This
operation has practical benefits for computation time which will be discussed
in Section 5.2.6. Since the vertical slices exhibited intensities which rapidly de-
creased with distance from the focal plane, the mean intensity[5] at each depth
was normalized prior to any displacement tracking.

5.2.5 Manual tracking of individual particles

To obtain a basic picture of cell-induced ECM deformation over time,
polystyrene beads embedded in the Matrigel substrate at selected regions of in-
terest were identified and tracked manually in the transverse (xy-plane) image
sequences. For this pilot study, this manual tracking was a simple alternative

---

[5]Note that in this work, 'intensity' was used to refer to the *magnitude* of the complex-valued
OCT image signal. This is an unfortunate oversight in terminology from my 'younger years'.

to automating the identification of cells, their orientation, and their behavior. It also served as a simple means to assess the reliability of the automated displacement tracking discussed in Section 5.2.6. In principle, automating the identification of cell features in combination with our automatic tracking could eliminate this step, but was not explored in this work.[6]

The manual tracking consisted of two steps. First, the approximate location of a chosen bead was manually identified at each time-point. Second, the bead centroid was computed using the image intensity. The centroid location was assumed to correspond to the location of the bead. For both the control and experimental cases, four beads were selected from four different regions of interest in the vicinity of the imaged cell body/bodies. The selection of each specific bead was arbitrary, as the manual tracking data are only meant to represent the general behavior of the neighborhood surrounding each bead. The regions of interest for bead selection included the neighborhood near the leading edge of the cell (in the general direction of migration, determined from time-lapse animations, such as Visualization 1 and Visualization 2 of Ref. [110]), the neighborhood of the trailing edge of the cell (opposite the leading edge), the neighborhood immediately adjacent to the cell body (neither leading nor trailing, and less than 100 μm away), and a neighborhood far from the cell body (at least 100 μm) that does not lie in the leading or trailing paths. The first three neighborhoods are intended to demonstrate cell-induced ECM deformations, while the fourth is meant to be a region of little to no deformation activity. In the event that a suitable particle could not be found in a given region, a close alternative was selected instead. For example, the control sample shown in Fig. 5.3(a) contained two adjacent cells with opposite migration paths, so that

---

[6]See Chapter 6 for automated methods.

no definite trailing edge could be identified. As a result, the trailing edge measurement was replaced with another adjacent edge measurement.

5.2.6   Automated 3D displacement tracking

ECM displacement maps were obtained in a fully automated fashion using a digital image correlation (DIC) based technique to process the registered maximum intensity projection time sequences described in Section 5.2.4 [47, 164, 50, 118]. For a given time series of 2D maximum intensity projections, a 2D grid of interrogation points was established to specify where displacement data would be computed. In the xy-planes, the interrogation point grid spacing was 4.1 μm (10 pixels). In the zx-planes, interrogation point grid spacings were 7.5 μm (10 pixels) and 4.1 μm (10 pixels) along the z and x directions, respectively. For each interrogation point, a reference image was windowed from the current time-point image, centered at the interrogation point. This reference image was $41.4 \times 41.4 \, \mu$m^2 (101×101 pixels) in the xy-planes, and $75.8 \times 41.4 \, \mu$m^2 (101×101 pixels) in the zx-planes. This reference image was cross-correlated with a deformed-state image, obtained from the *next* time-point image and centered at the same interrogation point. This deformed-state image was $33.2 \times 33.2 \, \mu$m^2 (81×81 pixels) in the xy-planes, and $72.8 \times 33.2 \, \mu$m^2 (97×97 pixels) in the zx-planes. It should be noted that the difference in size between the reference and deformed-state images only allows for the measurement of displacements that do not exceed ± 10 pixels in the xy-planes or ± 2 pixels in the zx-planes. Although this limits the range of local displacements that may be detected between time points, it helps to speed up computation over the many cross-correlation operations required across a time-lapse data set. Any

bulk drift present between time points would further reduce the maximum detectable local displacement, if the reference and deformed state image windows were not increased to compensate. This makes the image registration step described in Section 5.2.4 vital for efficient performance of displacement tracking in this work.

The cross-correlation of the reference and deformed-state images was up-sampled by a factor of 11 via zero-padding in the Fourier domain to allow measurement of sub-pixel displacements.[7] The coordinates of the peak of the up-sampled cross-correlation were taken to provide the 2D translation between the reference and deformed-state images. This process was repeated for all interrogation points between all pairs of images adjacent in time. The output of this process is a local ECM displacement field at all interrogated locations in the image sequence. A median filter was applied to reduce noise artifacts in the computed displacement fields. This 2D filter spanned 10×10 interrogation points.[8] Using a method based on simulated sinusoidal deformations of an imaged phantom [188], the spatial resolution of the displacement tracking algorithm (that is, the full-width-at-half-maximum of the algorithm response to an idealized point displacement) was found to be approximately 35 μm and 51 μm in the transverse and axial directions, respectively.

To determine the algorithm's sensitivity to small displacements, displacement tracking was performed on sequential images of a stationary Matrigel phantom (described in Section 5.2.1). This measurement yielded a displacement

---

[7]In hindsight, up-sampling is not necessary to obtain sub-pixel displacements. One can instead perform local quadratic fitting about the peak of the cross-correlation function. Identifying the peak of this quadratic function yields sub-pixel displacement measurements.

[8]Due to the way MATLAB performs median filtering, odd-valued edge lengths should always be used. The even-valued edge lengths used here must have caused a slight (subpixel-to-pixel scale) diagonal shift in the profile of the computed displacement field.

noise floor of approximately 110 nm and 60 nm between time points in the *xy*-and *zx*-planes, respectively. Results and discussion of more generalized sensitivity measurements using different correlation window and median filter sizes may be found in Fig. 5.1 and Section 5.3.1.

To obtain the cumulative displacements of the ECM over time, the computed displacements between time points must undergo a cumulative integration with respect to time. However, the process described above computes displacements at interrogation points which are defined at fixed locations with respect to the *lab* coordinate frame. Thus, a direct cumulative summation of the data over time will not accurately represent the displacement experienced by individual particles unless performed in the *material* coordinate frame. Let the vector $\mathbf{r}$ denote a fixed position, defined with respect to the origin of the lab coordinate frame, and let $n \in \{0, 1, \ldots, N - 1\}$ denote the integer time step, where $N = 19$ is the total number of time-points acquired. Now, we define two displacement fields. The first is $\mathbf{u}_n(\mathbf{r})$, defined as the computed displacement undergone by a particle between time $n - 1$ and time n, given that its position in the lab coordinate frame is $\mathbf{r}$ at time $n - 1$. The second is $\mathbf{U}_{0,n}(\mathbf{r})$, defined as the cumulative displacement undergone by a particle between time 0 and time n, given that its position in the lab coordinate frame is $\mathbf{r}$ at time 0. In this work, the cumulative particle displacement was computed using the relation:

$$\mathbf{U}_{0,n}(\mathbf{r}) = \mathbf{U}_{0,n-1}(\mathbf{r}) + \mathbf{u}_n\left(\mathbf{r} + \mathbf{U}_{0,n-1}(\mathbf{r})\right), \text{ given } \mathbf{U}_{0,0} = \mathbf{0} \qquad (5.1)$$

This relation was evaluated using the computed (lab frame) displacement data obtained by the cross-correlation algorithm described previously, with values computed using the built-in MATLAB function `interp2` in order to evaluate the computed displacement data across a continuous domain. The output is the desired, time-varying 2D cumulative ECM displacement field, an example of

which may be viewed in Visualization 1 and Visualization 2 of Ref. [110]. By examining the displacement fields in both the *xy*- and *zx*-planes, we can study the 3D ECM deformations occurring around the cells in the experiments. The results of this analysis are described in the sections that follow.

5.3 Results

5.3.1 Sensitivity of automated displacement tracking

Images of stationary Matrigel phantoms (discussed in Section 5.2.1) were used to test the displacement measurement noise floor of our fully automated displacement tracking algorithm under varying conditions, including both changes in cross-correlation window size and median filter size, in order to study how these parameters affect our algorithm's performance. The results of this testing are summarized in Fig. 5.1. The correlation window side length values correspond to the size of the windowed deformed state image. (The final window side lengths used in this work were 81 pixels and 97 pixels in the transverse and vertical planes, respectively.) In all cases, the side length of the windowed reference-state was maintained at a constant 20 pixels greater than the deformed-state window side length. In this way, each case was able to detect displacements over a fixed range of ±10 pixels. After the initial correlation-based displacement tracking was performed, median filters of different sizes were applied across the data obtained at each interrogation point. (The final median filtering used in this work took place over 10×10 interrogation points.) The noise floor of the automated displacement tracking algorithm was taken
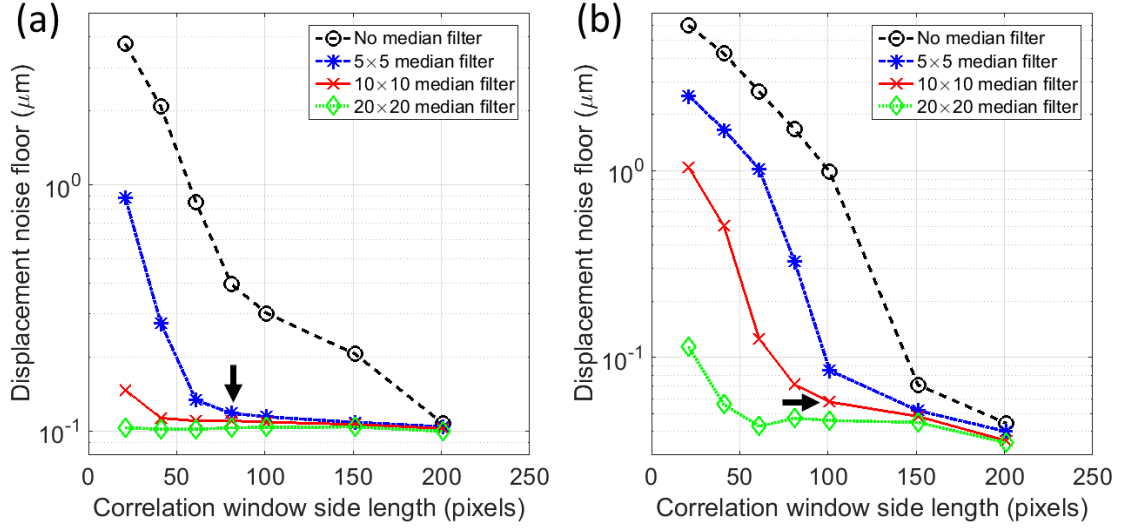
Figure 5.1: Measurement noise floor of the DIC-based ECM displacement tracking algorithm (described in Section 5.2.6) in the (a) *xy*-plane and (b) *zx*-plane, respectively. The variable 'correlation window side length' refers to the side length of the windowed deformed-state image. The different curves represent the use of median filters of different sizes following the cross-correlation operation. Displacement noise floors corresponding to the final parameters used in the tracking of cell-induced displacements are denoted by black arrows. Reprinted with permission from Ref. [110] © The Optical Society (2017)

to be the standard deviation of the resulting computed displacement field. As stated previously, the displacement sensitivity achieved under the processing conditions used in the remainder of this work was 110 nm (~0.25 transverse pixels) and 60 nm (~0.1 axial pixels) in the *xy*- and *zx*-planes, respectively, comparable to that reported in prior DIC work in optical coherence elastography (OCE) literature [164].

There are two trends evident in these results. First, as the correlation window size increases, displacement tracking noise declines. This is likely due to the fact that larger window sizes capture larger numbers of scattering beads embedded in the sample substrate. The added structure and signal makes the

cross-correlation more robust to noise in the reconstructed OCM images. However, this reduction in noise comes at the cost of a larger window, which acts as spatial low-pass filter when measuring the displacement field. Second, as median filter size increases, displacement tracking noise declines. The median filter acts to suppress rapid changes across space in the measured displacement field, and so also exhibits low-pass filter-like behavior. Though both of these trends are related to the principles of low-pass filtering, it should be noted that both the cross-correlation-based tracking and the median filtering are nonlinear operations on the space domain displacement field signal. As a result, although the general trends discussed here may be useful when designing experiments and selecting processing parameters, the methods remain vulnerable to potentially unpredictable and inconsistent behaviors that may depend on the images being used.

Another feature that affects displacement measurement sensitivity is CAO (performed here as a digital refocusing across depth, as described in Section 5.2.4). To demonstrate the impact of CAO, out-of-focus *en face* planes (located 30 μm below the focus) were extracted from the volumetric images of the stationary phantoms described previously. Displacement tracking was performed on both raw and digitally refocused versions of these *en face* planes in a manner almost identical to the previously described method, with the only difference being that these *en face* planes were extracted directly from the image volume and not through a maximum intensity projection along depth. The resulting displacement noise floor in the raw and digitally refocused cases were 1270 nm and 340 nm, respectively. The use of CAO therefore improved sensitivity of the displacement tracking algorithm by nearly a factor of 4. We attribute this to the signal-to-noise ratio and resolution improvement that accompanies

CAO [3]. The decrease in performance of these cases relative to the 110 nm transverse displacement noise floor previously reported is likely due to a reduction in both signal content and signal strength, since the *en face* planes in *this* test were not obtained via maximum intensity projection, and therefore lacked additional signal contributions from nearby depths.

5.3.2 Three-dimensional ECM displacements of control versus force-inhibited cells

The results of fully automated 3D displacement tracking are summarized in Fig. 5.2 (as well as Visualization 1 and Visualization 2 of Ref. [110]). Figure 5.2 depicts ECM displacements at a single time-point, whereas the visualizations depict displacements over time as animations. Although every sample underwent displacement tracking, only one control sample and one contractility-inhibited sample are fully illustrated in Fig. 5.2 and the visualizations. These samples will be discussed in detail in the following sections as representative results of our algorithm. The remaining imaged samples and their behaviors will be discussed at the end of Section 5.3.3.

The control sample, visible in Figs. 5.2(a-c) (and Visualization 1 of Ref. [110]), contains two adjacent fibroblasts (indicated by white arrows in Fig. 5.2(a)). Although the cells are distinct during the final 10 minutes of the experiment, it was unclear whether the cells were fully independent, or were a pair of daughter cells in an ongoing cell division. These cells appear to pull on the ECM in opposing directions toward the top and bottom of the *en face* image frame, respectively. In the path of the upper cell lies a thin scattering
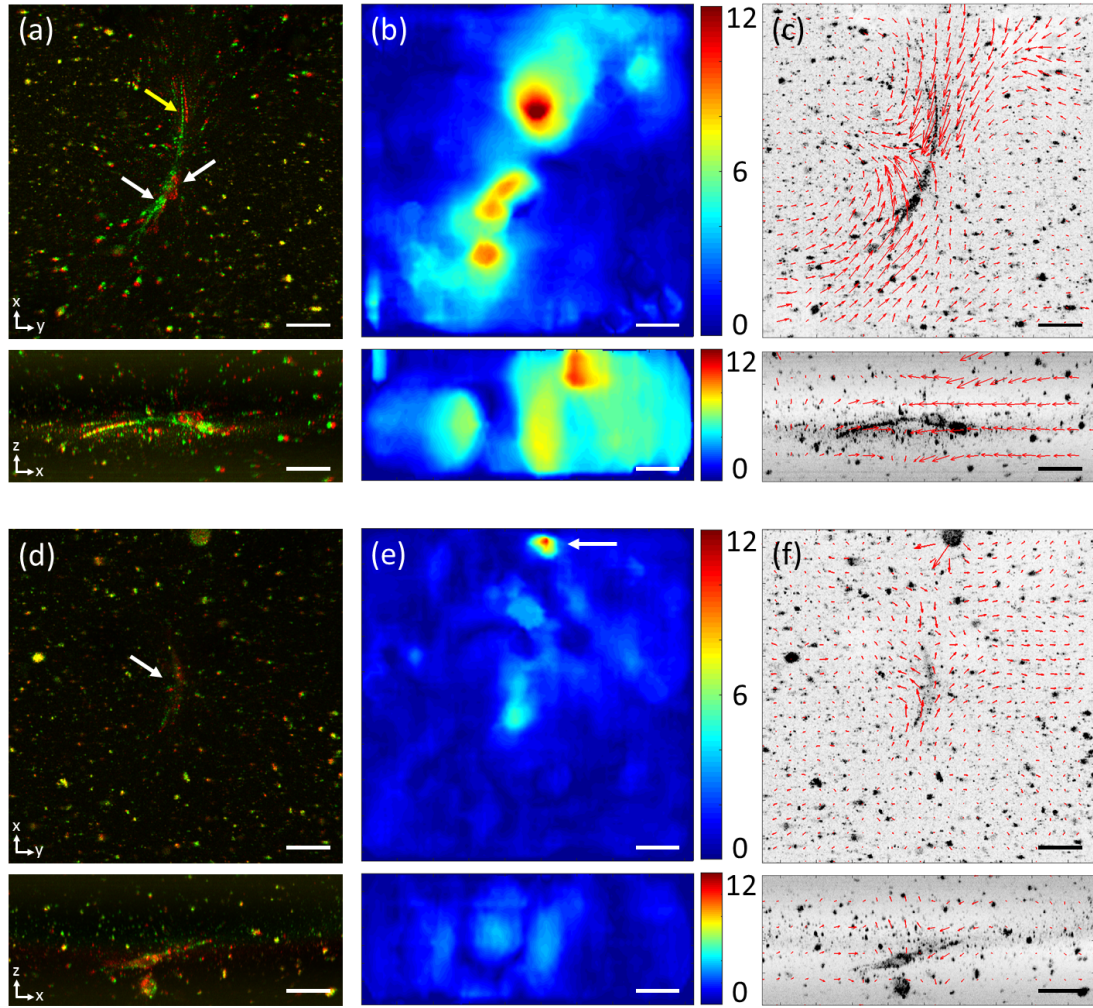
Figure 5.2: Automated tracking of 3D deformations induced by NIH-3T3 fibroblasts cultured in a Matrigel. These images represent the deformations accumulated over a 90-minute imaging time, with reagents introduced to the sample after the first 30 minutes of imaging. Cells were exposed to pure DMSO (a-c), or cytochalasin D solution (d-f). Each sub-figure depicts displacements in the *en face* (upper panels) and vertical (lower panels) orientations. (a,d) Superposition of the initial ($t = 0$ minutes, red channel) and final ($t = 90$ minutes, green channel) states of the sample, obtained from the initial and final registered maximum intensity projection images described in Section 5.2.4. (b,e) Cumulative displacement magnitude of the extracellular matrix (in μm) from a given initial location. (c,f) Cumulative displacement field depicting the direction and relative magnitude of ECM displacement (with arrow lengths exaggerated for visibility), superimposed on the initial ($t = 0$) maximum intensity projection images. Scale bars = 50 μm. Refer to the text for a discussion of the arrows in (a), (d), and (e). Reprinted with permission from Ref. [110] © The Optical Society (2017)

spindle (indicated by the yellow arrow in Fig. 5.2(a)), which may be a protein fiber, dead cell, or other structure. As the upward-migrating cell reaches this structure, ECM deformation in the vicinity of this object increases and extends over a large area (see Visualization 1 of Ref. [110]). In fact, Figs. 5.2(a-c) show that both cells influence ECM deformation as far as 100 μm or more away from their bodies, consistent with prior literature [185]. The areas of greatest displacement appear along the leading edges of cells, where cellular protrusions can be seen dynamically changing structure and interacting with the ECM in Visualization 1 of Ref. [110]. It should be noted that the calculated displacement magnitudes and fields (Figs. 5.2(b,c,e,f)) may have greater error near the edge of the FOV or in the vicinity of objects with variable scattering structure. This may be due to boundary effects of CAO, cross-correlation, and median filtering, and/or due to speckle decorrelation resulting from fast sub-resolution changes in object structure. For example, see the region indicated by the white arrow in Fig. 5.2(e). This region of apparent high displacement overlaps with a round cell intersecting the edge of the FOV. As can be seen in Visualization 2 of Ref. [110], the large local displacements reported by the tracking algorithm do not appear to be truly occurring in the neighborhood of the cell. This may be due to the constantly changing speckle pattern formed by the internal structure of the round cell. This speckle pattern, which changes quickly relative to the time-lapse sampling rate, could cause the assumptions underlying DIC (in this case, assuming small changes in scattering structure between time points) to break down, resulting in incorrect reported displacements.[9]

As shown by the images and computed displacement fields, the deformations are not confined to a single plane, but extend in all three dimensions

---

[9]As it turns out, rapidly varying speckle patterns from cells would be of critical importance to the studies in Chapters 6 and 7.

radiating away from the cellular protrusions into the ECM, forming a pattern reminiscent of a dipole field [151]. The physiological significance of such long-range, 3D deformations is an open area of investigation. Since cells have been shown to respond to mechanical stimuli, the study of these deformation fields may shed further light on mechanical communication and collective behaviors among neighborhoods of cells [177].

The sample exposed to cytochalasin D, visible in Figs. 5.2(d-f) (and Visualization 2 of Ref. [110]), exhibits differing temporal behavior compared to the control case. Early in the experiment, the cell (indicated by the white arrow in Fig. 5.2(d)) can be seen deforming the ECM in a similar fashion to the control sample discussed previously. It should be noted that the baseline rate of cell-induced deformation (apparent in Visualization 1 and Visualization 2 of Ref. [110]) differs between the cytochalasin D and control experiments. We attribute this to natural variability in cellular activity. Such variability is apparent both between and within the control and contractility-inhibited experimental groups, as is discussed in Section 5.3.3 and can be seen in Figs. 5.4 and 5.5. Future studies that seek to identify novel biological responses under uncharacterized conditions will require large numbers of imaged cells and large quantities of raw imaging data which are far in excess of that presented in this initial pilot study.

Following the baseline activity of the first 30 minutes, Visualization 2 of Ref. [110] shows that shortly after exposure to the contractility inhibitor at the 30 minute time-point, the cell and embedded scattering beads in both the *en face* and cross-sectional planes can be seen to relax back toward their initial locations. This relaxation is not complete, suggesting plastic deformation of the substrate,

ECM remodeling, and/or some lingering contractility of the cell. Shortly before the end of the sequence, the cell can be seen to begin contraction again. Unfortunately, further observation of this event was cut short by the end of the experiment, since the behavior was not noticed until the data was studied in post-processing. Overall, the observed particle displacements show that cell contractility inhibition by cytochalasin D is measurable through the analysis of OCM data.

5.3.3 Time-lapse particle displacements at selected positions around cell bodies

Single particle tracking was used to assess the temporal dynamics of both samples. The results of both manual tracking of individual particles and automated DIC-based displacement tracking are depicted in Figs. 5.3, 5.4, and 5.5. The manual tracking can be considered the 'true' displacement. Discrepancies between the manual and automated tracking may arise from several factors affecting the automated tracking, including the low-pass nature of the cross-correlation operation and median filter, measurement noise, and interpolation error. However, both cases exhibit comparable results, and may both be used to distinguish the behaviors of the control and contractility-inhibited samples.

As shown in Fig. 5.3, in both the control and contractility-inhibited samples, particles far from the cell bodies exhibit little displacement from their initial positions (less than 2 μm) over the 90-minute duration of both experiments. This helps to confirm that the displacements measured in this study are true cellular traction forces and are not due to other factors. In contrast, particles near

156

cells or placed in the leading or trailing paths of cell migration exhibited much greater total displacements (with magnitudes up to 10 μm). In the control experiment, the cells continually deformed the ECM over time, causing particles to displace progressively further from their points of origin. The sample exposed to cytochalasin D exhibits distinctly different ECM deformation dynamics. Ten minutes after introduction of the contractility inhibitor, particle displacements attain a maximum, shortly followed by motion back toward their points of origin. After the 70-minute time-point, this ECM relaxation appears to level off at approximately half of the peak measured displacements. As stated previously, this partial relaxation may be due to plastic deformation/remodeling of the ECM or residual cellular traction forces not inhibited by the cytochalasin D during the experiment.

The trends discussed in these example cases are shared throughout the experimental groups, which are summarized in Figs. 5.4 and 5.5. For both the control and contractility-inhibited groups, a total of 8 separate samples were prepared, imaged, and analyzed for each case, using the same procedure as that used to obtain the results presented in Fig. 5.3. As shown in Fig. 5.4, cells exposed to DMSO tend to continually deform the ECM in an approximately linear fashion throughout the duration of the imaging experiment. Although each sample exhibited this trend, the rate of ECM deformation is variable. Particles located near the leading edges of cells exhibited average displacements rates of 76 ± 29 nm/min (where the error bounds here, and in the remainder of this section, denote plus or minus one standard deviation). We attribute this variation in displacement rates to both biological variability in cell behavior, and to variability in the selected tracking location with respect the cell boundary and orientation.
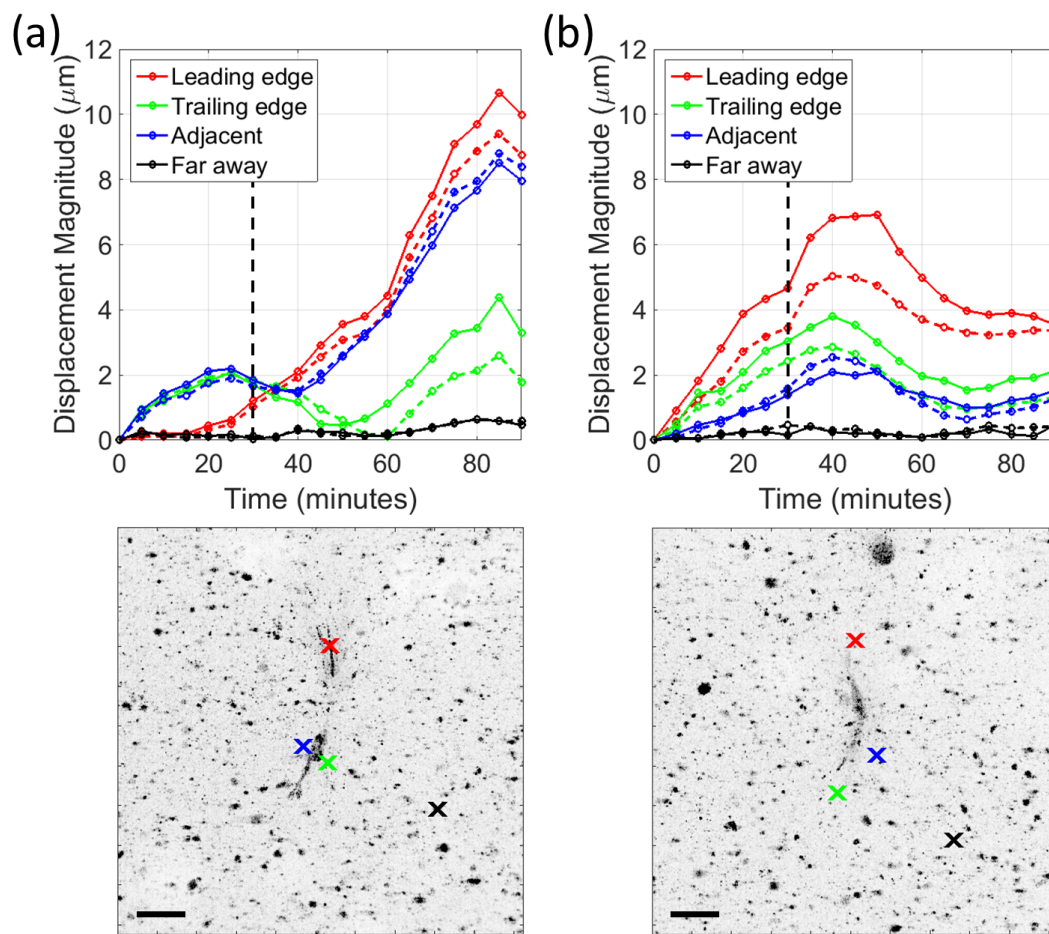
Figure 5.3: Automated and manual tracking of embedded polystyrene bead cumulative displacement magnitudes in time (top) at varying locations around the cells (bottom) exposed to (a) pure DMSO, or (b) cytochalasin D dissolved in DMSO. All displacement magnitudes are defined with respect to the initial location of a given bead. Solid curves depict results of manual single particle tracking; dashed curves depict results of automated DIC-based displacement tracking. The vertical dashed lines in the displacement plots mark the time at which the DMSO or cytochalasin D was added to the samples. Scale bars = $50\,\mu$m. Reprinted with permission from Ref. [110] © The Optical Society (2017)
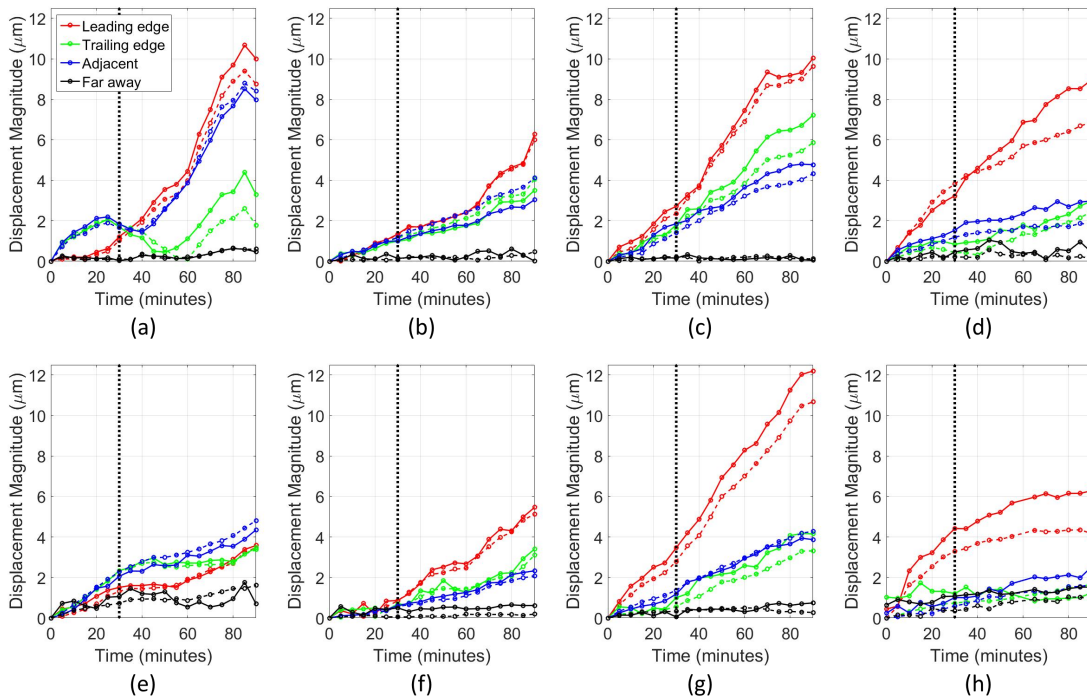
Figure 5.4: Automated and manual tracking of cumulative displacement magnitudes undergone by embedded polystyrene beads at various selected locations around fibroblasts exposed to the control conditions (DMSO). Each subplot (a-h) depicts the results obtained from independent trials of the experimental protocol. The first subplot (a) depicts the same data discussed in Fig. 5.3(a). All displacement magnitudes are defined with respect to the initial location of a given bead. Solid curves depict results of manual single particle tracking; dashed curves depict results of automated DIC-based displacement tracking. The vertical dotted lines mark the time at which the samples were exposed to DMSO. Reprinted with permission from Ref. [110] © The Optical Society (2017)

Similar to the control case, samples exposed to cytochalasin D (as shown in Fig. 5.5) also exhibit the approximately linear ECM deformation behavior (with average leading edge deformation rates of 102 ± 45 nm/min) until sometime after the introduction of cytochalasin D. As the compound takes effect, particles embedded in the ECM relax back toward their initial positions. The features of this behavior manifest cell-to-cell variability. These include the time that passes until relaxation begins (16 ± 8 min), the average rate of relaxation
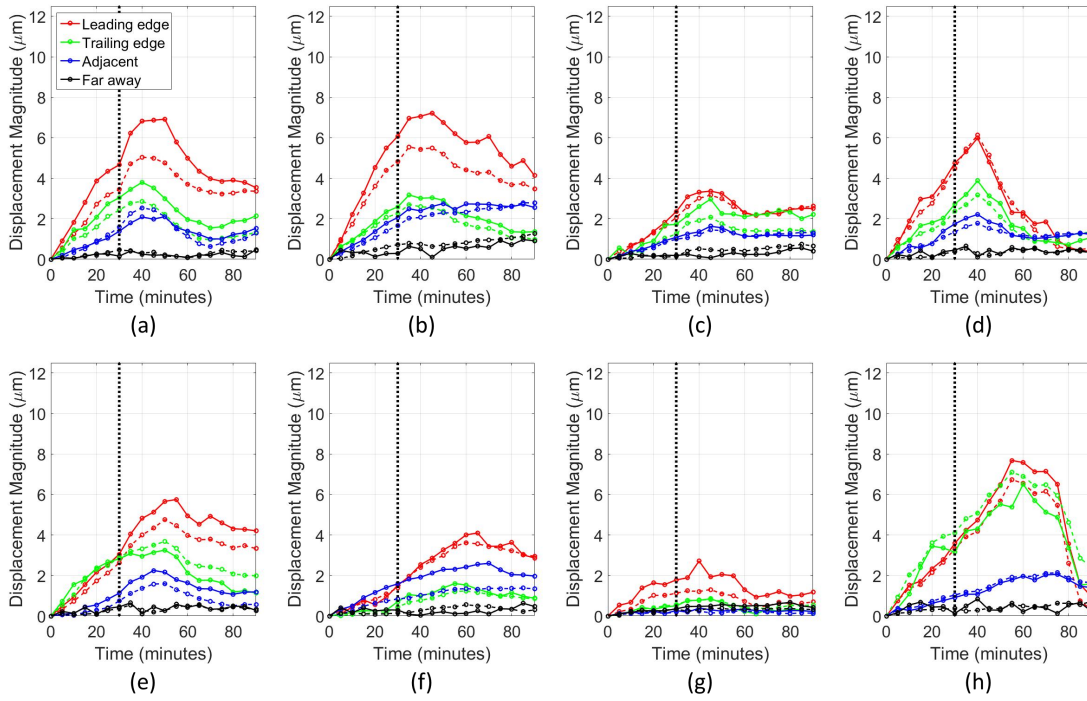
Figure 5.5: Automated and manual tracking of cumulative displacement magnitudes undergone by embedded polystyrene beads at various selected locations around fibroblasts exposed to the contractility inhibiting conditions (cytochalasin D + DMSO). Each subplot (a-h) depicts the results obtained from independent trials of the experimental protocol. The first subplot (a) depicts the same data discussed in Fig. 5.3(b). All displacement magnitudes are defined with respect to the initial location of a given bead. Solid curves depict results of manual single particle tracking; dashed curves depict results of automated DIC-based displacement tracking. The vertical dotted lines mark the time at which the samples were exposed to cytochalasin D solution. Reprinted with permission from Ref. [110] © The Optical Society (2017)

$(-56 \pm 60 \, \text{nm}/\text{min})$, and the amount of relaxation that occurs before reaching a steady state or the end of the experiment time (relaxation to $46 \pm 30\%$ of the peak displacement). Such variations may not only result from biological variability, but from other factors such as the time required for cytochalasin D to diffuse to the imaged cell.

160

5.4 Discussion

5.4.1 Sample preparation for effective cross-correlation-based displacement tracking

The 3D displacement tracking shown in this work is derived from performing 2D cross-correlation-based displacement tracking in transverse and vertical planes. Full 3D displacement tracking throughout an imaged volume is possible, in principle, using digital volume correlation and/or single particle tracking [89, 47, 188, 172, 13]. A key parameter for future work will be the density of scattering particles present in a sample. Each particle acts as a sampling point of the local deformation field. Successful tracking using correlation-based methods benefits from the use of windows that capture several particles at once, so that the arrangement can form a distinct structure that can be uniquely tracked over time. As such, higher particle density allows for the capture of the deformation field with a higher spatial resolution. In this work, the bead concentration resulted in a mean particle spacing of approximately 12.5 μm. By comparison, recent work in TFM makes use of mean particle spacings in the range of 1.5-25 μm. High sampling frequency methods tend to keep within the 1.5-3 μm regime [62].

A key assumption of cross-correlation based methods is that local deformations are the result of purely translational motion. Other forms of deformation can degrade or corrupt results (if not accounted for with additional processing algorithms) [188, 172]. However, the high temporal sampling frequency offered by OCM could help reduce the severity of this problem, by capturing more intermediate time-points between deformation states. Future work will have to

investigate the limits of OCM for detecting small and variable deformations in artificial samples. More advanced algorithms may be adopted from the existing TFM literature to build 'smarter' and more efficient algorithms than those discussed so far [172]. Looking toward the future, tracking native scattering features or speckle patterns may offer an avenue toward new processing techniques and investigations of cell traction forces *in vivo*. Such algorithms are already in development for application within the optical coherence elastography community [164, 50].

5.4.2 Computing cellular traction forces from measured displacement fields

Cellular traction forces are related to ECM deformations via the constitutive relationship between stress and deformation in the ECM. Reconstructing cell traction forces from raw displacement data is a formidable challenge for 3D TFM. Reconstruction is an ill-posed problem, and requires extensive knowledge of local material properties, boundary conditions, and reliable regularization techniques [89, 188, 152, 111]. The most sophisticated method for solving this inverse problem is to use finite element analysis, but even this approach may fail to account for the complexities of biological systems. Many TFM studies have used simple linear elastic, isotropic hydrogels as a substrate for easy experimentation and modeling. However, both natural and artificial ECM can violate many of these conditions. Biological materials are often viscoelastic, nonlinear, anisotropic, and have varying properties at different spatial scales [185, 68, 24]. Furthermore, since cells are capable of modifying their environment, even suc-

162

cessful measurement of these properties in the neighborhood of a cell will only be valid over a limited time-frame. For these reasons, TFM research must include a thorough accounting of assumptions and limitations of the approach that is used to reconstruct cellular traction forces. If cell forces cannot be calculated, other metrics of cell behavior, such as mean deformation mechanics [162] or ECM strain energy [78], may still extract useful information from an experiment. In this work, the raw displacement data yielded results that could be used to reveal differences in cell behavior between the control and experimental groups. If cell traction forces or a quantification of ECM remodeling are desired, the field of TFM and mechanobiology at large will require new methods to capture the complex properties of biological materials.[10]

5.4.3   The 'big data' problem, TF-OCM system design, and data acquisition/reconstruction strategies

Volumetric TF-OCM requires cellular resolution over a cuboidal FOV with side dimensions on the order of $\sim 10^2$ μm for single/isolated cell studies, or side dimensions on the order of $\sim 10^3$ μm for studies on cell populations/networks. When coupled with the requirement of high temporal resolution, in order to provide sensitivity to fast cellular mechano-transduction events on the minute time-scale or shorter, this will require the acquisition, and (ideally real-time) processing, of large ('big data') volumetric data sets. A major challenge to the practical implementation of TF-OCM will be to obtain as much relevant biological information as possible per volumetric acquisition, while minimizing the

---

[10]For a more thorough review of this topic, see Chapter 2.4.

amount of raw data that must be stored and processed to reconstruct images.[11]

In the present study, we employed CAO to increase the usable OCM depth range from ~75 μm (limited by degraded transverse resolution due to defocus) to ~200 μm (limited by photon collection of the confocal response and sensitivity of our system). Furthermore, we pre-aligned the location of isolated cells to be near the focal plane at the beginning of each experiment, so as to improve signal strength and reduce the distance from the focal plane that needed to be reconstructed with CAO. Finally, analysis of the resulting 150 GB[12] of raw spectral data per experiment (~2.5 TB in total) was streamlined to 'ignore' depths that were outside the usable CAO-OCM depth range (see Sections 5.2.2 and 5.2.4 for details). As a result, only 1.4 TB of useful space domain data needed to be reconstructed, as opposed to the 19.2 TB that would have been required for a full volumetric OCT reconstruction using standard methods (assuming double-precision complex numbers in MATLAB). Using these combined methods, a greater amount of useful information could be obtained from each data set acquired, and computational resources were not wasted reconstructing data that contained no useful information to contribute toward the results of this work.[13]

In the more general case, such as the 3D tracking of ECM displacements due to multiple isolated cells or cellular networks, or when imaging multiple cell cultures to obtain statistically significant biological results, employing additional strategies to address the 'big data' problem will become essential. One

---

[11]In hindsight, although this is a noble goal, I ultimately ended up relying on computing resources becoming better and cheaper over time. 'Big data' remains a major problem. And since the *ability* to acquire large data sets practically *necessitates* acquiring the biggest data sets you can possibly accommodate (such is the life of a researcher), this problem will likely be here to stay for the foreseeable future. That being said, I encourage everyone to do what they can to improve efficiency wherever possible. You might just get a publication out of it!

[12]I laugh at such 'tiny' data sets only three years later!

[13]Note that *this* study was the one behind the story I told in Chapter 3.7.1.

approach, in the case of sparse or low density samples, is the use of compressed sensing [108].[14] Another approach is to maximize the information content of each volumetric CAO-OCM data set, for example through alternative hardware designs. In particular, the rapid degradation of signal with distance from focus that currently limits the usable depth range could be improved through the use of an astigmatic optical system to equalize photon collection vs. depth, while maintaining diffraction-limited focal-plane resolution throughout the volume with CAO [3, 95].[15] This could be coupled with real-time volumetric visualization to optimize sample pre-alignment at the beginning of each TF-OCM experiment.

Other OCT system designs can provide alternative approaches to address the 'big data' problem. The use of full-field OCT (FF-OCT) [5, 11, 50], where the scanning of the reference arm can be coupled with focus tracking, can provide highly efficient data acquisition spanning only the depth range of interest. This approach offers a simpler image reconstruction procedure (relative to CAO-OCM), together with enhanced focal-plane photon collection. Another approach offering enhanced depth-dependent photon collection for volumetric imaging is full-field swept-source (FF-SS)-OCM [66].[16] This approach can offer ultra-high volumetric acquisition rates, but the use of spatially-coherent full-field illumination makes FF-SS-OCM more susceptible to cross-talk/multiple scattering than beam-scanning OCM systems [72, 73].[17] An alternative fast imaging scheme with enhanced depth-dependent photon collection is parallel

---

[14]They are still working on it. I am not sure if it is 'there' yet, but you might still check it out.

[15]We looked into this idea in Ref. [96]. I would employ this method with caution, since it can impose *peak* SNR penalties which may be unacceptable in samples with low scattering contrast (i.e., cells in aqueous media). See Ref. [96] for details.

[16]This area has grown *a lot* during my PhD and appears poised to grow even more as laser sources and data acquisition hardware improve.

[17]In recent years, promising attempts have been made to address this weakness of FF-SS-OCM [15].

Fourier domain OCT, which uses line illumination to collect A-scans in parallel, with reduced cross-talk effects compared to FF-SS-OCM [56]. Photon collection in beam-scanned OCM can be enhanced via the use of Bessel beam illumination, that can provide spatially-invariant transverse resolution and uniform photon collection over an extended depth range [88, 12]. This approach requires the use of separate illumination and collection beams (that can be difficult to align in practice[18]) to enhance SNR [90, 33].

5.4.4 Potential synergy with optical coherence elastography

TF-OCM may benefit from ongoing research in the field of optical coherence elastography (OCE). OCE is a technique used to infer sample mechanical properties by measuring material deformations resulting from a known perturbation. The scientific problem addressed by OCE is very similar to that of TFM [113, 75, 184]. Both forms of microscopy make use of the fundamental relationship between forces, ECM properties, and deformations. They simply differ in which part of this relationship is treated as an unknown quantity, and from what source the deformations originate (externally applied vs. cell-induced). In fact, OCE could benefit TF-OCM by providing access to the ECM mechanical properties required for reconstructing cellular traction forces in mechanically heterogeneous media. We envision that, compared to existing approaches for TFM, an OCM platform could provide a more complete measurement of cell-ECM interactions, where OCE is used to quantify material properties of a substrate or tissue, followed by TF-OCM to monitor how cells behave and modify the environment. The ability to perform both OCE and TFM in parallel, to monitor

---

[18]Update since the original publication: Former lab member Gavrielle Untracht has informed me from experience that these systems are *very* hard to align and maintain!

dynamic changes in mechanical properties and cellular forces in 3D environments, would constitute a significant advance that could support studies into the dynamics of biological systems that are not possible with current methods used in mechanobiology research.

5.5   Conclusion

In this study, we have demonstrated the first usage of OCM to quantify dynamic displacements induced in 3D media by cellular traction forces. This marks a first step toward the development of TF-OCM as a new imaging technique in the field of mechanobiology. By imaging and analyzing cells exposed to both control and contractility-inhibiting conditions, we have shown that our technique allows for comparison of cell traction force behavior in an *in vitro* system of interest to mechanobiology research. The high-speed volumetric acquisition capabilities of TF-OCM offers several advantages over existing techniques, and may create opportunities for new discoveries in cell mechanics at previously inaccessible spatiotemporal scales, in both low- and highly-scattering biological media. With the potential to leverage the existing foundation and future advances in both traditional TFM and elastography, TF-OCM is primed for future development and application as a technique for advancing mechanobiology.

CHAPTER 6

QUANTITATIVE RECONSTRUCTION OF TIME-VARYING 3D CELL FORCES WITH TRACTION FORCE OPTICAL COHERENCE MICROSCOPY

Content reuse disclosure   The contents (text, figures, etc.) of this chapter have been reprinted/adapted from a previously published journal paper of which I was the first author.[1] Some sections/passages of the original work have been replaced with updated/alternative content (e.g., the Introduction). To view the full contents of the original paper, please see Ref. [112].

Author contributions statement   The following contributions pertain to the originally published study (Ref. [112]) on which this dissertation chapter is based. **J.A. Mulligan:** Performed all cell culture, sample preparation, image data acquisition, and data processing. Developed all components of the computational image formation module and the bead localization, motion correction, speckle reduction, and image segmentation components of the traction force microscopy module. Wrote the original manuscript. **X. Feng:** Devised the algorithm for bead tracking (J.A. Mulligan developed a MATLAB implementation) and the mesh generation and force reconstruction components of the traction force microscopy module. Performed testing for the validity of the infinitesimal strain approximation (located in Appendix L). **S.G. Adie:** Provided guidance and funding throughout this study. **All authors** reviewed and edited the full contents of the original publication.

6.1 Introduction

In our previous study (Chapter 5), we proposed traction force optical coherence microscopy (TF-OCM) as a new technique for conducting traction force microscopy (TFM, Chapter 2). Specifically, by leveraging the capabilities of optical coherence microscopy (OCM, Chapter 3) and computational adaptive optics (CAO, Chapter 4), TF-OCM would enable 3D TFM in scattering media with high spatiotemporal resolution and high spatiotemporal coverage, thus meeting as yet unmet imaging needs of mechanobiologists who study dynamic, 3D, and collective cell behavior (Chapter 1). Although our pilot study demonstrated that we could indeed use OCM+CAO to observe and measure deformations induced by cellular traction forces (CTFs) exerted within a Matrigel substrate, we did not demonstrate the feasibility of all components (e.g., quantitative force reconstruction) required to make TF-OCM a full-fledged experimental technique.

In this Chapter (and Ref. [112]), we refine and expand upon our previously developed methods, and present a complete quantitative implementation of TF-OCM. With this new technique, we quantified time-varying 3D CTFs exerted by isolated NIH-3T3 fibroblasts embedded within a Matrigel substrate. This was achieved by analyzing OCM images acquired with five-minute temporal sampling, spanning a $500 \times 500 \times 500 \, \mu\mathrm{m}^3$ field-of-view (FOV). In order to obtain OCM images suitable for TFM, we developed a computational image formation procedure which mitigates a variety of detrimental image artifacts.[2] Although this procedure was developed for TF-OCM, the underlying mechanisms and techniques are relevant to other applications of computed OCT/OCM imaging which require geometrically accurate (i.e., low-distortion) reconstructions of ob-

---

[2]These methods were previously discussed in Chapter 4.4. This was the study in which we developed and first employed those methods.

ject structure [95, 189]. The results shown here represent the first quantitative implementation of TF-OCM. This work set the stage for future (and ongoing) research toward the application of TF-OCM to more complex model systems, such as multicellular spheroids embedded in collagen substrates (Chapter 7).

This study was originally published in *Scientific Reports* in 2019 (Ref. [112]).

6.2 Overview of quantitative TF-OCM

For a detailed discussion of TFM concepts and methods, see Chapter 2. A brief review is provided here, for convenience and clarity.

TFM does not measure CTFs directly. Instead, CTFs are numerically reconstructed based upon how they deform the surrounding environment. CTF reconstruction requires the measurement of three key pieces of information: (1) substrate mechanical properties, (2) substrate deformations in response to CTFs, and (3) boundary conditions (e.g., environment boundaries and cell geometry). The first is obtained through mechanical characterization of the substrate material (e.g., polyacrylamide, Matrigel, collagen, etc.). The latter two are obtained through a combination of optical imaging and appropriate assumptions/constraints. To measure substrate deformations in particular, the sample structure must be known from both a 'deformed state' (when CTFs are present) and a 'reference state' (when CTFs are not present). The 'reference state' is typically induced by a chemically-mediated inhibition of CTFs at the end of an experiment. Once the three key pieces of information are known, numerical methods are used to reconstruct the CTFs.[3] This entire procedure can be per-

---

[3]Note that this only yields a best *estimate* of the CTFs that would be expected to generate the

formed in a variety of ways, creating opportunities for the development of new methods, such as the TF-OCM technique presented here [110, 111, 112].

Our implementation of TF-OCM follows these same general procedures. Here, NIH-3T3 fibroblasts were embedded in a Matrigel susbtrate containing scattering polystyrene beads. The cells exerted contractile CTFs, causing the Matrigel to deform, resulting in displacement of the scattering beads from their resting (i.e., reference) positions. A contractility inhibitor (cytochalasin D) was then added to the culture. In response, the cells relaxed, allowing the scattering beads to return to their resting positions (due to the elasticity of the substrate). This process was observed over a three-hour period with five-minute temporal sampling using a spectral domain OCM imaging system. Volumetric images (spanning a $500 \times 500 \times 500 \, \mu m^3$ FOV) were reconstructed using a customized procedure which combined CAO and additional computational methods [112, 3, 155, 156, 55]. These images were then used to obtain measurements of time-varying bead displacements, and to generate time-varying discrete meshes of cell surfaces. These data, in addition to the mechanical properties of the Matrigel substrate (as characterized by bulk rheology), were fed into a previously reported finite element method (FEM) procedure [44] to obtain quantitative reconstructions of time-varying 3D CTFs.

The computational workflow underlying TF-OCM is a union of two modules, which are depicted by the flowchart in Fig. 6.1. The computational image formation module generates a time series of high resolution, volumetric OCM images of a cell and its surroundings. The TFM module uses this image data to quantify time-varying 3D CTFs. It is important to note that, although CAO can

---

observed deformation data, given a particular mechanical model, regularization parameters, etc.
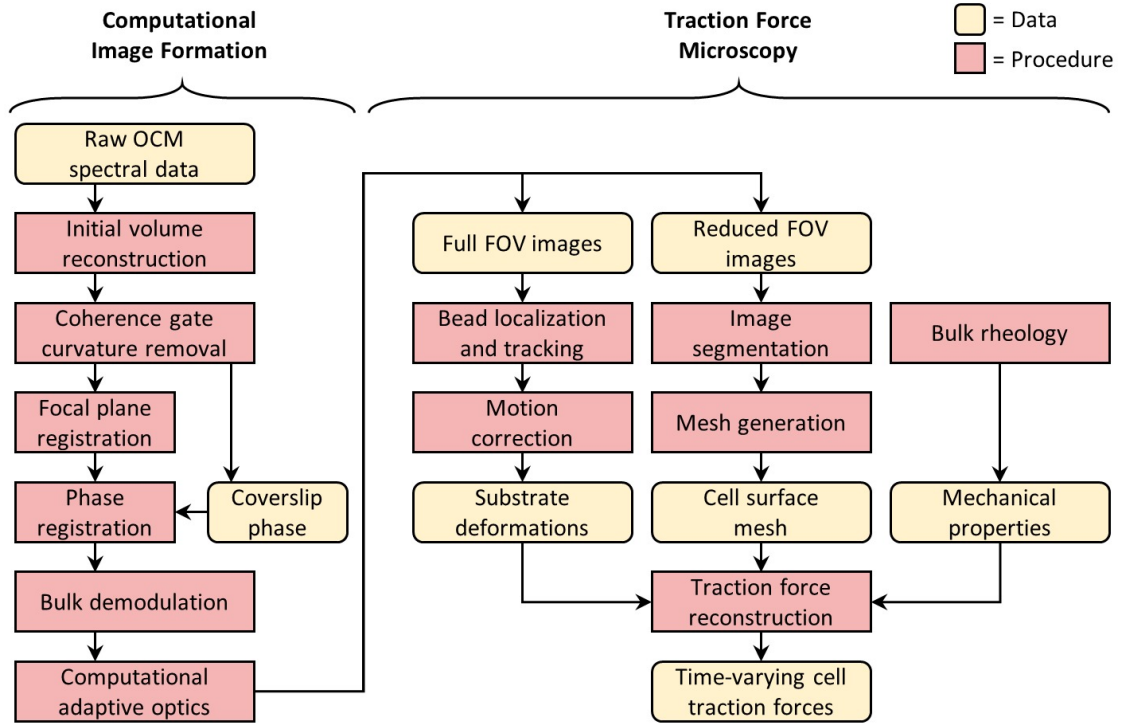
Figure 6.1: Data processing workflow of traction force optical coherence microscopy. A time series of volumetric images is reconstructed via the computational image formation module (left). These images are then used to quantify time-varying 3D CTFs via the traction force microscopy module (right). Reprinted from Ref. [112] as permitted under the CC BY 4.0 license for the original work.

restore focal plane resolution throughout an imaged volume, the structure of the resulting image is not necessarily a reliable representation of the true sample structure. This can be detrimental to the accurate measurement of substrate deformations and subsequent quantification of CTFs. The numerous steps preceding CAO were used to mitigate factors that corrupt the image formation process, and thus played a critical role in our implementation of TF-OCM.

6.3 Results

6.3.1 Phase registration and bulk demodulation mitigate shearing and motion artifacts in computationally refocused images

Since our implementation of TF-OCM relies upon the accurate reconstruction of high resolution volumes via CAO, we had to design our computational image formation module to ensure that interferometric phase instability and other factors would not corrupt the image data [155, 156]. Figure 6.2 and Supplementary Movie 1 (of Ref. [112]) demonstrate the impact and necessity of our phase registration and bulk demodulation procedures for mitigating such effects. In Fig. 6.2, the red and green channels (which correspond to images generated by our computational image formation module with and without these procedures, respectively) exhibit a depth-dependent transverse misalignment with respect to one another. The severity of this misalignment increases linearly with distance from the focal plane. In addition, the direction of the misalignment has opposite signs on opposite sides of the focal plane. The red and green channels are therefore distorted relative to one another by a shearing deformation (analogous to pushing against the side of a deck of cards). Supplementary Movie 1 of Ref. [112], which depicts a time-lapse of the *en face* planes shown in Fig. 6.2, reveals additional features of this misalignment. In panels (a) and (c) of the animation, the embedded scattering particles are at depths far away from the imaged NIH-3T3 fibroblast cell, and are expected to exhibit little to no motion in the animation. This expected behavior is exhibited by the red (phase-
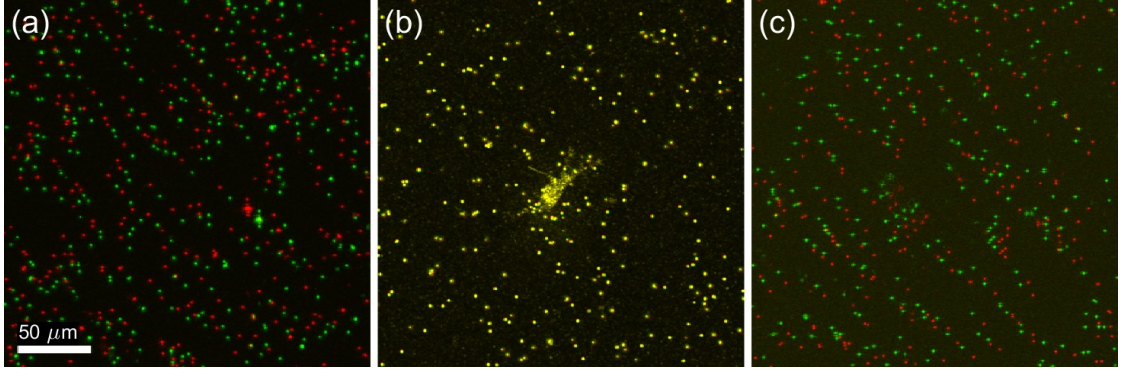
Figure 6.2: Shearing artifacts in computationally refocused images. Panels (a-c) were obtained from 3 separate depths, located $200\,\mu$m above, at, and $200\,\mu$m below the focal plane, respectively. The red channel corresponds to images obtained using our phase registration and bulk demodulation procedures, whereas the green channel corresponds to images obtained without these procedures. The green channel exhibits a depth-dependent translation artifact, corresponding to a shearing of the reconstructed volumetric image. Additional spatial and temporal variations in this artifact are visible in Supplementary Movie 1 of Ref. [112]. Reprinted from Ref. [112] as permitted under the CC BY 4.0 license for the original work.

registered and demodulated) channel. In contrast, bead positions in the green (uncorrected) channel fluctuate over time. These fluctuations are non-uniform across the FOV and are most prevalent along the left-right axis, corresponding to the slow scanning axis of our imaging system (which is known to be more susceptible to interferometric phase fluctuations [155, 156]). Given that the red channel exhibits the behavior we expect to observe (i.e., little to no motion of beads far from the cell), we conclude that our phase registration and bulk demodulation procedures are effective at mitigating shearing and motion artifacts in computationally refocused OCM images, and are therefore beneficial to the accuracy of TF-OCM.[4]

---

[4]Theoretical predictions of the described image artifacts may be found in Chapter 4.4. Similar analyses are also available in the Supplementary Methods of Ref. [112].

6.3.2 Focal plane registration facilitates CAO over a wide field-of-view for systems with non-ideal optics

Non-idealities in the sample arm optics can negatively impact the reconstructed resolution and signal-to-noise-ratio (SNR) of computationally refocused OCM images, and are therefore detrimental to both the tracking of bead displacements and identification of cell boundaries in TF-OCM. In this study, non-idealities in our optics caused the axial position of the focal plane to vary as a function of lateral position (such that the focal plane appears slightly tilted and/or curved).[5] This resulted in an imaging point spread function (PSF) that varied across the 500×500 μm^2 lateral FOV of our images. Since our implementation of CAO applies a refocusing operation that is laterally invariant, it cannot account for lateral non-uniformity in the imaging PSF.

In the absence of our focal plane registration procedure[6], refocused images exhibited a non-uniform lateral resolution after CAO, as demonstrated in Fig. 6.3(b). To mitigate this effect, we devised a focal plane registration procedure which maps the image data to a coordinate system in which the axial position of the focal plane is laterally invariant. (See Fig. 6.3(a) for a visual example of this transformation.) Following this procedure, images refocused with CAO exhibited a lateral resolution that was uniform across the lateral FOV, as shown in Fig. 6.3(c). These results show that our focal plane registration technique allows for a standard implementation of CAO to refocus volumetric data over a wide FOV (500×500 μm^2), even when non-idealities in the optical system cause the focal plane to be tilted or curved with respect to the axes of the image data.

---

[5]See the discussions of focal plane curvature in Chapter 4.4 and Appendix J.

[6]'Focal plane registration' is the original name that I used to refer to 'focal plane curvature (FPC) removal', which is discussed in Chapter 4.4.

Of course, spatially-varying CAO reconstructions may instead be employed to address this problem at the cost of greater complexity [83, 84]. However, the methods used in this study may be considered as a simple alternative to be used when the tilt/curvature of the focal plane is small.

6.3.3 Speckle reduction aids automated analysis of cell geometry from OCM images

As discussed previously, the reconstruction of CTFs requires knowledge of cell shape/geometry. Cell tracing based on automated image segmentation of OCM images can be difficult, due to the presence of speckle (such as that shown in Fig. 6.4(a)), which is ubiquitous to coherent imaging modalities like OCT/OCM, ultrasound, radar, etc. However, the alternative prospect of performing manual cell tracing would have been prohibitive to conducting TF-OCM in time-lapse settings. For example, the 10 time-lapse experiments performed in this preliminary study spanned a total of 370 distinct time-points. Performing manual 3D tracing typically would have required manual 2D tracing of at least 15 slices from the volumetric image corresponding to each time-point. For this study alone, that would have entailed performing manual tracing for more than 5500 individual 2D images. To overcome this obstacle and keep TF-OCM feasible for larger experiments in the future, we employed speckle reduction methods to aid the automated analysis of cell geometry from OCM images. To reduce speckle artifacts in and around the cell body, we combined multiple sequentially-acquired OCM images (as detailed in Section 6.6.7), which resulted in images like the one shown in Fig. 6.4(b). The reduction in speckle
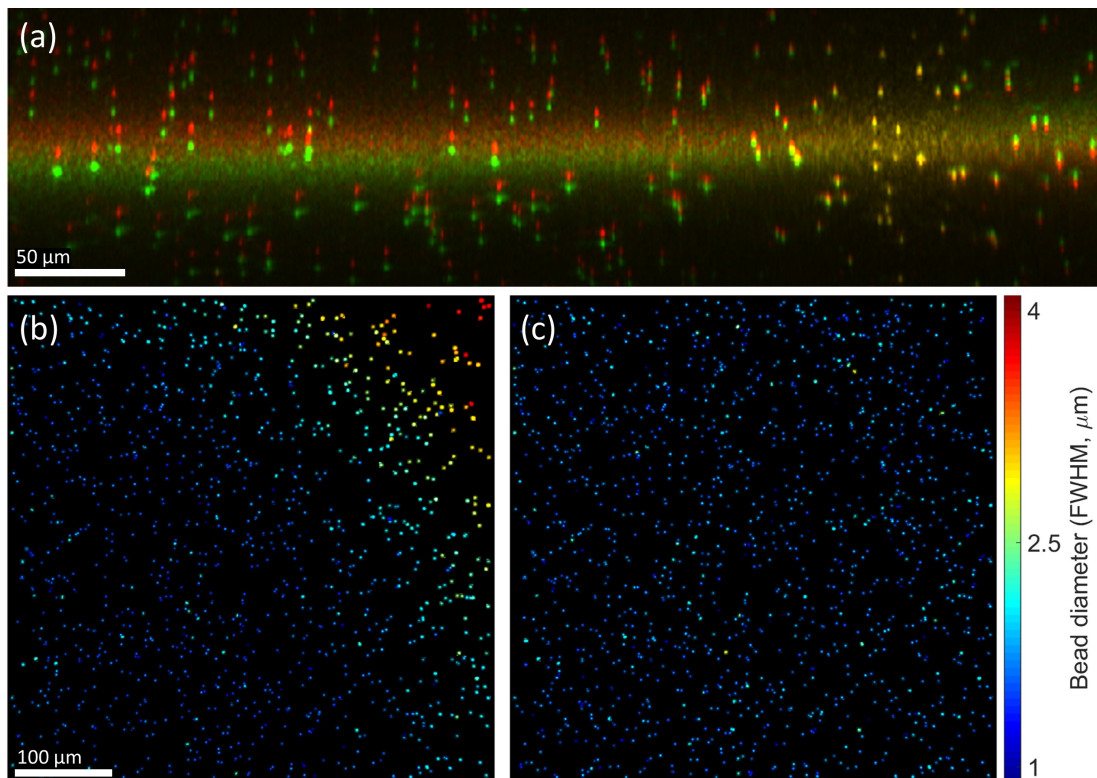
Figure 6.3: Effects of focal plane registration on volumetric image reconstructions. (a) Cross-section of a volumetric image obtained with (red channel) and without (green channel) focal plane registration. The bright horizontal band spanning both channels corresponds to the focal plane. (b,c) *En face* planes obtained from a region centered 50 μm above the focal plane in volumetric images reconstructed with CAO. Only beads which exhibited little to no overlap with neighboring beads were retained in these images. The methods for generating these panels are detailed in Appendix L.1.3. (b) *En face* plane reconstructed without focal plane registration, exhibiting a lateral resolution which varies across the FOV. (c) *En face* plane reconstructed with focal plane registration, resulting in a uniform lateral resolution. FWHM indicates the full-width-at-half-maximum diameter of the polystyrene beads shown in (b,c). This value is not a measurement of the post-CAO imaging resolution, but is directly correlated to resolution and is therefore used here to demonstrate the impact of focal plane registration. Color bar applies only to (b,c). Reprinted from Ref. [112] as permitted under the CC BY 4.0 license for the original work.

177

provided by our technique enabled automated image segmentation and identification of the cell body via K-means clustering [133], yielding 3D segmented regions like that depicted in Fig. 6.4(c). Segmented regions were converted to 3D discrete meshes, as in Fig. 6.4(d), for use in our FEM solver.

Note that some of the finer structures visible in Fig. 6.4(a,b) were not retained in the segmentation shown in Fig. 6.4(c). We found that our speckle reduction method can suppress cellular structures which exhibit more static speckle patterns over short time scales (e.g., static regions of fine filipodial extensions). Unlike the remainder of the cell body (which exhibited dynamic speckle patterns), these suppressed structures were not effectively captured by our K-means clustering algorithm. For the purposes of this preliminary study, we assumed that the 3D image segmentation (and resulting 3D meshes) generated by our automated methods provided a sufficiently accurate approximation of the cell surface for quantifying time-varying CTFs. Additional future experiments will be needed to determine whether the loss of fine cellular structures by our algorithm has any significant impact on the accuracy of CTF reconstructions. More advanced algorithms may yield improved cell tracings with higher fidelity [32], and this aspect of TF-OCM merits further work. Future iterations of TF-OCM may also benefit from the incorporation of hardware-based speckle reduction methods [95, 92]. However, the methods presented here do have the advantage that they may be performed using standard OCM microscopes without modification. That is, our methods only require the acquisition of additional images in time, and do not require the introduction of additional hardware or specialized scanning geometries.
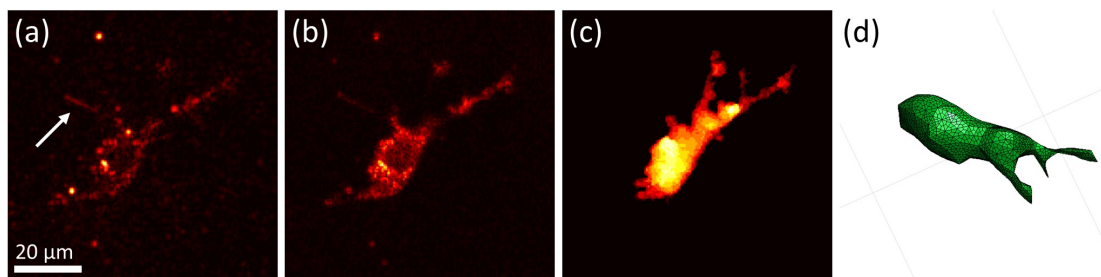
Figure 6.4: Automated segmentation of cell bodies aided by speckle reduction. (a) *En face* plane extracted from a single depth in a single volumetric image. The imaged NIH-3T3 fibroblast exhibits significant speckle artifacts, which hinder automated segmentation. Arrow indicates cellular structure not retained by our segmentation procedure (see text for details). (b) The same *en face* plane as in (a), after combining eight sequential volumetric acquisitions. Speckle contrast is reduced, allowing for segmentation via K-means clustering. (c) Summation projection of the 3D segmented volume, which approximates the cell body. (d) 3D mesh of the cell body, generated from the data depicted in (c). Note that (d) was generated from a different viewing angle as (a-c) to more clearly depict the cell's 3D shape. Reprinted from Ref. [112] as permitted under the CC BY 4.0 license for the original work.

6.3.4 TF-OCM quantifies 3D substrate deformations induced by time-varying CTFs

Unlike the cell body or Matrigel substrate, the polystyrene beads embedded in the sample generated very strong scattering signals, and so were readily segmented for the purposes of localization and tracking over time. Figure 6.5 and Supplementary Movie 2 (of Ref. [112]) depict the resulting measurements of 3D substrate deformations (in the form of bead displacement data) from three representative cells (referred to as cells 1, 2, and 3). These data show that, at the beginning of each time-lapse experiment, cell force-induced deformations extended further than $100\,\mu$m from the cell body. After the addition of the contractility inhibitor (cytochalasin D) 30 minutes into the experiment, there was a delayed onset of cell relaxation, consistent with our prior work (Chapter 5)using

similar force inhibition protocols [110]. Once relaxation began, bead displacements declined until the beads arrived at their reference (i.e., *assumed* zero deformation) positions at the end of the experiment. (Note that although the final (reference) image in each time-lapse experiment was assumed to correspond to a state when cells were completely relaxed, this was not necessarily the case for all cells. Details about this possible assumption failure and its consequences can be found in Appendix L.2.3.) Cell 1 and cell 3 (Fig. 6.5(a,c), respectively) demonstrated gradually increasing contractility, until the inhibitor took effect and caused contractility to decline. Cell 2 (Fig. 6.5(b)), on the other hand, demonstrated a relatively static level of contractility, which then declined in response to the inhibitor.

Figure 6.6 summarizes the time-varying deformations observed in the vicinity of each of the 10 cells examined for this study. These data demonstrate a gradual decline in bead displacement by all cells after introduction of the contractility inhibitor. The variability in contractility observed across these data may be due to multiple sources, such as variable cell health and behavior (e.g. migratory, resting, dividing, etc.) or errors in our image reconstruction procedures. Overall, these results show that TF-OCM offers the capability to measure CTF-induced deformations with minute-scale temporal sampling, enabling the study of dynamic processes, such as the cell relaxation shown here.

6.3.5 TF-OCM quantifies time-varying, 3D cell traction forces

The results so far have depicted substrate deformation data and cell surface geometry data obtained by our TF-OCM workflow (Fig. 6.1). After obtaining
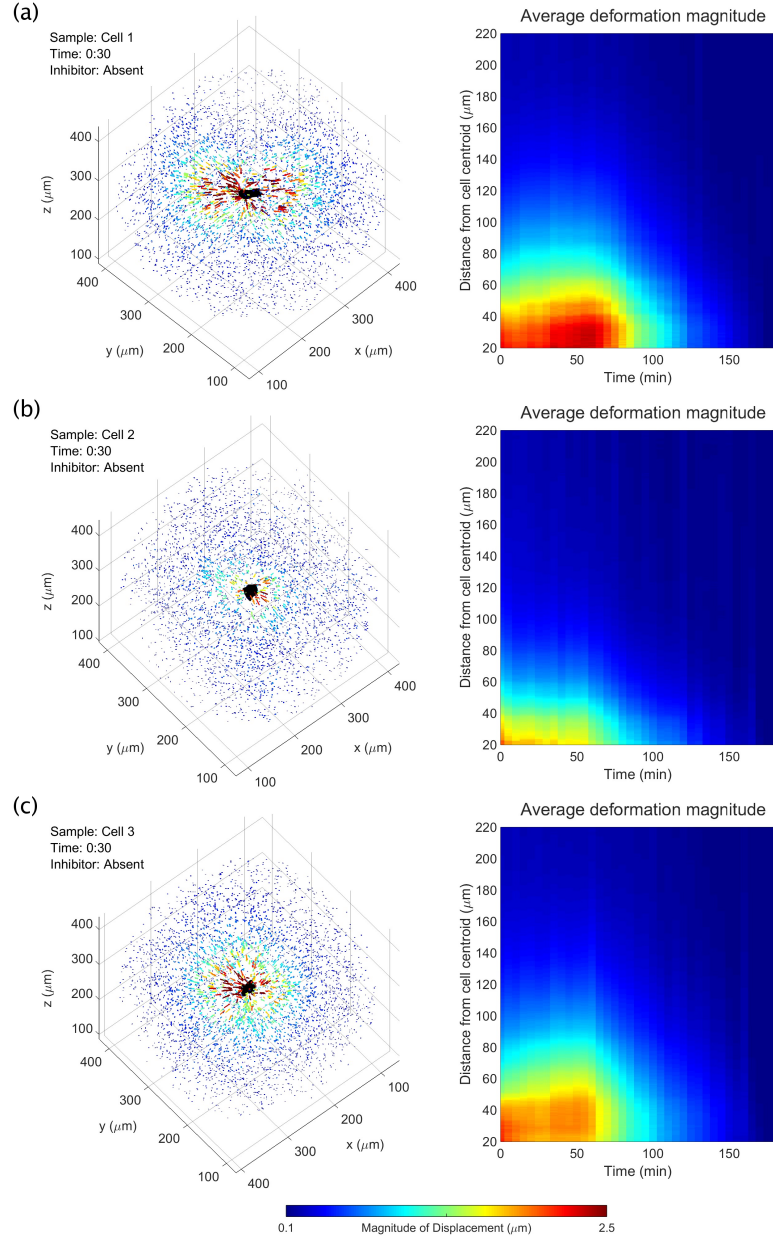
Figure 6.5: Time-varying, 3D substrate deformations measured with TF-OCM. (a-c) Bead displacement data for three NIH-3T3 fibroblasts. Left panels depict bead displacements at the time point immediately preceding the addition of the contractility inhibitor, cytochalasin D. Arrows indicate bead displacements with respect to their 'reference' positions. Arrow lengths are exaggerated for visualization. Animations over time may be found in Supplementary Movie 2 of Ref. [112]. Right panels depict the mean magnitude of bead displacement as a function of time and distance from the cell centroid (see Appendix L.1.3 for details). The bead localization sensitivity along the x, y, and z axes were 37 nm, 32 nm, and 86 nm, respectively (see Section 6.6.6). Reprinted from Ref. [112] as permitted under the CC BY 4.0 license for the original work.

Average bead displacement (near cell) versus time (n=10 cells)
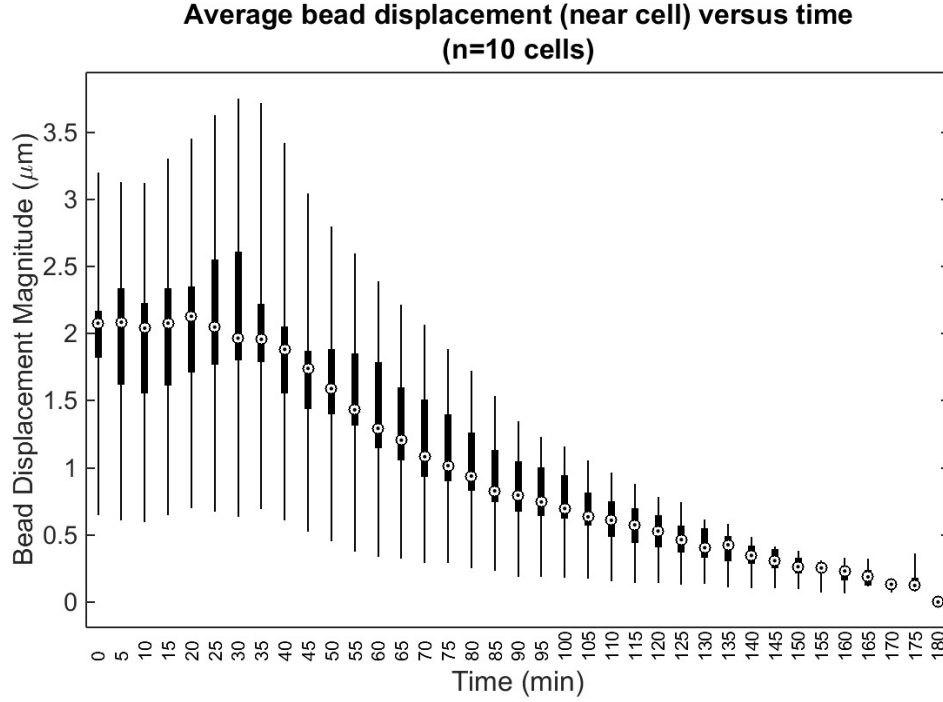
Figure 6.6: Average (mean) bead displacement magnitude for beads located within 50 μm of the cell body, over time. The whiskers, boxes, and circles depict the full range, interquartile range, and median value of the data (n=10 cells), respectively. The contractility inhibitor (cytochalasin D) was added immediately after time t = 30 minutes. Reprinted from Ref. [112] as permitted under the CC BY 4.0 license for the original work.

the mechanical properties of the Matrigel substrate (see Section 6.6.2), time-varying CTFs were reconstructed using FEM software [44]. Figure 6.7 depicts CTF reconstructions at a single time point for the three fibroblast cells previously shown in Fig. 6.5. Animations of these reconstructions are provided in Supplementary Movie 3 (of Ref. [112]). Note that cell 1 (shown in Fig. 6.7(a)) exhibited the greatest degree of polarization among the three cells shown, with protrusions extending lengthwise into the surrounding medium. Cell traction forces can be found concentrated at either end of the cell, consistent with prior results from other TFM studies [89, 111]. Cells 2 and 3 (shown in Fig. 6.7(b,c)) were more spherical in shape. The reconstructed traction fields seem to reflect

this relative lack of polarization, since the tractions appear more irregularly distributed across the cell surface, suggesting that a more non-directional contractile behavior is present. Irregular/fluctuating CTF distributions may also result from measurement noise and/or numerical instabilities. This is a major challenge for most CTF reconstruction methods, especially in 3D settings [89, 152, 111].

Figure 6.8 summarizes how reconstructed CTFs of cells 1-3 changed over time. Each data point represents the 'total force' exerted by a cell at a given time point, oriented along its 'principal axis of stress' (defined in Appendix L.1.3). These plots show that the forces exerted by the fibroblast cells tended to increase until approximately 30 minutes after the addition of the contractility inhibitor, after which their contractility declined. These curves also resemble the deformation distributions in Fig. 6.5, as would be expected. Similar trends of initial contractile behavior followed by relaxation are shown in Fig. 6.9, which summarizes the total force reconstructed across all 10 cells examined in this study. The variability between individual time-points (visible in Supplementary Movie 3 of Ref. [112], Fig. 6.8, and Fig. 6.9) may be due to a combination of factors, including actual changes in CTF distribution, noise, and artifacts emerging from the use of FEM. In particular (as detailed in Appendix L.2.4), the relatively low bead density used in our samples may have impacted the quality of CTF reconstructions in this study, and hence reduced the sensitivity of our TF-OCM system to time-varying CTFs. Overall, these data have demonstrated the ability of TF-OCM to measure trends in time-varying CTFs exerted by isolated cells with minute-scale temporal sampling.
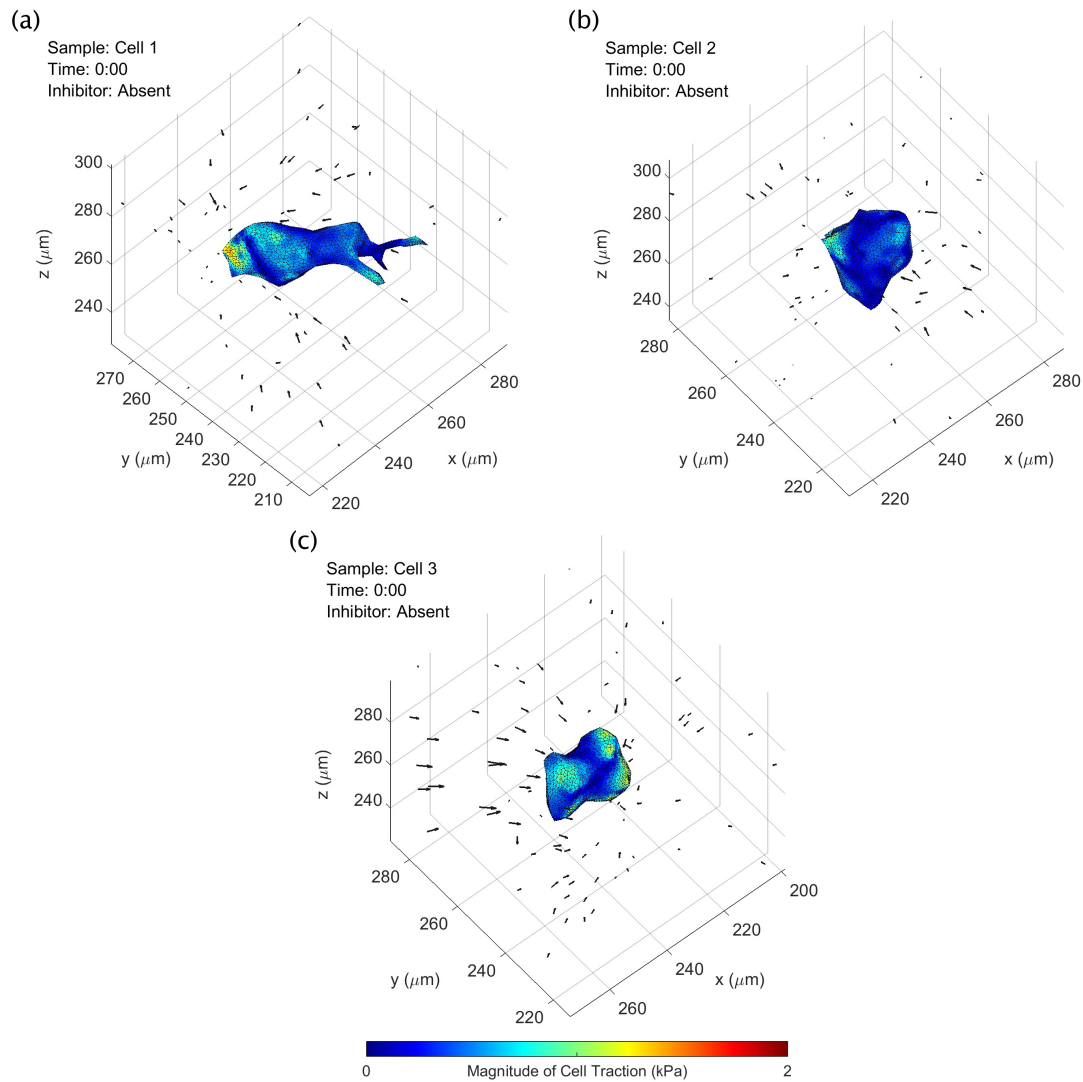
Figure 6.7: CTF reconstructions at a single time point for three NIH-3T3 fibroblast cells (shown previously in Fig. 6.5). A time-lapse animation of this figure is provided in Supplementary Movie 3 of Ref. [112]. Black arrows indicate measured bead displacements with respect to their reference positions. See text for details. Reprinted from Ref. [112] as permitted under the CC BY 4.0 license for the original work.

184
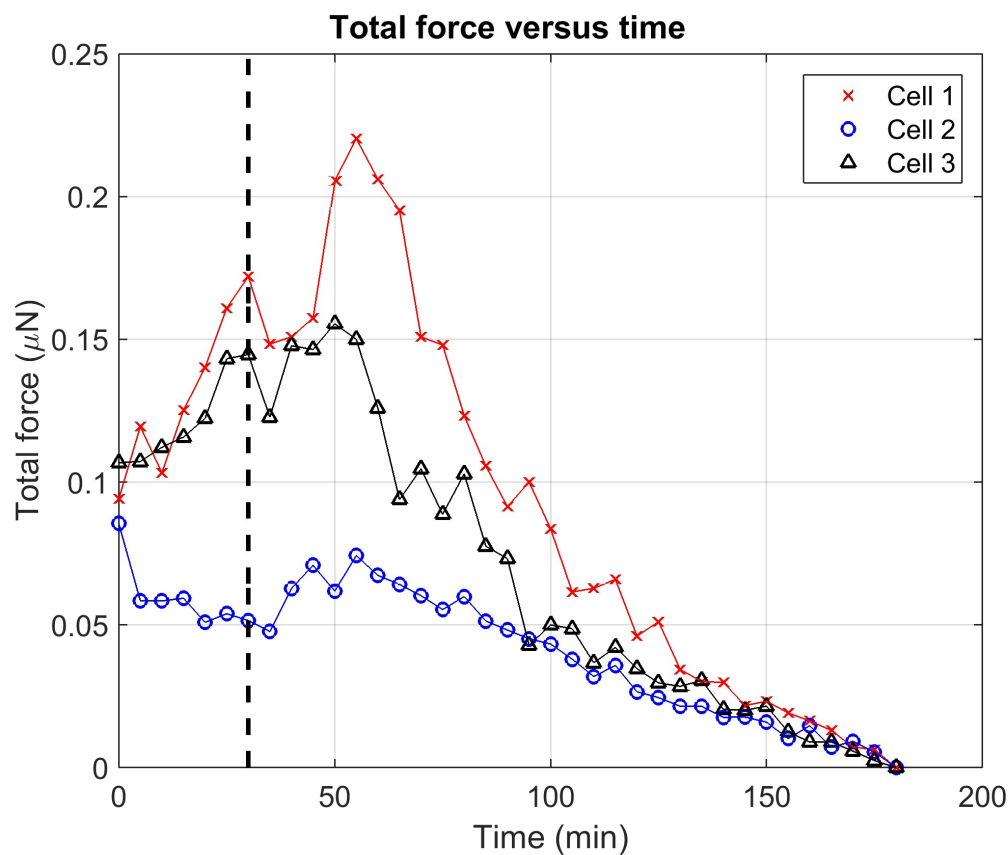
Figure 6.8: Total force exerted by three NIH-3T3 fibroblast cells (shown previously in Figs. 6.5 and 6.7) over time. Black dashed line indicates when the contractility inhibitor (cytochalasin D) was introduced to the samples 30 minutes into the experiment. See Appendix L.1.3 for a description of the measurement of 'total force' from 3D CTF distributions. Reprinted from Ref. [112] as permitted under the CC BY 4.0 license for the original work.

6.4 Discussion

6.4.1 Computational image formation

TFM relies on the ability to perform accurate quantitative analysis of substrate deformations. The implementation of TF-OCM in this study relied upon numerous computational operations (in both the space and spatial frequency domains) to achieve its objectives. These operations (shown in Fig. 6.1) included stan-
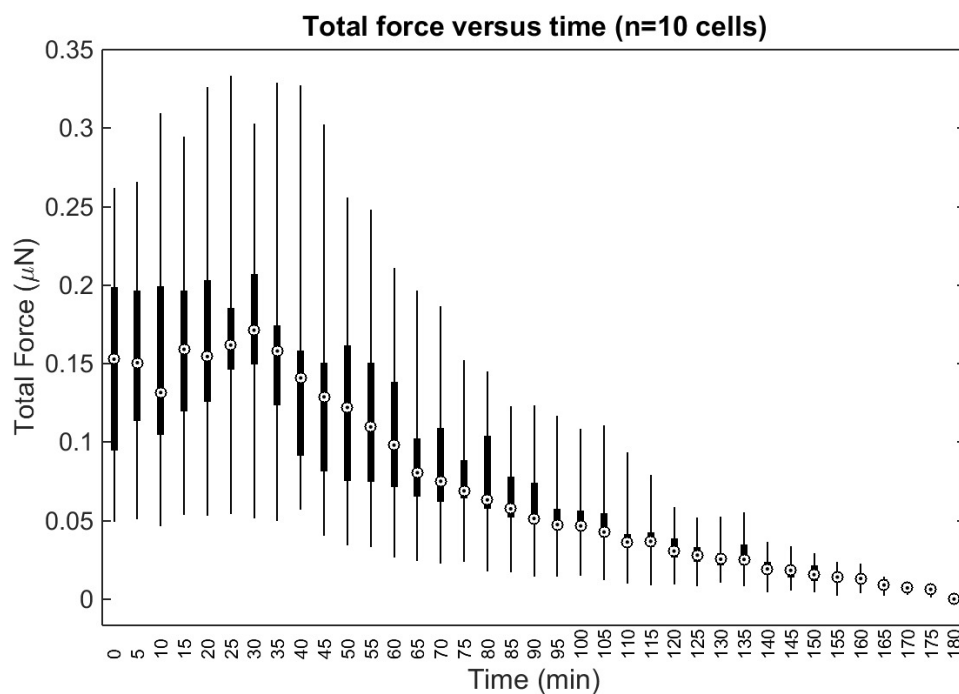
Figure 6.9: Total force exerted by all (n=10) cells examined for this study. 'Total force' is defined as in Fig. 6.8 and Appendix L.1.3. The whiskers, boxes, and circles depict the full range, interquartile range, and median value of the data, respectively. The contractility inhibitor (cytochalasin D) was added immediately after time t = 30 minutes. Reprinted from Ref. [112] as permitted under the CC BY 4.0 license for the original work.

dard OCM image reconstruction procedures, coherence gate curvature (CGC) removal, focal plane registration, phase registration, bulk demodulation, CAO, and motion correction. Each of the steps in our computational image formation module involved coordinate transformations and/or phase manipulations which can have dramatic effects on the final image structure, substrate deformation data, cell tracings, and CTF reconstructions. As a result, these steps offer several opportunities for errors to emerge before the final image structure is generated. Optical distortions and the question of image fidelity are problems faced when using any type of imaging system. Whether formed physically or through computation, an image can only be a best attempt to represent the true underly-

ing sample structure in a controlled and consistent manner. It is recommended for any researchers interested in adopting our methods to carefully study and understand the theory and implementations outlined in Chapters 4 and 7. You may yet find more accurate or efficient methods than those developed during this line of research.

6.4.2   Bead size and density

One potential disadvantage of the experimental methods shown here is the use of relatively large (1 μm diameter) scattering beads. High concentrations of beads allow for substrate deformations to be sampled more densely in space, and therefore can help to mitigate the impact of error/measurement noise and/or resolve the forces exerted by smaller cellular structures [29, 28]. In general, beads used for TFM are typically at least one order of magnitude smaller than the minimum desired bead spacing [61, 89, 126]. Using 1 μm beads allows for a minimum bead spacing of approximately 10 μm (the actual spacing in the experiments reported here was approximately 18 μm, thereby limiting our ability to resolve stress features on the cell surface below this length scale). We found that our current bead density limited the sensitivity of our system to CTFs by contributing noise on the order of 18 nN, at the worst-case time point. However, the median cell forces (as in Fig. 6.9) exceeded this noise contribution by approximately one order of magnitude at the time points which exhibited the poorest sensitivity. (A detailed description of these findings is provided in Appendix L.2.4.) Future experiments with TF-OCM may use smaller beads to allow for greater bead densities without disrupting substrate mechanics or cell behavior. However, since a decrease in bead size tends to decrease the strength

of the scattered signal from a given bead, any reduction in bead size must optimize a trade-off between bead density and SNR of the bead signal with respect to the imaging noise floor. In addition, the presence of highly scattering particles may obstruct any co-registered fluorescence imaging which may accompany a TF-OCM experiment. One solution to this problem may be to abandon scattering beads entirely. TFM has been demonstrated using confocal reflectance microscopy to track the motion of collagen fibers, instead of embedded beads [76, 161]. OCT/OCM could similarly be used to image the deformation of fibrous extracellular matrix constituents for TF-OCM (see Chapter 7). If the scattering structures (e.g., collagen fibers) are too small to resolve, speckle tracking methods (analogous to those used for optical coherence elastography [113]), may be a possible solution.

6.4.3   Speckle

Speckle is another limitation of TF-OCM. This study required the use of speckle reduction methods to perform TF-OCM based on automated analysis of time-lapse OCM image data. Future implementations of TF-OCM based purely upon OCT/OCM imaging will likely continue to rely on speckle reduction procedures [32, 95, 92]. Alternatively, TF-OCM could be performed in conjunction with co-registered fluorescence imaging to capture images of cell geometry without speckle. If the cell shape changes slowly over time, fluorescence imaging would not have to take place at every time-point, so as not to limit the temporal sampling provided by the rapid volumetric acquisition of OCT/OCM imaging. Moreover, fluorescence imaging may be confined solely to the cell/s of interest while OCM is used to capture the full volumetric FOV under study, thereby

keeping any photobleaching/phototoxicity from fluorescence imaging to a minimum during extended experiments.

6.4.4 Assumptions used for force reconstruction

Similar to many existing TFM procedures, the reconstruction of CTFs in this study relied on several assumptions about the substrate medium (e.g., that the material is linear elastic, and its mechanical properties are isotropic, homogeneous, and time-invariant). In practice, biopolymer substrates often violate these assumptions. Inappropriate reliance on linear elastic (etc.) models can result in inaccurate CTF reconstructions and can create significant discrepancies between experimentally measured substrate deformations and those predicted by the (inadequate) mechanical model. The TFM field in recent years has seen a growth in the development and adoption of more advanced mechanical models to improve the accuracy of CTF reconstructions (see Chapter 2) [111]. Nonlinear elastic models have been particularly useful in TFM for describing the behaviors of biopolymer substrates (such as collagen, fibrin, and Matrigel) [61, 161]. Viscoelastic models have also been shown to offer accuracy benefits over purely elastic models in some situations [173]. For the Matrigel substrate used in this study, we found our linear elastic model to be sufficient (additional details and justification may be found in Appendix L.2.2). However, due to the inherent modularity of TFM, future studies using TF-OCM could likely benefit from the adoption of nonlinear and/or viscoelastic models for CTF reconstruction, even if the image acquisition and image formation protocols developed for this study remained unchanged. This may be especially important for future applications of TF-OCM for the analysis of cell behaviors in substrates like collagen, which

are typically of greater physiological relevance than the Matrigel substrate used in this study.

6.5   Conclusion

In this study, we implemented quantitative TF-OCM for the first time, enabling the reconstruction of time-varying 3D cell traction forces with minute-scale temporal sampling. This was achieved by combining rapid OCM image acquisition with computational image formation methods, applied to an otherwise standard TFM experimental protocol. As a result, TF-OCM has been demonstrated to be a viable method for overcoming the limitations of typical TFM methods by providing millimeter-scale volumetric coverage, high temporal sampling, and a low risk of photobleaching/phototoxicity. Currently, TF-OCM has only been applied to single cells. However, due to the ability of OCT/OCM to image over large volumes in scattering media, TF-OCM may find its most impactful niche in the study of physiologically-relevant multicellular constructs on spatial scales ranging from hundreds of micrometers to millimeters, such as cell networks and spheroids (see Chapter 7). Since OCM is capable of imaging native scattering contrast, future implementations of TF-OCM may also enable the study of CTFs in systems that do not have fiducial marker beads, a capability that is currently uncommon in the TFM field. Moreover, TF-OCM is compatible with optical coherence elastography [113, 87], making OCT imaging systems an attractive platform for mechanobiology research as both techniques continue to develop. Finally, due to the highly modular nature of the TF-OCM protocol, the procedures used in this study may be readily improved, modified, or adapted to a variety of alternative experimental settings, imaging preferences, and me-

chanical models. Consequently, TF-OCM has significant potential for making contributions to research in mechanobiology.

6.6 Methods

6.6.1 Sample preparation

Samples consisted of NIH-3T3 fibroblasts embedded in Matrigel containing scattering polystyrene beads. Cells were maintained in tissue culture flasks with media consisting of Dulbecco's Modified Eagle Medium (DMEM), supplemented with 10% bovine calf serum, and 1% penicillin-streptomycin. To prepare samples, the cells were trypsinized, pelleted, and resuspended in chilled (4°C) media at a concentration of 3.33×10^4 cells/mL. $1\,\mu$m-diameter polystyrene beads (Spherotech Inc.) were added to the suspension to achieve a concentration of 5.3×10^8 beads/mL. The cell-bead suspension was added to Matrigel in a 30:70 ratio, resulting in a final cell concentration of 1×10^4 cells/mL, and final bead concentration of 1.6×10^8 beads/mL (yielding an average bead spacing of approximately $18\,\mu$m). (The impact of bead density on the level of noise in CTF reconstructions is explored in Appendix L.2.4.) The resulting mixture was deposited in $100\,\mu$L aliquots on glass-bottomed petri dishes and left to gel in an incubator for 20 minutes, before being covered in culture media. Samples were kept in an incubator overnight (~12 hours) prior to imaging.

6.6.2 Bulk rheology

Sample stiffness was characterized using a TA Instruments DHR3 shear rheometer in a (flat) plate-plate geometry. Cell culture media and Matrigel were mixed in a 30:70 ratio. For each test, the mixture was loaded and gelled underneath a 40 mm diameter plate on a temperature controlled testing stage at 37°C for 20 minutes. The sample stage was covered/sealed to mitigate evaporation. We approximated the Matrigel hydrogel as a nearly incompressible substance, by assuming a Poisson's ratio of 0.45. (Note that the treatment of Matrigel as a nearly/fully incompressible material has precedent in prior literature [26, 64]). The Young's modulus was found to be approximately 90 Pa. This value was used as an input to the Finite Element Method solver used to reconstruct CTFs. See Appendix L.2.2 for additional information regarding the validity of our linear elastic model.

6.6.3 Imaging system

All samples were imaged using a spectral domain OCM (SD-OCM) system. Illumination was supplied by a Ti:Sapph laser (Femtolasers, INTEGRAL Element) with a central wavelength of 800 nm and a bandwidth of 160 nm. Light was split between the sample and reference arms by a 90:10 fiber coupler, yielding an incident power of ~5 mW in the sample arm beam. The sample arm was built in a double-pass configuration with an Olympus XLUMPlanFL 20×/0.95 W ∞/0 objective lens in an inverted configuration (i.e., samples were imaged through the bottom of the glass-bottomed petri dish). Spectral data was acquired with a Cobra 800 spectrometer (Wasatch Photonics) and 2048-pixel line scan camera (e2v,

Octopus[7]). The axial and lateral resolutions of the system were approximately 2.4 μm and 1.5 μm, respectively. All data acquisition was performed with a line scan rate of 65 kHz and an exposure time of 10 μs. Under these conditions, the system exhibited a sensitivity of ~90 dB and fall-off of −5 dB/mm. The system was controlled using custom software built in LabVIEW.

6.6.4   Time-lapse imaging protocol

Samples were held in position by an Okolab UNO-PLUS incubating stage mounted to a (non-motorized) 3-axis translation stage. This incubating stage maintained physiological temperature, humidity, and pH levels in the samples during imaging. Due to the use of a non-motorized stage, only a single embedded fibroblast cell was imaged per time-lapse experiment.[8] For each time-lapse, an isolated cell (i.e., a cell which occupied its own 'personal' $500 \times 500 \times 500$ μm^3 FOV within the Matrigel substrate) was located. This cell was aligned to the focal plane of the OCM system and centered within the lateral FOV. Time-lapse imaging was then begun. Each time-lapse imaging experiment spanned a total of 3 hours. This 3-hour period was divided into two phases. The first phase spanned the first 30 minutes of imaging. During this time, the baseline (contractile) behavior of the cell was monitored. At the end of this phase, a contractility inhibitor (0.5 mM cytochalasin D dissolved in DMSO) was added to the petri dish to achieve a final cytochalasin D concentration of 1 μM. The second phase spanned the remaining time of the experiment (2.5 hours). During this phase, cell relaxation in response to the contractility inhibitor was observed.

---

[7]For the reference of future readers in our lab: this specific spectrometer camera was a prototype model for what is now the Teledyne e2v OctoPlus series of spectrometer cameras.

[8]We rectified this limitation for the work in Chapter 7.

Bursts of volumetric images were acquired at five-minute intervals across both phases of each time-lapse experiment. Each burst captured a single 'full FOV' volume (spanning $2560 \times 500 \times 500 \, \mu m^3$ with $2048 \times 1024 \times 1024$ voxels) and eight 'reduced FOV' volumes (spanning $2560 \times 125 \times 125 \, \mu m^3$ with $2048 \times 256 \times 256$ voxels). This multi-acquisition/multi-FOV scheme was used to aid in speckle reduction for automated segmentation of cell bodies. Each burst of images took approximately 1.5 minutes to acquire. The laser shutter was closed between each burst to limit sample exposure to laser light between acquisitions.

6.6.5 Computational image formation

The reconstruction of volumetric time-lapse images from raw OCM spectral data consisted of six steps: (1) initial volume reconstruction, (2) coherence gate curvature removal, (3) focal plane registration, (4) phase registration, (5) bulk demodulation, and (6) computational adaptive optics. This procedure was designed to provide accurate high resolution volumetric image data that is well-suited for quantitative TFM applications. For a given time-lapse dataset, our implementation of this procedure processed each time-point in series. However, it should be noted that this procedure is also amenable to parallelization. All steps were performed in MATLAB R2014b using CPU-based processing. In addition, all procedures were automated, requiring no human input except where otherwise noted in the detailed procedures, which are provided in Appendix L.1.1. Data processing was performed on a work station equipped with 2 Intel(R) Zeon(R) CPU E5-2650 v3 @ 2.30 GHz processors and 128 GB of memory. All image formation and image processing steps (including image segmentation and bead tracking) were performed at a rate of approximately 20 minutes per

imaging time-point (including data read time from a remote server).

6.6.6 Measurement of substrate deformations

Substrate deformations were determined from the motion of the scattering polystyrene beads embedded in the Matrigel substrate. Bead motion was tracked using a time series consisting of the 'full FOV' images (described previously) in order to capture substrate deformations both near and far away from the cell surface.

Since the scattering polystyrene beads exhibited a high signal strength well above the noise floor, bead positions were localized with a simple segmentation procedure. Volumetric image intensities were first normalized across depth. This was followed by binarization via single-level thresholding. The binarized images were then cleaned to remove objects that were too small or too large to be scattering beads. Objects removed included those smaller than 16 voxels (i.e., those too small to be a bead), and those larger than the 99th percentile of all objects larger than 16 voxels (such as the cell body, bead aggregates, or protein debris). All remaining objects in the binarized images were assumed to be beads. The location of each bead, was measured by calculating the intensity-weighted centroid of each object in the binary image. The sensitivity of this bead localization procedure was determined by measuring the standard deviation of apparent (i.e., measured) bead displacements between two sequential images, acquired in the absence of CTFs. The localization sensitivity was found to be 86 nm, 32 nm, and 37 nm along the vertical, fast, and slow axes of the imaging system, respectively. (These values correspond to approximately one-fifteenth

195

of the voxel size along each dimension.) The impact of this localization sensitivity on the level of noise in CTF reconstructions is explored in Appendix L.2.4.

Bead motion over time was determined using a feature vector-based point tracking algorithm [43]. (Details regarding algorithm design and performance under various conditions may be found in the original publication [43].) In brief, the algorithm searches for pairs of bead positions (spanning pairs of time-points) which are most likely to correspond to the same bead. Candidate pairs of positions are then determined to be a 'match' based upon the relative motion of other nearby beads (i.e., the algorithm assumes the substrate behaves as an elastic solid with deformations varying on scales longer than the bead spacing). Using this algorithm, bead positions were tracked across the full temporal span of each time-lapse dataset.

Once the positions of all individual beads were determined across time, bead displacements were calculated with respect to the final bead positions (i.e., the reference positions, as discussed in Section 6.2) at the end of the experiment (i.e., time $t = t_{max}$, or $t = 3$ hours, in our imaging procedure). Details about this procedure, as well as motion correction, may be found in Appendix L.1.2. We assumed both that the fibroblast cells exerted no forces and that the substrate had no internal stresses or strain remaining at the end of each time-lapse experiment. This is a standard practice in TFM experiments which use chemical reagents to inhibit cell contractility or induce cell death [111]. We did find evidence of incomplete cell relaxation, in particular for cells 2, 5, and 6, which violates this assumption. Details may be found in Appendix L.2.3.

6.6.7 Image segmentation for the measurement of time-varying cell geometry

Knowledge of time-varying cell shape and location was required in order to provide the boundary conditions necessary for CTF reconstruction. The 8 'reduced FOV' images (described previously) at each time-point were used to reduce speckle, and thereby enable a simple automated image segmentation procedure to identify the cell body. Due to the motion of intracellular components, the speckle pattern varied between individual images. At each time-point, the corresponding set of reduced FOV images was combined via a projection operation. Specifically, the (speckle-reduced) output image was obtained via the standard deviation of the magnitude of the corresponding reduced FOV images, taken on a voxel-by-voxel basis.[9] This caused regions of high speckle fluctuation to be emphasized, and regions of static background scattering to be suppressed. It also had the effect of reducing the speckle contrast within the cell body. K-means clustering of a given speckle-reduced volumetric image yielded a binary image from which a volumetric approximation of the cell body was obtained (see Fig. 6.4).

6.6.8 Mesh generation

For each time-point, the binary image generated by image segmentation was converted into a discretized 3D triangular surface mesh using the

---

[9]That is, assume you have 8 complex-valued 'reduced FOV' image signals $S_i(x, y, z, t)$ for $i \in \{1, 2, \ldots, 8\}$. The speckle-reduced image $S_{sr}(x, y, z, t)$ was obtained via: $S_{sr}(x, y, z, t) = \left[(1/7) \sum_{i=1}^{8} \left(|S_i(x, y, z, t)| - \bar{S}(x, y, z, t) \right)^2 \right]^{1/2}$, where $\bar{S}(x, y, z, t) = (1/8) \sum_{i=1}^{8} |S_i(x, y, z, t)|$.

`iso2mesh` [42] and 'Smooth Triangulated Mesh' [82] packages in MATLAB (see Appendix L.1.2 for details about motion correction). This surface mesh was then used to generate a volumetric tetrahedral mesh of the imaged volume in the open source program, *Gmsh* [52]. The outer surface of the mesh was a cube defined by the image boundaries, and the inner surface was defined by the cell surface at that time-point. Finally, this volumetric tetrahedral mesh was converted into a volumetric hexahedral mesh using the open source software package, *tethex* [2]. The final output of this procedure was a sequence of volumetric meshes suitable for use in our CTF reconstruction software.

6.6.9   Reconstruction of time-varying 3D cell traction forces

The substrate mechanical characterization data, bead displacement data, and 3D mesh data produced by all the methods described above were used to reconstruct time-varying 3D cell traction forces. CTF reconstruction was performed using a previously reported custom FEM software package [44] based on the open-source deal.II library [1]. (Details regarding performance using simulated data may be found in the original publication [44].) In brief, the reconstruction of cell traction forces is formulated as an inverse problem, which was solved by minimizing the discrepancy between the measured bead displacements and those that would be predicted to result from a candidate hypothesized traction field. The Matrigel substrate was assumed to be linear elastic, homogeneous, isotropic, and time-invariant. (These are standard, although neither universal nor mandatory, assumptions used to make the inverse problem posed by traction force reconstruction tractable) [111]. Since cell motion was quasi-static for any given time-point, the reconstructed traction field was required to satisfy

force and moment balance. To optimize the trade-off between accuracy and instability of the numerical solution, Tikhonov regularization was applied (using a regularization coefficient value of 10^{-7}, which was determined using the L-curve method) [44]. The mechanical properties used as input were a Young's modulus of 90 Pa (measured, as described previously) and Poisson's ratio of 0.45 (assumed). CTF reconstruction was carried out independently for each time-point in a given time-lapse experiment. All force reconstructions were performed on a work station equipped with 2 Intel(R) Zeon(R) CPU E5-2680 v2 @ 2.8 GHz processors and 190 GB of memory. As a result, all 370 time-points processed for this study were computed in approximately 80 hours.

CHAPTER 7

LABEL-FREE 4D IMAGING OF COLLECTIVE CELL INVASION IN COLLAGEN FOR TRACTION FORCE OPTICAL COHERENCE MICROSCOPY

Content reuse disclosure Figures and passages of this chapter have been reprinted/adapted from a previously published journal paper of which I was a contributing (second) author.[1] The figures/passages of this chapter which have been reprinted/adapted will be indicated, as appropriate. To view the full contents of the original paper, please see Ref. [94].

Notice of intent to publish A majority of the findings, figures, and methods in this dissertation chapter (i.e., not originating from Ref. [94]) form the contents of a manuscript which is currently (as of this writing) under preparation for submission to a scientific journal. Please note that those contents have not yet (as of this writing) been subjected to independent peer review. The purpose of the prospective manuscript is to highlight and detail the key TF-OCM methods which were developed here. These methods provided critical experimental capabilities which enabled key components of the scientific study in Ref. [94]. The detailed methods provided here (which are focused on microscope design, signal processing, and imaging capabilities) are not available in Ref. [94] (a study on the role of obesity in breast cancer progression).

---

[1]Reprinted/adapted with permission from John Wiley & Sons, Inc.: L. Ling, J.A. Mulligan, Y. Ouyang, A.A. Shimpi, R.M. Williams, G.F. Beeghly, B.D. Hopkins, J.A. Spector, S.G. Adie, C. Fischbach. ObesityAssociated Adipose Stromal Cells Promote Breast Cancer Invasion through Direct Cell Contact and ECM Remodeling. *Adv. Funct. Mater.* 2020, 1910650. `https://doi.org/10.1002/adfm.201910650` © WILEY-VCH Verlag GmbH & Co. KGaA, Weinheim (2020)

Author contributions statement The following contributions pertain only to the contents of this dissertation chapter. **J.A. Mulligan:** Devised, developed, and implemented all hardware and software methods. Performed all data processing, figure generation, and writing. **L. Ling** Performed all cell culture and sample preparation. **J.A. Mulligan and L. Ling:** Performed all time-lapse imaging experiments together. **S.G. Adie and C. Fischabch:** Provided guidance, funding, and other input throughout the study.

7.1 Introduction

In our previous study (Chapter 6, Ref. [112]), we presented the first quantitative implementation of traction force optical coherence microscopy (TF-OCM). TF-OCM was used to reconstruct the time-varying cell traction forces (CTFs) exerted by isolated NIH-3T3 fibroblasts embedded within a 3D Matrigel substrate laced with scattering polystyrene beads (which served as fiducial markers of CTF-induced substrate deformations). Although this study successfully demonstrated the ability of TF-OCM to serve as a new technique for performing dynamic 3D TFM of isolated cells, it did not demonstrate the full imaging capabilities of TF-OCM for the study of dynamic, 3D, collective behavior within scattering media. Such capabilities are currently lacking in the TFM field and could be of great value to the mechanobiology research community.

In this study, we refined and adapted our previously developed TF-OCM imaging methods [112] to enable label-free 4D imaging of collective cell invasion in collagen. Specifically, we used our TF-OCM imaging protocols and image formation routines to perform time-lapse analysis of a tumor spheroid invasion model. Spheroids consisting of monocultures and co-cultures of murine adipose stromal cells (ASCs) and/or MCF10AT1 cells (a premalignant human breast cancer model) were embedded in collagen. Invasion of cells into the surrounding 3D substrate were observed for the next 48 hours via optical coherence microscopy (OCM) with a 40-minute imaging interval. This multi-day invasion process was associated with substantial changes in spheroid geometry, as well as degradation and deformation of the collagen substrate. Before going into further detail, we will review the underlying motivations for these experiments.

7.1.1 Background and context

In a 2015 paper [153], the Fischbach Lab at Cornell University presented findings which suggest a link between obesity, altered extracellular matrix (ECM) mechanics, and altered cell behaviors which together promote the formation of malignant breast cancer tumors. In brief, obesity alters the phenotype of ASCs, which exhibit increased proliferation and deposit mechanically stiffer ECMs. In turn, this promotes an increase in the number of myofibroblasts, which further modify and stiffen the ECM (and promote further increases in myofibroblast count via positive feedback). Finally, this (fibrotic) altered tissue promotes proliferation and malignant behavior in mammary epithelial cells. In summary, obesity alters the behavior of ASCs to induce fibrosis, which promotes malignant cell behavior.

In a new study [94], the Fischbach Lab wished to investigate whether obesity-associated ASCs could promote the *invasion* of tumor cells into surrounding tissue (in addition to their previously described role in promoting malignancy by modifying ECM architecture). It was shown that MCF10A-derived tumor cell lines (when embedded as a multicellular spheroid in collagen) invade insignificantly on their own. However, direct contact with ASCs from either lean (wildtype, WT) or obese (*ob/ob*) mice enabled the collective migration of tumor cells into the surrounding substrate, with obese ASCs promoting invasion more effectively than their lean counterparts. In order to better understand the mechanisms by which obesity-associated ASCs promote invasion, we explored the role of ECM *degradation* (via matrix metalloproteinases) versus ECM *deformation* (via cellular traction forces, CTFs).

My role, as an imaging scientist, was to develop new imaging capabilities

that would provide access to critical data for new experiments, and thus allow this investigation to take place.

7.1.2 Adaptation to required imaging capabilities

Carrying out the aforementioned investigation imposed various conditions/restrictions which differ substantially from our previously reported TF-OCM scenarios and methods [110, 112]:

1. Since we wished to observe the *progression* of collective cell invasion, spheroids were monitored for 48 hours (with a 40-minute interval between time-points), which is much longer than the 3-hour experiments that we previously reported.[2] Nevertheless, due to the label-free nature and low incident power of OCM, we anticipated no significant hurdles here beyond the large quantities (~50 TB) of raw data that would be acquired. Due to the length of these experiments, we also automated our imaging system, and enabled parallel imaging of at least 2-3 spheroids at a time.

2. Furthermore, since we wished to observe both degradation and deformation of collagen (which can occur simultaneously), we could no longer rely upon the chemically-induced CTF inhibition protocols that TFM studies typically rely on. This is because the inhibition of CTFs is meant to allow the substrate medium to relax back to an unstressed and undeformed state. Images from other time-points (i.e., when the substrate is

---

[2]Note that the 40-minute imaging interval was not chosen due to limits on image acquisition speed. Rather (due to the large quantities of raw data required), the interval was chosen to balance the quantity of data which we acquired, the speed at which spheroid morphology evolved over time, and the rate at which data could be transferred to remote storage during active imaging experiments.

stressed/deformed by CTFs) are compared to this state in order to measure substrate deformations. However, since we allowed sufficient time for collagen degradation to take place, we could not determine the amount of irreversible plastic deformations/residual stresses that accumulated prior to CTF inhibition without additional *a priori* information. Therefore, imaging began *immediately* after spheroid embedding so that the collagen substrate could be imaged in its unstressed/undeformed state before the spheroid had sufficient time to act upon it. As a result, we eliminated the need to perform CTF inhibition. This had the additional benefit of allowing us to continuously monitor the behavior of individual spheroids for long periods of time (since CTF inhibitors would disrupt normal cell behavior and physiological conditions at all subsequent time-points).

3. The collagen substrate generates strong scattering signals in OCM images. This poses a challenge for distinguishing and segmenting cell bodies from the surrounding medium using only native scattering contrast. Previously, we had only used optically clear Matrigel substrates for TF-OCM [110, 112]. However, as will be shown, our previously developed methods for speckle reduction [112] adapted remarkably well to providing a solution to this problem.

4. TFM methods typically rely on the addition of fluorescent/scattering fiducial marker beads to measure substrate deformations. However, concerns were raised that the addition of scattering beads to the substrate (as in our prior studies [110, 112]) could influence/alter cell behavior. Therefore, we decided to use the scattering contrast of OCM to measure the displacement of collagen fibers *directly* (in similar fashion to a previous TFM study using confocal reflectance microscopy [76]).

5. Finally, the sheer size of our spheroids (hundreds of micrometers) necessitated a lateral imaging FOV of at least 1×1 mm^2. At these scales, non-idealities in the imaging system can start to have substantial effects on the fidelity of volumetric image data (e.g., by inducing image distortions). This is detrimental to the quantitative measurement and analysis of CTF-induced substrate displacements. In order to address this challenge, we refined our previously reported computational image formation module [112] and modified our optical hardware (see Fig. 7.7 and Appendix I).

7.2 Results

7.2.1 Temporal speckle contrast enables label-free, 4D visualization of spheroid invasion behavior in collagen

One challenge of using label-free imaging (as in OCM/TF-OCM) is to identify the boundary between cells and the surrounding collagen substrate. In order to address this challenge, we leveraged a 'burst' imaging protocol similar to our previously reported TF-OCM methods [112]. For each time-point in a given time-lapse experiment, a 'burst' of nine volumetric images was acquired in rapid succession. Due to the short time period (~12-15 seconds) between individual acquisitions in a given 'burst', the observed speckle pattern from (quasi-) static collagen fibers remained practically constant. In contrast, the observed speckle pattern from cells exhibited significant changes over time, due to the rapid motion of sub-resolution intracellular components between images.

206

In order to take advantage of this temporal speckle contrast, the images of a given 'burst' were combined into a single volumetric image via a 'standard deviation projection' operation, which is defined in Eqn. 7.2. The resulting image exhibited strong/enhanced contrast in regions with temporally unstable speckle patterns, and weak/suppressed contrast in regions with temporally stable speckle patterns, consistent with similar existing methods [112, 191, 114]. This enabled the generation of two synthetic 'channels' from otherwise label-free OCM image data: 1) A 'cell' channel which strongly correlates to live/active cells and 2) a 'collagen' channel which strongly correlates to nonliving/static collagen. (Quotes are used here to signify that the correspondence of a given signal to actual cells and/or collagen lacks the direct specificity of fluorescent labeling agents.)

The results of this process are depicted in Figs. 7.1 and 7.2. Row 1 (structural OCT) contains standard label-free OCM images, corresponding to *en face* planes which intersect the center (i.e., the 'equator') of the given spheroid. Although it may be easy to distinguish the spheroid from the surrounding collagen at time $t = 0$, the distinction between cells and collagen becomes less clear as time progresses, especially in Fig. 7.1.[3] However, in row 2 (cell channel overlay), we obtain a clear picture of invasion activity by 'labeling' regions of high temporal speckle contrast. We can further gain a sense of the 3D structure of the invading spheroids by looking exclusively at the synthetic 'cell' channel (rows 3-5). Row 3 depicts a top-down view of this 'cell' channel, wherein each depth in the image is assigned a different color based on its distance from the plane shown in rows 1 and 2, and the final image is obtained via a maximum intensity projection of

---

[3]This may be due to the initial formation of a smooth and distinct boundary between the spheroid and collagen upon initial embedding, which becomes 'rough' and degrades as cells invade the surrounding substrate.

each color channel along the depth axis. Rows 4 and 5 depict 3D renderings of the 'cell channel', where row 4 shows the surface of the spheroid from an isometric viewing angle, and row 5 shows a 'cutaway' which reveals the interior structure of the spheroid. The wild-type (WT, lean) ASC monoculture spheroid in Fig. 7.1 exhibits a solid/confluent internal structure over time, whereas the WT ASC + MCF10AT1 co-culture spheroid in Fig. 7.2 exhibits a central 'core' of cells which detached from the exterior 'shell' and migrated along the depth axis until it was no longer visible to the imaging system. The presence of these distinct structures in the co-culture spheroid is consistent with histology, such as that shown in Fig. S1 of Ref. [94].

7.2.2 Label-free scattering contrast provides visualization of collagen degradation

In addition to the 'cell' and 'collagen' channels discussed above, we also observed a third feature: 'voids'. These regions of low scattering signal correspond to one of two features: 1) areas which cells initially occupied but vacated over time, leaving behind fluid-filled spaces and cavities, or 2) areas in the collagen substrate which have been degraded by invading cells (and are not currently occupied by cells). Both of these features are depicted in Fig. 7.3, with Fig. 7.3(c) highlighting regions with degraded collagen, in particular. The ability to identify these ECM modifications is useful for understanding the mechanisms underlying the invasion process [94]. Unfortunately, these regions are also prohibitive to conducting quantitative CTF reconstructions with TFM/TF-OCM due to the complicated and heterogeneous mechanical environment and

Spheroid composition: WT ASC
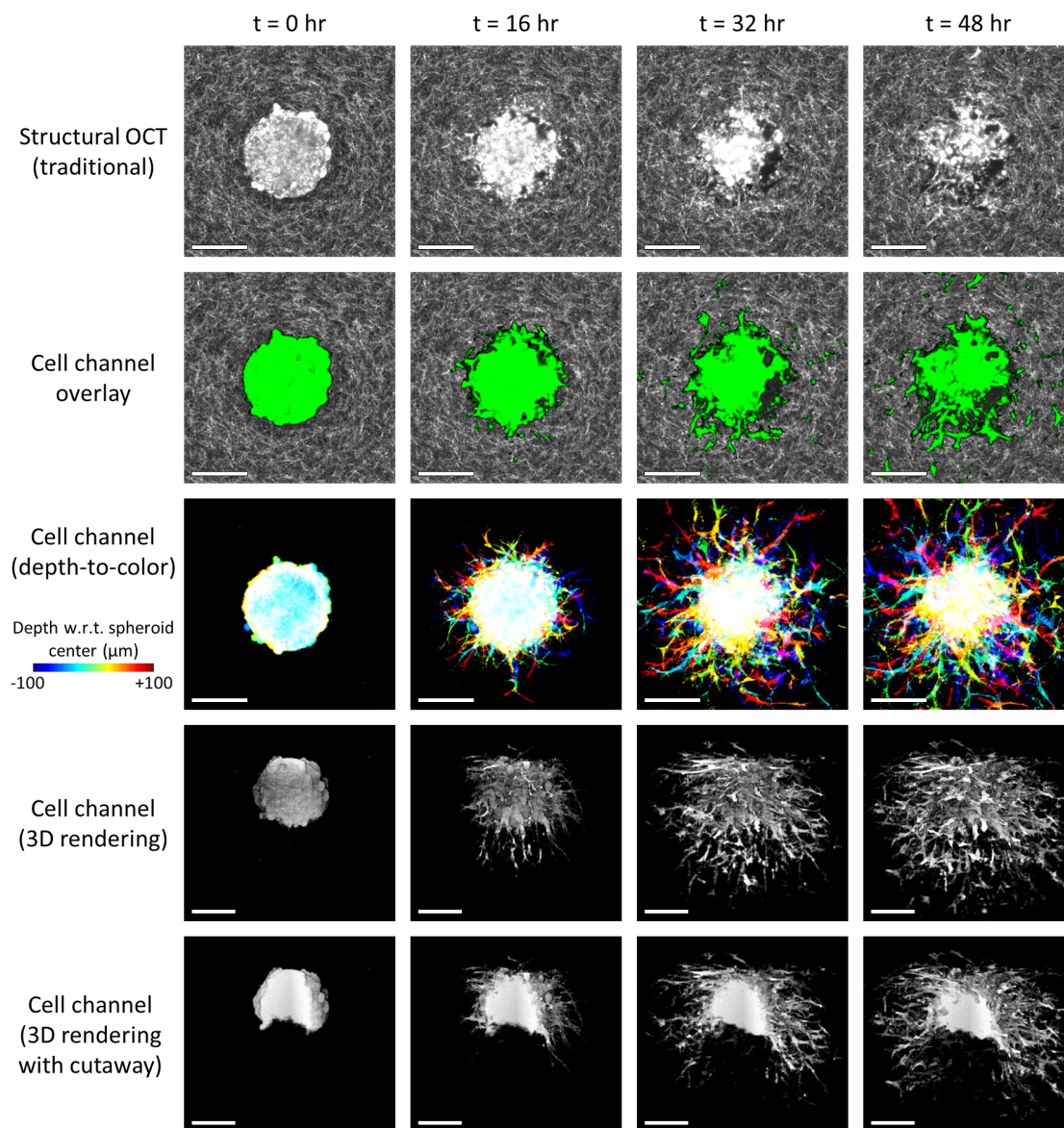
Figure 7.1: Invasion of WT ASC monoculture spheroid into collagen substrate revealed via label-free OCM imaging and temporal speckle contrast. Traditional OCM imaging (top row) records scattering signals of cells and collagen alike. Temporal speckle contrast enables segmentation of volumetric data into synthetic 'cell' and 'collagen' channels (rows 2-5). Scale bars = 200 μm. See text for details.

Figure 7.2: Invasion of WT ASC + MCF10AT1 co-culture spheroid into collagen substrate revealed via label-free OCM imaging and temporal speckle contrast. Traditional OCM imaging (top row) records scattering signals of cells and collagen alike. Temporal speckle contrast enables segmentation of volumetric data into synthetic 'cell' and 'collagen' channels (rows 2-5). Scale bars = 200 μm. See text for details.

boundary conditions that they present.

7.2.3 Elastic image registration reveals space- and time-varying collagen displacements

Time-varying deformations of the collagen substrate were observed in conjunction with the previously described changes in spheroid morphology and collagen degradation/remodeling. Unlike standard TFM methods which track the motion of embedded fiducial marker beads, here, the motion of collagen fibers was tracked directly (analogous to a previously reported TFM method based on confocal reflectance microscopy [76]). Elastic image registration (via the built-in MATLAB function `imregdemons`) was employed to estimate the time-varying 3D displacement field which would map the original collagen substrate at time $t = 0$ hours to the deformed collagen substrate observed at any given timepoint during the first 24 hours of imaging. As a result, the time-varying collagen displacement field could be quantified and visualized, as in Fig. 7.4. These data revealed contraction of the collagen toward the spheroid body, with the strength of contraction varying as a function of position. Regions of collagen with stronger displacements likely indicate areas where the spheroid may be exerting stronger contractile forces, although a quantitative reconstruction of CTFs would be required to verify this hypothesis. However, even in the absence of CTF reconstructions, this deformation data alone can provide valuable information for learning about cell/spheroid behavior [94, 162].
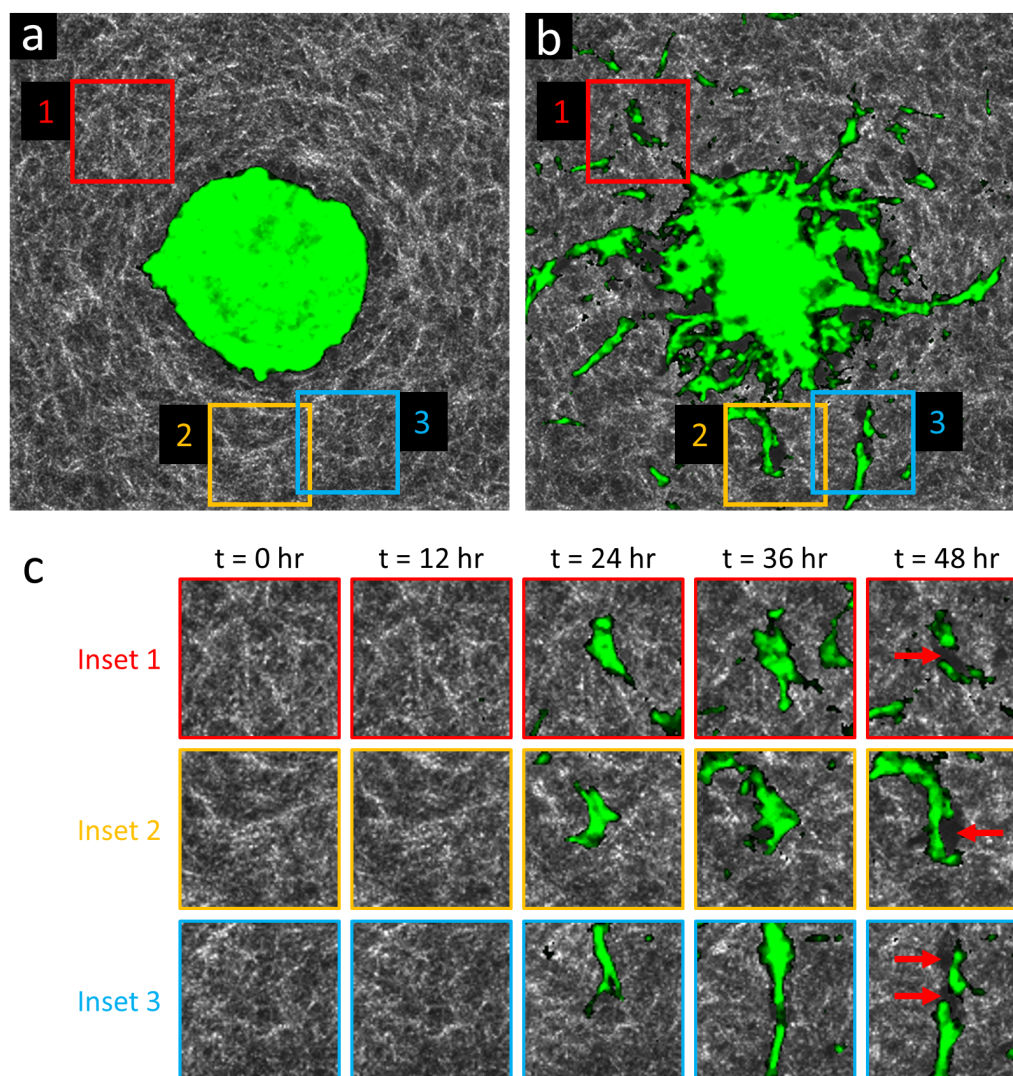
Figure 7.3: Time-lapse OCM imaging reveals collagen degradation by invasive strands. (a) *En face* plane intersecting the center (i.e., the 'equator') of a WT ASC monoculture spheroid, acquired at time $t = 0$ hr. The spheroid (green, highlighted via temporal speckle contrast) is recently embedded, and has not yet invaded the surrounding collagen (white). (b) The same *en face* plane as in (a), acquired at time $t = 48$ hr. Invasive protrusions are abundant. Large dark regions surrounding the spheroid and invasive strands correspond to 'voids' with low/weak scattering signals, suggesting a lack of either cells or collagen. (c) Time-lapse view of insets 1-3 from (a,b). Red arrows at time $t = 48$ hr indicate newly formed 'void' regions where only collagen was initially present. These new 'voids' are likely due to degradation of the collagen matrix by invasive strands with matrix metalloproteinase activity. Panels (a,b) span a $750 \times 750 \ \mu m^2$ lateral FOV.
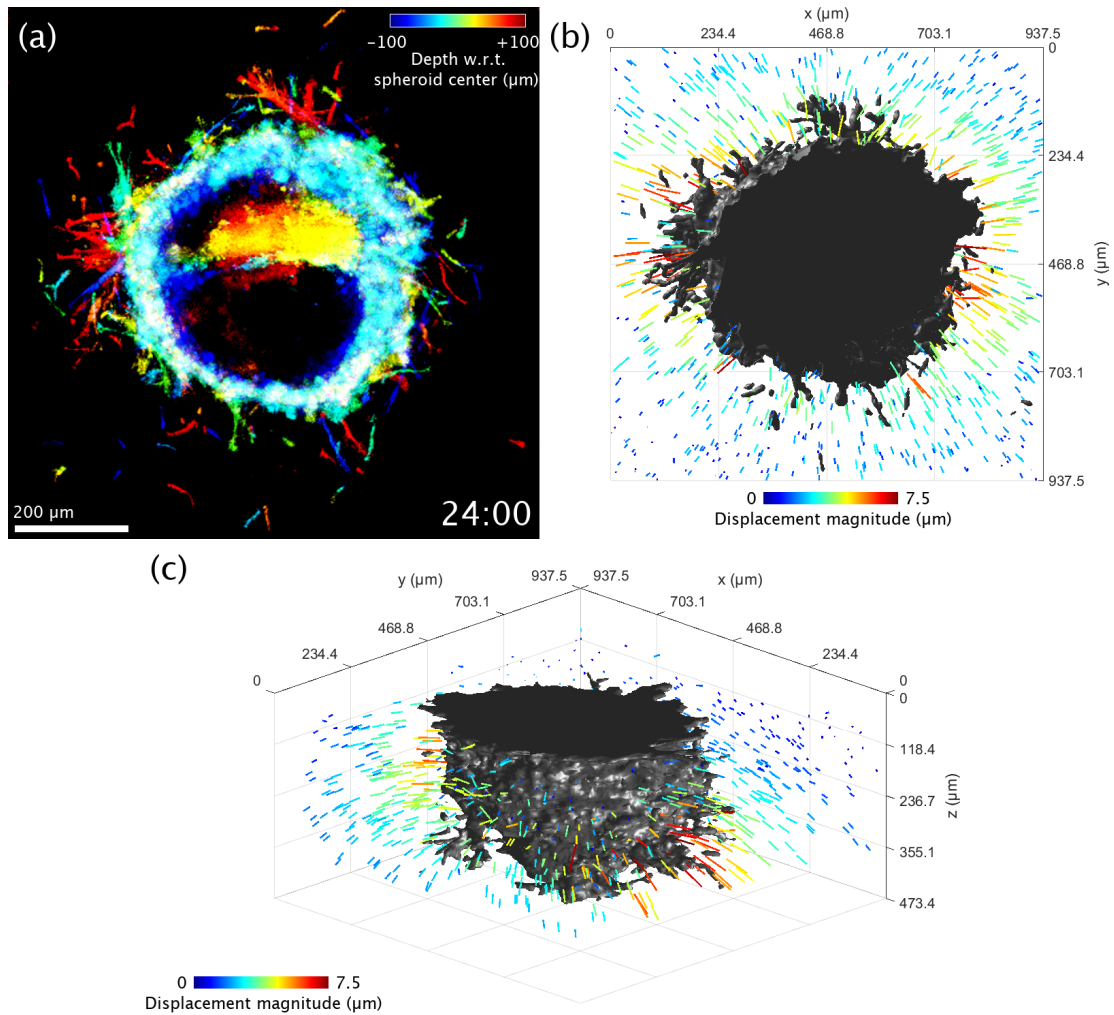
Figure 7.4: Visualization of 3D collagen displacements in the vicinity of an obese (*ob/ob*) ASC + MCF10AT1 co-culture spheroid at time t = 24 hr. (a) Top-down view of the spheroid, using the same depth-to-color projection as in row 3 of Figs. 7.1 and 7.2. (b) Top-down rendering of the spheroid (shown in gray) accompanied by colored arrows which indicate displacement of the collagen matrix as measured with respect to its initial configuration at time t = 0 hr. Arrow lengths have been exaggerated for visualization purposes. (c) Re-rendering of panel (b) from an isometric viewing angle. The flat surface of the spheroid corresponds to a region where the spheroid comes into contact with the coverslip bottom of the petri dish.

213

7.2.4 ASC-mediated tumor cell invasion correlates with matrix metalloproteinase-independent collagen contraction

Given the substantial presence of collagen degradation in these experiments, quantitative CTF reconstructions could not be performed at this time. However, our TF-OCM imaging methods, and the resulting data, could still be used to assess cell invasion behavior.

Elastic image registration was used to track displacements of the collagen matrix over time. Representative displacements are depicted in the false-color images and line plots of Fig. 7.5. These data show that MCF10AT1 cells induce negligible deformations in the surrounding collagen. In contrast, both lean and obese ASCs generate strong local deformations. Co-cultures of obese ASCs with MCF10AT1 cells exhibited substantially greater collagen deformations than their lean co-culture counterparts. This suggests that force-based mechanisms may play an important role in enabling invasion by obese ASCs.

To investigate this further, *ob/ob* ASC + MCF10AT1 co-culture spheroids were treated with 10 μM batimastat, a broad spectrum inhibitor of matrix metalloproteinases (MMPs). (That is, batimastat inhibits the ability of cells to degrade the collagen substrate.) Control and batimastat-treated co-culture spheroids (*ob/ob* ASC + MCF10AT1) are depicted in Fig. 7.6. These data show that, although batimastat-treated spheroids exhibited significant global reduction in invasion (Fig. 7.6(a)), local regions of invasion were still present. These local invasive regions were associated with collagen displacements that were comparable to those of control spheroids. This demonstrates that the inhibition of collagen degradation via MMP inhibitors is insufficient to halt invasion by obese ASCs,
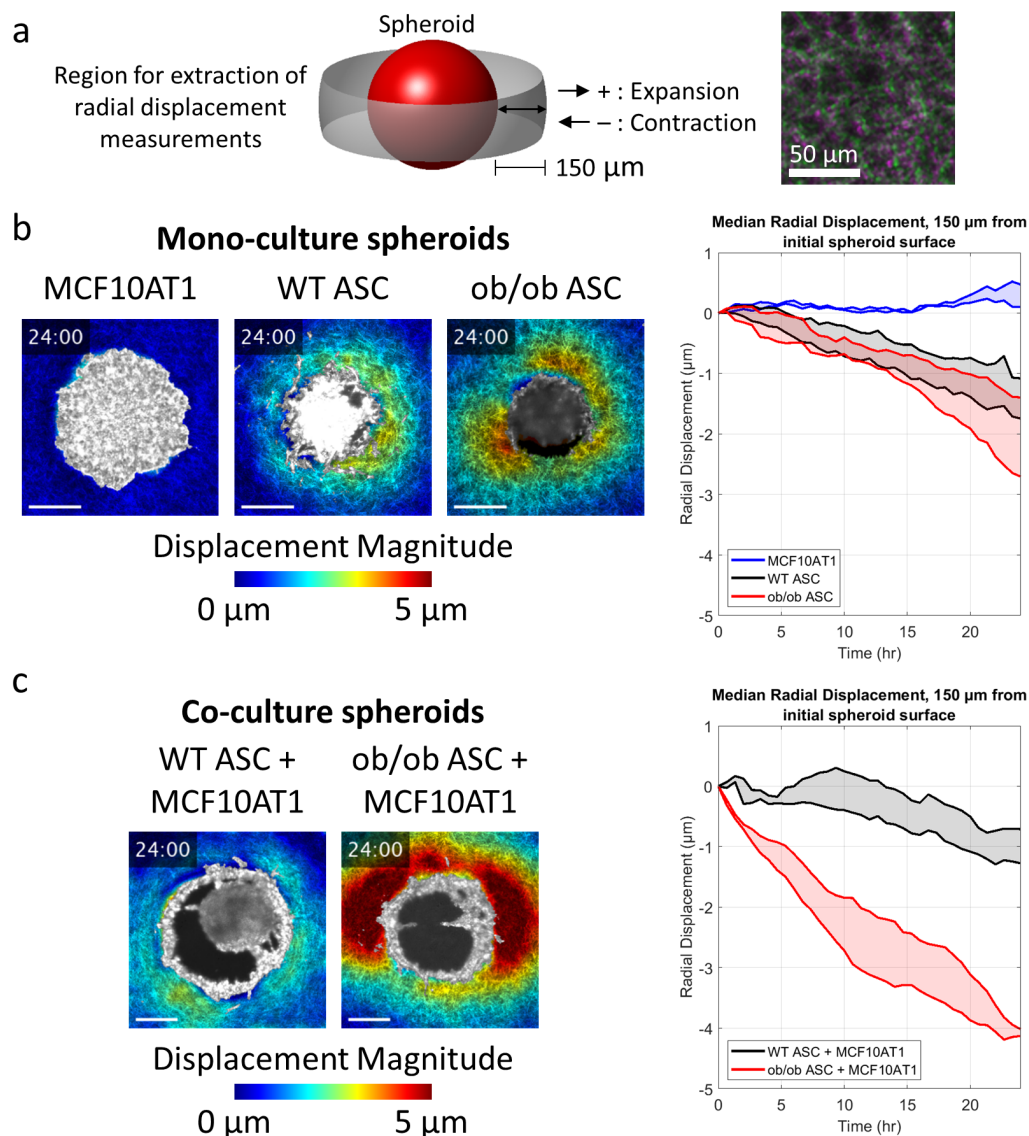
Figure 7.5: Collagen displacement for monoculture and co-culture spheroids. (a) Schematic for quantification of collagen displacement. The line plots in (b,c) were computed from the median radial displacement of collagen fibers, as measured across the gray surface (described in Section 7.5.9). The right-hand panel depicts collagen fibers at $t = 0$ hr (green) and $t = 24$ hr (purple). Displacements were tracked via elastic image registration. (b) Representative images of local collagen displacement near monoculture spheroids at $t = 24$ hr. Median radial displacements depict the full range of the data obtained from all spheroids of the given type (MCF10AT1: n=2, WT ASC: n=3, and *ob/ob* ASC: n=3). (c) Representative images of local collagen displacement near co-culture spheroids at $t = 24$ hr, with plots of median radial displacement on the right (WT ASC + MCF10AT1: n=3 and *ob/ob* ASC + MCF10AT1: n=2). Adapted with permission from Ref. [94] © WILEY-VCH Verlag GmbH & Co. KGaA, Weinheim (2020)

since these cells retain invasion competency via force-based mechanisms. Indeed, it was shown in follow-up experiments (with confocal fluorescence microscopy) that invasion was significantly reduced by a co-inhibition of *both* collagen degradation and cell forces [94].

7.3 Discussion

7.3.1 Image segmentation based on temporal speckle contrast

Although temporal speckle contrast proved remarkably useful for distinguishing invading cells from the surrounding (quasi-static) collagen substrate, this method does have weaknesses. In particular, in our previous study [113], we showed that fine cellular protrusions (e.g., filipodia) can exhibit relatively static speckle patterns over the time-scales of our 'burst' imaging protocol (i.e., fluctuations on the order of 0.1 Hz observed for approximately 1.5-2 minutes). We expect similar limitations to be present in this study. As a result, fine/static structures may exhibit weak contrast after performing our 'standard deviation projection' operation, and thus be incorrectly placed within the 'collagen' channel of our data. Future work with co-registered OCM and confocal fluorescence microscopy images will be required to quantify the severity of this effect. Our use of temporal speckle contrast also increases the amount of raw data that must be acquired by nearly an order of magnitude. However, the ability to generate synthetic imaging channels from label-free, long-term OCM image data may outweigh this cost. Nevertheless, future work which seeks to reduce the amount of data that must be acquired would be of great value. If large quantities of data
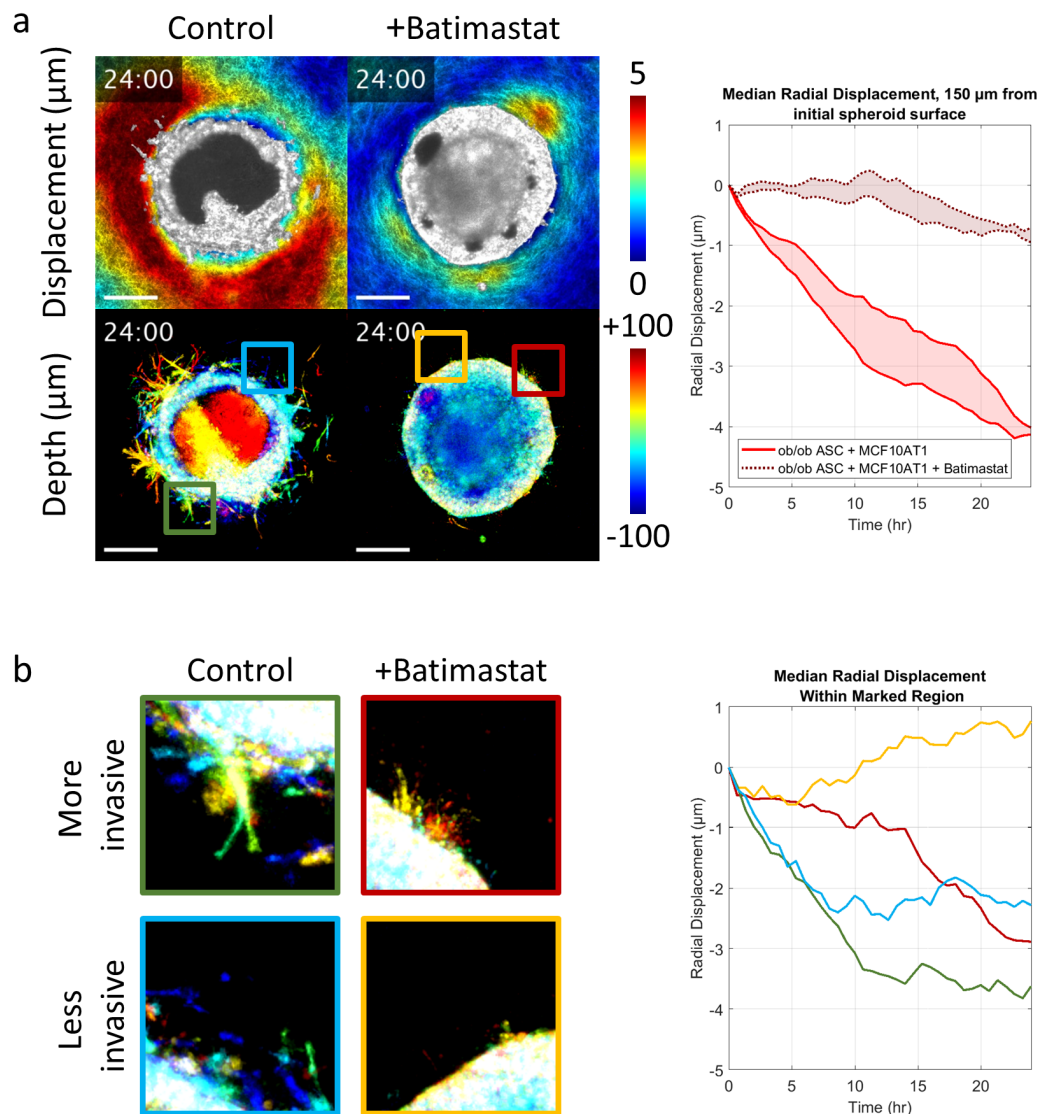
Figure 7.6: (a) (Top) Representative images of local collagen displacement near *ob/ob* ASC co-culture spheroids at *t* = 24 hr, under control and batimastat-treatment conditions. Plots of median radial displacement were computed using the same method as Fig. 7.5(b,c) (control: n=2 and batimastat: n=3). (Bottom) Corresponding morphology of the spheroids shown above. Color encodes depth over a range of ±100 μm with respect to the spheroid equator. (b) Expanded view of the inset regions shown in (a). The green and red insets (top) depict regions with greater local invasion than the regions corresponding to the blue and yellow insets (bottom). Median radial displacements computed within these local regions are shown at the right. All color bars are in units of micrometers. All scale bars = 200 μm. Adapted with permission from Ref. [94] © WILEY-VCH Verlag GmbH & Co. KGaA, Weinheim (2020)

are acceptable, and high-speed OCT/OCM imaging is available, the utility of temporal speckle contrast may be further enhanced by enabling the generation of multiple synthetic channels which correspond to different structures and/or levels of metabolic activity [114].

7.3.2 Displacement tracking in collagen

Although we were able to quantify the displacement of collagen fibers via elastic image registration (using the MATLAB function `imregdemons`), these measurements cannot be expected to be reliable very close to the cell-collagen boundary. This is because `imregdemons` uses Thirion's 'Demons algorithm' [125, 178], which performs image registration via an iterative optimization procedure inspired by the optical flow equations. This is an ill-posed problem which is often regularized via a diffusion (blurring/smoothing) process over the computed displacement field and/or by imposing other constraints (such as requiring that the computed displacement field correspond to a diffeomorphic transformation) [125, 178]. Unfortunately, since invading cells can degrade and migrate through the collagen substrate, a displacement field which 'perfectly' registers collagen fibers over time may exhibit jump discontinuities and/or be non-invertible. The typical regularization schemes of the Demons algorithm (i.e., isotropic and homogeneous spatial averaging) cannot accommodate these types of features. Algorithms based on local cross-correlation/matching would be simiarly vulnerable [76, 10], due to the spatial averaging inherent to cross-correlation windows. In the event that migrating cells deposit new collagen substrate, a valid displacement field may not even exist at all locations within the collagen substrate at a given time-point. In order to obtain reliable collagen

displacement data near the cell-collagen boundary (when such a measurement is possible), alternative algorithms must be found or devised which account for the complex boundary conditions which occur over long-term multicellular invasion processes.

For example, regularization of the Demons algorithm via a spatial averaging scheme which ignores cell-occupied regions (via spatially-varying averaging kernels) may be a viable option. If such a solution cannot be found, the incorporation and tracking of scattering fiducial marker beads within the collagen substrate may be a suitable alternative so long as the presence of beads does not appreciably alter cellular behavior. One advantage of the label-free contrast leveraged by TF-OCM is that, unlike fluorescence-based TFM techniques for which marker beads are typically *required*, our results here demonstrate that marker beads are merely *optional* for TF-OCM.

7.3.3 Quantifying cellular traction forces

The reconstruction of CTFs exerted by large multicellular constructs embedded in collagen over long time-scales is a problem that has yet to be addressed by the TFM field. In addition to the challenges of image segmentation and displacement tracking (described above), force reconstruction within collagen is a challenging problem. In particular, collagen is mechanically nonlinear and often exhibits heterogeneity across spatial scales. Moreover, cells can remodel the collagen matrix, altering its mechanical properties over time. This makes collagen supremely difficult to characterize and model to the degree necessary for numerical CTF-reconstruction schemes. Although TFM researchers have be-

gun to make forays into addressing this challenge [111] (see Chapter 2.4) much work remains to be done to enable CTF reconstructions in complex multicellular settings. In the meantime, our technique provides data that is useful to mechanobiology research (spheroid/cell morphology and collagen displacement data) even in the absence of quantitative CTF reconstructions. By making such data more readily available for studies of multicellular systems embedded in scattering media, our TF-OCM imaging methods may help provide the data necessary to aid future research in quantitative CTF reconstructions. Other OCM-based techniques, such as optical coherence elastography, may also be used alongside our TF-OCM imaging methods to aid the characterization of local, dynamic mechanical properties within biopolymer substrates [112, 87].

7.4   Conclusion

In this study, we adapted our previously reported TF-OCM imaging methods [112] to enable the study of collective cell invasion within scattering media. We demonstrated label-free 4D imaging capabilities, which used temporal speckle contrast to reveal the evolving 3D morphology of invasive tumor spheroids embedded in a collagen substrate. Using our methods, we were further able to identify collagen degradation by invading cells and quantify deformations in the collagen substrate surrounding the spheroid. These deformation data in particular contributed critical data and results to a broader biological investigation on the role of obesity in promoting breast cancer invasion [94]. Although much work remains to be done in order to enable quantitative TF-OCM in such mechanically complex settings, our results demonstrate that our TF-OCM imaging methods provide a promising and useful tool for enabling new studies of

dynamic, 3D, and collective behavior within optically scattering media.

7.5 Methods

The following sections of the Methods below have been reprinted/adapted with permission from Ref. [94] © WILEY-VCH Verlag GmbH & Co. KGaA, Weinheim (2020):

1. Section 7.5.1 (Animal use)

2. Section 7.5.2 (Cell culture)

3. Section 7.5.3 (Spheroid/sample preparation)

4. Section 7.5.9 (Collagen displacement tracking)

7.5.1 Animal use

All experiments (described below) using cells isolated from animals were approved by the Cornell University Institutional Animal Care and Use Committee (IACUC) under protocol number 2009-0117.

7.5.2 Cell culture

Adipose stromal cells (ASCs) were isolated from inguinal fat of 10-week-old B6.Cg-Lepob/J (*ob/ob*) mice and their age-matched C57BL/6J wild-type (WT) controls (Jackson Laboratories) according to previously published protocols

[153]. MCF10AT1 cells were obtained from the Barbara Ann Karmanos Cancer Institute. (For the purposes of the broader study performed in Ref. [94]) MCF10AT1 cells were transfected with a commercially available turbo-green fluorescent protein (GFP) vector (Thermo). Successfully transfected GFP+ cells were sorted on a BD FACS Aria cytometer.

ASCs were cultured in DMEM/F12 media supplemented with 10% fetal bovine serum and 100 U/mL penicillin-streptomycin. MCF10AT1 cells were cultured in enriched DMEM/F12 media supplemented with 5% horse serum, 10 μg/mL insulin, 0.5 μg/mL hydrocortisone, 100 ng/mL cholera toxin, 20 ng/mL EGF, and 100 U/mL penicillin-streptomycin. All cell lines were maintained in incubators at 37°C and 5% CO_2, with media changes every two days. For co-culture experiments, a 1:1 ratio of the respective media for each cell type was used. Batimastat-treated spheroids used modified media containing 10 μM batimastat.

7.5.3   Spheroid/sample preparation

96-well tissue culture plates were coated with 50 μL/well of 1.5% agarose diluted in DMEM/F12. This coating solidified to form a non-adherent surface (which promotes the coalescence of cells into spheroids). MCF10AT1 cells, ASCs, or co-cultures of the two (in a 1:1 ratio) were seeded into each well of the agarose-coated plate and placed on a rotating shaker (60 rpm) overnight to form multicellular spheroids.

Glass-bottomed petri dishes (Matsunami, 35 mm diameter well) were divided into three distinct wells/sectors via the addition of a handcrafted divider.

This divider was made from a 1.5 mm thick sheet of PDMS with three equal-sized compartments cut out, and was covalently bonded to the glass-bottomed petri dishes following plasma treatment.

High concentration rat tail collagen I (Corning) was reconstituted and neutralized with sodium hydroxide (NaOH) and 10× DMEM/F12 to a final concentration of 6 mg/mL. Collagen and spheroids were deposited on the prepared 3-well dishes (1 spheroid/well). In order to promote the formation of thick collagen fibers, the dishes were held at 4°C for 15 min, 20°C for 15 min, and finally 37°C for 15 min. Each gel was then immersed with media and transported to the incubating bio-chamber (described below).

7.5.4 Imaging system

All images were acquired using a custom-built spectral domain OCM imaging system (depicted in Fig. 7.7) which was developed based upon our previously reported system (Chapter 6, Ref. [112]) with minor modifications. Light was supplied by a Ti:Sapph laser (Femtolasers, INTEGRAL Element, central wavelength = 800 nm, bandwidth = 160 nm) and distributed within the microscope by a fiber coupler (Thorlabs TW805R2A2, 90% to the reference arm, 10% the to sample arm). (The power incident upon biological samples was approximately 4-5 mW.) Polarization in each arm was controlled and matched via manual fiber polarization controllers (Thorlabs FPC560). Custom-length fiber patch cords were added to reduce the total dispersion mismatch between the two arms (see Appendix D).

In the sample arm, light exiting the optical fiber was collimated using a
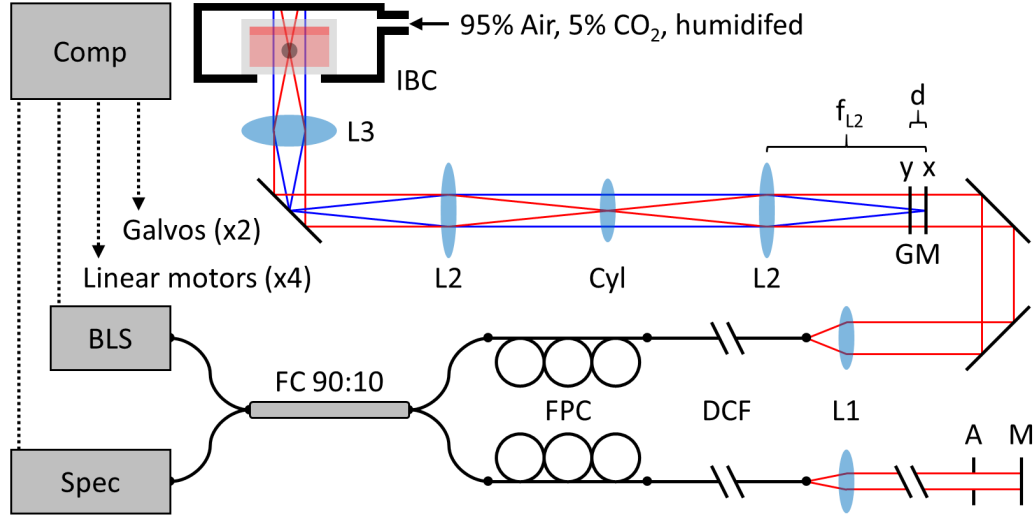
Figure 7.7: Diagram of our custom-built OCM imaging system for performing high-resolution, wide-FOV, low-distortion imaging. Comp: computer. BLS: broadband laser source. Spec: spectrometer + line-scan camera. FC: fiber coupler (90% to reference arm, 10% to sample arm). FPC: fiber polarization controller. DCF: dispersion compensating fiber (each arm contains different lengths of fiber). A: aperture. M: mirror/retro-reflector. GM: galvanometer mirror (x,y denote the axis along which each mirror tilts). (Note: Only the position of the galvanometer mirrors along the optical path is depicted here.) d: galvanometer mirror separation (13.69 mm, imposed by housing). L1: Collimating lens ($f_{L1} = 19$ mm). L2: Telescope lens ($f_{L2} = 100$ mm). Cyl: Cylindrical lens ($f_x = \infty$, $f_y = +700$ mm, which helps to compensate for coherence gate curvature resulting from the physical separation between the x and y galvanometers along the optical axis). L3: Objective lens (idealized). IBC: incubating bio-chamber.

(Thorlabs AC127-019-B) lens. Beam angle was scanned using a pre-mounted galvanometer mirror pair (Cambridge Technologies, ProSeries 1, 10 mm aperture, 10 V analog communication, S4 coating). The separation of the two galvanometer mirrors along the optical axis (as determined by their housing) was d=13.69 mm. The two galvanometer mirrors were (approximately) imaged to the back focal plane of the objective lens (Olympus LCPlan N 20×/0.45 IR, air immersion) via a custom-built 1:1 magnification 4F telescope. The telescope consisted of three lenses: two f=100 mm lenses (Thorlabs AC508-100-B) at the front and back, and one $f_x = \infty$, $f_y = +700$ mm cylindrical lens (Thor-

labs LJ1836L1-B) at the center. The cylindrical lens was used to compensate for coherence gate curvature (CGC) [55, 112], which emerges due to the separation (*d*) of the galvanometer mirrors along the optical axis (see Appendix H). A theoretical model and validation experiment for this system is detailed in Appendix I. As shown in that analysis, the 'optimal' focal length of the cylindrical lens was predicted to be approximately $(100 \text{ mm})^2/(13.69 \text{ mm}) \approx +730$ mm. The +700 mm lens that was used here was the nearest readily available 'off-the-shelf' part. With this design, our system reduced CGC to at most 6% (and may be capable of reducing CGC to as little as 1.5%) of its original severity (i.e., compared to the case when no CGC-compensating cylindrical lens is used).

In the reference arm, light was collimated as in the sample arm and then reflected via a retro-reflector (Thorlabs PS975M-B) mounted to a single-axis micrometer stage (Newport 9064-X, for fine position adjustment), which was further mounted to a rail (for coarse position adjustment). The amount of returning light was controlled via a manual tunable aperture.

The objective lens was mounted so as to image samples in an inverted configuration (i.e., from underneath). Samples were held above the objective lens in an incubating bio-chamber (Okolab UNO-PLUS), which was used to maintain physiological temperature, humidity, and pH throughout time-lapse experiments. The bio-chamber was mounted to a 3-axis micrometer stage (Newport 9064-XYZ-R). Linear stepper motors (Thorlabs ZST225B motor, KST101 controller, and KCH601 controller hub/power supply) were used to control the position of all 4 micrometer stages in the system (3 axes to control the position of the bio-chamber in the sample arm, and 1 axis to control the distance to the retro-reflector in the reference arm). These motors were controlled via

commands issued in MATLAB R2017a.

Raw image data were acquired using a spectrometer (Wasatch Photonics, Cobra 800) with a 2048-pixel line scan camera (Teledyne e2v OctoPlus). Galvanometer mirror scanning and data acquisition were controlled via custom software built in LabVIEW. Data was acquired using a line-scan rate of 55 kHz and an exposure time of 10 μs. The system exhibited a sensitivity of ~90 dB and a fall-off of −5 dB/mm. The axial and lateral resolutions of the system were approximately 2.4 μm and 1.5 μm, respectively. In order to perform automated multi-day time-lapse imaging, the data acquisition software, motors, laser, and computer-to-server data transfers were orchestrated via a master control program implemented in MATLAB R2017a.

7.5.5 Time-lapse imaging protocol

Immediately after spheroid embedding, the sample dish (containing 2-3 spheroids) was placed within the bio-chamber. Manual adjustment of the 4 linear motors was used to establish a set of control points for each spheroid. These control points defined a fixed position for each motor to hold when acquiring images of the corresponding spheroid. The control points for a given spheroid were selected such that: (1) the spheroid was centered within the lateral FOV of the system (sample arm x/y control points), (2) the 'equator' of the spheroid was roughly aligned to the focal plane (sample arm z control point), and (3) the spheroid and coverslip surface (at the base of the dish) appeared within an acceptable range of locations within the axial FOV of the imaging system (reference arm z control point). Establishing control points for all of the spheroids in

a given dish required approximately 10-15 minutes, in total.

Prior to beginning time-lapse imaging, a 'calibration image' was acquired for each spheroid. For a given spheroid, the motors were commanded to move to their corresponding control points. Then, one of the lateral (x/y) motors was adjusted such that the FOV was centered at a point 1-1.25 mm to the side of the spheroid. This resulted in the spheroid being removed from the FOV, such that only 'empty' collagen substrate remained. An image of this region was then acquired for use during OCT image reconstruction. (The use of this calibration image is detailed in Section 7.6.3.) This process (which was performed manually for each spheroid in the dish) required approximately 5-10 minutes, in total.

Once the above procedures were completed, time-lapse imaging was begun. Images of each spheroid in the dish were acquired at 40-minute time intervals for a total of 48 hours. (In between rounds of imaging, the laser shutter was closed to avoid optical heating of the sample.) For a given spheroid and time-point, nine volumetric images were acquired in rapid succession, similar to the 'burst protocol' used in our previous study (Chapter 6, Ref. [112]). The nine images consisted of 1 'full FOV' volume (spanning a lateral FOV of 1.25×1.25 mm^2 for larger co-culture spheroids, or 1×1 mm^2 for smaller mono-culture spheroids, using 1024×1024 lateral pixels) and 8 'reduced FOV' volumes (spanning a lateral FOV of 937.5×937.5 μm^2 for larger co-culture spheroids, or 750×750 μm^2 for smaller mono-culture spheroids, using 768×768 lateral pixels). Each such 'burst' of volumetric data generated approximately 24 GB of raw data (resulting in each time-series experiment generating approximately 1.75 TB of raw data per spheroid). Each burst required ~2 minutes to acquire. Imaging of 3 spheroids in a single dish (including sample repositioning between spheroids)

required approximately 8-10 minutes per time-point. This left approximately 30 minutes of 'down time' between each (40-minute interval) time-point for raw data to be transferred to a remote high-capacity server.

7.5.6   OCT image reconstruction (summary)

Volumetric OCT images were reconstructed from raw image data using a custom procedure similar to that described in our previous study (Chapter 6) [112]. In brief, this procedure was designed to minimize both spatial distortions within individual OCT volumes and relative spatial distortions between OCT images in a single time-series. The procedure consisted of 6 key components: (1) (depth-selective) OCT volume reconstruction, (2) coherence gate curvature removal, (3) phase registration, (4) focal plane curvature mitigation, (5) bulk demodulation, and (6) computational adaptive optics. (Evidence and discussions regarding the need/reasoning for these procedures may be found in our previous publication [112].) Since the implementation of these procedures has been modified since our previous study, flow charts and equations detailing these updated procedures have been provided in Section 7.6. All OCT image reconstruction and subsequent image processing was performed in MATLAB R2018a.

7.5.7   Drift correction

Despite the use of precision motors for sample positioning, small amounts of bulk drift (along x, y, and/or z) were present between time-points. Our OCT

image reconstruction procedures (Section 7.6) automatically corrected for drift along the *z*-axis. Drift along the lateral dimensions was measured and corrected separately after OCT image reconstruction.

In order to measure the lateral drift at each time-point, first, an average OCT image was computed via a 'mean projection' of the 8 reduced FOV images obtained for a given time-point. That is, denoting the $N = 8$ reduced FOV images by $S_i(x, y, z, t)$ for $i \in \{1, 2, \ldots, N\}$, the average OCT image $\bar{S}(x, y, z, t)$ was obtained via:

$$\bar{S}(x, y, z, t) = \frac{1}{N} \sum_{i=1}^{N} |S_i(x, y, z, t)| \tag{7.1}$$

For a given time-point, 4 sub-volumes were extracted from this average OCT image, corresponding to regions along each of the 4 sides of the lateral FOV. The lateral dimensions of these sub-volumes were selected to be as large as possible while still excluding the spheroid body and glass surface (which appeared at the center of the FOV) and thus only contained signals from the surrounding collagen substrate. (For a visual representation, these regions of interest are analogous to the four sides of the region depicted in Fig. 7.14.) The drift of each sub-volume with respect to the corresponding sub-volume of the previous time-point was computed to sub-pixel precision via 3D cross-correlation. The total lateral drift of a given time-point with respect to the previous time-point was taken to be the median value of the individual drift values reported across all 4 sub-volumes. Total drift with respect to the first time-point was then computed via cumulative summation from time $t = 0$ up to the given time-point. This lateral drift was removed from all OCT images which were used for subsequent processing.

7.5.8 Cell and collagen channel synthesis

Reconstructed OCT images were split into two synthetic 'channels' correspond-
ing to cells and collagen/background medium, respectively. To achieve this, the
8 reduced FOV images acquired for a given spheroid and time-point were com-
bined via a 'standard deviation projection'. That is, denoting the $N = 8$ reduced
FOV images by $S_i(x, y, z, t)$ for $i \in \{1, 2, \ldots, N\}$, the output image $S_\sigma(x, y, z, t)$ was
obtained via:

$$S_\sigma(x, y, z, t) = \sqrt{\frac{1}{N-1} \sum_{i=1}^{N} \left(|S_i(x, y, z, t)| - \bar{S}(x, y, z, t) \right)^2} \qquad (7.2)$$

where $\bar{S}(x, y, z, t)$ is defined as in Eqn. (7.1). Similar to our previously reported
method [112], this technique leverages temporal speckle contrast to distinguish
rapidly changing structures (primarily cells) from static background structures
(primarily collagen), resulting in a synthetic 'cell' channel. 'Cell' channel im-
ages were down-sampled by a factor of 768:400 via the MATLAB function
`imresize3` in order to perform smoothing and reduce computational load.
These images exhibited a depth-dependent additive 'background'. This depth-
dependent background profile was estimated by computing the median depth-
dependent intensity profile from a volumetric region along the periphery of the
lateral FOV of the 'cell' channel image (analogous to the previously described
region of interest used to perform lateral drift correction). This background pro-
file was then subtracted from the original image, yielding the completed 'cell'
channel image.

Preliminary binary images were generated from each (down-sampled) 'cell'
channel image by applying a $5 \times 5 \times 5$ voxel median filter followed by thresh-
olding via Otsu's method. Noise and non-cell structures in these preliminary
binary images were mitigated/removed via 4D region growing. Specifically, at

the first time-point, only the spheroid (the largest connected structure) was retained from the preliminary binary image. The resulting 'clean' binary image then served as the 'seed' image for the second time-point. The only structures retained from the preliminary binary image of the second time-point were those which exhibited partial or complete spatial overlap with the structure present in the seed image. This resulted in a clean binary image for the second time-point, which then served as a seed image for the third time-point, and so on. (Note that this algorithm is vulnerable to 'losing' cells which break away from the spheroid body and migrate away fast enough as to exhibit no spatial overlap with cells in the image of the previous time-point. However, we did not observe substantial instances of this phenomenon with our 40-minute imaging interval. Decreasing this interval could be used to mitigate this problem in the future.)

In order to generate the 'collagen' channel, first, $\bar{S}(x, y, z, t)$ was computed from the 8 reduced FOV images for each time-point. Similar to the 'cell' channel images, these volumes were down-sampled by a factor of 768:400. The values of any voxels corresponding to 'cells' (as determined by the cleaned binary images described above) were set to 0, yielding the complete 'collagen' channel image.

7.5.9   Collagen displacement tracking

Collagen deformations were measured across the first 24 hours of images using elastic image registration via the built-in MATLAB function `imregdemons` (which uses Thirion's 'Demons Algorithm', an iterative, large-deformation extension to optical flow techniques) [125, 178]. Specifically, this function was used to compute the 3D displacement field required to register the 'collagen'

channel image of the first time-point to the 'collagen' channel image of any given time-point acquired during the first 24 hours of imaging. Displacements were not computed for later time-points beyond the 24 hour mark because the progression of invasive protrusions (and associated collagen digestion/degradation and deformation) became substantial, and so the assumptions underlying the Demons Algorithm (and most other standard elastic image registration algorithms) break down [125]. As detailed in Section 7.3, further work with more advanced image registration algorithms will be required to enable reliable quantitative reconstruction of cell traction forces. However, the methods used here have been assumed to be sufficiently accurate to demonstrate the value of our imaging methods/capabilities for TF-OCM and mechanobiology research.

For a given time-point, the resulting output displacement field $\mathbf{u}$ was given in Cartesian coordinates: $\mathbf{u}(\mathbf{r}) = \langle u_x(x, y, z), u_y(x, y, z), u_z(x, y, z) \rangle$. Radial components of the measured displacement field were computed from these data via the relation:

$$u_r(\mathbf{r}; \mathbf{r}_0) = \mathbf{u}(\mathbf{r}) \cdot \frac{\mathbf{r} - \mathbf{r}_0}{|\mathbf{r} - \mathbf{r}_0|} \tag{7.3}$$

where $\mathbf{r}_0 = \langle x_0, y_0, z_0 \rangle$ is defined as the center of the spheroid body at time $t = 0$. z_0 was determined by the depth (z) for which the initial spheroid body displayed the greatest lateral area (i.e., $z_0 = \arg\max A_{sph}(z)$). x_0 and y_0 were obtained from the lateral center of mass of the spheroid body.

The line plots in Figs. 7.5(b,c) and 7.6(a) depict the median radial displacement of collagen fibers across a fixed set of positions (the gray surface in Fig. 7.5(a)). This surface was located $150\,\mu$m from the surface of the initial spheroid body (at time $t = 0$) and spanned $\pm 15°$ with respect to the spheroid

'equator'. More precisely, assume the initial spheroid body is approximately spherical with center $\mathbf{r}_0$ and radius R_0 (computed as $R_0 = \sqrt{A_{sph}(z_0)/\pi}$). The median radial displacement was then obtained via:

$$\hat{u}_{r,\Omega} = \text{median}\left[\{u_r(\mathbf{r};\mathbf{r}_0) : \mathbf{r} \in \Omega\}\right] \qquad (7.4)$$

where

$$\Omega = \left\{ \mathbf{r} : |\mathbf{r} - \mathbf{r}_0| = R_0 + 150\,\mu\text{m} \wedge \frac{|(\mathbf{r} - \mathbf{r}_0) \cdot \langle x - x_0, y - y_0, 0 \rangle|}{(|(\mathbf{r} - \mathbf{r}_0)|)\,(|\langle x - x_0, y - y_0, 0 \rangle|)} \geq \cos(15°) \right\} \quad (7.5)$$

7.6 OCT image reconstruction procedure

In this section, we provide detailed flow charts and equations for the OCT image reconstruction procedure that we developed and used in this study. Note that more detailed explanations/justifications underlying many of the operations below may be found in Ref. [112] and/or Chapters 3 and 4.

7.6.1 Depth-selective OCT volume reconstruction

OCT images were reconstructed from spectral data by applying the standard operations of background subtraction, spectrum resampling, dispersion compensation, and the Fourier transform. In order to enable the reconstruction of small/specific depth ranges (as opposed to the full depth range of the available axial FOV), a matrix multiplication-based method analogous to previously reported algorithms [27, 97, 140] was employed. Specifically, for a (post-background subtraction) A-scan of spectral data $v(k_b, x, y)$ for $b \in \{1, 2, \ldots, 2048\}$, the OCT image signal $s(z_a, x, y)$ at a given integer depth index a was computed

via:

$$s(z_a, x, y) = \sum_{b=1}^{2048} v(k_b, x, y) \exp\left(-j\left(2k_b z_a + \alpha_2 \left(k_b - \bar{k}\right)^2 + \alpha_3 \left(k_b - \bar{k}\right)^3\right)\right) \quad \text{(7.6a)}$$

$$= \sum_{b=1}^{2048} \Theta_{ab} v(k_b, x, y) \quad \text{(7.6b)}$$

where a is constrained to the set of integers $a \in \{1, 2, \ldots, 2048\}$, $j = \sqrt{-1}$, k_b denotes the wavenumber of the bth spectrometer pixel (determined by manufacturer generated data sheets), $\bar{k} = 0.5(k_1 + k_{2048})$, $z_a = \Delta z(a - 1025)$ for $\Delta z = (2047/2048)(\pi/|k_{2048} - k_1|)$, and (α_2, α_3) denote (manually calibrated) dispersion compensation parameters. Note that Δz corresponds to the height of each voxel in terms of optical path length (OPL). The physical height of a given voxel is $\Delta z/n$, where n is the local refractive index of the imaged medium (taken to be $n = 1.34$ within the collagen medium).

There were two regions of interest within the imaged volumes. The first is a narrow range of depths $z_a \in Z_{\text{coverslip}}$ which contain the coverslip surface (i.e., the base of the glass-bottomed sample dish) across all time-points. The second is a larger range of depths $z_a \in Z_{\text{spheroid}}$ which contain the spheroid and surrounding regions across all time-points. Examples of these regions are depicted in Fig. 7.8.

7.6.2 Coherence gate curvature removal and phase registration

As detailed in Chapter 4 and Appendices H and I, coherence gate curvature (CGC) is a consequence of non-idealities in imaging system design/implementation and/or sample positioning which distort OCT images. A flat surface may appear to be tilted and/or curved in OCT images acquired by a system corrupted by CGC. Unlike our previously described methods (Chapter 6
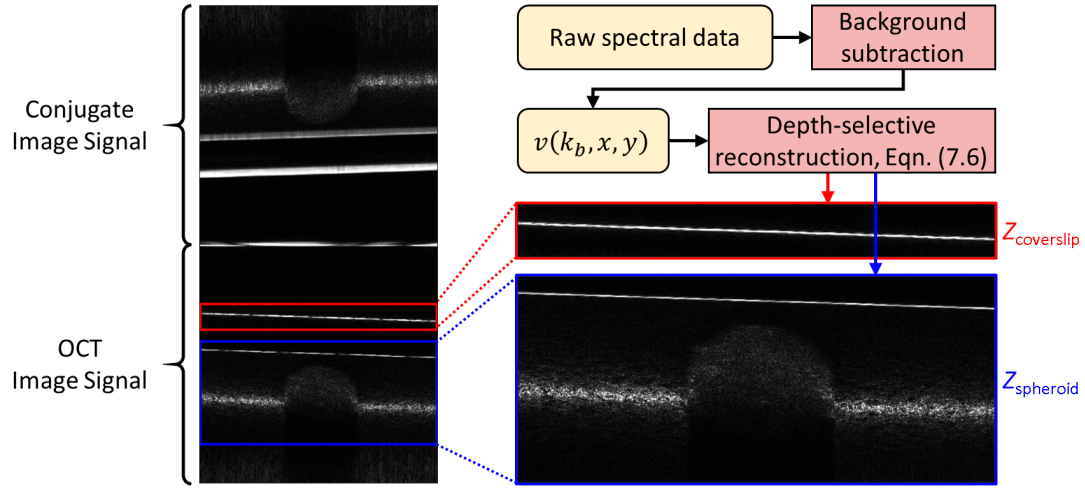
Figure 7.8: Depth-selective OCT image reconstruction and regions of interest. See text for details.

and Ref. [112]), which used a single computational procedure for mitigating CGC, here we employed a three-pronged hybrid approach to obtain more robust results. The majority of CGC was removed via the cylindrical lens incorporated into our updated imaging system (discussed in Section 7.5.4 and Appendix I). Residual CGC was removed computationally in two steps, hereafter called coarse and fine CGC removal. The latter step simultaneously performs phase registration (another key operation for OCT image reconstruction). CGC calibration and removal were performed independently for each image and time-point (except where otherwise noted).

Calibration

The first step is a calibration stage (depicted in Fig. 7.9), which performs calibrations for both coarse and fine CGC removal (and phase registration). An OCT image of the $Z_{coverslip}$ region is reconstructed according to Eqn. (7.6a). The
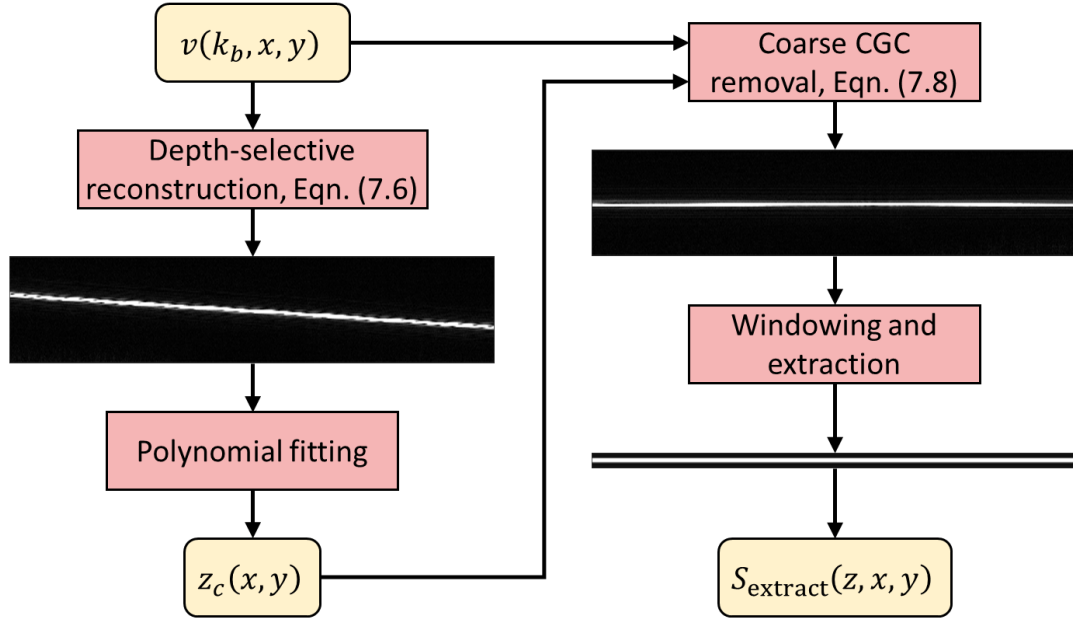
Figure 7.9: Calibration procedure for both 'coarse' (left column) and 'fine' (right column) coherence gate curvature removal (and phase registration). See text for details.

laterally varying axial position of the coverslip surface (in units of single-pass OPL) is then approximated by the function:

$$z_c(x, y) = c_{xx}x^2 + c_{xy}xy + c_{yy}y^2 + c_x x + c_y y + c_0 \tag{7.7}$$

This completes the calibration stage for coarse CGC removal. Next, the $Z_{\text{coverslip}}$ region is reconstructed *again* while applying coarse CGC removal via:

$$\hat{S}(z_a, x, y) = \sum_{b=1}^{2048} \Theta_{ab} v(k_b, x, y) \exp\left(-j2k_b \left(z_c(x, y) - z_0\right)\right) \tag{7.8}$$

where z_0 is defined as the value c_0 obtained for the *first* time-point in the time-lapse data set. In the resulting 3D image, the coverslip will appear *nearly* flat and level, and will be centered at the OPL position $z = z_0$. Note that by using the same value of z_0 for all time-points, all reconstructed images in a given time-series will be automatically registered/aligned along the z-axis. The coarsely-corrected image is next cropped along the z-axis such that only ~11–21 voxels

remain along the z-axis centered around the position $z = z_0$. This cropped volume will be referred to as $S_{\text{extract}}(z, x, y)$. This completes the calibration stage for fine CGC removal and phase registration.

Execution

The cropped volume $S_{\text{extract}}(z, x, y)$ is used to perform both fine CGC removal and phase registration. Note that although this volume was extracted from the $Z_{\text{coverslip}}$ region of the sample, it may be used for the reconstruction of *any* sub-region from the full OCT data set (e.g., the Z_{spheroid} region). In order to perform fine CGC removal and phase registration to a volume $P(z, x, y)$, $S_{\text{extract}}(z, x, y)$ is first zero-padded along the z-axis until it is of the same size as $P(z, x, y)$. Then, the following operation is performed:

$$P_r(z, x, y) = \mathcal{F}^{-1}_{z \to q_z} \left[\mathcal{F}_{z \to q_z} \left[P(z, x, y) \right] \exp \left(-j \arg \left(\mathcal{F}_{z \to q_z} \left[S_{\text{extract}}(z, x, y) \right] \right) \right) \right] \qquad (7.9)$$

where $\mathcal{F}_{z \to q_z}$ and $\mathcal{F}^{-1}_{z \to q_z}$ denote the forward and inverse Fourier transform along the z-axis, respectively, and $P_r(z, x, y)$ denotes the output volume (which lacks CGC and is phase-registered). This procedure is depicted in Fig. 7.10.

7.6.3 Focal plane curvature removal

Focal plane curvature (FPC) is another consequence of non-optimal system design and/or sample positioning. This results in the focal 'plane' appearing tilted and/or curved, even after CGC removal has been performed (i.e., the curvature of the focal plane does not necessarily match that of the 'coherence gate'). This results in OCT images which exhibit a laterally-varying point spread function
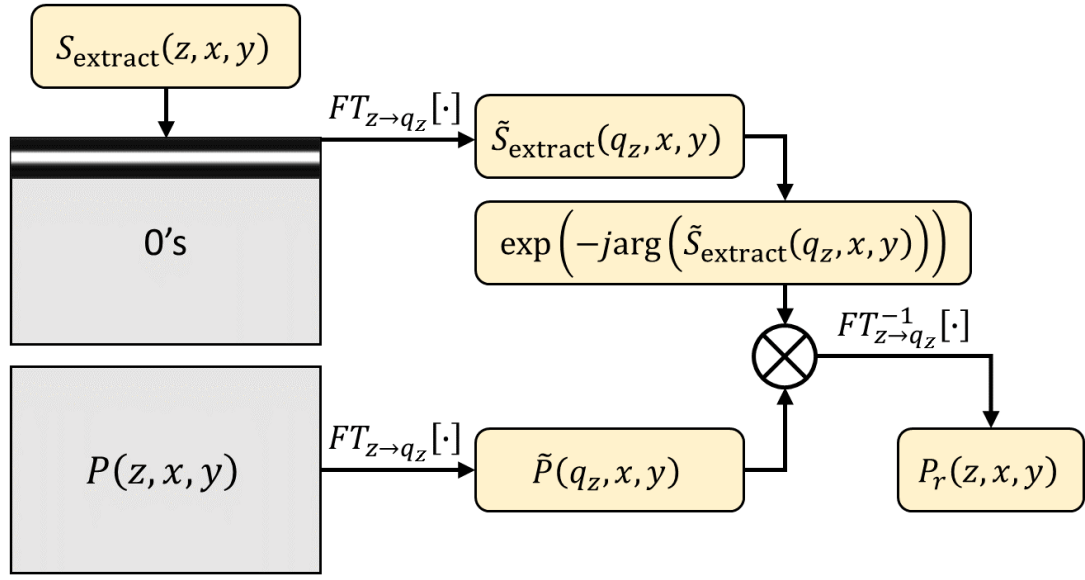
Figure 7.10: Fine coherence gate curvature removal and phase registration. See text for details.

(PSF), which conventional refocusing algorithms (such as the computational adaptive optics (CAO) procedure used in this study) do not accommodate, due to the assumption of a laterally-invariant PSF. Alternative formulations of CAO which account for lateral variation do exist [84, 83]. However, such procedures can be computationally expensive and complicated to calibrate and perform. In our previous study [112], we demonstrated an alternative procedure for FPC mitigation which enables the use of computationally efficient CAO algorithms that leverage lateral invariance assumptions.

Calibration

Unlike our previous study (which measured/calibrated FPC from images of the sample directly), here we used a separate calibration data set (which is described in the Section 7.5.5). This calibration data set was used to obtain a mea-
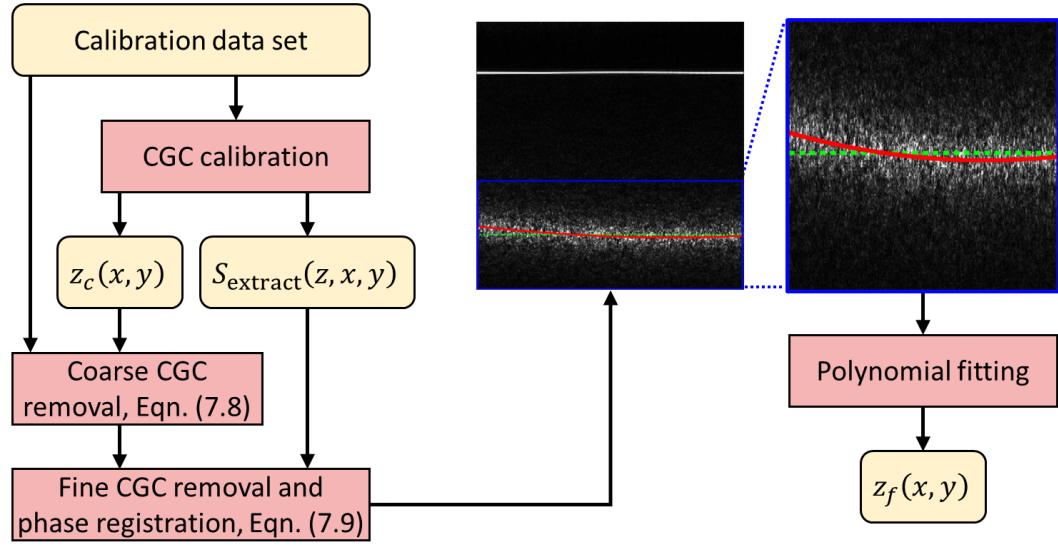
Figure 7.11: Calibration procedure for focal plane curvature removal. Note that the focal plane appears curved even though the coverslip surface appears flat and level. See text for details.

surement of FPC, which was subsequently applied to all images in the corresponding time-series. The reason for this change in procedure is a consequence of the new experimental settings encountered in this study. In our previous study, we imaged isolated cells which occupied a miniscule fraction of the total volumetric FOV. Therefore, FPC was readily measured from images of the sample. However, the spheroids imaged in this study occupied a large fraction of the volumetric FOV, and substantially obstructed the focal plane across much of the FOV. This prevented automated measurements of FPC using only images of the spheroid(s). The calibration data sets used in this study contained no spheroid (but were instead acquired *near* the corresponding spheroid). This provided a clear and unobstructed view of the geometry of the focal plane across the entire FOV. The FPC measured from this data set was assumed to be a suitable proxy for the otherwise infeasible FPC calibration of the spheroid images.

FPC calibration was performed as depicted in Fig. 7.11. First, CGC calibra-

tion is performed on the calibration data set. Then, the 'focal plane region' of the sample (which is analogous to the Z_{spheroid} region, but with no spheroid present, given the nature of the calibration data set) is reconstructed while applying coarse CGC removal, fine CGC removal, and phase registration. The laterally varying position of the focal 'plane' (in units of single-pass OPL) is approximated via:

$$z_f(x, y) = f_{xx}x^2 + f_{xy}xy + f_{yy}y^2 + f_x x + f_y y + f_0 \tag{7.10}$$

This completes the calibration stage for FPC removal.

Execution

In order to apply FPC removal (as depicted in Fig. 7.12), the Z_{spheroid} region of the spheroid image is first reconstructed via:

$$\hat{S}(z_a, x, y) = \sum_{b=1}^{2048} \Theta_{ab} v(k_b, x, y) \exp\left(-j2k_b\left(z_c(x, y) - z_0\right)\right) \exp\left(-j2k_b\left(z_f(x, y) - \bar{z}_f\right)\right) \tag{7.11}$$

where $\bar{z}_f$ is defined as the mean value of $z_f(x, y)$ across the lateral FOV. Note that this formula is nearly identical to that for coarse CGC removal (Eqn. (7.8)), with an extra phase term added for performing FPC removal as well. Following this reconstruction, fine CGC removal and phase registration are performed via Eqn. (7.9) to obtain a phase registered image in which the focal plane appears flat and level (although the coverslip surface appears curved, due to the mismatch between CGC and FPC). This volume, which we will call $S_r(z, x, y)$, is compatible with digital refocusing procedures which assume a laterally invariant PSF.
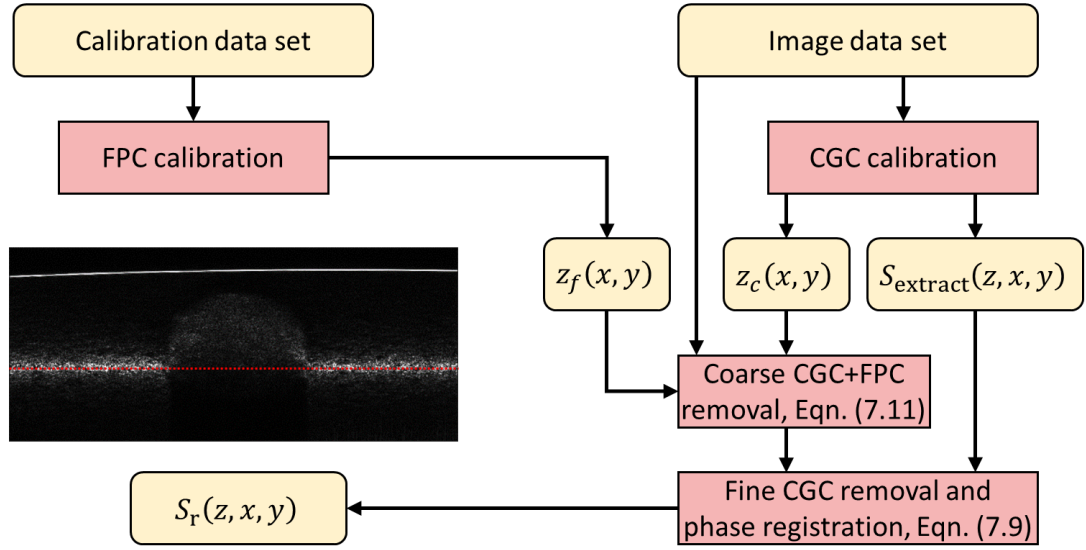
Figure 7.12: Procedure for joint application of coarse CGC removal, fine CGC removal, phase registration, and FPC removal. Note that this results in an image where the focal plane is flat and level, but the coverslip surface is not. See text for details.

7.6.4 Bulk demodulation

Optical misalignments and/or sample tilt can result in the OCT image signal undergoing a bulk phase modulation across the lateral dimensions. Failing to account for this modulation can result in depth-dependent shearing artifacts which emerge after applying CAO (see Chapter 4.4).

Calibration

Calibration/measurement of the bulk modulation in the system was performed as depicted in Fig. 7.13. First the 'full FOV image' (defined in the Section 7.5.5) from the first time-point in a given time-series is reconstructed using the CGC and FPC removal procedures detailed previously. Next, any depths containing a glass surface are windowed out from the volume or set to 0 (since the

signal from such reflective surfaces can overwhelm/corrupt the calibration procedure). The remaining volume then undergoes the following operation:

$$M(q_x, q_y) = \int \left| \mathcal{F}_{(x,y,z)\to(q_x,q_y,q_z)}\left[S_r(z, x, y)\right] \right| dq_z \tag{7.12}$$

where $\mathcal{F}_{(x,y,z)\to(q_x,q_y,q_z)}$ denotes the 3D Fourier transform operation. The resulting real-valued function $M(q_x, q_y)$, which is displayed in the upper-right panel of Fig. 7.13, approximates the lateral spatial frequency content of the image signal. Given the use of Gaussian beams in our system, $M(q_x, q_y)$ has an approximately Gaussian profile and is off-centered with respect to the origin ($q_x = 0, q_y = 0$) due to the bulk phase modulation of the image signal (which we wish to measure and remove). Performing peak-finding along the q_x- and q_y- axes results in a measurement of the bulk modulation coefficients: ($q_{x,0}, q_{y,0}$).

Execution

Once this calibration was performed, all volumes in the time-lapse data set were demodulated according to:

$$S_d(z, x, y) = S_r(z, x, y) \exp\left(-j\left(q_{x,0}x + q_{y,0}y\right)\right) \tag{7.13}$$

In doing so, it was assumed that the bulk modulation was constant across the entire time-lapse data set.

7.6.5 Computational adaptive optics

Computational adaptive optics (CAO) [3] was used to compensate for depth-dependent degradation of the lateral resolution of the OCT system. Here, we assumed that this degradation was due entirely to defocus (and not higher-order

242
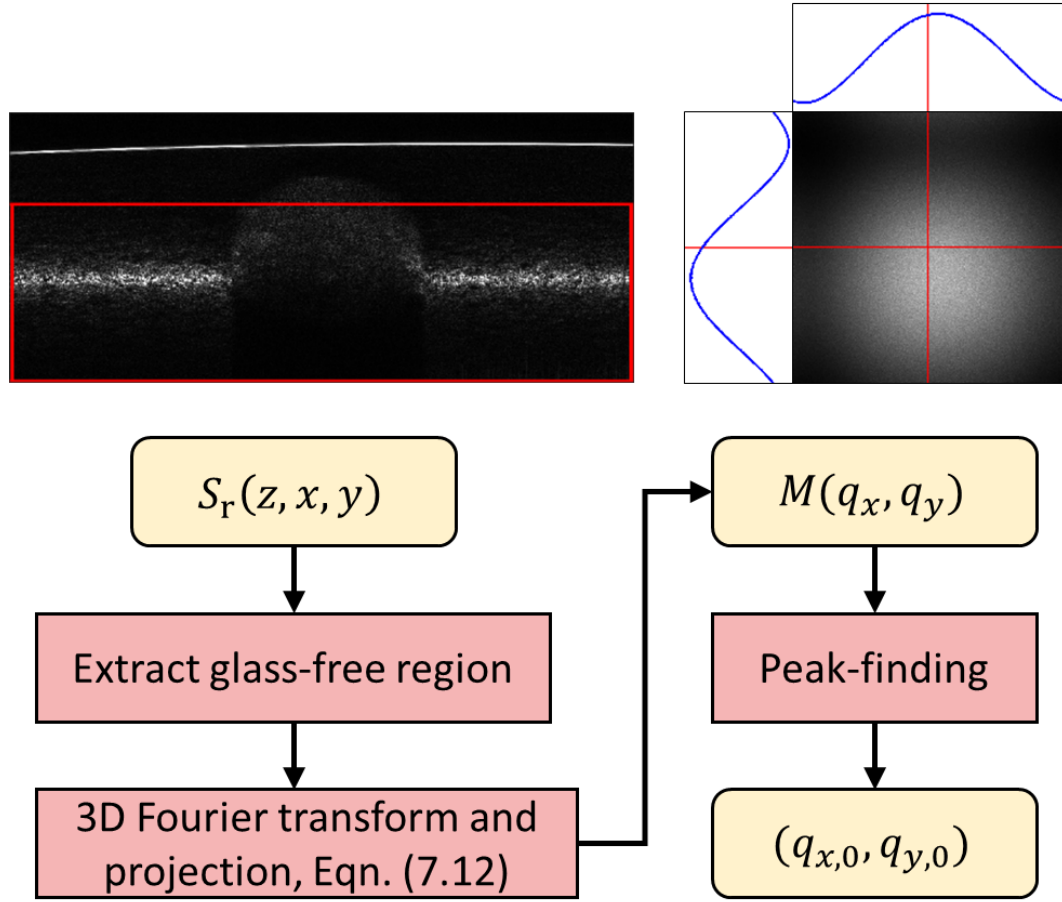
Figure 7.13: Calibration procedure for bulk demodulation. See text for details. The red boxed region in the upper-left panel shows the region that is used to perform the calibration (note that it excludes the glass surface which appears near the top of the image). $M(q_x, q_y)$ (defined in the text) is shown in the upper-right panel. The intersection of the two red lines denotes the origin of the lateral spatial frequency domain.

optical aberrations). In order to perform CAO, first the depth of the focal plane must be calibrated.

Calibration

For a given time-point, the 'full FOV' image was reconstructed using the procedures described above (CGC removal, FPC removal, phase registration, and
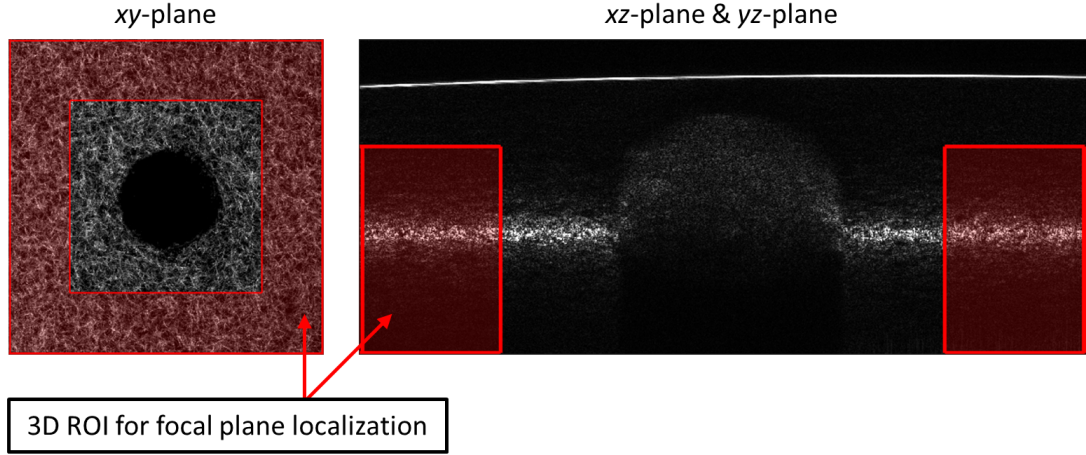
Figure 7.14: 3D region of interest for axial localization of the focal plane. The image shown in the right-hand panel intersects the origin of the lateral FOV. See text for details.

bulk demodulation). Next the average axial intensity profile was computed from the 3D region of interest depicted in Fig. 7.14. (Note that this region excludes both the spheroid body as well as any glass surfaces which appear in the image.) Curve-fitting was performed in order to find the peak of this axial intensity profile and thus obtain the depth z_{focus} of the focal plane (in terms of physical distance). This z_{focus} position was used for performing CAO across all images of the spheroid acquired for the given time-point.

Execution

Next, CAO/defocus-compensation was performed via:

$$S_f(z, x, y) = \mathcal{F}^{-1}_{(x,y) \rightarrow (q_x, q_y)} \left[\mathcal{F}_{(x,y) \rightarrow (q_x, q_y)} \left[S_d(z, x, y) \right] \exp \left(-j(z - z_{\text{focus}}) \sqrt{\left(2n\bar{k}\right)^2 - q_x^2 - q_y^2} \right) \right]$$

(7.14)

where $\mathcal{F}_{(x,y) \rightarrow (q_x, q_y)}$ and $\mathcal{F}^{-1}_{(x,y) \rightarrow (q_x, q_y)}$ denote the forward and inverse 2D Fourier transform across the lateral dimensions, respectively, n denotes the refractive
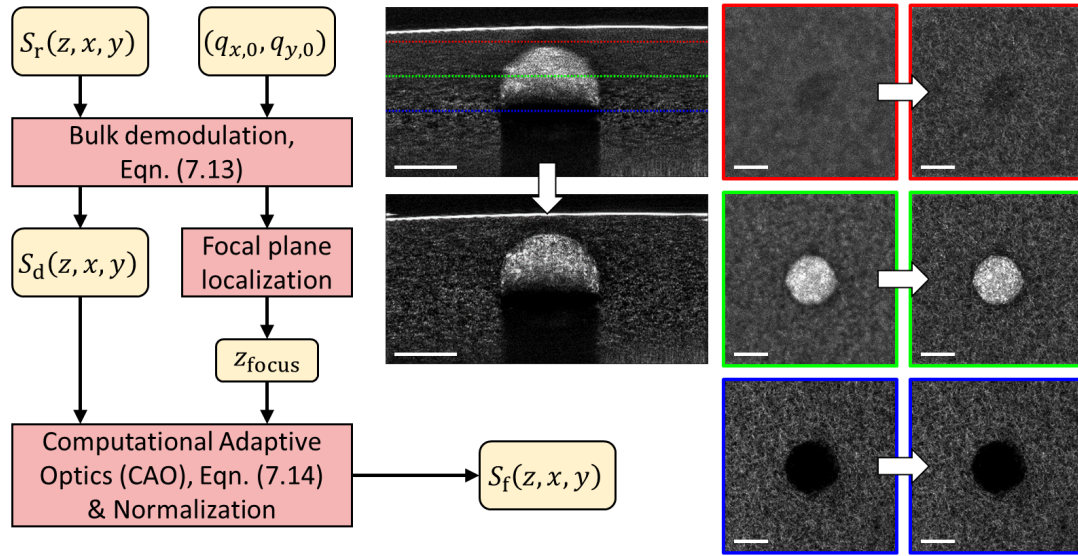
Figure 7.15: Procedure for defocus compensation with computational adaptive optics. See text for details. Panels at the right depict *en face* planes before and after CAO at the depths indicated by the three colored lines spanning the top-middle panel. Red/top: 225 μm above the focal plane. Green/middle: 112.5 μm above the focal plane. Blue/bottom: Focal plane. Scale bars = 200 μm.

index of the sample (here, $n = 1.34$ was used), and $\bar{k}$ is defined as before (and corresponds to the central wavenumber measured by the spectrometer of the imaging system). Following this operation, the magnitude of the (complex-valued) image signal was normalized with respect to depth z. (Note that the normalized image remains complex-valued!) The results of this procedure are depicted in Fig. 7.15.

7.6.6 Focal plane curvature restoration

In this study, we applied the same 'ideal coordinate system' heuristic established in our previous study [112] (and defined in Chapter 4.4). That is, the ideal/final coordinate system for our reconstructed OCT images was assumed/defined as the one in which the coverslip surface appears both flat and
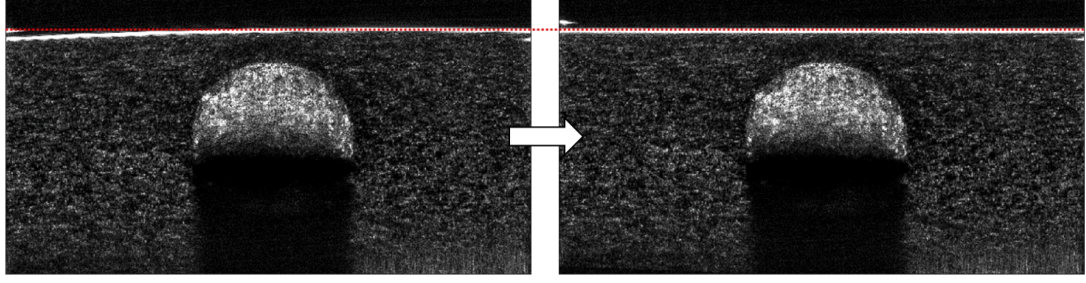
Figure 7.16: Focal plane curvature restoration. The CAO-processed image (left) is transformed to a final output image (right) wherein the coverslip surface appears both flat and level. See text for details.

level. However, CAO could only be performed while the *focal plane* was flat and level. Therefore, the final step in OCT image reconstruction is to restore the focal plane curvature to its original curved state, which returns the coverslip surface to its 'ideal' flat and level state.

For a reconstructed OCT volume with $N \leq 2048$ pixels along the axial dimension (recall that our spectrometer camera had 2048 pixels), a frequency-axis vector $\mathbf{q}_z \in \mathbb{R}^{N \times 1}$ is defined such that:

$$q_{z,i} = \frac{2\pi}{\Delta z}\left(\frac{i-1}{N}\right), \text{ for } i \in \{1, 2, \ldots, N\} \tag{7.15}$$

where Δz is defined as before. Then, FPC restoration is performed via:

$$\mathcal{F}^{-1}_{z \to q_z}\left[\mathcal{F}_{z \to q_z}\left[S_f(z, x, y)\right] \exp\left(-j q_z \left(z_f(x, y) - \bar{z}_f\right)\right)\right] \tag{7.16}$$

The final reconstructed image that results from this procedure is depicted in Fig. 7.16. Note that this volumetric image signal is a complex-valued function. All subsequent image processing (detailed in Section 7.5), were performed on the *magnitude* of this image signal.

CHAPTER 8

CONCLUSION

8.1   Scientific contributions

The scientific contributions of this dissertation and its associated research program are two-fold. First, Chapters 2-4 have provided a strong educational foundation which can help new researchers to understand and (hopefully) continue the work outlined in the remainder of this dissertation. Second, Chapters 5-7 have presented key methods and findings which enabled the development of TF-OCM as a new experimental technique to study the dynamic mechanical behavior of cells and multicellular collectives within scattering media.

TF-OCM was demonstrated to enable the quantitative reconstruction of dynamic 3D cell forces exerted by isolated cells within a 3D hydrogel medium [110, 112]. This was enabled by the development of image formation routines which mitigate numerous system non-idealities, and have since proven useful to other research pursuits in the OCT/OCM field [95, 189]. Finally, these TF-OCM imaging methods were adapted to enable the study of multicellular invasion within scattering collagen substrates over multi-day time-lapse experiments. These experiments would not have been feasible without TF-OCM. The resulting image data (although not suitable for quantitative cell traction force reconstruction due to the limitations of image processing methods and available mechanical characterization/modeling capabilities) provided valuable insights and key findings in a collaborative study led by mechanobiology researchers investigating the role of obesity in breast cancer metastasis [94].

These achievements demonstrate the utility of the TF-OCM methods developed here to enable and promote research into the dynamic, 3D, and collective behavior of cells within optically scattering media. Moreover, the capabilities provided by TF-OCM have been shown to offer an unprecedented range of spatiotemporal imaging capabilities compared to current standard imaging methods in TFM (i.e., confocal microscopy). With a millimeter-scale volumetric FOV, micrometer-scale resolution, second-to-minute-scale volume acquisition rates, compatibility with long-term time-lapse experiments, label-free contrast suitable for possible future *in vivo* applications, and deep imaging penetration depths up to the millimeter-scale in optically scattering bio-polymers, TF-OCM provides a truly unparalleled capacity to adapt and thrive in the demanding settings of modern research into the biophysical interactions of cells with their surrounding environments. Since no other TFM imaging platforms have been demonstrated to provide such capabilities to date, these methods currently hold a unique position for contributing to the field of mechanobiology. These contributions could be substantial, especially if TF-OCM finds widespread adoption across the OCT research community, which has close ties to both fundamental science and clinical research settings.

8.2   Future work

Many possibilities remain to further adapt and improve the methods outlined in this dissertation.

8.2.1 OCT image formation

The methods that were developed here for the mitigation of imaging system non-idealities (Chapter 4.4) were based on simplified models and heuristics which enable the use of simple, efficient, and consistent algorithms. More advanced models and algorithms may further enhance the quality of reconstructed images. One question which remains unanswered is whether various system non-idealities (such as CGC, FPC, and bulk modulation) can be coupled together with a single model. A model that connects these phenomena could be used to address the inherent ambiguity that is present in current mitigation procedures. For example, it is currently difficult to distinguish true sample tilt from tilt which emerges due to coherence gate curvature. However, perhaps bulk demodulation or other features could be used to infer the relative contributions of true tilt and CGC to the total apparent tilt of an imaged sample. Likewise, perhaps knowledge of true sample tilt and measured CGC could be used to predict the shape of FPC, and thus eliminate the need for the extra 'calibration images' that were required for the spheroid imaging experiments in Chapter 7.

8.2.2 Image segmentation

Temporal speckle contrast has proved to be immensely useful for enabling speckle reduction and image segmentation within both clear and highly scattering media. As a result, otherwise label-free OCT images reveal detailed structures that would not be readily visible with typical 'monochrome' OCT imaging. Of course, work remains to be done to further validate and characterize the ability of temporal speckle contrast to capture fine cellular features

against a background of scattering media. Co-registered confocal fluorescence imaging would be a useful feature to incorporate into an OCT/OCM imaging system, especially since so much of biological research relies upon fluorescent labeling. The fluorescence microscope could provide critical labeling information at sparse moments in time, while the OCT system provides rapid volumetric imaging for time-resolved observation of dynamic cell behavior. Of course, generating temporal speckle contrast is extremely costly in terms of data load, and so any methods that might be used to reduce the amount of data required to generate sufficient contrast would be extremely valuable to both rapid and long-term imaging experiments.

On the other end of the spectrum, if a large data load is acceptable, temporal speckle contrast may be used to generate a more detailed picture of biological activity on cellular and sub-cellular scales [114, 191]. Perhaps differences in the *spectral profile* of temporal speckle contrast (i.e., across a wide range of *rates* of speckle evolution) could be used to distinguish different cell types, or identify the response of cells to stimuli. In this manner, novel information may be accessed without ever needing to resort to fluorescent labels. Although this may be a somewhat fanciful notion for many *in vitro* applications where labels are already ubiquitous, *in vivo* or clinical applications may make deeper investigations into temporal speckle contrast a valuable endeavor.

8.2.3   Image processing

As discussed in Chapter 7, current standard image registration routines are ill-suited to the tracking of collagen deformations in the near vicinity of invasive

cellular protrusions. Collagen degradation and cell migration create jump discontinuities and non-invertible transformations which standard algorithms are not designed to accommodate. Algorithms which enable the independent tracking of cell motion and collagen motion (without blurring the displacement field across their mutual boundary) would likely be helpful in resolving this problem. If all else fails, scattering fiducial marker beads may be incorporated. Scattering beads typically exhibit strong signals that are easy to track. However, these beads may alter cell behavior and may not be able to 'sample' the collagen displacement field as densely as 'direct' tracking methods.

8.2.4   Quantitative force reconstruction

As detailed in Appendix L, numerous tests are required to validate even simple TFM experiments involving isolated cells in mechanically linear media. Future experiments with quantitative TF-OCM will likely require equivalent or similar validation experiments in the future, as well as investigations of sources of noise and other errors.

One interesting experiment to perform would be to acquire two distinct 'reference' states in a TFM experiment. The first would be a 'natural' reference state (as in the time $t = 0$ images of the experiments in Chapter 7, which recorded a collagen substrate in an undeformed and unstressed state immediately after spheroid embedding). The second would be a 'synthetic' reference state (as in the final time-point of the experiments in Chapter 6, which recorded a Matrigel substrate after cells were exposed to a contractility inhibiting reagent). Discrepancies between the 'natural' and 'synthetic' reference states would pro-

vide a potential means to quantify plastic deformations due to residual stresses and/or remodeling of the substrate medium. I am not currently aware of any TFM methods which do this.

Quantitative force reconstructions in viscoelastic and/or nonlinear media will require a combination of high-quality displacement tracking, mechanical characterization, and numerical solving routines. Since attaining these capabilities requires diverse teams, and potentially *a lot* of time and funding, TFM/TF-OCM researchers may need to step back and evaluate how their methods can have the greatest research impact, if not the greatest accuracy. As in Chapter 7/Ref. [94], if quantitative forces are not explicitly required to test a given hypothesis, then seeking other forms of data may be of greater benefit to advancing research. Displacement/deformation/strain data may prove equally valuable for quantifying the mechanical behavior of biological systems [162]. In fact, if we think forward to clinical settings, deformation data may be the most viable/valuable option, assuming wide-scale mechanical characterization and modeling of tissues will remain difficult for at least the next decade or so. Even if micro-scale deformations at the cell level prove infeasible to measure in patients, large-scale deformations during tumor development/suppression, wound healing, etc. may provide valuable insights into biological processes, even if quantitative force reconstructions are never achieved in these settings.

8.2.5   An OCT/OCM-based platform for mechanobiology

Finally, as has been stated numerous times elsewhere in this dissertation, optical coherence elastography (OCE) [113] provides a potential means to quan-

tify spatially and temporally heterogeneous mechanical properties in biological media. OCE is much like TF-OCM. Whereas TF-OCM uses mechanical characterizations and substrate displacement data to infer cellular forces, OCE uses artifically applied forces and measurements of substrate displacement data to infer mechanical properties. This presents a natural potential synergy between the two techniques (OCE for mechanical characterization and TF-OCM for the analysis of cell forces and behavior, while sharing microscope hardware). A platform which unites these two techniques could provide valuable label-free imaging capabilities for probing tissue and cell mechanics in both laboratory and clinical settings. This has begun to appear all the more feasible with the emergence of OCE methods with strongly localized probing capabilities [87].

8.3 So many questions, so little time

I would hate to end this dissertation simply trailing off into silence while I muse about the possible future of my research field. However, I do not have much choice, do I? If you have already read through most of this work (you poor soul), then you already know I have said enough to merit an end to my writing (and release you too from my prison)! If you have simply found your way here *without* reading substantial portions of the rest of this dissertation, then I must question your motives! Are you trying to get ideas from me without doing the derivations that I asked you to learn?! No matter. If you are managing to move science forward, then I will leave you to your methods! I hope that I have been of help to you along your journey.

So with that, I will say...thank you for reading!

Take care,

Jeffrey
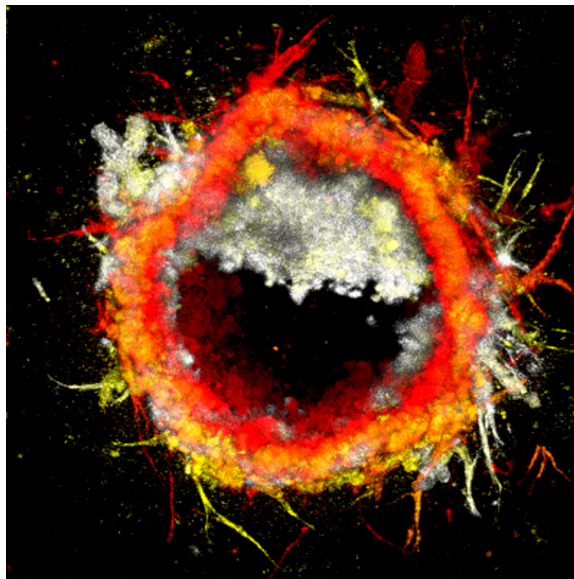
APPENDIX A

SELF-INTERFERENCE ARTIFACTS

If the sample contains a strongly reflective interface (e.g., a glass-air interface), that interface can act as a 'local reference mirror', meaning that the sample arm effectively contains a secondary *common-path* interferometer nested within the primary *double-path* interferometer of the OCT microscope. The image artifacts resulting from such a scenario can closely resemble the 'true' OCT image, but will be shifted along z, since the common-path interferometer is performing a TOF measurement with respect to the strongly reflective interface, which is likely to be located at a different OPL than the reference arm mirror. This image is typically weaker than the desired OCT image generated by the primary interferometer, but can still significantly corrupt the desired image signal.

A.1 A common mistake

On several occasions, I have observed researchers in the lab making a common mistake related to self-interference artifacts. I will narrate the scenario with the (understandably) confused perspective of the researcher.

Often, a researcher is imaging a sample with a glass-air interface at the surface. They adjust the axial position of the sample, and suddenly, their OCT image appears. That is well and good. *However*, something is wrong. The image signal appears weaker than they would expect. It also behaves strangely. The glass-air interface appears 'stuck' at the 'top' (i.e., $z = 0$) position of the OCT image. That is, when they *physically* move the sample up and down along

z, the reconstructed *image* of the sample does not move at all. Interestingly, the focal plane *can* be seen moving up and down within the static image. Similarly, adjusting the axial position of the reference arm mirror (which would likewise be expected to result in the reconstructed image moving up and down) results in no change. In fact, blocking the light of the reference arm (e.g., with an index card) does *not* cause the reconstructed image to vanish. As we learned in Chapter 3, however, the reference arm is a *necessary* contributor to the OCT signal. How can an image exist without the reference arm?!

Well, the answer is that:

1. The glass-air interface at the surface of the sample is acting as a 'local reference mirror'. Since the surface is so clean and well-behaved, the self-interference artifacts that result look just like a regular OCT image. We will call this phenomenon a 'self-interference image'.

2. The (self-interference) image signal is weak because the 'local reference mirror' is a poorer reflector than the 'real' reference mirror, and so the strength of the interference patterns that encode the self-interference image are weaker than those that encode a typical OCT image.

3. Since $z = 0$ is defined as the position at which the sample arm OPL matches the OPL of the 'reference surface' (be it the reference arm mirror or the 'local reference mirror'), the glass-air interface is automatically mapped to the $z = 0$ position in the self-interference image.

4. Since moving the sample up and down *also* moves the glass-air interface, the OCT image remains stationary, since the *difference* in OPL between the 'local reference mirror' and other parts of the sample never changes.

5. However, since the sample is still moving (along depth) with respect to the fixed focal plane of the imaging beam, the focal plane is observed to move up and down within the static self-interference image.

6. No change is observed when the 'real' reference mirror is moved because 1) the reference arm plays no part in the generation of a self-interference image and 2) the reference arm is misaligned. That is, the reference mirror likely needs significant axial repositioning and/or has failed to reflect light back into the detector. As a result, there is no 'true' OCT image that would otherwise appear superimposed over the self-interference image. This is also why blocking the reference arm does not cause any structures to vanish.

Once the researcher has realigned the reference arm, the self-interference image remains as a strong artifact superimposed over the desired OCT image. Therefore, additional strategies must be employed to mitigate the self-interference artifacts.

A.2   Mitigation strategies

There are several strategies to mitigate 'self-interference images/artifacts'. A few examples are listed below (in order of increasing effectiveness *and* difficulty). They may be used individually or combined.

- Increase the reference arm reflectivity coefficient R (but do not saturate the spectrometer camera). The desired image signal will scale proportionally

to $\sqrt{R}$ while the self-interference signal remains unchanged (see the discussion of $S(k)$ in Chapter 3).

- Adjust the axial position of the sample to increase the distance between the reflective surface and the focal plane of the imaging beam. This will reduce (but not eliminate) artifacts by reducing the amount of light that is collected from the reflective surface.

- Adjust the axial position of the reference arm mirror so that the image of the region-of-interest in the sample does not spatially overlap with self-interference artifacts. This *might* allow avoidance of artifacts, but will reduce the available axial FOV.

- Tilt the sample so that less light reflects from the surface of the sample into the detector. This will reduce (but not eliminate) artifacts.

- Incorporate an index matching fluid (typically paired with an appropriate immersion objective lens) into the sample arm to reduce the reflectivity/scattering potential of the sample surface. This will reduce (but not eliminate) artifacts.

- Incorporate additional components into the microscope to enable the use of a phase-shifting holography technique to eliminate the self-interference term from the OCT spectral signal in post-processing. This will increase the complexity of the microscope, increase the amount of image data required to reconstruct images, and decrease imaging speed. Note that this method can also be used to mitigate the conjugate image spectrum.

- If the above options are not feasible, and self-interference artifacts are severe, then imaging with a double-path interferometer may not be viable. Consider *intentionally* using the 'accidental' common-path interferometer

for imaging. Block the reference arm (set $R = 0$) and increase the illumination power incident on the sample (and/or increase the camera exposure time) to improve signal-to-noise ratio. This will not be effective if strong reflections/scattering signals emerge from many depths in the sample. The reflective surface must be clean to ensure good image quality.

APPENDIX B

BACKGROUND SPECTRUM CHARACTERIZATION

The background spectrum occupies a substantial fraction of the total energy of the raw OCT spectral signal and must be removed in order to reconstruct the OCT image signal. However, the value of the background spectrum in a given A-scan cannot be known precisely, since it is always measured while super-imposed with the self-interference spectrum, OCT image spectrum, conjugate image spectrum, and noise. Subtracting the background spectrum from the raw OCT spectral signal therefore requires a characterization procedure which provides a decent *estimate* of the background spectrum for any given A-scan in the image. The utility of a given characterization procedure will primarily depend upon the stability of the output spectrum of the light source. In my own research, I have used the following procedures:

Calibration data set   If the light source has a very stable spectrum, the background spectrum can be characterized by acquiring a separate calibration data set. To do so, block the sample arm optical path such that no light can enter or return from the sample. Inserting a (scattering/non-reflective) paper index card will usually suffice. Place the card as close to the sample as is feasible without disturbing the sample or getting close to a focal plane of the probing beam. Then, acquire an image with at least a few thousand A-scans. Since none of the collected light will be from the sample itself, spectral contributions related to the sample will be absent from the calibration data. The calibration data set will only contain information about light reflected by the reference mirror (and any other reflecting surfaces in the system). Compute the *average* spectrum from the calibration data set (using a mean or median operation). The resulting estimate

of the background spectrum can be used during the reconstruction of previously/subsequently acquired images of the sample. How long this calibration 'lasts' depends on instability or long-term drift in the light source.

Volume averaging   If the light source is unstable enough that calibration data sets must be frequently re-acquired, the background spectrum can be estimated from the raw OCT spectral signal itself.[1] Assuming *volumetric* acquisition[2], the spectral terms contributed by the sample will tend to fluctuate in a pseudo-random fashion. By computing the average A-scan from all of the available A-scans, a decent estimate of the background spectrum can be obtained. Since the presence of bright scatterers or reflective surfaces in the sample can bias the estimate of the background spectrum, a median operation is recommended in favor of a mean operation. Large lateral features (e.g., large bright or dark regions across the FOV) may also contribute bias, even with robust estimators.

Frame-by-frame averaging   If the light source exhibits instability/drift on time scales shorter than the volume acquisition time, the background estimate may need to be 'updated' as a function of position within the image. For 2D raster scanning of the imaging beam, a volumetric data set may be separated into 'frames'. Each frame consists of a collection of A-scans acquired while scanning along the 'fast axis' (and while the 'slow axis' remains stationary). The background spectrum of a given frame may be computed via averaging of all the A-scans in a given frame (or collection of frames that were acquired at similar times). This method will be even more prone to bias, but may be the only option available when using a source with an unstable spectrum.

---

[1] This method can also be used if you simply do not wish to acquire calibration data sets.
[2] This method will not work if the imaging beam stays 'parked' at one location.

If the background spectrum is unstable on even shorter time scales than the frame acquisition time, you must either use a more advanced background estimation method (which might require modifications to the optical system), or should consider an alternative light source.

PHASE AND OCT IMAGE FORMATION

Fourier analysis is a key component of every introductory signals and systems course. Students often work extensively on practice problems which teach them how to interpret and manipulate the *magnitude* of the Fourier transform of a signal. However, exercises related to the *phase* of these functions are often woefully neglected, in comparison. One might consider this only natural. The phase of the Fourier transform of a signal can be incredibly complicated and difficult or impossible to intuitively interpret. However, this complexity is a telltale sign of how important phase is to the analysis and manipulation of signals and systems. Understanding this importance is critical to gaining a deep understanding of imaging science, including OCT image formation.

C.1   The role of phase

Consider the Dirac delta function: $\delta(t)$. The delta function has two extremely useful properties for the purposes of Fourier analysis, its 'sampling property':

$$\int_{-\infty}^{\infty} f(t)\delta(t - T)\, dt = f(T) \tag{C.1}$$

and its direct consequence for convolution:

$$f(t) \star \delta(t - T) = \int_{-\infty}^{\infty} f(\tau)\delta((t - \tau) - T)\, d\tau = f(t - T) \tag{C.2}$$

This makes the delta function a vital tool for understanding the behavior of linear systems. Inputting a delta function into such a system yields the Green's function of the system (also known as the impulse response, or the point spread

function, for imaging systems). In the context of imaging, these functions can describe phase shifts, signal delays and translation, blurring, distortion, and so on. Fortunately (although fortune has nothing to do with it), we can also use the delta function to better understand the role of phase in Fourier analysis, and by extension, OCT image formation.

We begin with the Fourier transform of a shifted delta function, $f(t) = \delta(t-T)$:

$$\tilde{f}(\omega) = \mathcal{F}[f(t)] = \mathcal{F}[\delta(t - T)] = \int_{-\infty}^{\infty} \delta(t - T)e^{-j\omega t}\, dt = e^{-j\omega T} \tag{C.3}$$

Like any good student of signals and systems, we examine the magnitude and phase of this function:

1. $\left|\tilde{f}(\omega)\right| = \left|e^{-j\omega T}\right| = 1$

2. $\angle\tilde{f}(\omega) = \angle e^{-j\omega T} = -T\omega$

Note that *only* the phase contains *any* information about the location of the delta function (at $t = T$). Specifically, the *slope* of the phase in the frequency domain encodes the location of the signal in the time domain. I have used this simple example many times to teach my own students the role of magnitude and phase in Fourier analysis, namely:

1. The magnitude of the Fourier transform of a signal tells you *what* frequencies are present and *how much* each frequency contributes to the signal.

2. The phase of the Fourier transform of a signal tells you *how* those waves are positioned in time/space/etc. in order to *assemble* the signal from the available frequencies/waves.

3. In simpler terms, the magnitude is like an inventory of supplies, and the phase is like a blueprint for how to use those supplies to build a signal.

Thus, the phase of the Fourier transform of a signal can be incredibly complicated simply because the phase is where most of the information about the signal is stored. This richness of information can make phase and its interpretation something of a bogeyman for students of signals and systems. However, with the right systems to analyze, we can learn to make phase our friend by wielding it as a useful tool.

It stands to reason that, since phase dictates how a signal is assembled from its constiuent waves, manipulating the phase can drastically alter how a signal is built. This is of fundamental importance to the use of numerical refocusing algorithms in OCT, including dispersion compensation and defocus/aberration correction. To understand this, we must examine phase profiles beyond what our delta function example provides.

C.2 Phase profiles with curvature

As we saw above, the Fourier transform of a delta function has a linear phase profile, the slope of which determines where the impulse appears in space/time. Why does this relationship exist? Consider how it is possible to create a pulse (with an infinitely narrow width) from a collection of waves (which are infinitely wide). The impulse itself is located at a site of perfect constructive interference across the (infinite) bandwidth of waves that make up the delta function. Every other location experiences perfect (net) destructive interference, and so no signal energy can exist at those locations in space/time. As long as the phase profile remains linear, there will be only one location of perfect constructive interference among all the constituent waves (as determined by the slope), while

every other location experiences perfect destructive interference. For the sake of brevity, understanding this fundamental concept will be left as an exercise for you to explore. Once given this simple principle, we can infer what will happen when the phase profile deviates from a line–and acquires curvature.

Say we replaced our original linear phase profile with a quadratic profile:

$$\tilde{g}(\omega) = e^{ja\omega^2} \qquad (C.4)$$

What would $g(t) = \mathcal{F}^{-1}[\tilde{g}(\omega)]$ look like? Rather than solving this problem directly, we can take a more qualitative approach. If we define the phase profile $\phi(\omega) = a\omega^2$, then the *local* slope of this phase profile is $\partial\phi(\omega)/\partial\omega = 2a\omega$. This means that, for a wave of frequency ω, the waves of its local neighborhood (in the frequency domain) have a point of maximal constructive interference at approximately $t = -2a\omega$. However, since every frequency has a different local slope, each wave is 'trying' to 'focus' at a different location, and no single point in the time domain ever experiences a state of perfect constructive/destructive interference. As a result, the function is 'blurred' across time. Although the function possesses the same infinite bandwidth as a delta function ($\left|\tilde{f}(\omega)\right| = |\tilde{g}(\omega)| = 1$), the phase of $\tilde{g}(\omega)$ does not *allow* the waves to assemble into a delta function. (Recall the analogy that the magnitude of $\tilde{g}(\omega)$ is like an inventory of supplies while the phase dictates how those supplies are assembled to make a signal in time.) It is then clear that, although a broad bandwidth is *necessary* to form a narrow pulse, it is not *sufficient*. The phase profile will dictate whether the final assembled function is narrow or not.

Figure C.1 depicts the effect of various phase profiles upon a Gaussian pulse. The original pulse (shown in black) is centered about time $t = 0$. When a linear phase profile is applied, the pulse (shown in red) shifts to a new time. With a
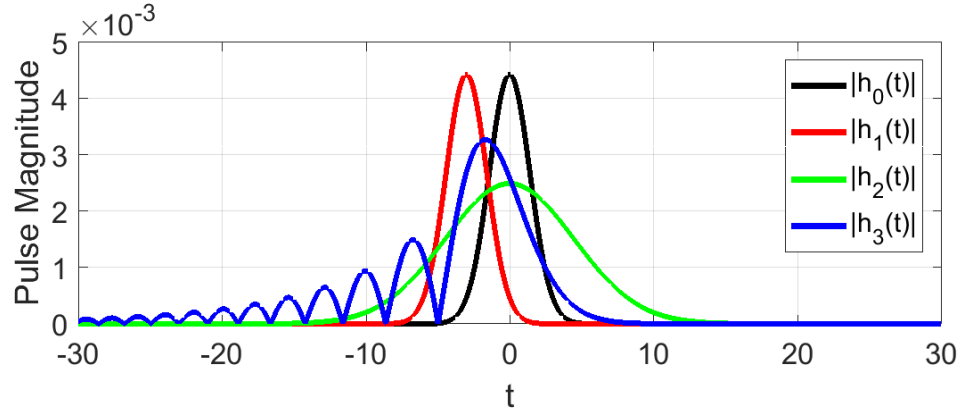
Figure C.1: Magnitude profiles of time-domain pulses defined by $h_i(t) = \mathcal{F}^{-1}\left[H(\omega)e^{j\alpha\omega^i}\right]$, where $H(\omega) = e^{-\omega^2}$ and $\alpha = 3$.

quadratic phase profile, curvature is introduced to the phase profile, degrading the constructive interference between differing frequency components and blurring the pulse (shown in green) across time. Note that the blurring is symmetric (like the quadratic phase profile itself). With a cubic phase profile, the pulse (shown in blue) is likewise blurred, but the blurring is no longer symmetric (analogous to the cubic phase profile itself). Higher-order phase profiles follow similar trends. Phase profiles consisting of a summation of polynomials compound the individual effects of each contributing term.

C.3 Phase and OCT image formation

Imaging systems are a tangible manifestation of the concepts of Fourier analysis. Optical fields are a superposition of waves of varying spatial frequency (defined by a vectorial wavenumber $\mathbf{k}$). Since the 3D OCT image signal $S(\mathbf{r})$ records a backscattered optical field, the Fourier transform of an OCT image $\tilde{S}(\mathbf{q})$ (very nearly) corresponds to a decomposition of the optical field into a collection of plane waves with differing spatial periods and directions of prop-

agation. As a result, computational manipulation of the magnitude and phase of $\tilde{S}(\mathbf{q})$ is closely analogous to manipulating waves and fields with a real optical system. Magnitude operations act like elements which manipulate field strength (masks, apertures, pinholes, etc.), while phase operations act like elements which manipulate the optical phase (lenses, aberrating layers, mirrors, gratings, dispersive materials, etc.).

Non-ideal (i.e., curved) phase profiles contribute to three major sources of resolution degradation in OCT images: dispersion, defocus, and optical aberrations. When these phenomena are sufficiently weak, their effects can be mitigated by manipulating the phase of the Fourier transform of the image signal. That is, if the Fourier transform of the ideal image signal (given by $\tilde{S}(\mathbf{q})$) is corrupted by a perturbing phase profile $\phi(\mathbf{q})$ via:

$$\hat{\tilde{S}}(\mathbf{q}) = \tilde{S}(\mathbf{q})e^{j\phi(\mathbf{q})} \tag{C.5}$$

then the 'ideal' function $\tilde{S}(\mathbf{q})$ can be restored by multiplying $\hat{\tilde{S}}(\mathbf{q})$ by $e^{-j\phi(\mathbf{q})}$. This is the core principle underlying dispersion compensation and computational adaptive optics. (Note that defocus correction and/or mitigation of highly dispersive media requires depth-dependent phase corrections.[1] However, the main idea holds.) By applying a phase profile that cancels out the corrupting phase profile, optimal spatial resolution can be restored.

As implied by our prior discussions, the ability to manipulate the phase of an optical field is a powerful tool for image formation. It allows us to use post-processing techniques which act as virtual optical systems. These systems, being purely numerical, can defy conventional optical limitations and enable the formation of images which exhibit enhanced resolution and depth-of-field.

---

[1]See Chapter 4 or Appendix E, respectively.

Such powerful capabilities are not available to conventional intensity-based microscopes, since these systems fail to record the phase of optical fields.[2] For OCT, however, phase measurements are inherent to the image acquisition process. So for any OCT researchers who may be reading, I cannot recommend highly enough that you make phase your friend! It will serve you well.

---

[2]Although we can take a Fourier transform of a standard intensity-based image and manipulate its magnitude and phase, these functions do not have a correspondence to the physical propagating waves within the original optical system.

APPENDIX D

TUTORIAL ON HARDWARE-BASED DISPERSION-MATCHING

As discussed in Chapter 3.5.3, a net *mismatch* in the dispersive properties of the sample and reference arms of an OCT imaging system will result in a *residual* dispersion effect which acts upon the axial point spread function (PSF). This induces axial blurring and concomitant degradation of axial resolution. For small amounts of dispersion mismatch, a simple numerical manipulation of the phase of the OCT spectral signal is sufficient to mitigate this mismatch and restore the ideal axial PSF. However, large amounts of residual dispersion can result in irreparable degradation of the OCT signal (via the 'roll-off' effect and/or aliasing of the spectral signal). In such scenarios, it is best to remove as much residual dispersion as possible via hardware-based mechanisms.

When an OCT system uses only one type of dispersive material (e.g., a single type of glass), the solution to achieving hardware-based dispersion-matching is relatively simple. One must merely ensure that there is an *equal* length of glass in the sample and reference arms of the microscope. However, OCT systems must often have different types of optics/glass in the sample and reference arms.[1] In that case, how can one determine the length of additional glass required in one arm or the other? More generally, if one arm contains a block of some exotic dispersive material that cannot be duplicated within the other arm of the microscope, is there a way to compensate the resulting residual dispersion using a block of *different* material(s) in the other arm?

Here we will review some simple methods that I used to address these ques-

---

[1]Unless you have extra grant money to spend on duplicate microscope objectives! (Do not do that! The methods outlined here are much cheaper and practically just as effective.)

tions. The procedures below were vital for fine-tuning the design(s) and performance of multiple systems in our lab.

D.1 Inferred dispersion-matching

This method involves measuring/inferring residual dispersion based on OCT image data. Once the residual dispersion is inferred, refractive index data for compensating materials (such as N-BK7 glass windows or fused silica optical fibers) are used to determine an optimal (or nearly so) length of additional glass (and possibly air) to incorporate into one arm of the OCT microscope. Note that although this method works well for large amounts of dispersion, *very* large amounts of dispersion (which cause significant signal loss and blurring of the axial PSF to lengths larger than the axial FOV of the system) may require *predictive* dispersion-matching (see Section D.2) and/or other methods.

D.1.1 Derivation

When performing OCT image reconstruction, numerical dispersion compensation can be a key step for obtaining an optimal axial resolution. Assume that OCT images were acquired with an existing (dispersive) OCT system and numerical dispersion compensation was performed via the operation: $\tilde{S}_{out}[k_i] = \tilde{S}_{in}[k_i]\exp(-j\phi_\alpha[k_i])$, where $\tilde{S}_{in}$ is the (dispersed) input spectral signal, $\tilde{S}_{out}$ is the optimized output spectral signal, and $\phi_\alpha[k_i]$ is a phase function which describes the residual phase profile that the numerical dispersion compensation routine removes. Typically, ϕ_α is defined using a minimal, truncated Taylor se-

ries $\phi_\alpha[k_i] = \alpha_2(k_i - k_c)^2 + \alpha_3(k_i - k_c)^3$, where k_i is the uniformly spaced (i.e., post-spectrum resampling) set of wavenumbers which make up the support of the OCT spectral signal, and k_c is the central wavenumber of the set of all k_i. α_2 and α_3 capture/describe symmetric and asymmetric blurring of the axial PSF, respectively. Alternatively, ϕ_α may be obtained from the phase of an isolated spectral signal obtained from a strongly-scattering and axially-thin object (such as a glass-air interface) in the sample.

Assume that adding some length of glass and air to the reference arm of the microscope will allow dispersion to be automatically canceled out in subsequently acquired raw spectral data. For this to occur, one could seek to satisfy the following relation:

$$x k_i n_{\text{glass}}[k_i] + y k_i n_{\text{air}}[k_i] = \phi_\alpha[k_i], \text{ for } i \in \{0, 1, \ldots, N - 1\} \tag{D.1}$$

where x and y are the amount of glass and air to add, respectively, n_{glass} and n_{air} are the wavenumber-dependent refractive indices of the compensating glass and air, respectively, and N is the number of pixels/entries in the spectral data. One way to think about this equation is that the left-hand side describes new phase/dispersion which is being added to the reference arm, whereas the right-hand side describes the measured excess phase/dispersion of the sample arm. If the two sides are equal, then they will cancel out during the interferometric OCT imaging process and no net residual dispersion will be present in the raw OCT data. Perfect cancellation would mean that numerical dispersion compensation would no longer be necessary! However, it is often impossible to satisfy Eqn. (D.1) for all relevant wavenumbers simultaneously. Therefore, there will almost always be residual dispersion which numerical dispersion compensation

must be used to remove. Define a residual phase function by:

$$f(x, y)[k_i] = xk_i n_{\text{glass}}[k_i] + yk_i n_{\text{air}}[k_i] - \phi_\alpha[k_i] \qquad \text{(D.2)}$$

Now, we must simply determine values of x and y which will yield the best possible realization of $f(x, y)[k_i]$. However, we must also define what we mean by 'best'. One obvious choice could be to find x and y such that $f(x, y)[k_i] \approx 0$, for $i \in \{0, 1, \dots, N - 1\}$ (i.e., to achieve near-perfect cancellation of the phase difference between the sample and reference arms). However, and perhaps counter to intuition, this does not necessarily yield the 'best' values of x and y that will minimize the dispersion-induced *axial blurring* of the PSF/OCT image.

As discussed in Appendix C, the shape of the residual phase profile determines the effect that the phase profile will have on the axial PSF and reconstructed OCT image. If the residual phase profile $f(x, y)[k_i]$ is approximated with a Taylor series, then each term of the series will have the following effects:

- 0th-order/constant: Bulk phase shift; no effect on image structure

- 1st-order/linear: Axial translation of the OCT image

- 2nd-order/quadratic: Symmetric axial blurring of the OCT image

- 3rd-order/cubic: Asymmetric axial blurring of the OCT image

- Higher-order: Higher-order axial blurring of the OCT image

Therefore, in order to minimize *axial blurring* due to residual dispersion (and thereby optimize axial resolution) we need only ensure that $f(x, y)[k_i]$ is a *linear* function. Thus, we need to find values of x and y such that $f(x, y)[k_i] \approx pk_i + q$, for p and q a slope and constant offset, respectively. However, a non-zero value of p could potentially result in a large amount of axial translation of the OCT

image (e.g., such that the focal plane of the OCT system lies far outside the axial FOV of the imaging system). Therefore, we apply an additional constraint and require that $p = 0$. This means that we only need to find values of x and y such that $f(x, y)[k_i] \approx q$, for q an arbitrary constant. We can minimize the non-constant components of $f(x, y)[k_i]$ by minimizing the *variance* of $f(x, y)[k_i]$ about its mean.

First, we convert the function-based notation of Eqn. (D.2) to vector-based notation (since we are working with only a finite set of N values of $f(x, y)[k_i]$, k_i, $n_{\text{glass}}[k_i]$, $n_{\text{air}}[k_i]$, and $\phi_\alpha[k_i]$):

$$\mathbf{F}(x, y) = x\mathbf{k} \circ \mathbf{n}_{\text{glass}} + y\mathbf{k} \circ \mathbf{n}_{\text{air}} - \phi_\alpha \tag{D.3}$$

where '$\circ$' denotes the Hadamard product (element-wise multiplication). To simplify our equations, we define:

$$\mathbf{A} = \mathbf{k} \circ \mathbf{n}_{\text{glass}} \tag{D.4a}$$

$$\mathbf{B} = \mathbf{k} \circ \mathbf{n}_{\text{air}} \tag{D.4b}$$

$$\mathbf{C} = \phi_\alpha \tag{D.4c}$$

We then rewrite Eqn. (D.3) as:

$$\mathbf{F}(x, y) = x\mathbf{A} + y\mathbf{B} - \mathbf{C} \tag{D.5}$$

We next define a set of 'mean vectors':

$$\mathbf{a} = \left(\frac{1}{N} \sum_{i=0}^{N-1} \mathbf{A}_i \right) \mathbf{1}^{N \times 1} \tag{D.6a}$$

$$\mathbf{b} = \left(\frac{1}{N} \sum_{i=0}^{N-1} \mathbf{B}_i \right) \mathbf{1}^{N \times 1} \tag{D.6b}$$

$$\mathbf{c} = \left(\frac{1}{N} \sum_{i=0}^{N-1} \mathbf{C}_i \right) \mathbf{1}^{N \times 1} \tag{D.6c}$$

$$\mathbf{f} = \left(\frac{1}{N} \sum_{i=0}^{N-1} \mathbf{F}_i \right) \mathbf{1}^{N \times 1} = x\mathbf{a} + y\mathbf{b} - \mathbf{c} \tag{D.6d}$$

where $\mathbf{1}^{N \times 1}$ denotes an $N \times 1$ vector with all entries equal to 1. Finding the values of x and y that minimize the variance of $f(x, y)[k_i]$ over our finite set of wavenumbers/values is achieved by solving:

$$(x, y) = \arg \min \left[g(x, y) \right], \text{ for } g(x, y) = \|\mathbf{F} - \mathbf{f}\|_2^2 \tag{D.7}$$

Note that $g(x, y)$ is merely N times the variance of the entries of $\mathbf{F}(x, y)$. In order to solve this problem, we will adopt the strategy of finding (x, y) such that $\langle \partial g(x, y)/\partial x, \partial g(x, y)/\partial y \rangle = \mathbf{0}$. First, we expand our expression for $g(x, y)$:

$$g(x, y) = \|\mathbf{F} - \mathbf{f}\|_2^2 \tag{D.8a}$$

$$= \|(x\mathbf{A} + y\mathbf{B} - \mathbf{C}) - (x\mathbf{a} + y\mathbf{b} - \mathbf{c})\|_2^2 \tag{D.8b}$$

$$
\begin{aligned}
= \; & (\mathbf{C} \cdot \mathbf{C} - (\mathbf{C} \cdot \mathbf{c} + \mathbf{c} \cdot \mathbf{C}) + \mathbf{c} \cdot \mathbf{c}) & + \ldots \\
& (\mathbf{A} \cdot \mathbf{C} - (\mathbf{A} \cdot \mathbf{c} + \mathbf{a} \cdot \mathbf{C}) + \mathbf{a} \cdot \mathbf{c})(-2x) & + \ldots \\
& (\mathbf{B} \cdot \mathbf{C} - (\mathbf{B} \cdot \mathbf{c} + \mathbf{b} \cdot \mathbf{C}) + \mathbf{b} \cdot \mathbf{c})(-2y) & + \ldots \\
& (\mathbf{A} \cdot \mathbf{B} - (\mathbf{A} \cdot \mathbf{b} + \mathbf{a} \cdot \mathbf{B}) + \mathbf{a} \cdot \mathbf{b})(2xy) & + \ldots \\
& (\mathbf{A} \cdot \mathbf{A} - (\mathbf{A} \cdot \mathbf{a} + \mathbf{a} \cdot \mathbf{A}) + \mathbf{a} \cdot \mathbf{a})(x^2) & + \ldots \\
& (\mathbf{B} \cdot \mathbf{B} - (\mathbf{B} \cdot \mathbf{b} + \mathbf{b} \cdot \mathbf{B}) + \mathbf{b} \cdot \mathbf{b})(y^2) &
\end{aligned}
\tag{D.8c}
$$

This is a little unwieldy. However, we can leverage a useful relation that

emerges from the definitions of our vectors:

$$\mathbf{A} \cdot \mathbf{B} - (\mathbf{A} \cdot \mathbf{b} + \mathbf{a} \cdot \mathbf{B}) + \mathbf{a} \cdot \mathbf{b} = \sum_{i=0}^{N-1} A_i B_i - \sum_{i=0}^{N-1} A_i b_i - \sum_{i=0}^{N-1} a_i B_i + \sum_{i=0}^{N-1} a_i b_i \tag{D.9a}$$

$$= \sum_{i=0}^{N-1} A_i B_i - \sum_{i=0}^{N-1} A_i \left(\frac{1}{N} \sum_{j=0}^{N-1} B_j \right) - \sum_{i=0}^{N-1} \left(\frac{1}{N} \sum_{j=0}^{N-1} A_j \right) B_i + \dots$$

$$\sum_{i=0}^{N-1} \left(\frac{1}{N} \sum_{j=0}^{N-1} A_j \right) \left(\frac{1}{N} \sum_{j=0}^{N-1} B_j \right)$$

$$\tag{D.9b}$$

$$= \sum_{i=0}^{N-1} \left(A_i - \left(\frac{1}{N} \sum_{j=0}^{N-1} A_j \right) \right) \left(B_i - \left(\frac{1}{N} \sum_{j=0}^{N-1} B_j \right) \right) \tag{D.9c}$$

$$= N \sigma_{A,B} \tag{D.9d}$$

where $\sigma_{A,B}$ denotes the covariance of the entries of $\mathbf{A}$ and $\mathbf{B}$. Thus, we obtain:

$$g(x, y) = N \left(\sigma_{C,C} - 2\sigma_{A,C} x - 2\sigma_{B,C} y + 2\sigma_{A,B} xy + \sigma_{A,A} x^2 + \sigma_{B,B} y^2 \right) \tag{D.10}$$

Finally, we have arrived at some reasonable notation![2] We continue with our objective to minimize $g(x, y)$:

$$0 = \partial g(x, y) / \partial x = 2N \left(-\sigma_{A,C} + \sigma_{A,A} x + \sigma_{A,B} y \right) \tag{D.11a}$$

$$0 = \partial g(x, y) / \partial y = 2N \left(-\sigma_{B,C} + \sigma_{A,B} x + \sigma_{B,B} y \right) \tag{D.11b}$$

Finally, we obtain our values of x and y via:

$$\begin{bmatrix} x \\ y \end{bmatrix} = \begin{bmatrix} \sigma_{A,A} & \sigma_{A,B} \\ \sigma_{A,B} & \sigma_{B,B} \end{bmatrix}^{-1} \begin{bmatrix} \sigma_{A,C} \\ \sigma_{B,C} \end{bmatrix} \tag{D.12}$$

D.1.2 Procedure

In order to make use of Eqn. (D.12), perform the following:

---

[2] I have always preferred to work with vectors before resorting to summations. I apologize for any confusion you may have experienced until this step.

1. Using your existing dispersive OCT system, acquire an image of a sample which exhibits sparsity along the axial/depth dimension (e.g., a glass slide or a 3D phantom containing embedded nano/microparticles).

2. Perform OCT image reconstruction as usual, including numerical dispersion compensation to optimize axial resolution. Your numerical dispersion compensation procedure should result in your defining a dispersion correction phase function $\phi_\alpha[k_i]$. Be sure to avoid phase wrapping!

3. Select your dispersion-compensating material (e.g., N-BK7 glass, fused silica, etc.). Find a data sheet which will allow you to determine the refractive index $n[k_i]$ of the compensating material for each wavenumber k_i.

4. Use Eqn. (D.12) to compute the values of x and y, which correspond to the length of additional glass and air, respectively, which you should install in order to compensate the current residual dispersion of your system.

Here are a few points to keep in mind:

- Note that positive values of x or y indicate the *total* length of the material(s) that should be installed into the reference arm and/or removed from the sample arm. For example, if x=50 cm, you should do *one* of the following: 1) install 50 cm of the selected type of glass into the reference arm, 2) remove 50 cm of the selected type of glass from the sample arm, or 3) install L_r of the selected type of glass into the reference arm *and* remove L_s of the selected type of glass from the sample arm such that $L_r + L_s$=50 cm. Negative values of x or y reverse the relationship of where materials should be installed/removed.

- It is always a good idea to confirm in simulation that your hardware-based dispersion compensation will perform in a desirable fashion. (I have not

yet encountered a scenario where this procedure does not work, but it cannot hurt to check before you invest in time and materials!)

- Sometimes, you only need to install a small amount of material. For example, say you need to install only 4 cm of additional optical fiber into the reference arm. This may be an impractically small length of fiber to obtain. Instead consider installing *two* fibers: one in the sample arm of length *L*, and one in the reference arm of length *L*+4 cm. Alternatively, cleave 4 cm off of an existing fiber in the sample arm.

- Always acquire a new image to ensure that dispersion in your system has been mitigated. If the dispersion *increased*, check that you did not install your compensating materials into the wrong arm(s) of the microscope.[3] If this does not resolve the problem, then something else has gone wrong.[4]

D.2 Predictive dispersion-matching

This method involves using glass and air to compensate for the dispersion introduced by a newly installed material with known properties and length. It is very similar to the inferred dispersion-matching method described previously. The set-up is just a little different. We will use an instructive example from my own prior work to help explain the differences.

---

[3]Depending on the design of your OCT image reconstruction procedure, you may have had a sign error in your initial definition of $\phi_\alpha[k_i]$. This is an easy problem to fix! Just try installing your compensating materials into the opposite arm(s) than what your model suggested. This should resolve any sign errors.

[4]Check your theoretical model. Did you miss a factor of 2 somewhere? (Recall the double-pass geometry of standard SD-OCT imaging systems.) If that is not the problem, I am afraid I cannot help you here. :(

D.2.1   Example

A few years back (as of this writing), we were working on a system which incorporated an electro-optical modulator (EOM) into the reference arm of an existing OCT system. We wished to use the EOM to apply known/controlled phase shifts within the reference arm so that we could employ a phase-shifting holography technique that would eliminate our conjugate image signal and self-interference artifacts (and thereby increase our usable axial FOV).

The EOM contained a 40 mm crystal of lithium niobate (LiNbO$_3$), a material whose refractive index and dispersion profile differ substantially from that of glass. Suffice it to say that this crystal absolutely demolished our axial resolution. Numerical dispersion compensation was insufficient. I eventually came up with the following solution:[5]

1. Define a dispersion-matching condition (as in Eqn. (D.1)):

$$xk_i n_{\text{glass}}[k_i] + yk_i n_{\text{air}}[k_i] = L_{\text{LiNbO}_3} k_i n_{\text{LiNbO}_3}[k_i] \qquad \text{(D.13)}$$

Here, the left-hand side of the equation indicates materials to be installed in the sample arm, whereas the right-hand side indicates the new material installed in the reference arm (i.e., L_{LiNbO_3}=40 mm of LiNbO$_3$). This left-right relationship is reversed compared to the dispersion-matching condition defined in Eqn. (D.1). (If you mix up this type of relationship in the future, you will get a sign error in your final results.)

2. Define a residual phase function (as in Eqn. (D.2)):

$$f(x, y)[k_i] = xk_i n_{\text{glass}}[k_i] + yk_i n_{\text{air}}[k_i] - L_{\text{LiNbO}_3} k_i n_{\text{LiNbO}_3}[k_i] \qquad \text{(D.14)}$$

---

[5]Note that this scenario was the first time I had ever done any kind of hardware-based dispersion compensation.

3. Define the following vectors (analogous to the definitions in Section D.1):

$$\mathbf{A} = \mathbf{k} \circ \mathbf{n}_{\text{glass}} \tag{D.15a}$$

$$\mathbf{B} = \mathbf{k} \circ \mathbf{n}_{\text{air}} \tag{D.15b}$$

$$\mathbf{C} = L_{\text{LiNbO}_3} \mathbf{k} \circ \mathbf{n}_{\text{LiNbO}_3} \tag{D.15c}$$

4. Solve for the required lengths of glass and air (x and y, respectively) to be installed in the sample arm via Eqn. (D.12).

In my case, I was concerned with the 700 nm–900 nm wavelength range. I chose to use fused silica (optical fiber) as my compensation material. The refractive indices for LiNbO$_3$[6] and fused silica[7] in the relevant wavelength range are:

$$n_{\text{LiNbO}_3}[k_i] = \left[1 + \frac{2.6734\lambda_i^2}{\lambda_i^2 - 0.01764} + \frac{1.2290\lambda_i^2}{\lambda_i^2 - 0.05914} + \frac{12.614\lambda_i^2}{\lambda_i^2 - 474.60} \right]^{0.5} \tag{D.16a}$$

$$n_{\text{glass}}[k_i] = n_{\text{silica}}[k_i] = \left[1 + \frac{0.6961663\lambda_i^2}{\lambda_i^2 - 0.0684043^2} + \frac{0.4079426\lambda_i^2}{\lambda_i^2 - 0.1162414^2} + \frac{0.8974794\lambda_i^2}{\lambda_i^2 - 9.896161^2} \right]^{0.5} \tag{D.16b}$$

where $\lambda_i = 2\pi/k_i$ in units of micrometers. Using the procedure above, I computed x=+475.63 mm and y=-603.48 mm. This means that in order to compensate for the dispersion introduced by the LiNbO$_3$ crystal, 475.63 mm of additional optical fiber should be installed into the sample arm and 603.48 mm of air should be removed from the sample arm. In practice, removing air from the sample arm was not possible, so 603.48 mm was added to the *reference* arm instead. If these installations were done perfectly, the dispersion introduced by the LiNbO$_3$ crystal would be expected to cancel out down to sub-wavelength

---

[6]Obtained from `https://refractiveindex.info/?shelf=main&book=LiNbO3&page=Zelmon-o`

[7]Obtained from `https://refractiveindex.info/?shelf=glass&book=fused_silica&page=Malitson`

precision. In practice, we could only obtain an approximately correct length of optical fiber. However, numerical dispersion compensation readily removed any residual dispersion.

Note that this procedure (or ones like it) may be performed in parallel to the inferred dispersion-matching discussed previously. You may either set up a combined set of equations and solve, or solve both problems independently and combine their results to yield the total length of compensating materials to install in each arm of your microscope.

APPENDIX E

NUMERICAL COMPENSATION OF DEPTH-DEPENDENT DISPERSION ARTIFACTS

In Chapter 3.5.3, we derived an expression (Eqn. (3.32a)) for the OCT spectral signal acquired by an OCT system constructed with dispersive optical elements:

$$\tilde{S}(k') = \tilde{h}(k')e^{j\Delta\phi(k')} \int_{-\infty}^{\infty} \eta(z_s)e^{-jk'nz_s} \, dz_s \tag{E.1}$$

Please refer to the text of Chapter 3.5.3 for a full explanation of this equation. In brief, the integral term encodes the Fourier transform of the scattering potential $\eta(z)$ of the sample with respect to the family of basis functions: $\exp(jk'nz) = \exp(-j2knz)$, where n was defined as the space- and wavenumber-invariant refractive index of the bulk medium of the sample. Assuming a reconstruction procedure which is 'blind' to the value of n, the reconstructed OCT image will appear axially 'stretched' by a factor of n, due to the fact that OCT microscopes measure the optical path length (*not* the physical distance) traveled by light. $\Delta\phi(k')$ encodes residual phase due to unmatched dispersion in the OCT imaging system. Expressing $\Delta\phi(k')$ as a Taylor series:

$$\Delta\phi(k') = \alpha_0 + \alpha_1(k' - k_c') + \alpha_2(k' - k_c')^2 + \alpha_3(k' - k_c')^3 + O\left((k' - k_c')^4\right) \tag{E.2}$$

we concluded that axial blurring of the OCT image would take place if $\alpha_i \neq 0$, for $i \geq 2$. When this 'dispersive blur' is very large, the hardware of the optical system must be modified in order to cancel out the second- and higher-order terms of $\Delta\phi(k')$ (see Appendix D). However, as discussed in Chapter 3.5.3, small amounts of dispersive blur can be compensated numerically via the operation:

$$\tilde{S}_\alpha(k') = \tilde{S}(k')e^{-j\left(\alpha_2(k'-k_c')^2 + \alpha_3(k'-k_c')^3 + \dots\right)} \tag{E.3}$$

Since dispersive blur can be corrected via multiplication in the spectral domain, it follows that the axial PSF of the imaging system is space-invariant. Every depth in the reconstructed OCT image has a spatially uniform axial resolution (with respect to OPL) both before and after numerical compensation of dispersive blur. However, this model breaks down when we realize that the bulk medium of biological samples (i.e., water) is *itself* dispersive.

E.1   Depth-dependent dispersion

If the bulk medium of the sample is dispersive, then the refractive index is given by $n(k)$. This requires that we modify our expression for the OCT spectral signal:

$$\tilde{S}(k') = \tilde{h}(k')e^{j\Delta\phi(k')} \int_{-\infty}^{\infty} \eta(z_s)e^{-jk'n(k)z_s}\, dz_s \qquad (\text{E.4})$$

For this analysis, it will be easier to work with the variable k, as opposed to the variable $k' = -2k$ which we defined in Chapter 3. Thus, we rewrite the above expression as:

$$\tilde{S}(k) = \tilde{h}(k)e^{j\Delta\phi(k)} \int_{-\infty}^{\infty} \eta(z_s)e^{j2kn(k)z_s}\, dz_s \qquad (\text{E.5})$$

where

$$\Delta\phi(k) = a_0 + a_1(k - k_c) + a_2(k - k_c)^2 + a_3(k - k_c)^3 + O\left((k - k_c)^4\right) \qquad (\text{E.6})$$

for k_c the central wavenumber collected by the OCT system. In order to analyze the axial PSF, we assume a scattering potential of $\eta(z) = \eta(z_s)\delta(z - z_s)$ in order to obtain the spectral signal of an isolated scatterer:

$$\tilde{S}(k; z_s) = \eta(z_s)\tilde{h}(k)e^{j\Delta\phi(k)}e^{j2kn(k)z_s} \qquad (\text{E.7})$$

If we perform a Taylor series expansion of $n(k)$ about k_c:

$$n(k) = n_0 + n_1(k - k_c) + n_2(k - k_c)^2 + n_3(k - k_c)^2 + O\left((k - k_c)^4\right) \qquad (\text{E.8})$$

then we obtain:

$$\tilde{S}(k; z_s) = \eta(z_s)\tilde{h}(k)e^{j\Delta\phi(k)}e^{j2kn_0 z_s}e^{j2k\left(n_1(k-k_c)+n_2(k-k_c)^2+n_3(k-k_c)^2+O\left((k-k_c)^4\right)\right)z_s} \qquad \text{(E.9)}$$

The last term of this expression is a new addition to our previous model,[1] which we will refer to as the 'depth-dependent dispersion' term. Note that the phase of the depth-dependent dispersion term is *nonlinear* with respect to k (i.e., the phase contains quadratic and higher-order functions of k). This curved phase profile will induce axial blurring in the reconstructed OCT image, analogous to the second- and higher-order components of $\Delta\phi(k)$. However, unlike $\Delta\phi(k)$, the phase of the depth-dependent dispersion term scales with the axial position z_s of the scatterer. That is, the axial blurring due to this term *increases with depth* in the dispersive sample medium.

This depth-dependent blurring (depicted in Fig. E.1) cannot be fixed with a simple multiplication operation like that shown in Eqn. (E.3). However, other numerical compensation methods are available which can be readily integrated into standard OCT image reconstruction paradigms.

E.2 Numerical compensation methods

E.2.1 Resampling

We have encountered depth-dependent blurring before. Specifically, we saw this phenomenon emerge as a consequence of failing to properly account for non-uniform discrete sampling of the OCT spectral signal (with respect to

---

[1]That is, without this term, Eqn. (E.9) would be consistent with the model in Eqn. (E.1), substituting $n = n_0$.

Depth-dependent evolution of axial PSF in water

Legend:
- Transform-limited axial PSF
- 250 μm in water
- 500 μm in water
- 750 μm in water
- 1000 μm in water
- 1250 μm in water
- 1500 μm in water
- 1750 μm in water
- 2000 μm in water
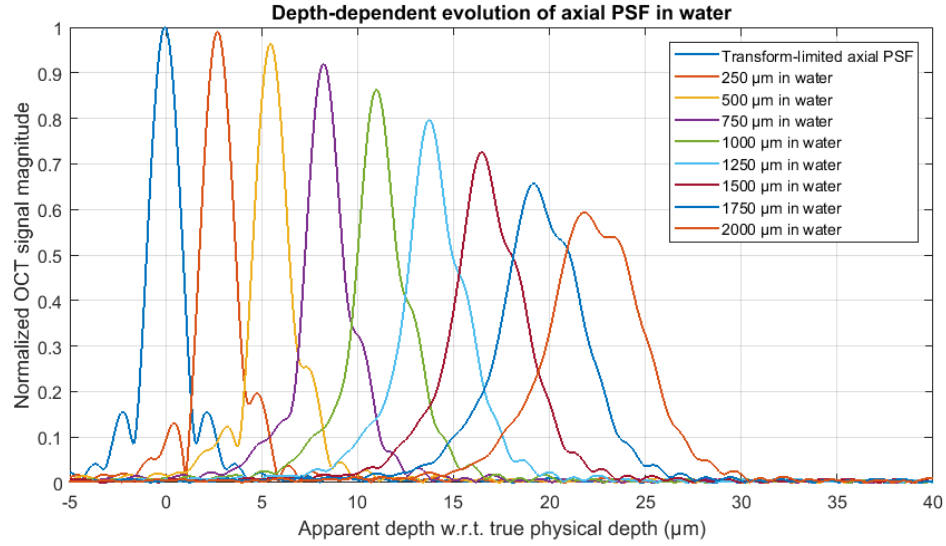
Figure E.1: Simulated axial point spread function (PSF) of an OCT system imaging in water. This simulated system has the same spectral profile as the Ti:Sapph laser in our lab (central wavelength = 790 nm, full-width-at-half-maximum bandwidth = 136 nm). There are two notable features: 1) As the system images deeper into the medium, the axial PSF broadens as the dispersive properties of the medium cause nonlinear phase profiles to accumulate. 2) As the system images deeper into the medium, the reconstructed axial PSF shifts to an *apparent* depth which is deeper than the true physical depth within the sample. (This axial shift is depicted along the horizontal axis of the plots above.) That is, if we use an OCT image reconstruction routine which assumes a constant refractive index, we will overestimate the depth from which a scattering signal emerged. The severity of this error will increase as we go deeper into the sample.

wavenumber) by the spectrometer camera (see Chapter 3.5.5). Just as spectrum resampling compensates for depth-dependent blurring due to non-uniformly sampled spectral data, so too can a resampling operation be used to compensate for depth-dependent dispersion. This method is particularly useful for FFT-based OCT image reconstruction routines.

Assume that we have an OCT spectral signal which has already undergone spectrum resampling. That is, we have a spectral signal $\tilde{S}[k_i]$ sampled along a uniformly spaced set of wavenumbers $k_i = k_0 + i\Delta k$ for $i \in \{0, 1, \ldots, N-1\}$. Define $\hat{k}_i = n(k_i)k_i$, for $n(k)$ the wavenumber-dependent refractive index of the

sample medium. $\hat{\kappa}_i$ corresponds to the set of *effective* wavenumbers of the light within the medium. Next, define $\kappa_i = n(k_c)k_i$ for $i \in \{0, 1, \ldots, N-1\}$ and $k_c = (k_0 + k_{N-1})/2$. κ_i corresponds to a uniformly spaced set of effective wavenumbers. Depth-dependent dispersion compensation is then achieved by resampling the spectral signal (defined for each value of $\hat{\kappa}_i$) at each of the query points κ_i. In MATLAB, this operation could be performed via:

```
S_out = interp1(kappa_hat,S_in,kappa,'spline');
```

or a related operation. Note that the 'bulk dispersion' of the system (i.e., that encoded by $\Delta\phi(k)$) will still need to be corrected using a separate dispersion compensation step (Eqn. E.3). Note that for the purposes of subsequent image reconstruction routines and/or image analysis, the imaged medium will now have an effective (constant) refractive index of $n(k_c)$.

Of course, using multiple resampling operations (spectrum resampling followed by depth-dependent dispersion compensation) increases computation time and may introduce unnecessary numerical errors. To mitigate these concerns, we can combine spectrum resampling and depth-dependent dispersion compensation into a single resampling operation! Assume that the spectral signal $\tilde{S}[\hat{k}_i]$ is sampled along a non-uniformly spaced set of wavenumbers $\hat{k}_i$ for $i \in \{0, 1, \ldots, N-1\}$. Analogous to the above procedure, define $\hat{\kappa}_i = n(\hat{k}_i)\hat{k}_i$. Next, define $\kappa_i = \kappa_0 + i\Delta\kappa$, for $i \in \{0, 1, \ldots, N-1\}$, $\kappa_0 = n(k_c)\hat{k}_0$, $\Delta\kappa = n(k_c)(\hat{k}_{N-1} - \hat{k}_0)/(N-1)$, and $k_c = (\hat{k}_0 + \hat{k}_{N-1})/2$. Finally resample the spectral signal (defined for each value of $\hat{\kappa}_i$) at each of the query points κ_i.

E.2.2 Depth-dependent phase correction

Alternatively, we may multiply our spectral signal by a dispersion-canceling phase function which changes for each depth that we wish to reconstruct. This is an attractive option for OCT image reconstruction methods which use matrix multiplication. For example, using the phase-only matched filter convention from Chapter 3.7.4, we define an expected spectral signal vector $\Psi^m \in \mathbb{C}^{N \times 1}$:

$$\Psi_i^m = \exp\left(j \left(2 \frac{n(\hat{k}_i)}{n(k_c)} \hat{k}_i m \Delta z + \phi[\hat{k}_i] \right) \right) \tag{E.10a}$$

$$\Delta z = \frac{\pi}{N \Delta k} = \frac{\pi(N-1)}{N(\hat{k}_{N-1} - \hat{k}_0)} \tag{E.10b}$$

$$\phi[\hat{k}_i] = \alpha_2(\hat{k}_i - k_c)^2 + \alpha_3(\hat{k}_i - k_c)^3 \tag{E.10c}$$

$$k_c = (\hat{k}_0 + \hat{k}_{N-1})/2 \tag{E.10d}$$

for $i \in \{0, 1, \ldots, N-1\}$. In order to reconstruct an (origin-centered, length N) set of depths $m \Delta z$ for $m \in \{-\lfloor N/2 \rfloor, \ldots, \lceil N/2 \rceil - 1\}$, we assemble a 'signal prediction matrix':

$$\Psi \in \mathbb{C}^{N \times N} = \left[\psi^{m=-\lfloor N/2 \rfloor} \quad \ldots \quad \psi^{m=0} \quad \ldots \quad \psi^{m=\lceil N/2 \rceil - 1} \right] \tag{E.11}$$

We can now reconstruct OCT images via multiplication of our (post-background subtration) OCT spectral data via:

$$\Psi^{\dagger} \tilde{s} \tag{E.12}$$

where '$\dagger$' denotes the Hermitian (conjugate transpose) operator, and $\tilde{s}$ denotes a vector of spectral data (which has only undergone background subtraction). As before, the medium will now exhibit an effective (constant) refractive index of $n(k_c)$ (i.e., the *physical* height of each voxel within the medium is $\Delta z/n(k_c)$).

E.2.3 Caveats

The methods defined above rely on a few assumptions:

1. The sample has a flat surface. Increasing amounts of tilt in the sample surface will result in a laterally-varying axial blurring artifact which these methods do not compensate for.

2. The region of interest in your sample consists of a single homogeneous medium. If imaging in a stratified sample, these methods will not work as intended. Note that having a thin glass coverslip/slide on the surface of your sample is fine. However, if in subsequent processing you perform phase registration via 'phase registration method 2' in Chapter 4.4 (or an analogous method), there may be a residual bulk dispersion artifact within your region of interest beneath the glass. This would be due to the mismatch between the refractive index profile of the glass layer versus that of your sample medium. In practice, however, this is likely to have only a small effect on your reconstructed image and may be acceptable to ignore.

E.3 Analogy to defocus mitigation methods

I want to take a moment to point out an interesting analogy/relationship. The two methods outlined above for depth-dependent dispersion compensation (resampling and depth-dependent phase correction) are analogous to the two classes of methods used to mitigate depth-dependent beam defocus (see Chapter 4). Interferometric synthetic aperture microscopy (ISAM) performs a 1D resampling operation, whereas computational adaptive optics performs a

depth-dependent phase correction. In general, resampling methods distort existing data (and corresponding phase profiles), whereas phase correction methods directly alter the phase 'in place'. Although this may make phase correction methods 'more exact', they are typically much more computationally expensive to perform than resampling operations.

TUTORIAL ON CUBIC SPLINE INTERPOLATION

F.1   A tale from the lab

During my program, our lab's OCT image acquisition software used a GPU-based image reconstruction routine [171] which enabled the visualization of cross-sectional (*zx-*) OCT image frames in real time/at video rates. In order to perform the critical step of spectrum resampling (see Chapter 3.5.5), this routine made use of a 'black box' spline-based interpolation scheme. The code for this scheme had been 'inherited' from a coworker of my advisor (Prof. Steven Adie, Cornell University) during his postdoctoral program (in the lab of Prof. Stephen Boppart, UIUC). Lacking comments from its original author beyond a link to a Wikipedia page, the interpolator was incorporated into our GPU-based reconstruction routine without any of us really understanding how it worked. It was not until later on in my program (when I was revamping *my own* OCT image reconstruction routines) that I finally learned about how these interpolators can be built. However, since I never worked on either the GPU codebase or the image acquisition software, the 'black box' interpolator remains present within our acquisition software to this day (as of *this* writing). The moral of the story is: Be careful when you share your code with others! For better or for worse, they may end up using it for a very long time!

This appendix has been included for those who might be interested in walking through the derivations/math behind a common interpolation scheme (cubic spline interpolation) as it pertains to OCT image reconstruction. If my own take on the subject provides any useful insights, then I will have achieved all

that I set out to do here. Please note that the math and code that follow are *not* meant to provide efficient representations/implementations of interpolators (I defer to computer scientists for *that!*). The materials here are merely meant as a learning exercise.

F.2 Derivation of the cubic spline interpolator

F.2.1 Preliminary definitions

Let $\tilde{S}(k)$ denote a spectral signal measured by the spectrometer camera of an SD-OCT system. Let the spectrometer camera perform discrete sampling of this continuous signal at N sampling points $\hat{k}_n$ for $n \in \{0, 1, \ldots, N-1\}$[1] such that the sequence $\hat{k}_0, \hat{k}_1, \ldots, \hat{k}_{N-1}$ is strictly increasing.[2] Let $\tilde{\mathbf{s}}$ denote an $N \times 1$ vector whose entries are $\tilde{s}_n = \tilde{S}(\hat{k}_n)$. As discussed in Chapter 3.5.5, if the set/sequence of sampling points $\hat{k}_n$ is non-uniformly spaced (i.e, $\hat{k}_{n+1} - \hat{k}_n$ is *not* constant for all $n \in \{0, 1, \ldots, N-2\}$), then we must perform spectrum resampling in order to *estimate* the value of $\tilde{S}(k)$ over a set/sequence of M uniformly spaced query points k_m for $m \in \{0, 1, \ldots, M-1\}$.[3]

We define k_m such that $k_m = \hat{k}_0 + m\Delta k$ for $m \in \{0, 1, \ldots, M-1\}$ and $\Delta k = (\hat{k}_{N-1} - \hat{k}_0)/(M-1)$. Let $\bar{\mathbf{s}}$ denote an $M \times 1$ vector whose entries are $\bar{s}_m = \bar{S}(k_m)$, where $\bar{S}(k)$ is a function which *approximates* $\tilde{S}(k)$. Specifically, $\bar{S}(k) \approx \tilde{S}(k)$ for $\hat{k}_0 \leq$

---

[1]Elsewhere in this dissertation, I typically use '*i*' as my indexing variable of choice, and reserve '*n*' to denote refractive index. However, I will be doing otherwise here. I tried not to do this, but there are so many conventions and only so many letters.

[2]See the MATLAB code at the end of this appendix for the handling of a *decreasing* set.

[3]Note that for typical OCT image reconstruction procedures, $M = N$. However, for instructional purposes, we will continue to treat both M and N as independent values.

$k \leq \hat{k}_{N-1}$. In many common interpolation schemes, each entry of $\bar{\mathbf{s}}$ is obtained via a weighted sum of the entries of $\tilde{\mathbf{s}}$, which we can describe by the operation:

$$\bar{\mathbf{s}} = \mathbf{W}\tilde{\mathbf{s}} \tag{F.1}$$

where $\mathbf{W}$ (which we will call a 'resampling matrix') is an $M \times N$ matrix of 're-sampling weights'. The entries of $\mathbf{W}$ are determined by the set of all sampling points $\hat{k}_n$, the set of all query points k_m, and the interpolation scheme. Here, we will use cubic (3rd-order) spline interpolation.

F.2.2 The cubic spline function

To perform cubic spline interpolation, first, we define $\bar{S}(k)$ as:

$$\bar{S}(k) = \begin{cases} f_n(k), \ \hat{k}_n \leq k < \hat{k}_{n+1}, \ n \in \{0, 1, \ldots, N-3\} \\ \\ f_n(k), \ \hat{k}_n \leq k \leq \hat{k}_{n+1}, \ n = N-2 \end{cases} \tag{F.2}$$

where

$$f_n(k) = a_n + b_n(k - \hat{k}_n) + c_n(k - \hat{k}_n)^2 + d_n(k - \hat{k}_n)^3 \tag{F.3}$$

That is, $\bar{S}(k)$ is a piecewise function, divided into $N-1$ distinct segments (which span the domains $[\hat{k}_0, \hat{k}_1)$, $[\hat{k}_1, \hat{k}_2), \ldots$, $[\hat{k}_{N-3}, \hat{k}_{N-2})$,$[\hat{k}_{N-2}, \hat{k}_{N-1}]$, respectively). Each segment is defined by its own function $f_n(k)$, which is a cubic polynomial with coefficients $\{a_n, b_n, c_n, d_n\}$. We will refer to these as our 'spline coefficents'. In order to determine the values of our spline coefficients from $\tilde{\mathbf{s}}$, we must precisely define what we meant when we said that $\bar{S}(k) \approx \tilde{S}(k)$. Since $4N - 4$ spline coefficients are required, we must define $4N - 4$ constraints.

F.2.3 Constraints

Left-hand equality constraint   Naturally, given that we know the value of $\tilde{S}(k)$ for each $\hat{k}_n$, we wish enforce that $\bar{S}(\hat{k}_n) = \tilde{S}(\hat{k}_n)$ for $n \in \{0, 1, \ldots, N-1\}$. From this, we first obtain $N-1$ constraints of the form:

$$\tilde{S}(\hat{k}_n) = f_n(\hat{k}_n) \tag{F.4a}$$

$$\tilde{S}(\hat{k}_n) = a_n + b_n(\hat{k}_n - \hat{k}_n) + c_n(\hat{k}_n - \hat{k}_n)^2 + d_n(\hat{k}_n - \hat{k}_n)^3 \tag{F.4b}$$

$$\tilde{S}(\hat{k}_n) = a_n \tag{F.4c}$$

for $n \in \{0, 1, \ldots, N-2\}$.

Right-hand equality constraint/0th-order continuity constraint   Since our real spectral signal $\tilde{S}(k)$ is expected to take the form of a continuous function, we also wish to make $\bar{S}(k)$ continuous. From this, we obtain an additional $N-1$ constraints of the form:

$$\tilde{S}(\hat{k}_{n+1}) = f_n(\hat{k}_{n+1}) \tag{F.5a}$$

$$\tilde{S}(\hat{k}_{n+1}) = a_n + b_n(\hat{k}_{n+1} - \hat{k}_n) + c_n(\hat{k}_{n+1} - \hat{k}_n)^2 + d_n(\hat{k}_{n+1} - \hat{k}_n)^3 \tag{F.5b}$$

$$\tilde{S}(\hat{k}_{n+1}) = a_n + b_n\Delta\hat{k}_n + c_n\Delta\hat{k}_n^2 + d_n\Delta\hat{k}_n^3 \tag{F.5c}$$

for $n \in \{0, 1, \ldots, N-2\}$ and $\Delta\hat{k}_n = \hat{k}_{n+1} - \hat{k}_n$.

1st-order continuity constraint   It is also reasonable to expect $\tilde{S}(k)$ (and by extension, $\bar{S}(k)$) to be smooth/differentiable. Assuming that the first derivative of

$\bar{S}(k)$ is continuous, we obtain $N - 2$ constraints of the form:

$$\frac{\partial f_{n+1}}{\partial k}(\hat{k}_{n+1}) = \frac{\partial f_n}{\partial k}(\hat{k}_{n+1}) \tag{F.6a}$$

$$b_{n+1} + 2c_{n+1}(\hat{k}_{n+1} - \hat{k}_{n+1}) + 3d_{n+1}(\hat{k}_{n+1} - \hat{k}_{n+1})^2 = b_n + 2c_n(\hat{k}_{n+1} - \hat{k}_n) + 3d_n(\hat{k}_{n+1} - \hat{k}_n)^2 \tag{F.6b}$$

$$b_{n+1} = b_n + 2c_n\Delta\hat{k}_n + 3d_n\Delta\hat{k}_n^2 \tag{F.6c}$$

for $n \in \{0, 1, \ldots, N - 3\}$.

2$^{\text{nd}}$-order continuity constraint   Using the same reasoning as above, assuming that the second derivative of $\bar{S}(k)$ is continuous, we obtain $N - 2$ constraints of the form:

$$\frac{\partial^2 f_{n+1}}{\partial k^2}(\hat{k}_{n+1}) = \frac{\partial^2 f_n}{\partial k^2}(\hat{k}_{n+1}) \tag{F.7a}$$

$$2c_{n+1} + 6d_{n+1}(\hat{k}_{n+1} - \hat{k}_{n+1}) = 2c_n + 6d_n(\hat{k}_{n+1} - \hat{k}_n) \tag{F.7b}$$

$$c_{n+1} = c_n + 3d_n\Delta\hat{k}_n \tag{F.7c}$$

for $n \in \{0, 1, \ldots, N - 3\}$.

Boundary conditions   In total, we have amassed $4N - 6$ constraints. We require two additional constraints in order to obtain a total of $4N - 4$. These constraints take the form of boundary conditions on the first and/or second derivative of $\bar{S}(k)$. Here, we will assume that:

$$\frac{\partial^2 \bar{S}}{\partial k^2}(\hat{k}_0) = \frac{\partial^2 \bar{S}}{\partial k^2}(\hat{k}_{N-1}) = 0 \tag{F.8}$$

This yields two distinct constraints of the form:

$$0 = \frac{\partial^2 f_0}{\partial k^2}(\hat{k}_0) \tag{F.9a}$$

$$0 = 2c_0 + 6d_0(\hat{k}_0 - \hat{k}_0) \tag{F.9b}$$

$$0 = c_0 \tag{F.9c}$$

and

$$0 = \frac{\partial^2 f_{N-2}}{\partial k^2}(\hat{k}_{N-1}) \tag{F.10a}$$

$$0 = 2c_{N-2} + 6d_{N-2}(\hat{k}_{N-1} - \hat{k}_{N-2}) \tag{F.10b}$$

$$0 = c_{N-2} + 3d_{N-2}\Delta\hat{k}_{N-2} \tag{F.10c}$$

F.2.4   Combined system of equations

Finally, we have all of the constraints that we need in order to define our $4N - 4$ spline coefficients. To recapitulate, our combined constraints are:

$$\tilde{s}_n = a_n \qquad\qquad \text{for } n \in \{0, 1, \ldots, N - 2\} \tag{F.11a}$$

$$\tilde{s}_{n+1} = a_n + b_n\Delta\hat{k}_n + c_n\Delta\hat{k}_n^2 + d_n\Delta\hat{k}_n^3 \quad \text{for } n \in \{0, 1, \ldots, N - 2\} \tag{F.11b}$$

$$0 = b_n + 2c_n\Delta\hat{k}_n + 3d_n\Delta\hat{k}_n^2 - b_{n+1} \quad \text{for } n \in \{0, 1, \ldots, N - 3\} \tag{F.11c}$$

$$0 = c_n + 3d_n\Delta\hat{k}_n - c_{n+1} \qquad\qquad \text{for } n \in \{0, 1, \ldots, N - 3\} \tag{F.11d}$$

$$0 = c_0 \tag{F.11e}$$

$$0 = c_{N-2} + 3d_{N-2}\Delta\hat{k}_{N-2} \tag{F.11f}$$

We merge these constraints into a single system of linear equations, which we express in matrix-vector form as:

$$\mathbf{X}_L\tilde{\mathbf{s}} = \mathbf{X}_R\mathbf{a} \tag{F.12}$$

295

where $\mathbf{X}_L$ and $\mathbf{X}_R$ are our 'condition matrices' (of size $(4N-4)\times N$ and $(4N-4)\times$ $(4N-4)$, respectively) and $\mathbf{a}$ is a $(4N-4)\times 1$ vector which concatenates all of our spline coefficients:

$$\mathbf{a} = \langle a_0, b_0, c_0, d_0, a_1, b_1, c_1, d_1, \ldots a_{N-2}, b_{N-2}, c_{N-2}, d_{N-2}\rangle^T \tag{F.13}$$

Equation (F.12) encodes a large and sparse system of equations (which do not fit well on paper). For example, if $N = 3$, then Eqn. (F.12) would be:

$$
\begin{bmatrix}
1 & 0 & 0 \\
0 & 1 & 0 \\
0 & 1 & 0 \\
0 & 0 & 1 \\
0 & 0 & 0 \\
0 & 0 & 0 \\
0 & 0 & 0 \\
0 & 0 & 0
\end{bmatrix}
\begin{bmatrix}
\tilde{s}_0 \\
\tilde{s}_1 \\
\tilde{s}_2
\end{bmatrix}
=
\begin{bmatrix}
1 & 0 & 0 & 0 & 0 & 0 & 0 & 0 \\
0 & 0 & 0 & 0 & 1 & 0 & 0 & 0 \\
1 & \Delta\hat{k}_0 & \Delta\hat{k}_0^2 & \Delta\hat{k}_0^3 & 0 & 0 & 0 & 0 \\
0 & 0 & 0 & 0 & 1 & \Delta\hat{k}_1 & \Delta\hat{k}_1^2 & \Delta\hat{k}_1^3 \\
0 & 1 & 2\Delta\hat{k}_0 & 3\Delta\hat{k}_0^2 & 0 & -1 & 0 & 0 \\
0 & 0 & 1 & 3\Delta\hat{k}_0 & 0 & 0 & -1 & 0 \\
0 & 0 & 1 & 0 & 0 & 0 & 0 & 0 \\
0 & 0 & 0 & 0 & 0 & 0 & 1 & 3\Delta\hat{k}_1
\end{bmatrix}
\begin{bmatrix}
a_0 \\
b_0 \\
c_0 \\
d_0 \\
a_1 \\
b_1 \\
c_1 \\
d_1
\end{bmatrix}
\tag{F.14}
$$

Generating compact expressions for $\mathbf{X}_L$ and $\mathbf{X}_R$ given an arbitrary value of N is a little more challenging. The expressions below are in a form which was convenient for the MATLAB example provided at the end of this appendix. Using our five types of constraints detailed previously, we define $\mathbf{X}_L$ as the vertical

concatenation of five constraint matrices: $\mathbf{X}_{L,1}, \mathbf{X}_{L,2}, \ldots, \mathbf{X}_{L,5}$ of the form:

$$\mathbf{X}_{L,1} = \begin{bmatrix} \mathbf{I}_{N-1} & \mathbf{0}^{(N-1)\times 1} \end{bmatrix} \tag{F.15a}$$

$$\mathbf{X}_{L,2} = \begin{bmatrix} \mathbf{0}^{(N-1)\times 1} & \mathbf{I}_{N-1} \end{bmatrix} \tag{F.15b}$$

$$\mathbf{X}_{L,3} = \mathbf{0}^{(N-2)\times N} \tag{F.15c}$$

$$\mathbf{X}_{L,4} = \mathbf{0}^{(N-2)\times N} \tag{F.15d}$$

$$\mathbf{X}_{L,5} = \mathbf{0}^{2\times N} \tag{F.15e}$$

where $\mathbf{I}_{N-1}$ denotes the $(N-1)\times(N-1)$ identity matrix and $\mathbf{0}^{P\times Q}$ denotes a $P \times Q$ matrix of zeroes. Analogously, we define $\mathbf{X}_R$ as the vertical concatenation of five constraint matrices: $\mathbf{X}_{R,1}, \mathbf{X}_{R,2}, \ldots, \mathbf{X}_{R,5}$ of the form:

$$\mathbf{X}_{R,1} = (\mathbf{I}_{N-1} \otimes [1\ 0\ 0\ 0]) \tag{F.16a}$$

$$\mathbf{X}_{R,2} = (\mathbf{I}_{N-1} \otimes [1\ 1\ 1\ 1]) \circ \left(\mathbf{1}^{(N-1)\times 1}\mathbf{\Delta}_0\right) \tag{F.16b}$$

$$\mathbf{X}_{R,3} = \left(\left(\begin{bmatrix} \mathbf{I}_{N-2} & \mathbf{0}^{(N-2)\times 1} \end{bmatrix} \otimes [0\ 1\ 2\ 3]\right) + \left(\begin{bmatrix} \mathbf{0}^{(N-2)\times 1} & \mathbf{I}_{N-2} \end{bmatrix} \otimes [0\ -1\ 0\ 0]\right)\right) \circ \left(\mathbf{1}^{(N-2)\times 1}\mathbf{\Delta}_1\right) \tag{F.16c}$$

$$\mathbf{X}_{R,4} = \left(\left(\begin{bmatrix} \mathbf{I}_{N-2} & \mathbf{0}^{(N-2)\times 1} \end{bmatrix} \otimes [0\ 0\ 1\ 3]\right) + \left(\begin{bmatrix} \mathbf{0}^{(N-2)\times 1} & \mathbf{I}_{N-2} \end{bmatrix} \otimes [0\ 0\ -1\ 0]\right)\right) \circ \left(\mathbf{1}^{(N-2)\times 1}\mathbf{\Delta}_2\right) \tag{F.16d}$$

$$\mathbf{X}_{R,5} = \begin{bmatrix} \begin{bmatrix} 0 & 0 & 1 & 0 \\ 0 & 0 & 0 & 0 \end{bmatrix} & \mathbf{0}^{2\times(4N-12)} & \begin{bmatrix} 0 & 0 & 0 & 0 \\ 0 & 0 & 1 & 3\Delta\hat{k}_{N-2} \end{bmatrix} \end{bmatrix} \tag{F.16e}$$

where '$\otimes$' denotes the Kronecker product, '$\circ$' denotes the Hadamard product, $\mathbf{1}^{P\times Q}$ denotes a $P \times Q$ matrix of ones, and $\mathbf{\Delta}_0$, $\mathbf{\Delta}_1$, and $\mathbf{\Delta}_2$ are $1 \times (4N-4)$ row vectors given by:

$$\mathbf{\Delta}_0 = \langle 1, \Delta\hat{k}_0, \Delta\hat{k}_0^2, \Delta\hat{k}_0^3, 1, \Delta\hat{k}_1, \Delta\hat{k}_1^2, \Delta\hat{k}_1^3, \ldots, 1, \Delta\hat{k}_{N-2}, \Delta\hat{k}_{N-2}^2, \Delta\hat{k}_{N-2}^3 \rangle \tag{F.17a}$$

$$\mathbf{\Delta}_1 = \langle 0, 1, \Delta\hat{k}_0, \Delta\hat{k}_0^2, 0, 1, \Delta\hat{k}_1, \Delta\hat{k}_1^2, \ldots, 0, 1, \Delta\hat{k}_{N-2}, \Delta\hat{k}_{N-2}^2 \rangle \tag{F.17b}$$

$$\mathbf{\Delta}_2 = \langle 0, 0, 1, \Delta\hat{k}_0, 0, 0, 1, \Delta\hat{k}_1, \ldots, 0, 0, 1, \Delta\hat{k}_{N-2} \rangle \tag{F.17c}$$

We can obtain the values of our $4N - 4$ spline coefficients via:

$$\mathbf{a} = \mathbf{X}_R^{-1}\mathbf{X}_L\tilde{\mathbf{s}} \tag{F.18}$$

Since the system of equations defined in Eqn. (F.12) is sparse, Eqn. (F.18) above is *not* how interpolation routines solve for $\mathbf{a}$, in practice. Instead, other efficient solving routines are typically available which do not require explicitly creating the matrices $\mathbf{X}_L$ and $\mathbf{X}_R$. However, we will not concern ourselves with computational efficiency here, since this is merely a learning exercise. It is time to move on to the next step!

F.2.5 Constructing the cubic spline interpolator

Now that we have our vector of spline coefficients $\mathbf{a}$, we must construct an interpolator which we can use to generate $\bar{\mathbf{s}}$. Define an indicator matrix:

$$\mathcal{I} \in \mathbb{R}^{M \times (N-1)} : \mathcal{I}_{m,n} = \begin{cases} 1, & \hat{k}_n \leq k_m < \hat{k}_{n+1}, \; m \in \{0, 1, \ldots, M-1\}, \; n \in \{0, 1, \ldots, N-3\} \\ 1, & \hat{k}_n \leq k_m \leq \hat{k}_{n+1}, \; m \in \{0, 1, \ldots, M-1\}, \; n = N-2 \\ 0, & \text{otherwise} \end{cases}$$

$$\tag{F.19}$$

The indicator matrix $\mathcal{I}$ contains a '1' wherever a given query point k_m lies within a given segment (of the $N - 1$ total segments) of our piecewise expression for $\bar{S}(k)$ (i.e., Eqn. (F.2)), and a '0' everywhere else. In other words, this function defines which of the $N - 1$ polynomial functions $f_n(k)$ should be used to evaluate $\bar{S}(k_m) \approx \tilde{S}(k_m)$ for a given value of k_m. We may now obtain $\bar{\mathbf{s}}$ via:

$$\bar{\mathbf{s}} = \mathbf{K}_{\mathcal{I}}\mathbf{a} \tag{F.20}$$

where

$$\mathbf{K}_{\mathcal{I}} = (\mathcal{I} \otimes [1\ 1\ 1\ 1]) \circ \mathbf{K} \tag{F.21}$$

and **K** is a block matrix of the form:

$$\mathbf{K} = \begin{bmatrix} \mathbf{k}_{0,0} & \mathbf{k}_{0,1} & \dots & \mathbf{k}_{0,N-2} \\ \mathbf{k}_{1,0} & \mathbf{k}_{1,1} & \dots & \mathbf{k}_{1,N-2} \\ \vdots & \vdots & \ddots & \vdots \\ \mathbf{k}_{M-1,0} & \mathbf{k}_{M-1,1} & \dots & \mathbf{k}_{M-1,N-2} \end{bmatrix} \tag{F.22}$$

where $\mathbf{k}_{m,n} = \begin{bmatrix} 1 & \Delta k_{m,n} & \Delta k_{m,n}^2 & \Delta k_{m,n}^3 \end{bmatrix}$ and $\Delta k_{m,n} = k_m - \hat{k}_n$.

Combining Eqns. (F.1), (F.18), and (F.20), we obtain:

$$\bar{\mathbf{s}} = \mathbf{W}\tilde{\mathbf{s}} = \mathbf{K}_{\mathcal{I}}\mathbf{X}_R^{-1}\mathbf{X}_L\tilde{\mathbf{s}} \tag{F.23}$$

That is, we do not even need to directly compute our spline coefficients in order to obtain our interpolated/resampled signal $\bar{\mathbf{s}}$. We can merely combine all of our prior steps into a single matrix multiplication step (i.e., multiplication of the input data vector $\tilde{\mathbf{s}}$ by **W**, an $M \times N$ matrix of 'resampling weights'). Since the set of sampling points $\hat{k}_n$ and query points k_m are unlikely to (and perhaps never) change for a given OCT system, we need only compute the entries of **W** once, after which the values can be 'recycled' during subsequent rounds of OCT image reconstruction.

Since **W** is a sparse matrix, we can approximate/sparsify **W** by, for example, only recording the values and indices of the L largest (in magnitude) elements along each row of **W**. This allows for the construction of a look-up table (LUT) which enables simple and efficient resampling of large quantities of OCT spectral data. A similar procedure can be performed for any other interpolation scheme which can be expressed via Eqn. (F.1) (e.g., sinc-weighted interpolation,

up-sampling followed by linear interpolation, etc.). Therefore, I will almost always recommend constructing a pre-built LUT[4] rather than spending time optimizing the speed of some interpolation routine. In fact, most 'good' high-order interpolators used for OCT image reconstruction will yield similar resampling matrices and/or LUTs, since they are (approximately) performing the same final task (i.e., approximating values of a function via local weighted sums).

F.3   Example implementation

```
%% SET UP ------------------------------------- %%
clear all, close all, clc
% Spectrometer parameters
c = [ 7.08048E2  ...
       9.91928E-2 ...
      -3.96682E-6 ...
      -3.84179E-10]; % Spectrometer coeffs
N = 2048; % Number of pixels

% Non-uniformly spaced sampling points
p      = (1:N)';
lambda = 1E-3*(c(1)+c(2)*p+c(3)*p.^2+c(4)*p.^3);
khat   = 2*pi./lambda;

% Handle ascending vs. descending order of khat
if (khat(2)-khat(1))>0
    flip = 'false';
else
    flip = 'true';
    khat = flipud(khat);
end

% Uniformly spaced query points
M  = N; % Number of query points
km = linspace(khat(1),khat(end),M)';

%% SPLINE CONSTRUCTION (INEFFICIENT) ---------- %%
% Left condition matrix
XL1 = [eye(N-1) zeros(N-1,1)];
XL2 = [zeros(N-1,1) eye(N-1)];
XL3 = zeros(N-2,N);
XL4 = zeros(N-2,N);
```

---

[4]Or perhaps an OCT reconstruction matrix. See Chapter 3.7.

```
XL5 = zeros(2,N);
XL  = cat(1,XL1,XL2,XL3,XL4,XL5);

% Right condition matrix
Delta_khat = khat(2:end) - khat(1:end-1);
Delta_0    = kron(Delta_khat',[1 1 1 1]).^...
             repmat([0 1 2 3],[1 N-1]);
Delta_1    = kron(Delta_khat',[0 1 1 1]).^...
             repmat([1 0 1 2],[1 N-1]);
Delta_2    = kron(Delta_khat',[0 0 1 1]).^...
             repmat([1 1 0 1],[1 N-1]);

XR1 = kron(eye(N-1),[1 0 0 0]);
XR2 = kron(eye(N-1),[1 1 1 1]).*...
      (ones(N-1,1)*Delta_0);
XR3 = (kron([eye(N-2) zeros(N-2,1)],[0  1  2 3])  +...
       kron([zeros(N-2,1) eye(N-2)],[0 -1  0 0])).*...
      (ones(N-2,1)*Delta_1);
XR4 = (kron([eye(N-2) zeros(N-2,1)],[0  0  1 3])  +...
       kron([zeros(N-2,1) eye(N-2)],[0  0 -1 0])).*...
      (ones(N-2,1)*Delta_2);
XR5 = zeros(2,4*N-4);
XR5(1,3)=1; XR5(2,end-1:end)=[1 3*Delta_khat(end)];
XR  = cat(1,XR1,XR2,XR3,XR4,XR5);

%% INTERPOLATOR CONSTRUCTION ----------------- %%
% Indicator function
I = (km >= khat(1:N-1)') & ...
    [(km < khat(2:N-1)')  (km <= khat(N))];

% Interpolation matrix
K   = kron(km-khat(1:N-1)',[1 1 1 1]).^...
      repmat([0 1 2 3],[M (N-1)]);
K_I = kron(I,[1 1 1 1]).*K;

%% RESAMPLING MATRIX (INEFFICIENT) ----------- %%
W = K_I*(inv(XR)*XL);
if (flip), W = flipud(fliplr(W)); end

%% EXAMPLE RESULTS -------------------------- %%
% Example signal to resample/interpolate
z       = 50; % Example observed OPL (um)
s_true  = cos(z*km);   % 'True' signal
s_tilde = cos(z*khat); % Raw data (Non-uniform)

% Handle acending/descending order
if (flip)
    s_tilde = flipud(s_tilde);
    s_true  = flipud(s_true);
end

s_bar = W*s_tilde;   % Interpolated signal
```

```
figure(1);
plot(p,s_true ,'b-','LineWidth',5); hold on
plot(p,s_tilde,'r-','LineWidth',2);
plot(p,s_bar  ,'g-','LineWidth',2); hold off
xlim([1 N]), ylim(1.5*[-1 1]); grid on
legend('True signal','Non-uniform sampling','Resampled');

%% SPARSIFICATION (LUT) --------------------- %%
L = 4; % # of weighting coeffs to preserve per row
[dummy,index] = sort(abs(W),2,'descend');
index  = index(:,1:L); % Resampling indices
extract = sub2ind(size(W),repmat((1:N)',[1 L]),index);
weight  = W(extract); % Resampling weights

% Look-up table consists of 'index' and 'weight'
s_bar_LUT = sum(weight.*s_tilde(index),2);

figure(2);
plot(p,s_bar    ,'b-','LineWidth',5); hold on
plot(p,s_bar_LUT,'r-','LineWidth',2); hold off
xlim([1 N]), ylim(1.5*[-1 1]); grid on
legend('Resampled','Resampled with LUT');
```

APPENDIX G

USEFUL FOURIER TRANSFORMS

For instructional purposes, this appendix derives useful Fourier transform relationships that appear throughout this dissertation.

G.1 The Fourier transform

Fourier analysis is used to decompose a given function into a weighted sum of parametrized basis functions. For 1D signals, these basis functions are of the form: $e^{j\omega t} = \cos(\omega t) + j\sin(\omega t)$, where $j = \sqrt{-1}$, and ω is the angular frequency. (For higher-dimensional functions, the ωt term is generalized to a dot product of 'frequency' and 'time/space' vectors $\omega \cdot \mathbf{t}$.) The Fourier transform computes the weight of each basis function via an inner product/projection operation:

$$\tilde{f}(\omega) = \mathcal{F}_{t\to\omega}\left[f(t)\right] = \int_{-\infty}^{\infty} f(t)e^{-j\omega t}\, dt \tag{G.1}$$

In contrast, the inverse Fourier transform 'rebuilds' a function by performing a weighted sum of basis functions:

$$f(t) = \mathcal{F}_{t\to\omega}^{-1}\left[\tilde{f}(\omega)\right] = \int_{-\infty}^{\infty} \tilde{f}(\omega)e^{j\omega t}\, d\omega \tag{G.2}$$

These transforms are often normalized to ensure that performing $\mathcal{F}\left[\mathcal{F}^{-1}\left[f(t)\right]\right]$ returns *exactly* $f(t)$ and not some proportionally scaled version of the function. However, in this dissertation, normalization coefficients will be ignored, since they do not have bearing on the final *structure* that appears in image signals.

G.2 Dirac delta function

The delta function frequently arises in the analysis of linear systems. For a delta function centered at $t = T$, the 'sampling property' of the delta function yields:

$$\mathcal{F}\left[\delta(t - T)\right] = \int_{-\infty}^{\infty} \delta(t - T)e^{-j\omega t}\, dt \qquad \text{(G.3a)}$$

$$= e^{-j\omega T} \qquad \text{(G.3b)}$$

Likewise, the inverse Fourier transform of a delta function in the frequency domain $\delta(\omega - \omega_m)$ will be $e^{j\omega_m t}$. These functions have interesting implications, some of which are discussed in Appendix C.

G.3 Shifting/Modulation

A function $f(t)$ may be converted to the shifted function $f(t - T)$ by using the sampling property of the delta function:

$$f(t - T) = \int_{-\infty}^{\infty} f(\tau)\delta((t - T) - \tau)\, d\tau \qquad \text{(G.4)}$$

We may now derive the Fourier transform of $f(t - T)$ as:

$$\mathcal{F}\left[f(t - T)\right] = \int_{-\infty}^{\infty}\left(\int_{-\infty}^{\infty} f(\tau)\delta((t - T) - \tau)\, d\tau\right)e^{-j\omega t}\, dt \qquad \text{(G.5a)}$$

$$= \int_{-\infty}^{\infty} f(\tau)\left(\int_{-\infty}^{\infty}\delta((t - T) - \tau)e^{-j\omega t}\, dt\right)d\tau \qquad \text{(G.5b)}$$

$$= \int_{-\infty}^{\infty} f(\tau)e^{-j\omega(T+\tau)}\, d\tau \qquad \text{(G.5c)}$$

$$= \int_{-\infty}^{\infty} f(\tau)e^{-j\omega\tau}\, d\tau\, e^{-j\omega T} \qquad \text{(G.5d)}$$

$$= \tilde{f}(\omega)e^{-j\omega T} \qquad \text{(G.5e)}$$

Likewise, the inverse Fourier transform of a shifted function in the frequency domain $\tilde{f}(\omega - \omega_m)$ will be $f(t)e^{j\omega_m t}$.

G.4 Convolution/Multiplication

The convolution product of two functions $f(t)$ and $g(t)$ is given by:

$$f(t) \star g(t) = \int_{-\infty}^{\infty} f(\tau)g(t - \tau)\,d\tau \tag{G.6}$$

The Fourier transform of this operation yields:

$$\mathcal{F}\left[f(t) \star g(t)\right] = \int_{-\infty}^{\infty} \left(\int_{-\infty}^{\infty} f(\tau)g(t - \tau)\,d\tau\right) e^{-j\omega t}\,dt \tag{G.7a}$$

$$= \int_{-\infty}^{\infty} f(\tau)\left(\int_{-\infty}^{\infty} g(t - \tau)e^{-j\omega t}\,dt\right)d\tau \tag{G.7b}$$

$$= \int_{-\infty}^{\infty} f(\tau)\left(\tilde{g}(\omega)e^{-j\omega\tau}\right)d\tau \tag{G.7c}$$

$$= \int_{-\infty}^{\infty} f(\tau)e^{-j\omega\tau}\,d\tau\,\tilde{g}(\omega) \tag{G.7d}$$

$$= \tilde{f}(\omega)\tilde{g}(\omega) \tag{G.7e}$$

Likewise, the inverse Fourier transform of the convolution product in the frequency domain $\tilde{f}(\omega) \star \tilde{g}(\omega)$ will be $f(t)g(t)$. This makes Fourier transforms extremely useful for calculating convolution products (by converting them into simple multiplication operations).

G.5   Differentiation

Fourier transforms are often used in solving differential equations. The Fourier transform of the derivative of $f(t)$ is given by:

$$\mathcal{F}\left[\frac{\partial}{\partial t}f(t)\right] = \int_{-\infty}^{\infty} \frac{\partial}{\partial t}\left[f(t)\right]e^{-j\omega t}\,dt \tag{G.8a}$$

$$= \int_{-\infty}^{\infty} \frac{\partial}{\partial t}\left[\int_{-\infty}^{\infty} \tilde{f}(\omega)e^{j\omega t}\,d\omega\right]e^{-j\omega t}\,dt \tag{G.8b}$$

$$= \int_{-\infty}^{\infty}\int_{-\infty}^{\infty} (j\omega)\tilde{f}(\omega)e^{j\omega t}\,d\omega\, e^{-j\omega t}\,dt \tag{G.8c}$$

$$= \mathcal{F}\left[\mathcal{F}^{-1}\left[(j\omega)\tilde{f}(\omega)\right]\right] \tag{G.8d}$$

$$= (j\omega)\tilde{f}(\omega) \tag{G.8e}$$

Likewise, the inverse Fourier transform of $\frac{\partial}{\partial \omega}\tilde{f}(\omega)$ will be $(-jt)f(t)$.

G.6   Gaussian function

Gaussian beams are commonly used in beam-scanning optical systems. Let $f(t)$ be a Gaussian function of the form $f(t) = e^{-at^2}$, for $a \in \mathbb{C}$. The Fourier transform

of $f(t)$ can be derived via the following procedure:

$$f(t) = e^{-at^2} \tag{G.9a}$$

$$\frac{\partial}{\partial t} f(t) = (-2at)e^{-at^2} \tag{G.9b}$$

$$\frac{\partial}{\partial t} f(t) = (2a/j)(-jt)f(t) \tag{G.9c}$$

$$(j\omega)\tilde{f}(\omega) = (2a/j)\frac{\partial}{\partial \omega}\tilde{f}(\omega) \tag{G.9d}$$

$$\frac{\partial \tilde{f}(\omega)/\partial \omega}{\tilde{f}(\omega)} = -\frac{\omega}{2a} \tag{G.9e}$$

$$\ln\left(\tilde{f}(\omega)\right) = -\frac{\omega^2}{4a} + c_0 \tag{G.9f}$$

$$\tilde{f}(\omega) = \tilde{f}(0)e^{-\omega^2/4a} \tag{G.9g}$$

The scalar coefficient $\tilde{f}(0)$ will be given by $\int_{-\infty}^{\infty} f(t)\,dt$. Rather than solve the 1D case, we will instead move on and solve the 2D case, since the analysis of Gaussian beams relies on 2D Gaussian functions. Let $f(x,y) = e^{-a(x^2+y^2)}$. The Fourier transform of $f(x,y)$ is given by:

$$\tilde{f}(q_x, q_y) = \mathcal{F}_{(x,y)\to(q_x,q_y)}\left[e^{-a(x^2+y^2)}\right] \tag{G.10a}$$

$$= \int_{-\infty}^{\infty}\int_{-\infty}^{\infty} e^{-a(x^2+y^2)}e^{-j(q_x x+q_y y)}\,dx\,dy \tag{G.10b}$$

$$= \int_{-\infty}^{\infty} e^{-ax^2}e^{-jq_x x}\,dx \int_{-\infty}^{\infty} e^{-ay^2}e^{-jq_y y}\,dy \tag{G.10c}$$

$$= \mathcal{F}_{x\to q_x}\left[e^{-ax^2}\right]\mathcal{F}_{y\to q_y}\left[e^{-ay^2}\right] \tag{G.10d}$$

$$= \tilde{f}(0,0)e^{-q_x^2/4a}e^{-q_y^2/4a} \tag{G.10e}$$

$$= \tilde{f}(0,0)e^{-(q_x^2+q_y^2)/4a} \tag{G.10f}$$

where $\tilde{f}(0,0)$ is given by:

$$\tilde{f}(0,0) = \int_{-\infty}^{\infty} \int_{-\infty}^{\infty} e^{-a(x^2+y^2)} \, dx \, dy \tag{G.11a}$$

$$= \int_{0}^{2\pi} \int_{0}^{\infty} e^{-ar^2} r \, dr \, d\theta \, , r = \sqrt{x^2 + y^2} \tag{G.11b}$$

$$= \int_{0}^{2\pi} \int_{0}^{\infty} re^{-ar^2} \, dr \, d\theta \tag{G.11c}$$

$$= \int_{0}^{2\pi} \left[-\frac{1}{2a} e^{-ar^2} \right]_{r=0}^{\infty} \, d\theta \tag{G.11d}$$

$$= \int_{0}^{2\pi} \frac{1}{2a} \, d\theta \, , \mathcal{R}[a] > 0 \tag{G.11e}$$

$$= \frac{\pi}{a} \tag{G.11f}$$

Likewise, the inverse Fourier transform of $\tilde{f}(q_x, q_y) = e^{-b(q_x^2+q_y^2)}$ will be $\frac{\pi}{b} e^{-(x^2+y^2)/4b}$. Note that given these derivations, we find that $\mathcal{F}^{-1}\left[\mathcal{F}\left[e^{-a(x^2+y^2)}\right]\right] = (2\pi)^2 e^{-a(x^2+y^2)}$. The extra factor of $(2\pi)^2$ is a consequence of our unnormalized (2D) Fourier transform. So if you are performing math where such factors matter, make sure to use normalized transforms instead of the ones used here!

APPENDIX H

ORIGIN AND CONSEQUENCES OF COHERENCE GATE CURVATURE

In the derivations of Chapters 3-4, we assumed that 3D SD-OCT data is collected along the dimensions (x, y, k), where (x, y) is the lateral position of the scanning beam and k is a spectral axis which can be directly converted to depth z through a Fourier transform relation. Although it would be nice to *assume* that our final OCT image data exists on some rectangular (Cartesian) grid[1] of points in (x, y, z), this will not necessarily be what actually happens.

Coherence gate curvature (CGC) is a phenomenon which emerges from non-ideal designs and/or implementations of the sample arm optics. Specifically, CGC manifests as set of image distortions which can warp the image across all three spatial dimensions. In order to gain a basic understanding of the origin and consequences of CGC, we will need to model the position, angle, and optical path length of light rays which traverse the sample arm optics.

H.1   Ray transfer matrix analysis model

Assume a beam-scanning SD-OCT imaging system with a double-pass configuration. For simplicity, we will only concern ourselves with scanning along a single lateral dimension x. We begin with a collimated beam that is co-localized and parallel to the optical axis of our sample arm (i.e., the position-angle vector which describes the 'chief ray' (i.e., the central ray) of the beam is $\{r, \theta\} = \{0, 0\}$). The beam immediately strikes a pivoting galvanometer mirror, which modifies

---

[1]This is essential if you want to make use of the FFT to perform Fourier transforms along the $x, y,$ and/or z dimensions of your data.

the angle of the collimated beam with respect to the optical axis. After reflecting off of the mirror, the beam propagates a distance L and then passes through a thin lens (the objective lens) with focal length f. Since the beam is no longer collimated, the beam diameter now evolves as a function of the propagation distance z from the lens. There are three types of optical elements to describe in this system:

1. **Reflection from an angled mirror.** Assume that the pivot of the galvanometer mirror is aligned to the optical axis. Rotation of this mirror modifies the angle at which the reflected beam propagates into the rest of the system. Specifically, we will define this operation such that some initial ray in our collimated beam $\{r, 0\}$ will be transformed to: $\{r, \theta\}$

2. **Propagation.** For propagation over a distance L, this operation is given by the matrix: $\{[1, L], [0, 1]\}$

3. **Focusing through a thin lens.** For a thin lens with focal length f, this operation is given by the matrix: $\{[1, 0], [-1/f, 1]\}$

We can now predict the output position and angle of a ray from our input beam with respect to the optical axis via:

$$
\begin{bmatrix} r_{out} \\ \theta_{out} \end{bmatrix} = \begin{bmatrix} 1 & z \\ 0 & 1 \end{bmatrix} \begin{bmatrix} 1 & 0 \\ -1/f & 1 \end{bmatrix} \begin{bmatrix} 1 & L \\ 0 & 1 \end{bmatrix} \begin{bmatrix} r \\ \theta \end{bmatrix} \tag{H.1a}
$$

$$
= \begin{bmatrix} 1 & z \\ 0 & 1 \end{bmatrix} \begin{bmatrix} 1 & L \\ -1/f & 1-L/f \end{bmatrix} \begin{bmatrix} r \\ \theta \end{bmatrix} \tag{H.1b}
$$

$$
= \begin{bmatrix} 1-z/f & L+z-Lz/f \\ -1/f & 1-L/f \end{bmatrix} \begin{bmatrix} r \\ \theta \end{bmatrix} \tag{H.1c}
$$

H.2 Optical path length of chief ray

We next need to determine the optical path length traversed by the rays from our model above. For the chief ray, we have:

1. **Reflection from an angled mirror.** Given the previously described co-alignment of the optical axis, galvanometer pivot, and chief ray, there is no effect on OPL.

2. **Propagation.** For propagation over an axial distance L at an angle θ, the total distance traveled by the ray is $L \sec \theta \approx L(1 + (\theta^2/2))$.

3. **Focusing through a thin lens.** For a ray incident upon a thin lens (of focal length f) at a lateral position r, the optical path length incurred (up to an additive constant) is approximately $-r^2/(2f)$.

All together, following the chief ray from our model above (given by $\{r = 0, \theta\}$ immediately after reflection off of the galvanometer mirror), the OCT system will measure a double-pass OPL (up to an additive constant) of:

$$\text{OPL}(\theta, L, z) = 2\left(L\left(1 + \frac{\theta^2}{2}\right) + -\frac{(L\theta)^2}{2f} + z\left(1 + \frac{((1 - L/f)\theta)^2}{2}\right)\right) \tag{H.2a}$$

$$= 2(L + z) + L(1 - L/f)\theta^2 + z(1 - L/f)^2\theta^2 \tag{H.2b}$$

where the factor of 2 emerges from the double-pass configuration of the system.

H.3 Ideal system parameters

For an 'ideal' OCT system, the pivot of the galvanometer mirror is located at the back focal plane of the objective lens. This condition is satisfied in our model

when $L = f$, yielding the ray transfer matrix:

$$
\begin{bmatrix} r_{out} \\ \theta_{out} \end{bmatrix} = \begin{bmatrix} 1 - z/f & f + z - fz/f \\ -1/f & 1 - f/f \end{bmatrix} \begin{bmatrix} r \\ \theta \end{bmatrix} \tag{H.3a}
$$

$$
= \begin{bmatrix} 1 - z/f & f \\ -1/f & 0 \end{bmatrix} \begin{bmatrix} r \\ \theta \end{bmatrix} \tag{H.3b}
$$

Under these conditions, the chief ray is given by $\{f\theta, 0\}$ after passing through the objective lens. This means that the lateral position of the imaging beam with respect to the optical axis is $r_{out} = f\theta$, and that the beam propagates parallel to the optical axis ($\theta_{out} = 0$). The optical path length measured for the chief ray when $L = f$ is given by:

$$
\text{OPL}(\theta, L = f, z) = 2(f + z) + f(1 - f/f)\theta^2 + z(1 - f/f)^2\theta^2 \tag{H.4a}
$$

$$
= 2(f + z) \tag{H.4b}
$$

These results correspond to the ideal behavior for an OCT image system. Let's explore why this is the case.

H.4 Ideal mapping from acquisition coordinates to physical coordinates

If we control lateral beam position via rotation of the galvanometer mirror, then we only have *direct* control over the input angle θ of our collimated beam (or rather, input angles (θ_x, θ_y) for 3D image acquisition). Furthermore, our spectral data can only provide *direct* measurements of OPL (which, as we will see, does not necessarily correspond to distance along the z dimension). Whether or not

our 'acquisition coordinates' $(\theta_x, \theta_y, \text{OPL})$ map to a Cartesian grid in the 'physical coordinate' space of (x, y, z) is entirely up to the combination of our scanning procedure and the optical design of the sample arm.

For our 'ideal' imaging system above (in which $L = f$), obtaining a rectangular grid of (x, y, z) points is trivial. Since the lateral beam position is given by our chief ray position $r_{out} = f\theta$, we know that our lateral scanning position x is directly proportional to the input angle θ of our collimated beam. Therefore, if we devise a scanning procedure wherein A-scans are acquired using uniform sampling along θ, we will obtain data which is uniformly sampled along x. Likewise, since the chief ray propagates parallel to the optical axis (and the measured OPL traversed by the chief ray scales linearly with propagation distance along the optical axis), we know that our OPL 'axis' will correspond to depth within the sample. As a result, obtaining a Cartesian grid of image data in (x, y, z) requires very little effort.

A non-ideal system results in a very different story.

H.5 Non-ideal system parameters

If the galvanometer mirror is not placed at the back focal plane of the objective lens (i.e., $L = f + d$), we obtain:

$$
\begin{bmatrix} r_{out} \\ \theta_{out} \end{bmatrix} = \begin{bmatrix} 1 - z/f & (f+d) + z - (f+d)z/f \\ -1/f & 1 - (f+d)/f \end{bmatrix} \begin{bmatrix} r \\ \theta \end{bmatrix} \tag{H.5a}
$$

$$
= \begin{bmatrix} 1 - z/f & (f+d) - (d/f)z \\ -1/f & -d/f \end{bmatrix} \begin{bmatrix} r \\ \theta \end{bmatrix} \tag{H.5b}
$$

Under these conditions, the chief ray is given by $\{((f+d)-(d/f)z)\theta, (-d/f)\theta\}$ after passing through the objective lens. The beam no longer propagates parallel to the optical axis, and the lateral position of the imaging beam changes with respect to the propagation distance z. The OPL measured for the chief ray when $L = f + d$ is given (up to an additive constant) by:

$$\text{OPL}(\theta, L = f + d, z) = 2\left((f + d) + z\right) + (f + d)(1 - (f + d)/f)\theta^2 + z(1 - (f + d)/f)^2\theta^2$$

$$(\text{H.6a})$$

$$= 2(f + d + z) + (f + d)(-d/f)\theta^2 + z(-d/f)^2\theta^2 \qquad (\text{H.6b})$$

$$= 2(f + d + z) + \left(-d - \frac{d^2}{f} + \frac{d^2}{f^2}z\right)\theta^2 \qquad (\text{H.6c})$$

$$(\text{H.6d})$$

These conditions will clearly give us trouble.

H.6 Non-ideal mapping from acquisition coordinates to physical coordinates

First, we return to ray transfer results. For the chief ray:

$$\begin{bmatrix} r_{out} \\ \theta_{out} \end{bmatrix} = \begin{bmatrix} ((f + d) - (d/f)z)\theta \\ -(d/f)\theta \end{bmatrix} = \begin{bmatrix} (f - (d/f)(z - f))\,\theta \\ -(d/f)\theta \end{bmatrix} \qquad (\text{H.7})$$

Note that our lateral beam position is still proportional to θ. Therefore, a beam-scanning procedure which performs uniform sampling along input beam angle θ will still acquire data with uniform sampling along spatial position $r_{out} = x$. However, due to the constant of proportionality $f - (d/f)(z - f)$, the lateral sampling period is a function of depth z within the sample. This has the effect of

introducing non-telecentricity (i.e., a depth-dependent lateral magnification) to the OCT image. The lateral magnification matches the ideal case at the focal plane ($z = f$), but deviates asymmetrically with increasing distance from the focal plane. Specifically, lateral magnification increases with depth for positive values of d and decreases with depth for negative values of d.

The laterally varying output beam angle $-(d/f)\theta$ results in a laterally varying signal modulation (since the chief ray marks the center of the angular bandwidth of the beam). This could contribute to space-varying image distortions following a naive CAO procedure. I have never analyzed this problem in detail (specifically, whether the post-CAO distortions resulting from this signal modulation would 'cancel out' the depth-dependent lateral magnification or exacerbate it). This may be worth exploring further.

Next, we examine the optical path length measurements from the chief ray:

$$\text{OPL} = 2(f + d + z) + \left(-d - \frac{d^2}{f} + \frac{d^2}{f^2}z\right)\theta^2 \tag{H.8}$$

First, we consider how OPL evolves with respect to depth z in the sample. Ignoring factors that are constant with respect to z, OPL varies with depth as:

$$\left(2 + \left(\frac{d}{f}\theta\right)^2\right)z \tag{H.9}$$

This means that our mapping between z and OPL varies as a function of scanning angle. However, for a sufficiently small FOV (small values of θ) and/or a sufficiently small misalignment of the galvanometer mirror from the back focal plane of the objective lens (small values of d/f), the assumption that the z-axis and OPL-axis of our data are interchangeable may be an acceptable approximation. Assuming that this is the case, we next consider the *remaining* non-constant

terms which govern how OPL varies with θ:

$$-\left(d + \frac{d^2}{f}\right)\theta^2 \tag{H.10}$$

This means that the measured OPL exhibits a laterally varying offset whose magnitude increases with increasing scan angle. Because this term is *quadratic* in θ, this will cause the image signal to 'shift' along the OPL axis such that planar surfaces appear *curved* (hence the name, coherence gate *curvature*). For example, suppose we were to image a level planar surface (such as a flat sheet of glass which is perpendicular to the optical axis). For positive values of d (i.e., the galvanometer mirror is too far away from the objective lens), the surface will appear to curve 'upward' (closer to the objective lens) toward its edges. Likewise, for negative values of d (i.e., the galvanometer mirror is too close to the objective lens), the surface will appear to curve 'downward' (farther from the objective lens) toward its edges.

It is this curvature which my various computational CGC mitigation procedures seek to remove. Depth-dependent lateral magnification, scanning angle-dependent axial sampling, and laterally-varying beam modulation effects were assumed to be negligible. It may be worthwhile to explore the impact of these neglected effects in both theory and experiment. By extension, developing more advanced computational mitigation techniques may help to generate better OCT images with reduced distortion artifacts. As always, it is recommended that you build your system such that CGC is minimized naturally via optical hardware (e.g., see Appendix I). However, this may not always be possible (e.g., due aberrations within the scanning field of the imaging system). Therefore, computational CGC mitigation methods will likely remain as an important contributing step for minimizing the distortions in OCT images.

HARDWARE-BASED MITIGATION OF COHERENCE GATE CURVATURE IN PAIRED GALVANOMETER SYSTEMS

Notice of intent to publish   The methods and results detailed in this appendix are components of a manuscript which is currently (as of this writing) under preparation for submission to a scientific journal. See the beginning of Chapter 7 for details.

As mentioned in Appendix H, computational mitigation of coherence gate curvature (CGC) is necessary because it is rarely feasible to construct an ideal optical system. However, with good design practices, we can significantly reduce CGC. Unfortunately, beam-scanning OCT microscopes are often plagued by CGC artifacts due to a rampant 'bad habit' in system design. Here, I will detail this issue and present a *post hoc* solution which I have implemented in my own OCT system.

I.1   A bad habit

As discussed previously, a beam-scanning double-pass OCT system will exhibit little to no CGC when the pivot of the scanning galvanometer mirror is placed at the back focal plane of the objective lens. However, a single galvanometer mirror only enables beam scanning along a single lateral dimension. Thus, two galvanometer mirrors are required in order to scan along both lateral dimensions. Common sense tells us that it is not physically possible to place both mirrors at a single location.

Of course, we do not need to *physically* place our galvanometers at the back focal plane of the objective lens. Simply placing an *image* of the mirrors at the back focal plane of the objective lens will suffice. Therefore, we can use a telescope relay to image the first galvanometer onto the second, and then we can place the second galvanometer (or an image of it, via another telescope relay) at the back focal plane of the objective lens. Of course, this design requires two distinct galvanometer mirrors that can be moved with respect to each other and complicates system design. However, the benefits typically outweigh the costs.

As a result, this telescope relay method is a standard practice across the field of microscopy. However, many OCT systems employ a different design. Instead of using a telescope relay, both mirrors are placed very close to each other along the optical axis (with only a few millimeters of separation). Then, the mirror pair is placed such that either: 1) one mirror lies at the back focal plane of the objective lens while the other does not, or 2) neither mirror lies at the back focal plane (i.e., one lies in front while the other lies behind). The former method results in a single scanning axis which exhibits CGC, while the latter method results in both scanning axes exhibiting CGC (but with lesser magnitude along each axis than the single axis of the former method).

This design does have benefits. Since the galvanometers are placed very close together, they can be integrated into a single unit (i.e., a 2-axis galvanometer device). In turn, this can make the OCT system more compact, cheaper and easier to build, and less vulnerable to mechanical disturbances. The reduction/elimination of telescope relay optics in paired-galvanometer setups also reduces potential sources of aberration/distortion/signal loss in the microscope. All of these traits are especially important for clinical applications. In addition

318

to these obvious practical benefits, consider the fact that up until recently, OCT systems have a history of usage in 'lower resolution' applications (with resolutions on the order of 10 μm or larger). Such systems do not require carefully designed, multi-component microscope objectives. Instead, single-component, wide entrance pupil, long focal length lenses would suffice. Since CGC severity is inversely proportional to the objective lens focal length (recall the d/f term which appeared in Appendix H), CGC would not be a significant problem, so long as the galvanometer separation and FOV remained sufficiently small.

However, as time has gone on, laser source technologies have improved and demand for high-resolution, large FOV, volumetric imaging has increased.[1] It has become commonplace for more modern OCT systems to pursue higher resolution designs (e.g., with resolutions of 1-2 μm or smaller). I propose that as OCT systems move toward high resolution designs, the historical precendent of using paired galvanometer mirrors without some form of compensating optics/telescope relays has become a 'bad habit' that makes OCT systems more vulnerable to otherwise avoidable problems like CGC.

Personally, I worked with a 'bad habit' OCT system for the first few years of my PhD. Once my project specialized toward *in vitro* traction force microscopy experiments, I began using commercial microscope objective lenses. Due to the short back focal lengths of these lenses, it was not possible to place the galvanometers near enough to the back focal plane without causing a collision. I therefore installed a 1:1 magnification 4F telescope after my paired galvanometer mirrors and placed the back focal plane of my objective lens at the midpoint between the *images* of my mirrors. However, since the images of the mirrors

---

[1]My own personal speculation: increasing laser source bandwidths led to better axial resolutions, thus making OCT systems with better lateral resolution (to match the improved axial resolution) more practical and desirable.
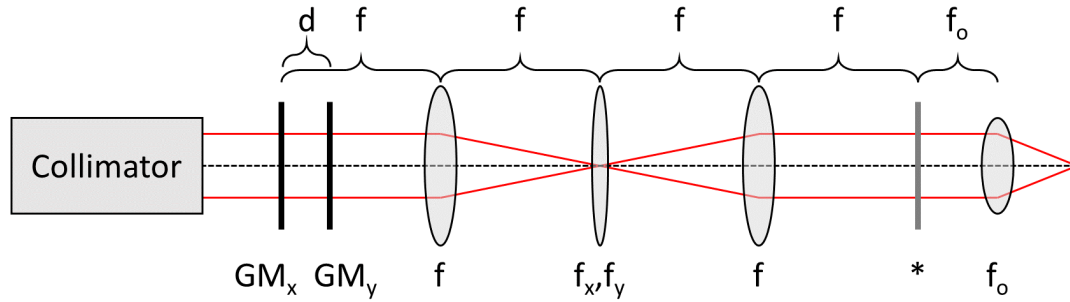
Figure I.1: Sample arm optical setup which provides a compact *post hoc* solution to coherence gate curvature (CGC) which arises from the use of paired galvanometer mirrors. A collimated beam strikes a pair of pivoting galvanometer mirrors which tilt the beam within the xz- and yz-planes (GM_x and GM_y, respectively). These mirrors are separated by a short distance d along the optical axis. After reflection, the beam enters a modified 4F telescope, consisting of a pair of lenses with focal length f and a thin cylindrical lens with focal lengths f_x and f_y (within the xz- and yz-planes, respectively) at its center. Assuming f_x and f_y are chosen properly, the two galvanometer planes are imaged to the back focal plane (denoted by '$*$') of the objective lens (with focal length f_o), thereby enabling 2D lateral beam scanning with minimal CGC artifacts.

existed at different planes along the optical axis, CGC remained a persistent problem. It was only toward the end of my program that I decided to kick the 'bad habit' and try out a new design that would minimize CGC. However, as an engineer, I wanted to achieve my goal with as little work and expenditure as possible. This motivated the solution detailed in the next section.

I.2   A *post hoc* solution to paired galvanometers

Consider the sample arm optical set up depicted in Fig. I.1. Using ray transfer matrix analysis (similar to that performed in Appendix H), we can describe the behavior of the chief ray of the input beam within the xz- and yz-planes, respectively. First, beginning at GM_x, we analyze the chief ray within the xz-plane

(while assuming $\theta_y = 0$) to obtain:

$$
\begin{bmatrix} x_{\text{out}} \\ \theta_{x,\text{out}} \end{bmatrix} = \begin{bmatrix} \frac{1}{f_o}(z - f_o) & -f_o + \frac{f^2}{f_o f_x}(z - f_o) \\ \frac{1}{f_o} & \frac{f^2}{f_o f_x} \end{bmatrix} \begin{bmatrix} 0 \\ \theta_x \end{bmatrix}
\tag{I.1a}
$$

where z denotes the propagation distance following the objective lens. Assuming that the thin cylindrical lens is flat within the xz-plane, then $f_x = \infty$ and:

$$
\begin{bmatrix} x_{\text{out}} \\ \theta_{x,\text{out}} \end{bmatrix} = \begin{bmatrix} \frac{1}{f_o}(z - f_o) & -f_o \\ \frac{1}{f_o} & 0 \end{bmatrix} \begin{bmatrix} 0 \\ \theta_x \end{bmatrix} = \begin{bmatrix} -f_o \theta_x \\ 0 \end{bmatrix}
\tag{I.2a}
$$

This corresponds to ideal beam-scanning behavior, since the lateral position of the output ray is directly proportional to the input scanning angle, and the output ray always propagates parallel to the optical axis. The OPL traversed by the chief ray through the system (in a double-pass imaging configuration) will be:

$$
\text{OPL}(z, \theta_x; \theta_y = 0) = 2(4f + f_o + z) + \text{constant}
\tag{I.3}
$$

This likewise corresponds to ideal behavior, since the OPL measured by the microscope increases linearly with z and has no dependence on θ_x. As a result, the imaging system will exhibit no CGC along the x-axis (within the limits of this idealized model).

Next, beginning at GM_y, we analyze the chief ray within the yz-plane (while assuming $\theta_x = 0$) to obtain:

$$
\begin{bmatrix} y_{\text{out}} \\ \theta_{y,\text{out}} \end{bmatrix} = \begin{bmatrix} \frac{1}{f_o}(z - f_o) & -f_o + \frac{f^2 - f_y d}{f_o f_y}(z - f_o) \\ \frac{1}{f_o} & \frac{f^2 - f_y d}{f_o f_y} \end{bmatrix} \begin{bmatrix} 0 \\ \theta_y \end{bmatrix}
\tag{I.4a}
$$

$$
= \begin{bmatrix} -f_o \theta_y + \alpha(z - f_o)\theta_y \\ \alpha \theta_y \end{bmatrix}, \text{ for } \alpha = \frac{f^2 - f_y d}{f_o f_y}
\tag{I.4b}
$$

Thus, although the lateral position of the output ray remains proportional to θ_y, since the ray no longer scans parallel to the optical axis, the system will exhibit a depth-dependent lateral magnification (i.e., non-telecentricity), which is one of the hallmarks of CGC. The OPL traversed by the chief ray through the system (in a double-pass imaging configuration, starting at GM_x) will likewise be:

$$\text{OPL}(z, \theta_y; \theta_x = 0) = 2(4f + f_o + z) + (-\alpha f_o + \alpha^2(z - f_o))\theta_y^2 + \text{constant} \qquad \text{(I.5)}$$

Here, we observe that OPL varies quadratically as a function of θ_y. This results in the namesake 'curvature' of CGC, as discussed in Appendix H. That is, *physically* flat surfaces will *appear* curved in the OCT image due to the fact that OCT microscopes use OPL measurements as a proxy for 'depth' along the z-axis (even when an exact correspondence does not necessarily hold).

Given this analysis, we can see that the parameter α describes the severity of CGC within the yz-plane.[2] I therefore hypothesized that choosing a value of f_y such that $\alpha = 0$ would remove all CGC artifacts from the imaging system. Such a scenario is realized when $f_y = f^2/d$. Given the system described in Chapter 7 (for which $f = +100$ mm and $d = +13.69$ mm), the optimal value of f_y was predicted to be $f_y = (100 \text{ mm})^2/(13.69 \text{ mm}) \approx +730$ mm. However, a non-optimal cylindrical lens with focal length $f_y = +700$ mm was used, since this was the nearest readily available component from vendors. Thus, my imaging system was not expected to completely eliminate CGC. However, compared to the case of applying no correction (i.e., when $f_y = \infty$), this system was *predicted* to reduce CGC to approximately $\alpha_{+700 \text{ mm}}/\alpha_\infty \approx 5\%$ of its original severity.

---

[2]α is analogous to the d/f term which appeared in the analyses of Appendix H.
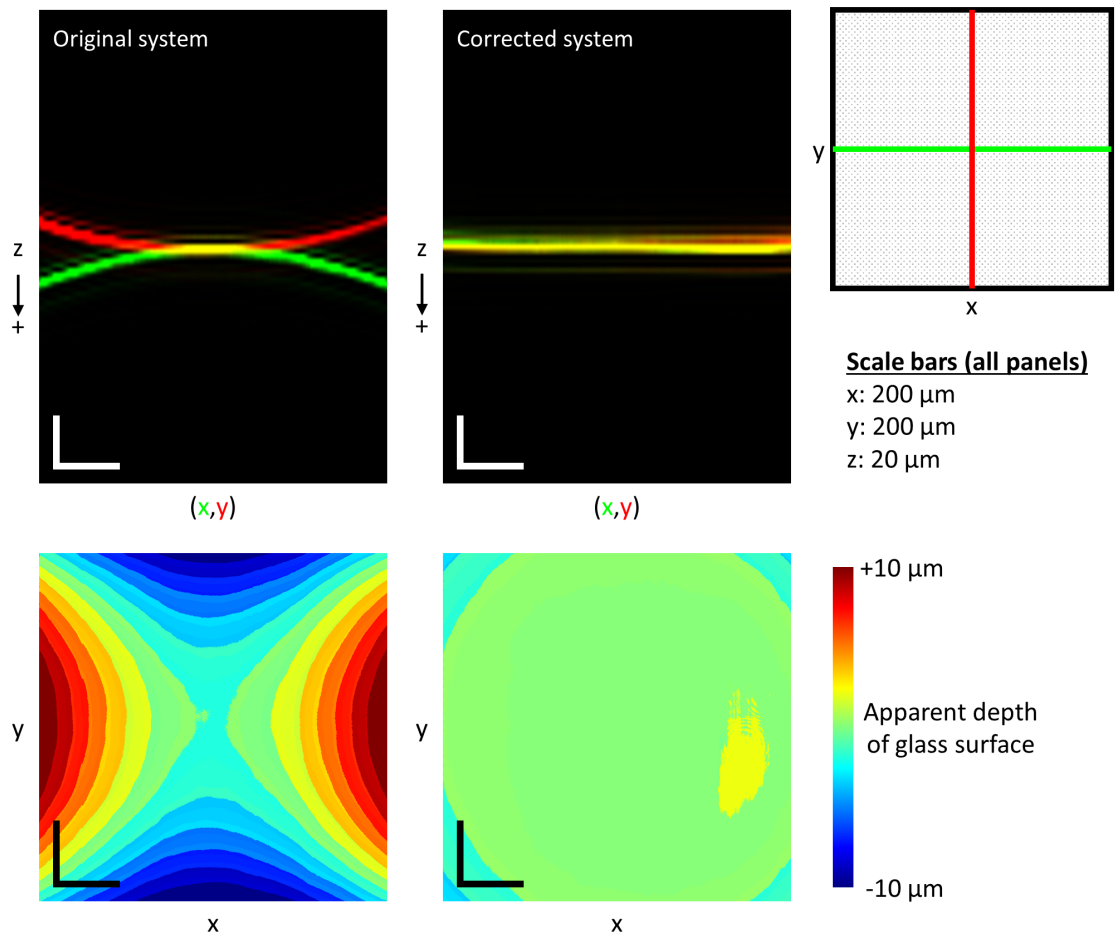
Figure I.2: Visualization of coherence gate curvature (CGC) before (left) and after (right) hardware-based compensation. The top panels depict the OCT image of a (*physically* flat) glass-air interface in the *xz-* (green) and *yz-* (red) planes intersecting the origin of the lateral FOV. Any *observed* curvature of the surface in these panels is a consequence of CGC distortions. The bottom panels depict the observed apparent depth (i.e., the optical path length) of the surface as a function of lateral position. In the original system, CGC causes image distortions which result in the (physically flat) glass surface appearing as a hyperbolic paraboloid surface. In the corrected system, the glass surface appears nearly flat (with a residual weak paraboloid shape due to non-optimal alignment). See text for details.

I.3 Experimental validation

In order to assess the performance of the proposed CGC-compensating system, I acquired images of a flat glass surface near the focal of the system, with and without the CGC-compensating cylindrical lens, and spanning a 1×1 mm² lateral FOV. The resulting images (and apparent curvature of the glass surface) are depicted in Fig. I.2. Each surface (hereafter denoted by indices $i = 1$ and $i = 2$, respectively) were fit with a quadratic polynomial:

$$z_i(x, y) = a_i x^2 + b_i xy + c_i y^2 + d_i x + e_i y + f_i \tag{I.6}$$

The terms a_i, b_i, and c_i record the apparent curvature of the glass surface and thus measure the severity of CGC. The terms d_i and e_i record the apparent tilt of the glass surface, which results from a combination of true sample tilt and/or non-ideal beam alignment within the sample arm optics (the latter of which can be compensated with an adjustable periscope placed prior to the galvanometers). The term f_i encodes the axial offset of the glass surface in the image.

The curvature terms for the imaged glass surfaces were found to have values (in units of μm^{-1}) of $a_1 = 4.585 \times 10^{-5}$, $b_1 = 0.015 \times 10^{-5}$, and $c_1 = -4.280 \times 10^{-5}$ for the uncorrected system, and $a_2 = -1.454 \times 10^{-6}$, $b_2 = 0.856 \times 10^{-6}$, and $c_2 = -2.415 \times 10^{-6}$ for the CGC-compensated system. In order to assess the total amount of CGC, a rotation of the lateral coordinate system was performed in order to make the cross-term $b_i = 0$. Specifically, defining:

$$\begin{bmatrix} x \\ y \end{bmatrix} = \begin{bmatrix} \cos\theta_i & \sin\theta_i \\ -\sin\theta_i & \cos\theta_i \end{bmatrix} \begin{bmatrix} x' \\ y' \end{bmatrix} \tag{I.7}$$

the transformed curvature terms (A_i, B_i, and C_i) were obtained via:

$$\begin{bmatrix} A_i \\ B_i \\ C_i \end{bmatrix} = \begin{bmatrix} \cos^2\theta_i & \cos\theta_i\sin\theta_i & \sin^2\theta_i \\ \sin 2\theta_i & \cos 2\theta_i & -\sin 2\theta_i \\ \sin^2\theta_i & \cos\theta_i\sin\theta_i & \cos^2\theta_i \end{bmatrix} \begin{bmatrix} a_i \\ b_i \\ c_i \end{bmatrix} \tag{I.8}$$

where $\theta_i = 0.5\arctan(b_i/(c_i - a_i))$, yielding $A_1 = 4.585 \times 10^{-5}$, $B_1 = 0$, and $C_1 = -4.280 \times 10^{-5}$ for the uncorrected system, and $A_2 = -1.291 \times 10^{-6}$, $B_2 = 0$, and $C_2 = -2.578 \times 10^{-6}$ for the CGC-compensated system. The opposite signs of A_1 and C_1 indicate positive CGC along one axis and negative CGC along the orthogonal axis, respectively. This corresponds to the scenario where the back focal plane of the objective lens is imaged by the telescope to a location that lies *between* the two galvanometer mirrors. In contrast, the matching negative signs of A_2 and C_2 indicate that the alignment of the CGC-compensated system was not optimal (i.e., the objective lens was placed too close to the telescope relay by a small margin). Despite this non-optimal alignment, the system managed to reduce CGC to *at most*:

$$\frac{\max(|A_2|, |C_2|)}{\min(|A_1|, |C_1|)} \approx 6\% \tag{I.9}$$

of its original severity, which is close to the predicted value of 5%. However, under optimal alignment conditions, we would expect to achieve the condition $A_i = -C_i$ for both systems (i.e., the back focal plane of the objective lens is imaged to a plane that lies at the midpoint between the galvanometer mirrors). Thus, defining the 'total' CGC of the system as:

$$|C_i - A_i| = |2A_i| = |2C_i| \tag{I.10}$$

under optimal alignment conditions, we can estimate that the system is capable of reducing CGC to approximately:

$$\frac{|C_2 - A_2|}{|C_1 - A_1|} \approx 1.5\% \tag{I.11}$$

of its original severity. This exceeds the predicted improvement and could be attributable to spherical aberration of the telescope lenses causing their effective focal lengths to decrease at large scanning angles (i.e., the effective value of f decreases for large values of θ_y, thus bringing the value of $\alpha_{+700\,\text{mm}}$ closer to 0 than would otherwise be expected, given the installed cylindrical lens).

Given these results, we can conclude that the modified OCT imaging system described here provides both a simple and effective method to mitigate CGC artifacts which emerge from the use of paired galvanometer mirrors. As a result, this system substantially reduces a potential source of distortions which would otherwise corrupt deformation data that is essential to traction force optical coherence microscopy. Since it remains difficult to realize an ideal system, computational methods should still be employed to mitigate small residual distortions. Such methods are detailed in Chapters 4 and 7.

APPENDIX J

A SIMPLE MECHANISM FOR GENERATING FOCAL PLANE CURVATURE

Focal plane curvature (FPC) is a phenomenon wherein the focal plane appears neither flat nor level in a reconstructed OCT image. This results in a PSF which varies with respect to the lateral variables (x, y) of the image data. As a consequence, standard defocus mitigation techniques (which assume a laterally invariant PSF) cannot restore optimal focal plane resolution across the entire FOV. FPC mitigation (detailed in Chp. 4.4) is an approximate method developed to mitigate this effect and improve resolution throughout large volumetric images. Here, we will review a simple mechanism which can induce FPC. Although this is not the *only* mechanism which can induce FPC, it is simple and instructive to model with ray transfer matrix analysis.

Consider a collimated beam (with rays described by $\{x, 0\}$) which strikes a thin lens of focal length f. The focused beam then propagates a distance $f - d$ (where $0 \leq d \leq f$) before entering a sample with refractive index n via a flat and level surface. The beam finally converges (i.e., the position component of all rays converges to zero) after propagation by a distance z into the sample. This scenario may be approximated by:

$$\begin{bmatrix} 0 \\ \theta_{out} \end{bmatrix} = \begin{bmatrix} 1 & z \\ 0 & 1 \end{bmatrix} \begin{bmatrix} 1 & 0 \\ 0 & 1/n \end{bmatrix} \begin{bmatrix} 1 & f - d \\ 0 & 1 \end{bmatrix} \begin{bmatrix} 1 & 0 \\ -1/f & 1 \end{bmatrix} \begin{bmatrix} x \\ 0 \end{bmatrix} \tag{J.1}$$

This yields the relation:

$$0 = \left(d - \frac{z}{n} \right) \frac{x}{f}, \ \forall x \tag{J.2a}$$

$$z = nd \tag{J.2b}$$

This means that the focal plane will be located at a depth of $z = nd$ *below* the sample surface. For a (slightly!) tilted sample surface (located at a position $z_c(x) = f - (d + ax)$ with respect to the objective lens), the focal plane will now be tilted (with respect to the objective lens), as given by $z_f(x) = f + (n - 1)(d + ax)$. That is, (for $n > 1$) the focal plane tilts in *opposition* to the sample surface tilt.

As a consequence, when we apply the coherence gate curvature (CGC) mitigation heuristics and procedures described in Chp. 4.4, although we obtain an image wherein the sample *surface* appears flat and level (i.e., $z_c'(x) = f - d$), the focal plane will still appear tilted (i.e., $z_f'(x) = f + (n - 1)d + nax$). In fact, the CGC mitigation procedure makes the tilt of the focal plane even *worse* than in the original image. This is why a separate procedure is required in order to 'flatten' the focal plane and restore a laterally invariant PSF such that standard (and efficient) defocus mitigation algorithms may be applied.

In practice, I have observed that the focal plane tends to exhibit very little curvature, and instead primarily exhibits tilt. This suggests that beam misalignment and/or sample tilt may be major contributing factors toward the generation of FPC. Perhaps measured values of focal plane *tilt* could be used to infer both the amount of *actual* (as opposed to apparent) sample tilt and/or bulk modulation (see Chapter 4.4)? If such a relationship could be established, perhaps it could be used to refine the coordinate system heuristics used for CGC mitigation and/or eliminate the need to perform a separate calibration step for bulk modulation (or conversely, bulk modulation calibration could be used to infer focal plane tilt)? I will leave such questions to you, dear reader, whoever you might be!

TUTORIAL ON LEAST-SQUARES POLYNOMIAL REGRESSION AND PEAK-FINDING

Least-squares polynomial regression and peak-finding were essential tools for the research of this dissertation. The equations and methods that were employed are as follows.

K.1 Least-squares polynomial regression

Assuming a function $f(x, y, z)$ can be described by a quadratic polynomial via:

$$f(x, y, z; \mathbf{a}) = a_0 + a_1 x + a_2 y + a_3 z + a_4 xy + a_5 yz + a_6 xz + a_7 x^2 + a_8 y^2 + a_9 z^2 \quad \text{(K.1)}$$

then N samples of the function ($f_i = f(x_i, y_i, z_i)$ for $i \in \{0, 1, \ldots, N-1\}$) will obey:

$$\mathbf{f} = \mathbf{X}\mathbf{a} \quad \text{(K.2)}$$

where $\mathbf{f} = \langle f_0, \ldots, f_{N-1} \rangle^T$, $\mathbf{a} = \langle a_0, \ldots, a_9 \rangle^T$, and $\mathbf{X}$ is a Vandermonde matrix:

$$\mathbf{X} = \begin{bmatrix} 1 & x_0 & y_0 & z_0 & x_0 y_0 & y_0 z_0 & x_0 z_0 & x_0^2 & y_0^2 & z_0^2 \\ \vdots & \vdots & \vdots & \vdots & \vdots & \vdots & \vdots & \vdots & \vdots & \vdots \\ 1 & x_{N-1} & y_{N-1} & z_{N-1} & x_{N-1} y_{N-1} & y_{N-1} z_{N-1} & x_{N-1} z_{N-1} & x_{N-1}^2 & y_{N-1}^2 & z_{N-1}^2 \end{bmatrix} \quad \text{(K.3)}$$

In order to perform quadratic regression/approximation of (noisy) data, $\mathbf{a}$ can be estimated from the data vector $\mathbf{f}$ and Vandermonde matrix $\mathbf{X}$. The least-squares solution to this problem is $\hat{\mathbf{a}} = \mathbf{X}^\dagger \mathbf{f}$, where '$\dagger$' denotes the left pseudo-inverse, such that $\mathbf{X}^\dagger = \left(\mathbf{X}^T \mathbf{X} \right)^{-1} \mathbf{X}^T$. Ensure that $N \gg \text{length}(\mathbf{a}) = 10$.

K.2 Peak-finding

Given a quadratic function $f(x, y, z; \mathbf{a})$, the locations of local extrema and saddle points may be found where $\nabla f(x, y, z) = \mathbf{0}$, i.e., where:

$$0 = \frac{\partial f}{\partial x} = a_1 + 2a_7 x + a_4 y + a_6 z \tag{K.4a}$$

$$0 = \frac{\partial f}{\partial x} = a_2 + a_4 x + 2a_8 y + a_5 z \tag{K.4b}$$

$$0 = \frac{\partial f}{\partial x} = a_3 + a_6 x + a_5 y + 2a_9 z \tag{K.4c}$$

Therefore, the location of a local extremum or saddle point (x_p, y_p, z_p) (if such a location exists) can be found by solving:

$$\begin{bmatrix} 0 \\ 0 \\ 0 \end{bmatrix} = \begin{bmatrix} a_1 \\ a_2 \\ a_3 \end{bmatrix} + \begin{bmatrix} 2a_7 & a_4 & a_6 \\ a_4 & 2a_8 & a_5 \\ a_6 & a_5 & 2a_9 \end{bmatrix} \begin{bmatrix} x_p \\ y_p \\ z_p \end{bmatrix} \tag{K.5}$$

K.3 Example implementation

Assume that we wish to locate the global maximum of a 3D grid of data. So long as the peak is not located near an 'edge' of the data set, we can use the following procedure in MATLAB:

```
%%----------------------------------------------%%
% VARIABLES ASSUMED TO EXIST                     %
% f : 3D Grid of data with peak far from 'edge'  %
%%----------------------------------------------%%

%% PRELIMINARY PEAK FINDING--------------------%%
[X1,X2,X3]            = size(f);
prelim                = find(f==max(f(:)));
[x1pre,x2pre,x3pre]   = ind2sub([X1 X2 X3],prelim);
% The peak is localized to an integer index!

%% LOCAL REGRESSION----------------------------%%
```

```matlab
SIZE    = 2; % Tune to adjust local neighborhood
range   = (-SIZE:SIZE)';
extract = f(x1pre+range,x2pre+range,x3pre+range);

[x1,x2,x3] = ndgrid(range,range,range);
x1 = x1(:); x2 = x2(:); x3 = x3(:);
X  = [ones(size(x1))       ...
      x1      x2      x3       ...
      x1.*x2 x2.*x3 x1.*x3 ...
      x1.^2  x2.^2  x3.^2  ]; % Vandermonde mtx
a  = X\extract(:);

%% PEAK REFINEMENT ----------------------------%%
mtx = [2*a(8)    a(5)    a(7) ;...
        a(5) 2*a(9)    a(6) ;...
        a(7)    a(6) 2*a(10)];
finetune = inv(mtx)*[-a(2); -a(3); -a(4)];

x1p = x1pre + finetune(1);
x2p = x2pre + finetune(2);
x3p = x3pre + finetune(3);
% The peak is localized to subpixel precision!
```

APPENDIX L

SUPPLEMENT TO CHAPTER 6

Content reuse disclosure   The contents (text, figures, etc.) of this appendix have been reprinted/adapted from a previously published journal paper of which I was the first author.[1] Specifically, the contents of this appendix originate in the Supplementary Information document for Ref. [112], and serve as a corresponding collection of supplementary information for Chapter 6 of this dissertation. Some sections/passages of the original work have been removed or reduced in order to avoid redundancy with other sections of this dissertation. To view the full contents of the original paper (and the associated Supplementary Information) document, please see Ref. [112].

Author contributions statement   Please see the 'Author contributions statement' provided at the beginning of Chapter 6 for an appropriate summary of author contributions.

---

[1]Reprinted/adapted as permitted under the Creative Commons Attribution 4.0 International License `http://creativecommons.org/licenses/by/4.0/`: J.A. Mulligan, X. Feng, S.G. Adie. Quantitative reconstruction of time-varying 3D cell forces with traction force optical coherence microscopy. *Sci Rep* **9**, 4086 (2019). `https://doi.org/10.1038/s41598-019-40608-4`

L.1 Methods

L.1.1 Computational image formation module

As of the writing of this dissertation, I consider this method for image reconstruction/formation to be outdated. I instead recommend using the (similar) procedure which is detailed in Chapter 7.6. However, I have included this procedure here, in reduced form, for completeness.

The procedures below detail the implementation of our computational image formation module (see Fig. 6.1). All image signal functions (denoted with an 'S') are complex-valued. For each time-point in a given time-lapse experiment, we will refer to time using an integer designation. That is, t_i will refer to the time of the ith time-point in an experiment with five-minute temporal sampling. For example, t_0 refers to zero minutes, t_1 refers to five minutes, and so on. All equations were designed for processing OCM data acquired with a Gaussian beam in a double-pass imaging configuration. All procedures were automated, except where indicated otherwise.

Initial volume reconstruction

Initial volumetric OCM images were reconstructed from raw spectral data via the standard operations of background subtraction, spectrum resampling, dispersion compensation, and the Fourier transform (see Chapter 3.7). The function $S_{\text{init}}(x, y, z, t_i)$ will refer to the image signal produced by this initial reconstruction. The full axial (z) range spanned by S_{init} contained two regions of interest, which were identified manually. The first was a 50-voxel thick region

centered on the coverslip surface of the glass-bottomed petri dish. This set of depths will be referred to as $Z_{\text{coverslip}}$. The second was a 400-voxel (500 μm) thick region centered on the imaged cell (and consequently, the focal plane, which was aligned to the cell as described in Chapter 6.6.4). This set of depths will be referred to as Z_{cell}.

Coherece gate curvature removal

Coherence gate curvature (CGC) was removed via 'CGC mitigation method 2', which is described in Chapter 4.4. CGC was measured/approximated by fitting a quadratic curve ($z_c(x, y)$ from Eqn. (4.46)) to the coverslip surface of the petri dish, as it appeared in the $Z_{\text{coverslip}}$ region of the 'full FOV' images. A different realization of $z_c(x, y)$ was obtained for each time-point t_i, which we will denote by $z_c(x, y, t_i)$. Likewise, we will denote each realization of the coefficient a_0 from Eqn. (4.46) by $a_0(t_i)$. CGC was then removed using a procedure analogous to Eqn. (4.47), specifically:

$$S_{\text{flat}}(x, y, z, t_i) = \mathcal{F}^{-1}_{z \to q_z} \left[\mathcal{F}_{z \to q_z} \left[S_{\text{init}}(x, y, z, t_i) \right] e^{j q_z \left(z_c(x,y,t_0) + z_{c,0}(t_i) \right)} \right] \tag{L.1}$$

where $z_{c,0}(t_i) = a_0(t_i) - 2a_0(t_0)$. Note that this implementation *assumes* that the curvature and tilt terms of CGC *do not change over time*.[2] This removal procedure was applied to all 'full FOV' and 'reduced FOV' images for a given time-point.

---

[2]The procedures in Chapter 7.6 do not rely on such assumptions and are therefore more robust than the method used here.

Phase registration

Following CGC removal, the coverslip surface appeared flat and level in the image signal.[3] Phase registration was then performed via 'phase registration method 1', defined in Eqn. (4.41), where $\phi_c(x, y)$ was uniquely calibrated for every individual image. We will denote the phase registered image signal by $S_{pr}(x, y, z, t_i)$.

Focal plane curvature removal

Focal plane curvature (FPC) removal followed next. FPC was measured/approximated by fitting a quadratic curve ($z_f(x, y)$ from Eqn. (4.48)) to the focal 'plane' (in reality, a curved surface) as it appeared in the Z_{cell} region of the 'full FOV' image from time t_0 (i.e., $S_{pr}(x, y, z, t_0)$). FPC was then removed using a procedure analogous to Eqn. (4.49), specifically:

$$S_f(x, y, z, t_i) = \mathcal{F}^{-1}_{z \to q_z} \left[\mathcal{F}_{z \to q_z} \left[S_{pr}(x, y, z, t_i) \right] e^{jq_z \left(z_f(x,y) - z_{f,0} \right)} \right] \tag{L.2}$$

where $z_{f,0}$ was taken to be the constant term b_0 from Eqn. (4.48). Note that this implementation *assumes* that the curvature and tilt terms of FPC *do not change over time*.[4] This removal procedure was applied to all 'full FOV' and 'reduced FOV' images.

---

[3]Rather, it appeared *nearly* flat and level, in the event of time-varying artifacts that the CGC removal methods used here did not accommodate for.

[4]I still retain *this* assumption in my current methods. Sometimes, it is simply not possible to calibrate FPC at each time-point. I also speculate that uncertainty in the FPC calibration stage likely exceeds any real changes in FPC that you would ever encounter when using a mechanically stable microscope set-up.

Bulk demodulation

Bulk demodulation followed next (see Chapter 4.4). First, modulation coefficients $(q'_x(t_i), q'_y(t_i))$ were measured from the 'full FOV' images at each time-point. Then, bulk demodulation was performed via:

$$S_{\text{demod}}(x, y, z, t_i) = S_f(x, y, z, t_i) \exp\left(-j\left(q'_x(t_i)x + q'_y(t_i)y\right)\right) \tag{L.3}$$

This bulk demodulation procedure was applied to all 'full FOV' and 'reduced FOV' images for a given time-point.[5]

Computational adaptive optics

Depth-dependent defocus was then removed via computational adaptive optics (CAO). First, each 'full FOV' image was used to measure the time-varying focal plane depth $z_{\text{focus}}(t_i)$. CAO was then performed via:

$$S(x, y, z, t_i) = \mathcal{F}^{-1}_{(x,y)\to(q_x,q_y)}\left[\mathcal{F}_{(x,y)\to(q_x,q_y)}\left[S_{\text{demod}}(x, y, z, t_i)\right] e^{-j(z-z_{\text{focus}}(t_i))\sqrt{(2nk_c)^2 - q_x^2 - q_y^2}}\right]$$
$$\tag{L.4}$$

where k_c is the central wavenumber of the raw spectral data, and $n = 1.34$ is the refractive index of the hydrogel medium. This refocusing procedure was applied to all 'full FOV' and 'reduced FOV' images for a given time-point. The resulting image signal $S(x, y, z, t_i)$ was the image used for all subsequent processing of the TFM module (e.g., bead localization and tracking, speckle reduction, segmentation, cell mesh generation, etc.).

---

[5]In practice, I found that $(q'_x(t_i), q'_y(t_i))$ did not vary substantially over time. In my most recent methods (Chapter 7.6), I have assumed that these coefficients do not vary in time (i.e., $(q'_x(t_i), q'_y(t_i))$ have been replaced with (q'_x, q'_y)). I speculate that this may indeed be the correct model, and that the slight variability observed over time is likely due to uncertainty in the calibration procedure. Such time-varying 'noise' in the calibration stage could be detrimental to image formation (by leading to time-varying bulk shearing artifacts). Thus, I have adopted the 'constant bulk demodulation parameters' approach.

Note that this image exhibits a flat *focal plane*, but still exhibits CGC (as a consequence of the FPC removal procedure).[6] This can be remedied by 'restoring' FPC to its original state in the image data (which simultaneously restores the 'zero CGC' state). However, that was not done in this study. FPC restoration was instead applied to bead displacement data and cell mesh data in later processing steps.

L.1.2 Traction force microscopy module

Pre-processing of bead position data

Time-varying bead positions were measured and tracked from OCM image data as described in Chapter 6.6.6. Let M denote the total number of tracked beads. The position of each bead $m \in \{1, 2, \ldots, M\}$ at time t_i is given by a column vector:

$$\mathbf{r}_{\text{raw},m}(t_i) = \left\langle x_{\text{raw},m}(t_i), y_{\text{raw},m}(t_i), z_{\text{raw},m}(t_i) \right\rangle \tag{L.5}$$

Note that this position data is defined in a warped coordinate system (where the focal plane, as opposed to the coverslip surface, appears flat and level), as established by Eqn. (L.2). Bead positions in the 'correct' (i.e., zero CGC) coordinate system were therefore obtained via:

$$\mathbf{r}_m(t_i) = \mathbf{r}_{\text{raw},m}(t_i) + \left\langle 0, 0, z_f\left(x_{\text{raw},m}(t_i), y_{\text{raw},m}(t_i)\right) - z_{f,0} \right\rangle \tag{L.6}$$

where $z_f(x, y)$ and $z_{f,0}$ are as defined as in Eqn. (L.2).

---

[6]Recall that CGC and FPC often do not match.

Motion correction for bead displacement data

The position data obtained from Eqn. (L.6) contained residual bulk motion artifacts.[7] Zero-order artifacts corresponded to a translational shift of the bead positions between time-points, and likely originated from drift of the sample or sample stage. First-order artifacts corresponded to small linear distortions of the entire volume spanned by the bead position data. Such artifacts could have resulted from assumption/calibration errors in our image formation routines and/or from swelling, shearing, and/or small rotational drift of the hydrogel medium (e.g., due to non-uniform temperatures). Motion-corrected bead position data $\mathbf{r}_{\mathrm{corr,m}}(t_i)$ were computed via:

$$\mathbf{r}_{\mathrm{corr,m}}(t_i) = \mathbf{r}_m(t_i) - \mathbf{u}_0(t_i) - \mathbf{A}(t_i)\mathbf{r}_m(t_i) \tag{L.7}$$

where $\mathbf{u}_0(t_i)$ is a time-varying vector which describes zero-order motion artifacts, and $\mathbf{A}(t_i)$ is a time-varying 3×3 tensor which describes first-order motion artifacts. Both motion correction parameters, $\mathbf{u}_0(t_i)$ and $\mathbf{A}(t_i)$, where estimated from the bead position data $\mathbf{r}_m(t_i)$. Specifically, both $\mathbf{u}_0(t_i)$ and $\mathbf{A}(t_i)$ were computed simultaneously via a linear least-squares procedure, achieved by solving the system of equations:

$$\mathbf{R}(t_i) - \mathbf{R}(t_{\max}) = \mathbf{R}_V(t_i) \left[\mathbf{u}_0(t_i) \quad \mathbf{A}(t_i)\right]^{\mathrm{T}} \tag{L.8}$$

where $\mathbf{R}(t_i)$ denotes a $M \times 3$ matrix of concatenated bead position data, given by:

$$\mathbf{R}(t_i) = \begin{bmatrix} \mathbf{r}_1(t_i)^{\mathrm{T}} \\ \vdots \\ \mathbf{r}_M(t_i)^{\mathrm{T}} \end{bmatrix} \tag{L.9}$$

---

[7]This might be due to the use of time-varying (as opposed to constant) bulk demodulation parameters. See Section L.1.1.

and $\mathbf{R}_V(t_i)$ is a Vandermonde matrix, given by

$$\mathbf{R}_V(t_i) = \begin{bmatrix} \mathbf{1}^{M \times 1} & \mathbf{R}(t_i) \end{bmatrix} \tag{L.10}$$

where $\mathbf{1}^{M \times 1}$ denotes a $M \times 1$ column vector with every entry equal to 1. Note that $t_{\max} = t_{36} = 3$ hours corresponds to the last time-point in our time-lapse experiment protocol, which we used to define the reference position of each bead.

Equation (L.8) relies on the assumption that the effects of CTF-induced substrate deformations were negligible across a large fraction of the beads tracked in the $500 \times 500 \times 500 \ \mu m^3$ FOV of our images, such that the output parameters of the fitting operations were not severely affected. (Further details are provided in Section L.2.1.) Bead displacement data was finally computed as:

$$\mathbf{u}_m(\mathbf{r}_{\text{corr,m}}(t_{\max}), t_i) = \mathbf{r}_{\text{corr,m}}(t_i) - \mathbf{r}_{\text{corr,m}}(t_{\max}) \tag{L.11}$$

This data was used as input for out CTF reconstruction procedure.

Pre-processing and motion correction for cell surface mesh data

In order to ensure that the bead displacement data (Eqn. (L.11)) and cell surface mesh data (acquired as described in Chapter 6.6.8) are defined in the same coordinate system, all position corrections applied to the bead position data (detailed in the previous sections) must also be applied to each node of the cell surface mesh data. Let Q denote the total number of nodes in the cell surface mesh at time t_i. For each node $q \in \{1, 2, \ldots, Q\}$, with raw positions denoted by the column vector $\mathbf{r}_{\text{raw},q}(t_i)$, the effects of focal plane registration were first removed (as in Eqn. (L.6)) via:

$$\mathbf{r}_q(t_i) = \mathbf{r}_{\text{raw},q}(t_i) + \left\langle 0, 0, z_f\left(x_{\text{raw},q}(t_i), y_{\text{raw},q}(t_i)\right) - z_{f,0} \right\rangle \tag{L.12}$$

This was followed by bulk motion correction (as in Eqn. (L.7)) via:

$$\mathbf{r}_{\text{corr,q}}(t_i) = \mathbf{r}_q(t_i) - \mathbf{u}_0(t_i) - \mathbf{A}(t_i)\mathbf{r}_q(t_i) \tag{L.13}$$

where $\mathbf{u}_0(t_i)$ and $\mathbf{A}(t_i)$ use the same values/coefficients as those obtained from Eqn. (L.8).

L.1.3 Figure generation

Impact of focal plane registration (Figs. 6.3(b,c)) Two different volumetric images were generated from the same raw image data, using our computational image formation procedure. The volumetric image used to produce Fig. 6.3(b) was generated without using focal plane registration[8], whereas the volumetric image used to produce Fig. 6.3(c) was generated with focal plane registration. To assess the impact of focal plane registration, both volumetric images were analyzed using the same procedure:

1. A 50 μm thick region, centered 50 μm above the focal plane, was extracted from the full volumetric image.

2. A 2D image was generated via a maximum intensity projection of this sub-volume, taken along the z-axis.

3. This 2D image was subjected to single-level thresholding, with the threshold set as the 99th percentile of the image histogram. This resulted in a binary image, where regions with a value of '1' corresponded to regions with strong scattering signals in the original image.

---

[8]Note that in this study, I used 'focal plane registration' to refer to 'focal plane curvature removal'. The two phrases are interchangeable.

4. The centroid of each 'object' (i.e., a region of connected pixels with a value of '1') in the binary image was computed and recorded. Each object was assumed to represent at least one scattering bead.

5. For each centroid computed in Step 4, the following was performed:

    (a) Extract an 11×11 pixel region (centered on the centroid) within the image from Step 2.

    (b) Up-sample the extracted region by a factor of 100 (using MATLAB's `imresize` function)

    (c) Threshold this up-sampled region at one-half its maximum value, to generate a binary image.

    (d) Compute the area and perimeter (A and P) of the largest object in this binary image.

    (e) Compute the 'circularity' $C = P^2/(4\pi A)$. If $C < 2$, the object is assumed to be approximately circular, and therefore corresponds to a single bead, whose full-width-at-half-maximum (FWHM) diameter is taken to be $D = 2\sqrt{A/\pi}$. Otherwise, the object is discarded and ignored (since it may contain overlapping beads or have an insufficient SNR).

6. Each 11×11 region from Step 5 which was determined to contain a single bead was assigned a color value (see the color bar in Fig. 6.3) based on the FWHM bead diameter D computed for that region. This region was inserted at its appropriate location in a synthetic image, corresponding to the images in Figs. 6.3(b,c).

Average displacement with respect to distance from the cell centroid (Fig. 6.5, right panels) 'Average deformation magnitude' (shown in the

right panels of Fig. 6.5) was computed using the procedure below. All mesh/position/deformation data refer exclusively to the data of a given cell (1, 2, or 3) and time-point (in the range $t_i = t_0, \ldots, t_{max}$).

1. Compute the centroid of each element of the cell surface mesh.

2. Compute the centroid of the cell body via the mean position of these element centroids.

3. Compute the distance of each bead to the cell centroid.

4. For each distance d depicted in the right panels of Fig. 6.5

   (a) Identify all beads whose position is within the range $d \pm 20\,\mu m$ from the cell centroid.

   (b) Compute the mean of the magnitude of the deformation vectors for this set of beads.

Measurement of 'total force' (Figs. 6.8 and 6.9)   The time-varying 'total force' (depicted in Figs. 6.8 and 6.9) was computed as described below. All mesh/position/traction data refer exclusively to the data of a given cell (1-10) and time-point (in the range $t_i = t_0, \ldots, t_{max}$).

As described in Chapter 6.6.9, the reconstructed CTF distribution must satisfy force and moment balance (as is required by the quasi-static/non-accelerating state of the cell). Therefore, calculation of the 'total force' exerted by the cell cannot be performed via a summation of the traction forces exerted by each element in the cell surface mesh (as the result would trivially be zero for any cell at any time). Instead, we measured the 'total force' by (1) measuring the direction along which cell forces are maximally oriented, followed by

(2) 'slicing' the cell with a plane perpendicular to this direction, such that the force exerted by each 'half' of the cell (in the direction normal to the plane) is maximal, and (3) taking this maximal force to be the 'total force'. The equations below give precise definitions for this process.

Let $\hat{\mathbf{n}}$ be a 3D normal vector (in column format) whose direction is described by a pair of angular coordinates (θ, ϕ) such that is components in x, y, and z are given by:

$$\hat{\mathbf{n}}(\theta, \phi) = \langle \cos\theta \sin\phi, \sin\theta \sin\phi, \cos\phi \rangle \tag{L.14}$$

Let the 'principal axis of stress' be defined as a normal vector which is maximally aligned with the stress distribution exerted by the cell. That is, let the principal axis of stress be defined as $\hat{\mathbf{n}}_p(\theta_p, \phi_p)$, where the principal angles (θ_p, ϕ_p) are computed via:

$$(\theta_p, \phi_p) = \underset{(\theta,\phi)}{\arg\max} \sum_{l=1}^{N} |(a_l \mathbf{t}_l) \cdot \hat{\mathbf{n}}(\theta, \phi)| \tag{L.15}$$

where N is the number of elements in the cell surface mesh, a_l and $\mathbf{t}_l$ denote the area and reconstructed traction stress of element l of the cell surface mesh, respectively, and '·' denotes the vector dot-product operator. Once the principal axis of stress is identified, the cell can be 'sliced' perpendicular to the principal axis with a plane:

$$\left(\langle x, y, z \rangle - \beta \hat{\mathbf{n}}_p \right) \cdot \hat{\mathbf{n}}_p = 0 \tag{L.16}$$

where β denotes the 'offset position' of the plane with respect to the origin. To determine whether or not a given element of the cell surface mesh is on one side or the other of this plane, we define an indicator function:

$$\chi_\beta \left(\mathbf{c}_l, \hat{\mathbf{n}}_p \right) = H \left[\left(\mathbf{c}_l - \beta \hat{\mathbf{n}}_p \right) \cdot \hat{\mathbf{n}}_p \right] \tag{L.17}$$

where $\mathbf{c}_l$ denotes the centroid of element l of the cell surface mesh, and H denotes the Heaviside step function. The total force exerted by the cell was then

approximated as:

$$F_{\text{total}} = \max_{\beta} \left| \sum_{l=1}^{N} \chi_{\beta} \left(\mathbf{c}_l, \hat{\mathbf{n}}_p \right) \left((a_l \mathbf{t}_l) \cdot \hat{\mathbf{n}}_p \right) \right| \tag{L.18}$$

The maximization with respect to β finds the location of the 'slicing' plane that yields the largest measurement of total force. Note that Eqn. (L.18) performs a summation of the CTF components parallel to the principal axis of stress.

L.2   Discussion

L.2.1   Motion correction

The motion correction procedure (which was applied only to bead displacement data and cell surface mesh data, and *not* to OCM images) attempted to remove any residual motion artifacts that were not corrected by previous data processing procedures. As described in Section L.1.2, the zero- and first-order terms used to perform this correction were determined by linear least-squares fitting, using the assumption that CTF-induced bead displacements would have a negligible impact on the results of the fit. This method of fitting is vulnerable to outliers and does risk erroneously incorporating cell-induced displacements into the correction functions, $\mathbf{u}_0(t_i)$ and $\mathbf{A}(t_i)$. To better avoid this risk in the future, we recommend measuring deformations over a larger volumetric FOV, reducing the weighting of bead displacements measured near the cell body, and/or using alternative robust regression models (such as nonlinear metric functions, mixture models, etc.). In general, motion correction may be thought of as a type of high-pass filter (in the space-domain), applied to remove deformations spanning volumes too large to be caused by the cell. Any alternative filtering

344

schemes should be optimized with this objective in mind. Note that low-pass filtering (to remove deformation fluctuations spanning volumes too small to be caused by the cell) was not directly performed in this study. Instead, low-pass filtering took place implicitly via the Tikhonov regularization used by our CTF reconstruction procedure [44].

L.2.2   Validity of linear elastic mechanical model

In order to reconstruct time-varying CTFs, our FEM solver employed a standard linear elastic model under the infinitesimal strain approximation. Any deviations of the Matrigel substrate's true behavior from this model could introduce errors to the reconstructed CTFs. The linear elastic model can be a poor model for many biopolymers (such as collagen), which tend to exhibit nonlinear elastic and/or viscoelastic behaviors. Moreover, if cells induce very large deformations in the surrounding substrate, infinitesimal strain theory may no longer be sufficient to describe substrate deformations, requiring a generalization to finite strain theory. In order to assess the validity of our linear elastic model, we tested our Matrigel substrate for both nonlinear and viscoelastic behaviors, and quantified discrepancies between the infinitesimal and finite strain tensors computed from our experimentally measured bead displacement data.

Bulk rheology testing for nonlinearity and viscoelasticity

Concerns regarding nonlinear and/or viscoelastic effects were raised during the peer review process for this study. At that time, our original batch of Matrigel had been exhausted, and a new batch was used for additional testing. Using
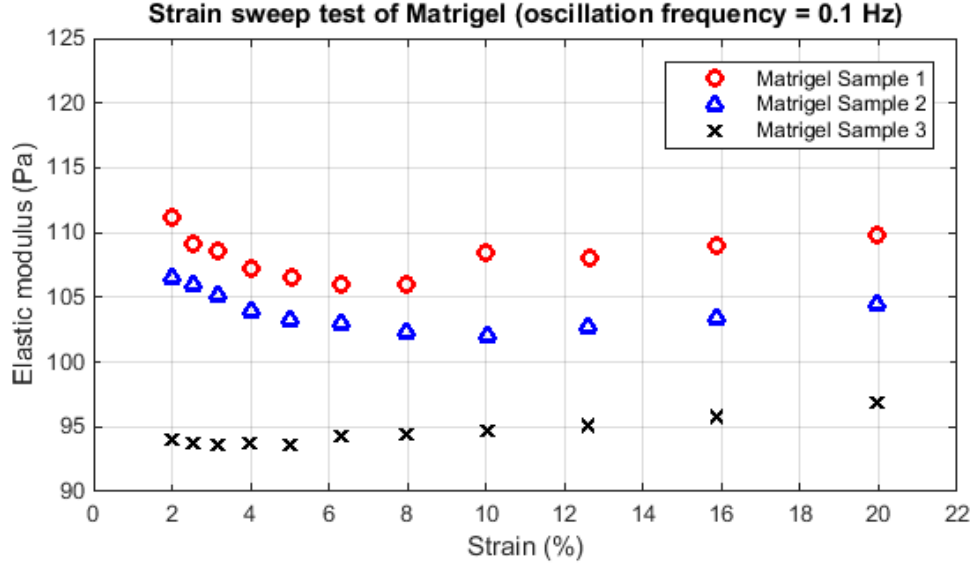
Figure L.1: Strain sweep test of Matrigel. The Matrigel samples exhibited approximately linear behavior, as indicated by an approximately constant stiffness over a strain range of 2-20%. Reprinted from Ref. [112] as permitted under the CC BY 4.0 license for the original work.

the procedure outlined in Chapter 6.6.2, the Young's modulus of the Matrigel substrates prepared from the new batch was found to be approximately 104 Pa. This is ~15% stiffer than the Young's modulus (90 Pa) measured from the original Matrigel batch used for our time-lapse experiments and CTF reconstructions. We assumed that despite this difference, any tests performed with the new Matrigel batch should provide a reasonable approximation of the mechanical properties of the original batch. Three distinct samples were tested for nonlinear behavior via an oscillating (0.1 Hz) strain sweep test over a strain range of 2-20% (Fig. L.1). For each sample, the Young's modulus deviated from the mean for that sample by less than ±3%, suggesting that our Matrigel samples exhibit approximately linear behavior for strains up to at least 20%.

The same three samples used for the strain sweep test were also subjected to a stress relaxation test (under an applied strain of 2%) to test the potential

impact of viscous effects. The stress relaxation curves (Fig. L.2) were fit to the function $\sigma(t) = c_1 + c_2 \exp(-t/\tau)$ via the MATLAB function `lsqcurvefit` to obtain the values of (c_1, c_2, τ). The output fitting parameters for each sample were (0.28 Pa, 0.56 Pa, 97.6 s), (0.18 Pa, 0.52 Pa, 122.5 s), and (0.24 Pa, 0.37 Pa, 117.5 s), respectively, with residual norms of 0.0157, 0.0424, and 0.0138, respectively. The stress relaxation constants τ are consistent with previously published characterizations of Matrigel [115], and do imply that Matrigel exhibits a degree of viscoelastic behavior. We can use the viscoelastic mechanical framework by Toyjanova et al. [173] to estimate the impact of neglecting viscous effects during CTF reconstruction. Given the applied strain (2%) of our stress relaxation test, the equilibrium shear modulus μ and non-equilibrium shear modulus μ_{neq} can be obtained by the relations $\mu = c_1/0.02$ and $\mu = c_2/0.02$. The ratio μ_{neq}/μ then takes a mean value of approximately 2.14. Using this ratio, a mean relaxation time of $\bar{\tau} = 112.5$ seconds, and Fig. 6 of Ref. [173], we estimate that applying a purely elastic model to analyze our samples will underestimate CTFs by < 5%, compared to the viscoelastic FEM solver described in that study [173]. This suggests that, for this study, viscous effects may be reasonably neglected. Combined with the nonlinearity test above, our mechanical characterization data suggest that a linear elastic model is likely to provide sufficiently accurate CTF reconstructions for this study. However, it is important to note that the future application of TF-OCM in other, less ideal materials (such as collagen) may benefit from the incorporation of nonlinear and/or viscoelastic models to obtain more accurate CTF reconstructions.
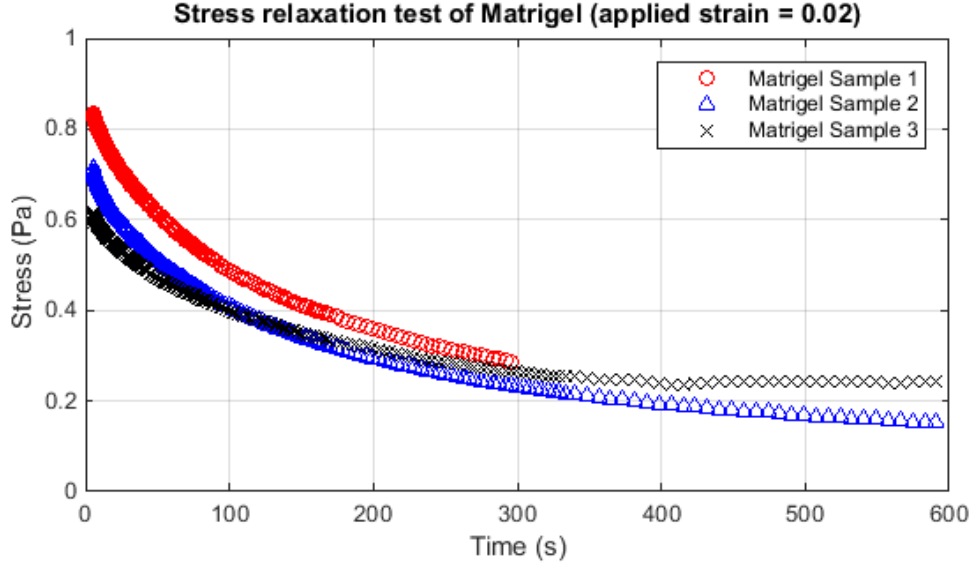
Figure L.2: Stress relaxation test of Matrigel. Parameters obtained from curve-fitting to these data were used to show that neglecting viscous effects is not expected to severely impact CTF reconstruction accuracy for this study. Reprinted from Ref. [112] as permitted under the CC BY 4.0 license for the original work.

Testing validity of the infinitesimal strain approximation

(Note that some of the variables/notation used in the equations below overload the variables/notation defined previously in this document. This has been done in order to maintain consistency between the equations below and Ref. [63].)

Validation: Strain estimations using moving least-squares method Consider a test scalar function $g(x, y, z) = \sin(x) + z^2 \sin(y)$ defined on a unit cube $[0, 1]^3$. We use the moving least-squares (MLS) method [63] to estimate the value of the function as well as its (spatial) derivatives, given a set of n point measurements of the function. Details can be found in Ref. [63]. Briefly, here we adopt a cubic

polynomial basis and the following exponentially decaying weight function:

$$f(\mathbf{x} - \mathbf{b}_i) = \begin{cases} \dfrac{\exp\left(1-(d/d_m)^2\right)-1}{e-1} & d \le d_m \\ 0 & d > d_m \end{cases} \quad , d = |\mathbf{x} - \mathbf{b}_i| \qquad \text{(L.19)}$$

where $\mathbf{x}$ is the point of interest, $\mathbf{b}_i$ is the position of the ith measurement point ($i \in \{1, 2, \ldots, n\}$), and d_m is a cut-off distance which we choose to be three times the mean separation distance of the measurement points. Different from Eqn. (7a) in Ref. [63], we define:

$$\mathbf{A} = r\mathbf{I} + \sum_{i=1}^{n} f(\mathbf{x} - \mathbf{b}_i)\mathbf{P}(\mathbf{b}_i)\mathbf{P}^{\mathrm{T}}(\mathbf{b}_i) \qquad \text{(L.20)}$$

where r is a regularization coefficient. In general, r reduces the condition number of the matrix $\mathbf{A}$ and improves the numerical stability of the MLS method. Figure L.3 shows a typical profile of the approximated value of the test function g and its derivatives at a random point in the unit cube as r varies. As r decreases, the MLS approximations (solid lines, black: g , red: $\partial g/\partial x$, green: $\partial g/\partial y$, blue:$\partial g/\partial z$) approach the true values (dotted lines) with less than 5% relative error. In the calculation, 50 measurements points were randomly sampled in the unit cube with a mean distance of approximately 0.177. Among them, the MLS weights of twenty measurement points are greater than 0.05 at the point of interest. We note that when the point of interest is close to the boundary of the unit cube, some estimated derivatives could yield significant numerical error (see Figure L.4). For this reason, in the next section, we only applied the MLS method near the center of the imaging domain where the cell-induced displacement is maximal.

Results from experimental data   We use the above approach to validate that the cell-induced deformations in our experiment are approximately linear over
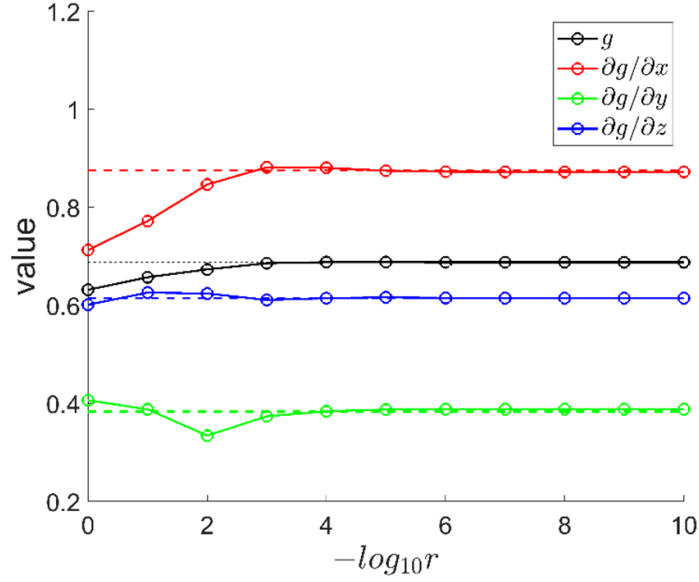
Figure L.3: MLS approximation of the test function (black) and its derivatives (red: *x*-derivative, green: *y*-derivative, blue: *z*-derivative) at the point of interest [0.5063, 0.4856, 0.6585] as the regularization coefficient *r* varies. As *r* decreases (from left to right), the MLS approximations approach the true values (dotted lines). Reprinted from Ref. [112] as permitted under the CC BY 4.0 license for the original work.

time (i.e., that the infinitesimal strain tensor is a good approximation of the more general finite strain tensor). To this end, we estimate the displacement gradient $\nabla \mathbf{u}$ at multiple locations where the cell-induced bead displacement is maximal by applying the MLS method on each component of the displacement. This allows us to calculate the finite Green's deformation tensor $\mathbf{E} = 0.5\left(\nabla \mathbf{u} + \nabla^{\mathrm{T}}\mathbf{u} + \nabla^{\mathrm{T}}\mathbf{u}\nabla\mathbf{u}\right)$ as well as the infinitesimal strain tensor $\mathbf{e} = 0.5\left(\nabla \mathbf{u} + \nabla^{\mathrm{T}}\mathbf{u}\right)$.

To quantify how well linear elasticity theory (i.e., using the infinitesimal strain approximation) approximates finite elasticity theory, we define ξ to be the relative error between $\mathbf{E}$ and $\mathbf{e}$, i.e., $\xi = \|\mathbf{E} - \mathbf{e}\|_F / \|\mathbf{E}\|_F$ where $\|\bullet\|_F$ is the Frobenius norm of a tensor. The time variation of ξ at multiple locations around
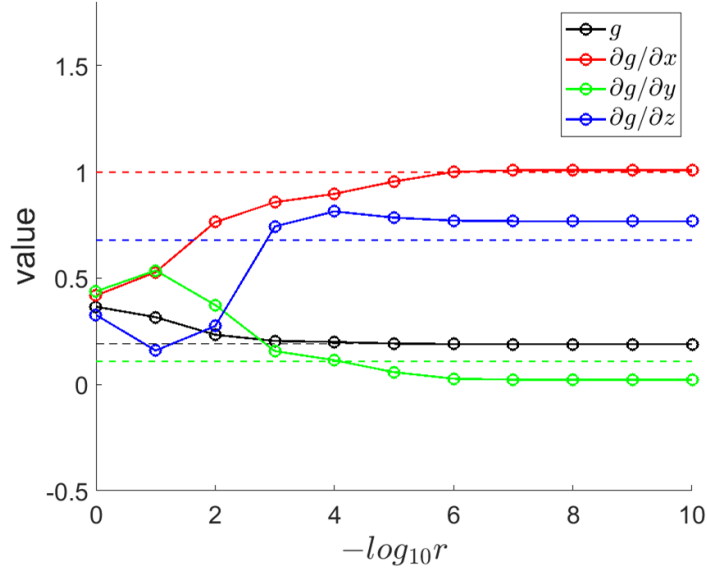
Figure L.4: MLS approximation of the test function (black) and its derivatives (red: *x*-derivative, green: *y*-derivative, blue: *z*-derivative) at the point of interest [0.0467, 0.9232, 0.4254] as the regularization coefficient *r* varies. As *r* decreases (from left to right), some approximated derivatives have significant error from the true values (dotted lines), e.g., for the blue and green curves, due to the fact that the point of interest is near the boundary of the domain. Reprinted from Ref. [112] as permitted under the CC BY 4.0 license for the original work.

cell 1, cell 2, and cell 3 is shown in the upper left panels of Figs. L.5-L.7, respectively, with measurement locations indicated by the red circles in the other three panels of each figure. For these cells, we found that ξ is below 3% and gradually decreases over time, indicating that the cell-induced deformations in our experiment can be reasonably approximated by the infinitesimal strain approximation, and hence linear elasticity theory. In applying the MLS method, values of $d_m \approx 35 \, \mu$m and $r = 10^{-10}$ were used.

Figure L.5: Top left: the relative error between the finite strain tensor and infinitesimal strain tensor over time at multiple locations around cell 1. The specific locations are indicated in the top right (*XY*-plane), bottom left (*XZ*-plane) and bottom right (*YZ*-plane) panels in which the arrows indicate the cell-induced displacement. Reprinted from Ref. [112] as permitted under the CC BY 4.0 license for the original work.

L.2.3 Possible underestimation of CTFs due to residual stresses

Substrate deformations were obtained by relying on the assumption that the last time-point in our time-lapse experiment corresponded to a 'proper' reference state, in which cell forces were completely relaxed. However, this assumption may fail due to the presence of residual stresses. Such stresses may either be active (i.e., due to incomplete cell relaxation) or passive (e.g., due to cell-induced substrate remodeling). TFM methods which generate a reference state
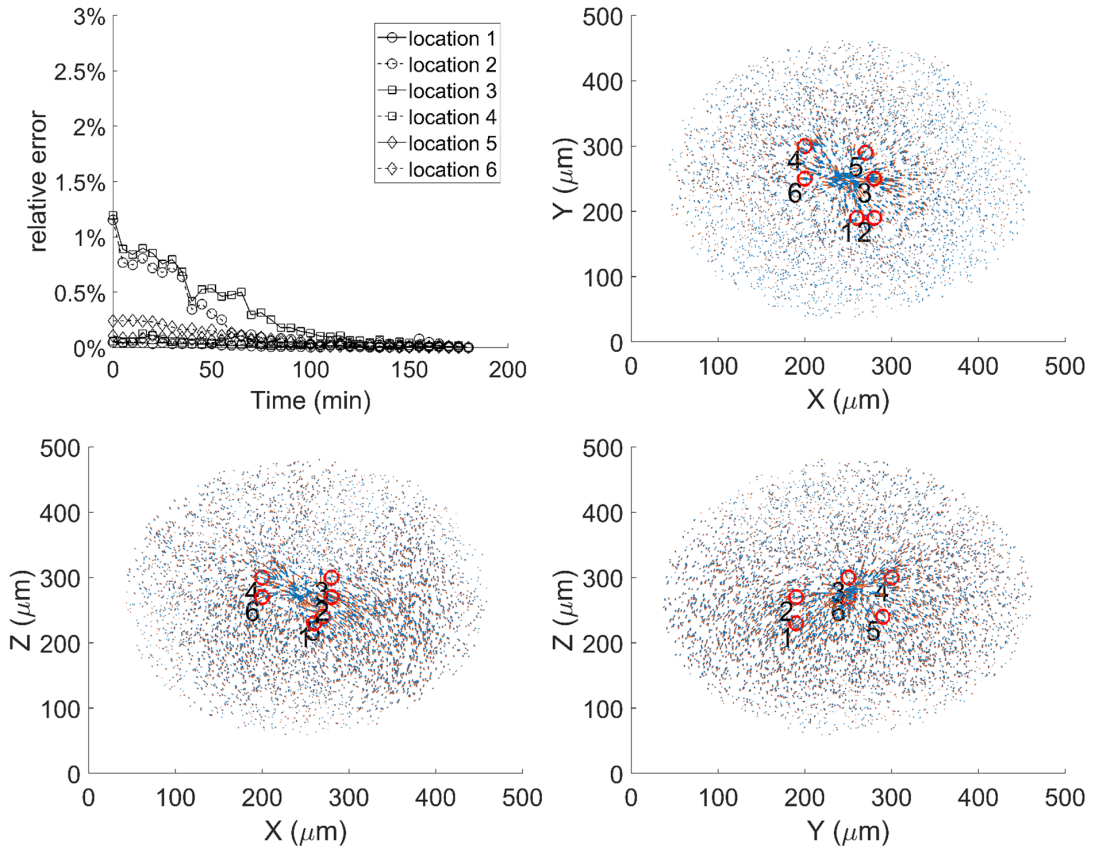
Figure L.6: Top left: the relative error between the finite strain tensor and infinitesimal strain tensor over time at multiple locations around cell 2. The specific locations are indicated in the top right (*XY*-plane), bottom left (*XZ*-plane) and bottom right (*YZ*-plane) panels in which the arrows indicate the cell-induced displacement. Reprinted from Ref. [112] as permitted under the CC BY 4.0 license for the original work.

via chemically-induced CTF inhibition cannot eliminate the possibility of residual passive stresses without additional *a priori* information about the sample structure prior to cellular activity (or alternatively, probing the substrate to detect changes in the local mechanical properties). Since the experimental protocol used for this study did not acquire any such data, our CTF reconstructions are vulnerable to inaccuracies resulting from the presence of passive stresses. Future TF-OCM protocols may be fortified against this vulnerability by acquiring a 'true' reference state immediately after sample preparation, which may act as
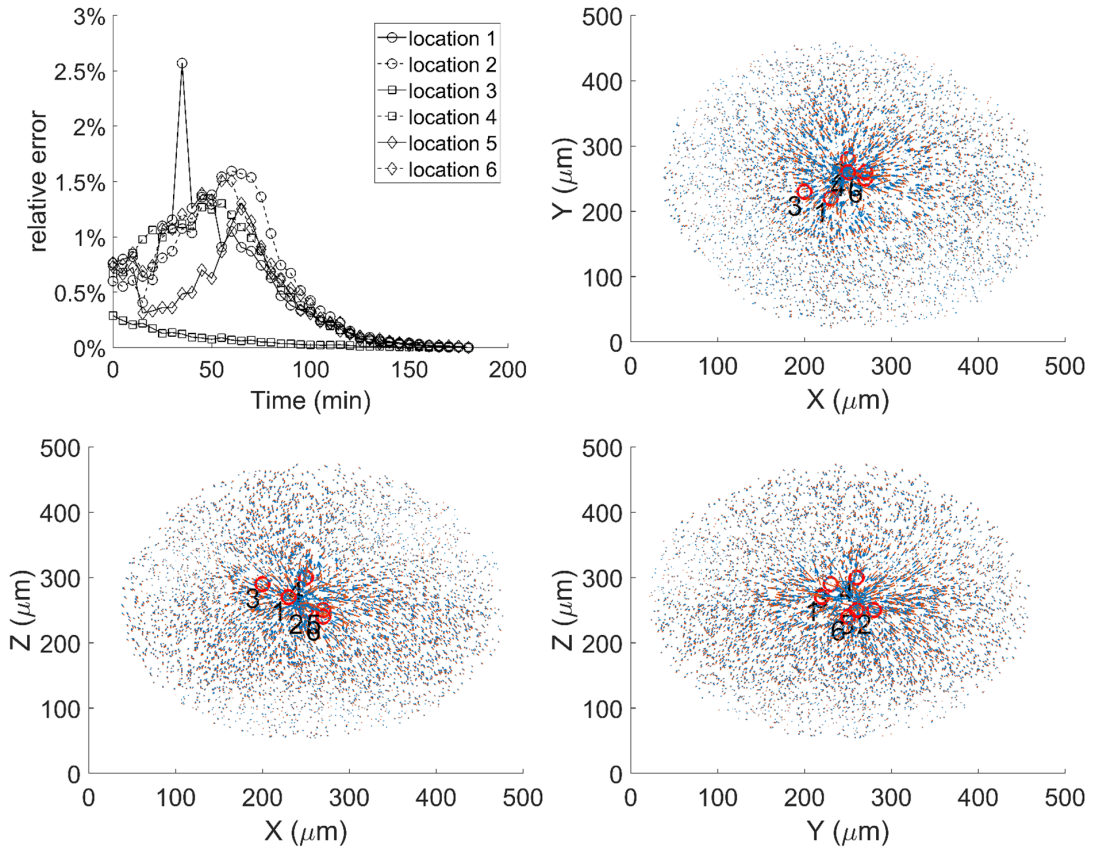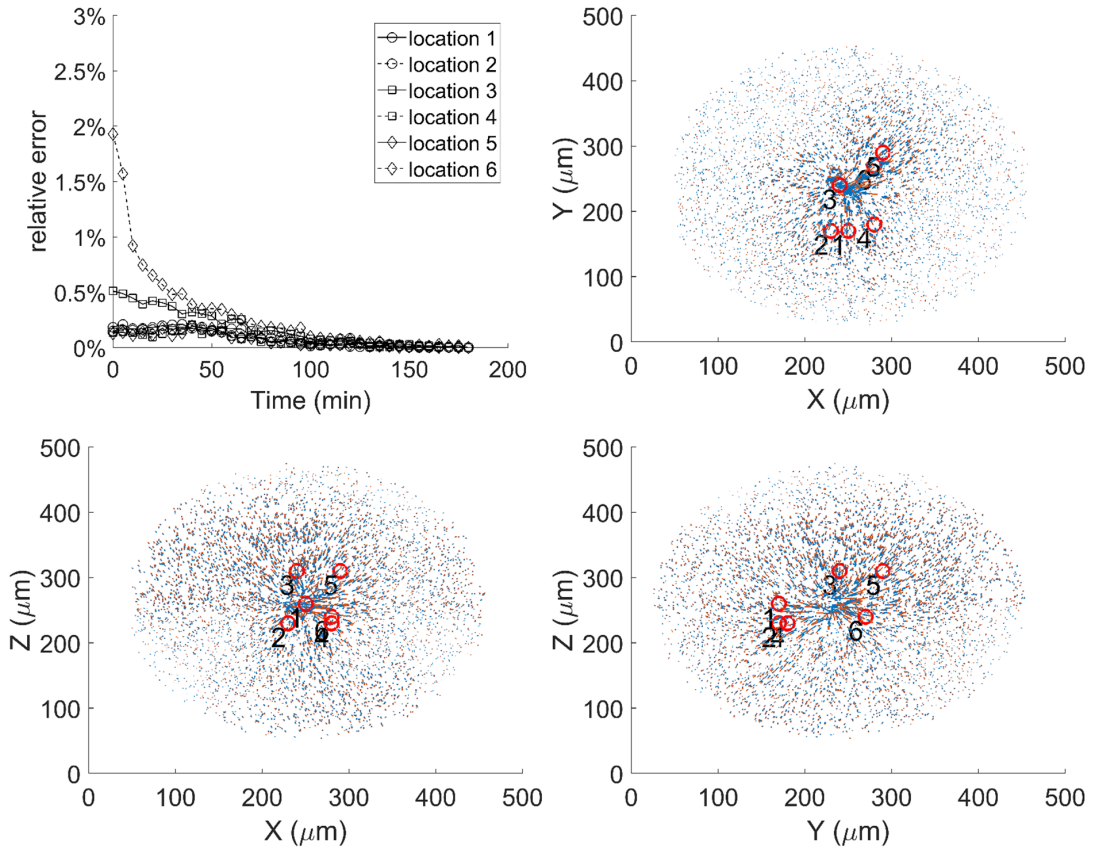
Figure L.7: Top left: the relative error between the finite strain tensor and infinitesimal strain tensor over time at multiple locations around cell 3. The specific locations are indicated in the top right (*XY*-plane), bottom left (*XZ*-plane) and bottom right (*YZ*-plane) panels in which the arrows indicate the cell-induced displacement. Reprinted from Ref. [112] as permitted under the CC BY 4.0 license for the original work.

a supplement or replacement for a chemically-induced reference state.

A loss of active stresses (in the case of nonlethal CTF inhibitors) may most readily be identified by the observation of a halt in mechanical activity. Upon closer inspection of our experimental data, we found reason to suspect that the cells shown in this study may not have completely relaxed by the reference time-point (defined at t_{36} = 3 hours). Specifically, we recomputed CTFs redefining both times t_{34} and t_{35} as reference points, and found that the total force curves (as in Fig. 6.8) displayed an average downward shift, indicating that the treated

NIH-3T3 cells may not have completely relaxed by time t_{36} (not shown). Under a linear elastic model, incomplete cell relaxation at the reference time-point may have caused the CTF curves in Figs. 6.8 and 6.9 to be underestimated by an additive constant.

To estimate the constant factor by which CTFs may have been underestimated, we first extracted the 'force decay phase' of the curves in Fig. 6.9. The first time-point in this phase was taken to be the time t_{peak} of the force peak after the application of cytochalasin D (i.e., any time after time t_6 = 30 minutes). All remaining time points (up to t_{36}) were included as part of the 'force decay phase' data. The extracted curves were fit to an exponential decay model of the form $F(t) = f_0 + f_1 \exp(-t/\tau)$ via the MATLAB function `lsqcurvefit`. If t_{36} corresponded to a 'true' reference state, the coefficient f_0 would be expected to be zero. On the other hand, if residual active stresses were present during the reference state, f_0 would be expected to take a negative value. Using the value of f_0 obtained from the curve fit, we found that the total forces exerted by cells 1-10 may have been underestimated by approximately 6 nN, 56 nN, 4 nN, 1 nN, 28 nN, 11 nN, 5 nN, 1 nN, 0 nN, and 0 nN, respectively. As a percentage of the force measured at time $t = t_{\text{peak}}$ for each cell, these values correspond to an error of approximately 3%, 75%, 2%, 1%, 9%, 9%, 2%, 1%, 0%, and 0%, respectively. The degree of potential error for cells 2, 5, and 6 in particular, suggests that future experiments using cytochalasin D may require longer imaging times. This problem also highlights the need to develop real-time TF-OCM data processing so that researchers may reliably identify when it is appropriate to end a given time-lapse experiment. Future applications of TF-OCM to biological studies will require more thorough confirmation of effective CTF inhibition.

L.2.4   Factors reducing the sensitivity of CTF reconstructions

The sensitivity of TF-OCM to CTFs can be reduced by any effect which contributes noise or errors to the final reconstructed CTF data. The experiments detailed below were performed in order to better understand the impact of both localization sensitivity and bead density on the noise level of CTF reconstructions (and hence, the sensitivity of our TF-OCM system to CTFs). These experiments made use of artificially modified bead displacement data. That is, experimental data were altered (e.g., by adding noise or removing data points) to obtain multiple realizations of modified displacement data. By comparing the CTF reconstructions resulting from these modified data sets with the original CTF reconstructions, the impact of localization sensitivity and bead density could be studied in a controlled manner. It is important to note that the performance of our TF-OCM method emerges as a net consequence of the entire experimental system (including sample preparation, the imaging system, algorithms, etc.). As a consequence, these results are intended to demonstrate the limitations of only this first iteration of TF-OCM, and not the theoretical limitations of TF-OCM as a whole.

Impact of localization sensitivity

Modified bead displacement data were generated by adding Gaussian noise to experimental bead displacement data. The standard deviations of this Gaussian noise along the x, y, and z axes were given by the experimentally measured localization sensitivities defined in Chapter 6.6.6 (37 nm, 32 nm, and 86 nm, respectively). To prevent the addition of unrealistic/excessive noise, any noise realization with a magnitude greater than three standard deviations (along any
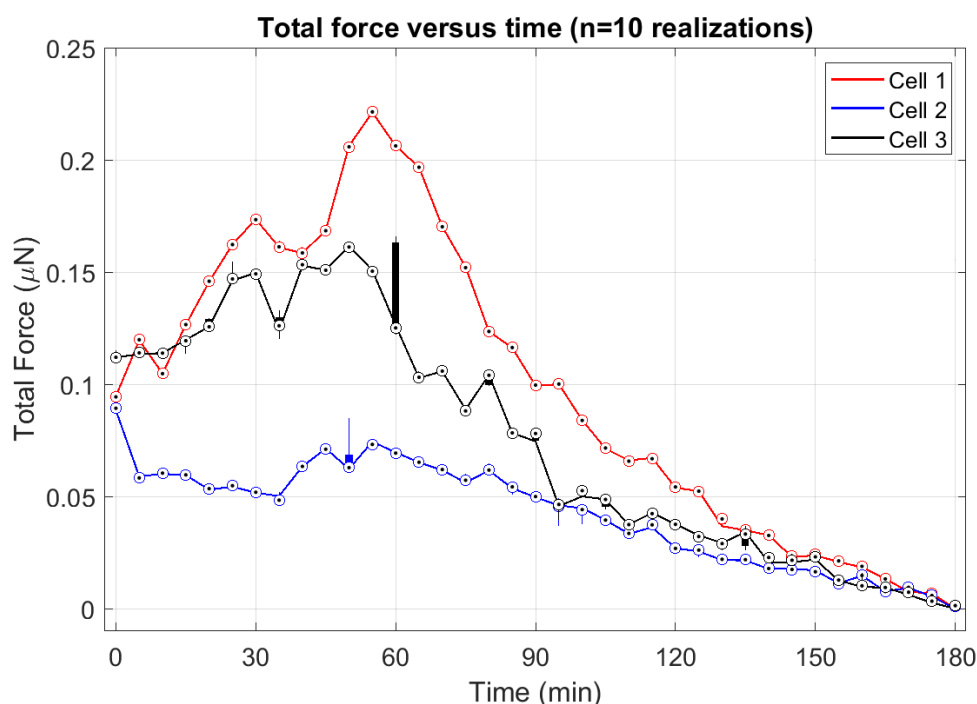
Figure L.8: Contribution of bead localization sensitivity to noise in reconstructed total force data. Original total force data (line plots, equivalent to data shown in Fig. 6.8) have been superimposed with total force data from the CTF reconstructions described in the text (box plots, obtained using bead displacement data modified with Gaussian noise). The whiskers, boxes, and circles depict the full range, interquartile range, and median value of the data, respectively. Note that most of the boxes exhibit so little deviation about the median data point that they effectively 'vanish' in the plot above. Reprinted from Ref. [112] as permitted under the CC BY 4.0 license for the original work.

axis) was discarded and replaced with another sample drawn from the Gaussian distribution. Ten independent realizations of this noise process were generated for each bead at each time-point in the data sets of cells 1, 2, and 3 (yielding a total of 1110 modified bead displacement data sets). CTF reconstruction was performed using each of these data sets (requiring approximately 10 days of computing time on our work station). Total force curves (as in Figs. 6.8 and 6.9) were generated from these reconstructions, and are displayed in Fig. L.8.

The standard deviation of these new total force curves with respect to the

original (unmodified) total force curves is 2.6 nN, which we interpret here as the approximate contribution of bead localization sensitivity to noise in the data shown in Figs. 6.8 and 6.9. These results suggest that the noise contributed by our bead localization sensitivity is so small as to be negligible in comparison to noise originating from other sources (such as low bead density, as detailed in the next section). It is important to note that, although the addition of Gaussian noise in this experiment had little impact on the measurement of total force, there are a few time-points at which large deviations in total force can be seen (e.g., cell 3 at time t = 60 minutes). Such large deviations may result from multiple factors, such as failure of the FEM solver to converge and/or a low bead density contributing to numerical instability of the inverse problem posed by CTF reconstruction. This latter factor is explored by the experiment below.

Impact of bead density

Modified bead displacement data were generated via sub-sampling of experimental bead displacement data obtained from cell 1. Specifically, each bead was discarded from the data set with a probability of 50%, resulting in bead displacement data which had an effective bead density approximately half that of the original experimental data. This process was repeated to obtain 10 realizations of sub-sampled data for each time-point. CTF reconstruction was performed using each of these data sets (requiring approximately 80 hours of computing time on our work station). Total force data (as in Figs. 6.8 and 6.9) were generated from these reconstructions, and are displayed in Fig. L.9. We note that these results do not demonstrate the impact of bead density at the true bead density used in our samples. However, we assume that the features demon-
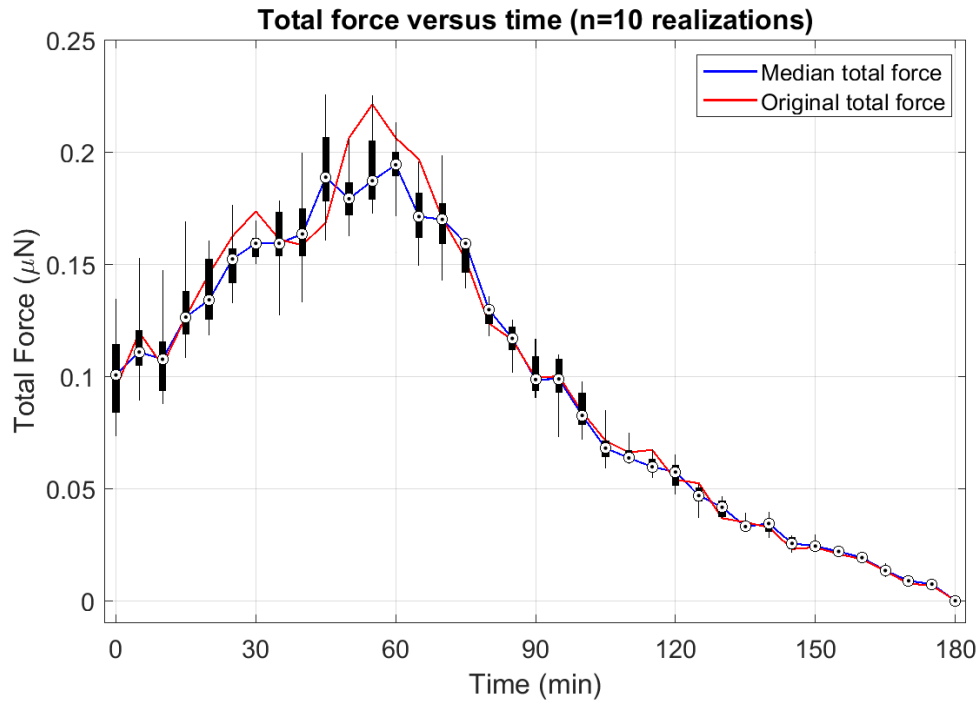
Figure L.9: Contribution of bead density to noise in reconstructed total force data (for cell 1). Box plots depict total force data from the CTF reconstructions described in the text (obtained using randomly sub-sampled realizations of the original bead displacement data). The whiskers, boxes, and circles depict the full range, interquartile range, and median value of the data, respectively. The median total force curve corresponds to the median values reported in the box plots. The original total force curve corresponds to the total force data from the CTF reconstructions obtained using the original experimental data. Reprinted from Ref. [112] as permitted under the CC BY 4.0 license for the original work.

strated by these 'half-density' data sets may serve as a sufficient proxy. Under the assumption that higher bead density reduces noise in CTF reconstructions, the noise measured using these 'half-density' datasets may serve as an approximate upper-bound on the noise contribution of the true bead density present in the original experimental data.

There are several features worth discussing in these results. First, due to the relatively smooth contraction/relaxation of the cell (as in panel (b) of Supplementary Movie 1 of Ref. [112]), we might have expected the original total

force curve of cell 1 (the red curve in Fig. L.9) to vary smoothly across time. However, the curve appears 'jagged', possessing noisy/rapid fluctuations in the computed total force. We note that the peaks and troughs of this jagged curve are on the order of the variations in the total force obtained from the 'half-density' reconstructions shown in the box plots of Fig. L.9, which suggests that the fluctuations seen in the original cell 1 curve may be due to the impact of low bead density, and not 'true' fluctuations in CTFs. We also note that the curve traced by the median of the 'half-density' reconstructions appears relatively smooth, and therefore more closely resembles the type of time series that would have been expected, based on the image data. It must be emphasized that this information is not sufficient to determine whether this curve is closer to the 'true' cell force. However, if future experiments demonstrate such a finding, it could suggest that the effects of low bead density can be mitigated by adding stochastic elements (such as the random sub-sampling used here) to force reconstruction procedures.

The variation of total force in Fig. L.9 is not uniform over time. In particular, the standard deviation of the total force obtained from the 'half-density' reconstructions increases with increasing time between the 'deformed state' and 'reference state' (shown in Fig. L.10). If we consider this time-varying standard deviation to represent the noise in our TF-OCM system, we see that noise increased at a rate of approximately 0.1 nN/min of temporal separation between the 'deformed' and 'reference' states. This implies that our TF-OCM system exhibited its worst sensitivity at time $t = 0$, with a sensitivity/noise floor of approximately 18 nN (which is approximately one-tenth the median cell force measured at time $t = 0$, as shown in Fig. 6.9). Note that this noise floor approximates the contribution of our (relatively) low bead density. As stated in

Chapter 6.6.1, our $1\,\mu$m diameter beads had an average separation of $18\,\mu$m, but standard TFM conventions would allow for a separation as small as $10\,\mu$m, corresponding to a bead density almost 6 times larger than that used in this study. It is currently unknown whether the noise floor calculated/inferred from the 'half-density' CTF reconstructions shown here captures the majority of the noise observed in our experimental measurements of total force. Future experiments using higher bead densities will be likely to add clarity to this question. The interpretation of such experiments will also require further analysis of the factors detailed in the paragraphs below. At minimum, the noise measured in this experiment may be considered as an approximate lower-bound on the reconstruction noise in our TF-OCM system (e.g., at the time of 'worst performance', time $t = 0$, our method could not reliably measure total forces smaller than approximately 20 nN).

There are multiple possible explanations for a time-varying sensitivity to CTFs. The fact that the noise floor changes approximately linearly in time *despite* the introduction of a contractility inhibitor at time $t = 30$ minutes suggests that strain/deformation dependent effects are unlikely to be the primary culprit. If such effects were at fault, we would expect the data in Fig. L.10 to show a change in behavior before versus after the addition of cytochalasin D. A reliable test of this hypothesis would likely require experiments with an extended observation time prior to the addition of cytochalasin D, beyond the 30 minutes used in this study.

Imaging and data processing effects may be more likely causes of time-varying sensitivity to CTFs. Errors in bead tracking may increase with increasing time from the 'reference' time-point. Alternatively (or in addition), sample
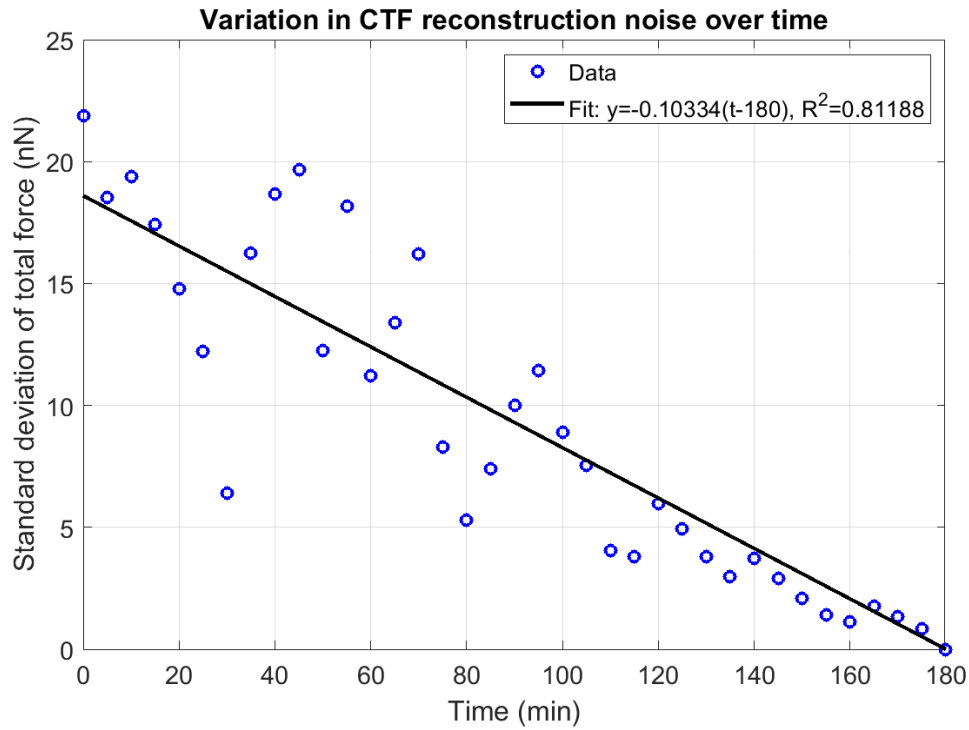
Figure L.10: Standard deviation of the total force data shown in the box plots of Fig. L.9. These results appear to indicate that the sensitivity of our TF-OCM method to CTFs decreases as the time between the 'deformed' and 'reference' states increases. See text for details. Reprinted from Ref. [112] as permitted under the CC BY 4.0 license for the original work.

drift may play a significant role. Although bead displacement data were corrected for bulk (zero-order) and linear (first-order) drift, a sufficiently large drift of the sample may cause the assumptions underlying our computational image formation module to fail, inducing higher-order image deformations which our algorithms do not currently accommodate. Coherence gate curvature correction and focal plane registration are likely candidates to suffer from such an effect. The surprisingly small standard deviation in the 'half-density' reconstruction in the latter half of the time-lapse suggest that such time-varying image distortions may be of greater concern than bead density. (That is, although a low bead density is not desirable, its impact may be amplified by the presence of image distortions.) Therefore, these results suggest that future iterations of TF-OCM

may benefit from further exploration and refinement of our computational image formation procedures.

BIBLIOGRAPHY

[1] deal.ii an open source finite element library. Online.

[2] Tethex. Online.

[3] S.G. Adie, B.W. Graf, A. Ahmad, P.S. Carney, and S.A. Boppart. Computational adaptive optics for broadband optical interferometric tomography of biological tissue. *Proc. Natl. Acad. Sci. U.S.A.*, 109:7175–7180, 2012.

[4] G. Antonacci and S. Braakman. Biomechanics of subcellular structures by non-invasive brillouin microscopy. *Sci. Rep.*, 6, 2016.

[5] C. Apelian, F. Harms, O. Thouvenin, and A.C. Boccara. Dynamic full field optical coherence tomography: subcellular metabolic contrast revealed in tissues by interferometric signals temporal analysis. *Biomed. Opt. Express*, 7:1511–1524, 2016.

[6] A.S., Crouch, D. Miller, K.J. Luebke, and W. Hu. Correlation of anisotropic cell behaviors with topographic aspect ratio. *Biomaterials*, 30:1560–1567, 2009.

[7] E. Auksorius. Light-efficient beamsplitter for fourier-domain full-field optical coherence tomography. *Opt. Letters*, 45:1240–1243, 2020.

[8] M. Azatov, S.M. Goicoechea, C.A. Otey, and A. Upadhyaya. The actin crosslinking protein palladin modulates force generation and mechanosensitivity of tumor associated fibroblasts. *Sci. Rep.*, 6, 2016.

[9] J. Ballester-Beltrn, M.J.P. Biggs, M.J. Dalby, M. Salmern-Snchez, and A. Leal-Egaa. Sensing the difference: the influence of anisotropic cues on cell behavior. *Front Mater.*, 2, 2015.

[10] E. Bar-Kochba, J. Toyjanova, E. Andrews, K.-S. Kim, and C. Franck. A fast iterative digital volume correlation algorithm for large deformations. *Exp. Mech.*, 55:261–274, 2015.

[11] E. Beaurepaire, A.C. Boccara, M. Lebec, L. Blanchot, and H. Saint-Jalmes. Full-field optical coherence microscopy. *Opt. Lett.*, 23:244–246, 1998.

[12] C. Blatter, B. Grajciar, C.M. Eigenwillig, W. Wieser, B.R. Biedermann, R. Huber, and R.A. Leitgeb. Extended focus high-speed swept source oct with self-reconstructive illumination. *Opt. Express*, 19:1214112155, 2011.

[13] R.J. Bloom, J.P. George, A. Celedon, S.X. Sun, and D. Wirtz. Mapping local matrix remodeling induced by a migrating tumor cell using three-dimensional multiple-particle tracking. *Biophys. J.*, 95:4077–4088, 2008.

[14] F. Bordeleau, B.N. Mason, E.M. Lollis, M. Mazzola, M.R. Zanotelli, S. Somasegar, J.P. Califano, C. Montague, D.J. LaValley, J. Huynh, N. Mencia-Trinchant, Y.L. Negrn Abril, D.C. Hassane, L.J. Bonassar, J.T. Butcher, R.S. Weiss, and C.A. Reinhart-King. Matrix stiffening promotes a tumor vasculature phenotype. *Proc. Natl. Acad. Sci. U.S.A.*, 114:492–497, 2017.

[15] D. Borycki, M. Hamkalo, M. Nowakowski, M. Szkulmowski, and M. Wojtkowski. Spatiotemporal optical coherence (stoc) manipulation suppresses coherent cross-talk in full-field swept-source optical coherence tomography. *Biomed. Opt. Express*, 10:2032–2054, 2019.

[16] M.B. Bouchard, V. Voleti, C.S. Mendes, C. Lacefield, W.B. Grueber, R.S. Mann, R.M. Bruno, and E.M. Hillman. Swept confocally-aligned planar excitation (scape) microscopy for high speed volumetric imaging of behaving organisms. *Nat. Photon.*, 9:113–119, 2015.

[17] M.T. Breckenridge, R.A. Desai, M.T. Yang, J. Fu, and C.S. Chen. Substrates with engineered step changes in rigidity induce traction force polarity and durotaxis. *Cell Mol. Bioeng.*, 7:26–34, 2014.

[18] D.T. Butcher, T. Alliston, and V.M. Weaver. A tense situation: forcing tumour progression. *Nat. Rev. Cancer*, 9:108–122, 2009.

[19] J.P. Butler, I.M. Toli-Nrrelykke, B. Fabry, and J.J. Fredberg. Traction fields, moments, and strain energy that cells exert on their surroundings. *Am. J. Physiol. Cell Physiol.*, 282:C595–C605, 2002.

[20] S.P. Carey, T.M. D'Alfonso, S.J. Shin, and C.A. Reinhart-King. Mechanobiology of tumor invasion: engineering meets oncology. *Crit. Rev. Oncol. Hematol.*, 83:170–183, 2012.

[21] S.P. Carey, Z.E. Goldblatt, K.E. Martin, B. Romero, R.M. Williams, and C.A. Reinhart-King. Local extracellular matrix alignment directs cellular protrusion dynamics and migration through rac1 and fak. *Integr. Biol.-Uk*, 8:821–835, 2016.

[22] S.P. Carey, K.E. Martin, and C.A. Reinhart-King. Three-dimensional collagen matrix induces a mechanosensitive invasive epithelial phenotype. *Sci. Rep.*, 7, 2017.

[23] S.P. Carey, A. Starchenko, A.L. McGregor, and C.A. Reinhart-King. Leading malignant cells initiate collective epithelial cell invasion in a three-dimensional heterotypic tumor spheroid model. *Clin. Exp. Metastasis*, 30:615–630, 2013.

[24] O. Chaudhuri, L. Gu, M. Darnell, D. Klumpers, S.A. Bencherif, J.C. Weaver, N. Huebsch, and D.J. Mooney. Substrate stress relaxation regulates cell spreading. *Nat. Commun.*, 6, 2015.

[25] O. Chaudhuri, L. Gu, D. Klumpers, M. Darnell, S.A. Bencherif, J.C. Weaver, N. Huebsch, H. Lee, E. Lippens, G.N. Duda, and D.J. Mooney. Hydrogels with tunable stress relaxation regulate stem cell fate and activity. *Nat. Mater*, 15:326–334, 2016.

[26] O. Chaudhuri, S.T. Koshy, C. Branco da Cunha, J.W. Shin, C.S. Verbeke, K.H. Allison, and D.J. Mooney. Extracellular matrix stiffness and composition jointly regulate the induction of malignant phenotypes in mammary epithelium. *Nat. Mater.*, 13:970–978, 2014.

[27] R.G. Chelliyil, T.S. Ralston, D.L. Marks, and S.A. Boppart. High-speed processing architecture for spectral-domain optical coherence microscopy. *J. Biomed. Opt.*, 13:044013, 2008.

[28] H. Colin-York, C. Eggeling, and M. Fritzsche. Dissection of mechanical force in living cells by super-resolved traction force microscopy. *Nat. Protoc.*, 12:783796, 2017.

[29] H. Colin-York, D. Shrestha, J.H. Felce, D. Waithe, E. Moeendarbary, S.J. Davis, C. Eggeling, and M. Fritzsche. Super-resolved traction force microscopy (stfm). *Nano. Lett.*, 16:2633–2638, 2016.

[30] A.M. Collinsworth, S. Zhang, and W.E. Kraus G.A. Truskey. Apparent elastic modulus and hysteresis of skeletal muscle cells throughout differentiation. *Am. J. Physiol. Cell Physiol.*, 283:C1219–C1227, 2002.

[31] M.W. Conklin, J.C. Eickhoff, K.M. Riching, C.A. Pehlke, K.W. Eliceiri, P.P. Provenzano, A. Friedl, and P.J. Keely. Aligned collagen is a prognostic signature for survival in human breast carcinoma. *Am. J. Pathol.*, 178:1221–1232, 2011.

[32] C. Cuartas-Velez, R. Restrepo, B.E. Bouma, and N. Uribe-Patarroyo. Volumetric non-local-means based speckle reduction for optical coherence tomography. *Biomed. Opt. Express*, 9:3354–3372, 2018.

[33] A. Curatolo, P.R.T. Munro, D. Lorenser, P. Sreekumar, C.C. Singe, B.F. Kennedy, and D.D. Sampson. Quantifying the influence of bessel beams on image quality in optical coherence tomography. *Sci. Rep.*, 6, 2016.

[34] W.P. Daley, S.B. Peters, and M. Larsen. Extracellular matrix dynamics in development and regenerative medicine. *J. Cell Sci.*, 121:255–264, 2008.

[35] J.C. del lamo, R. Meili, B. lvarez Gonzlez, B. Alonso-Latorre, E. Bastounis, R. Firtel, and J.C. Lasheras. Three-dimensional quantification of cellular traction forces and mechanosensing of thin substrata by fourier traction force microscopy. *PLoS One*, 8:e69850, 2013.

[36] M. Dembo and Y.L. Wang. Stresses at the cell-to-substrate interface during locomotion of fibroblasts. *Biophys. J.*, 76:2307–2316, 1999.

[37] R.A. Desai, S.B. Gopal, S. Chen, and C.S. Chen. Contact inhibition of locomotion probabilities drive solitary versus collective cell migration. *J. R. Soc. Interface*, 10, 2013.

[38] S. Dupont, L. Morsut, M. Aragona, E. Enzo, S. Giulitti, M. Cordenonsi, F. Zanconato, J. Le Digabel, M. Forcato, S. Bicciato, N. Elvassore, and S. Piccolo. Role of yap/taz in mechanotransduction. *Nature*, 474:179–183, 2011.

[39] H.W. Engl, M. Hanke, and A. Neubauer. *Regularization of inverse problems*. Kluwer Academic Publishers, 2000.

[40] J. Eyckmans, T. Boudou, X. Yu, and C.S. Chen. A hitchhikers guide to mechanobiology. *Dev. Cell*, 21:35–47, 2011.

[41] M. Fang, J. Yuan, C. Peng, and Y. Li. Collagen as a double-edged sword in tumor progression. *Tumor Biol.*, 35:2871–2882, 2014.

[42] Q. Fang. iso2mesh: a 3d surface and volumetric mesh generator for matlab/octave. Online.

[43] X. Feng, M.S. Hall, M. Wu, and C.Y. Hui. An adaptive algorithm for track-

ing 3d bead displacements: application in biological experiments. *Meas. Sci. Technol.*, 25, 2014.

[44] X. Feng and C.Y. Hui. Force sensing using 3d displacement measurements in linear elastic bodies. *Comput. Mech.*, 58:91–105, 2016.

[45] P. Fernandez and A.R. Bausch. The compaction of gels by cells: a case of collective mechanical activity. *Integr. Biol.*, 1:252–259, 2009.

[46] C. Franck, S. Hong, S.A. Maskarinec, D.A. Tirrell, and G. Ravichandran. Three-dimensional full-field measurements of large deformations in soft materials using confocal microscopy and digital volume correlation. *Exp. Mech.*, 47:427–438, 2007.

[47] C. Franck, S.A. Maskarinec, D.A. Tirrell, and G. Ravichandran. Three-dimensional traction force microscopy: a new tool for quantifying cell-matrix interactions. *PLoS One*, 6:e17833, 2011.

[48] P. Friedl and K. Wolf. Tumour-cell invasion and migration: diversity and escape mechanisms. *Nat. Rev. Cancer*, 3:362–374, 2003.

[49] A. Fritsch, M. Hckel, T. Kiessling, K.D. Nnetu, F. Wetzel, M. Zink, and J.A. Ks. Are biomechanical changes necessary for tumour progression? *Nat. Phys.*, 6:730–732, 2010.

[50] J. Fu, F. Pierron, and P.D. Ruiz. Elastic stiffness characterization using three-dimensional full-field deformation obtained with optical coherence tomography and digital volume correlation. *J. Biomed. Opt.*, 18:121512, 2013.

[51] B. Geiger, J.P. Spatz, and A.D. Bershadsky. Environmental sensing through focal adhesions. *Nat. Rev. Mol. Cell Biol.*, 10:21–33, 2009.

[52] C. Geuzaine and J. Remacle. A three-dimensional finite element mesh generator with built-in pre- and post-processing facilities. Online.

[53] P.M. Gilbert, K.L. Havenstrite, K.E. Magnusson, A. Sacco, N.A. Leonardi, P. Kraft, N.K. Nguyen, S. Thrun, M.P. Lutolf, and H.M. Blau. Substrate elasticity regulates skeletal muscle stem cell self-renewal in culture. *Science*, 329:1078–1081, 2010.

[54] N. Gjorevski and C.M. Nelson. Mapping of mechanical strains and

stresses around quiescent engineered three-dimensional epithelial tissues. *Biophys. J.*, 103:152–162, 2012.

[55] B.W. Graf, S.G. Adie, and S.A. Boppart. Correction of coherence gate curvature in high numerical aperture optical coherence imaging. *Opt. Lett.*, 35:3120–3122, 2010.

[56] B. Grajciar, M. Pircher, A. Fercher, and R. Leitgeb. Parallel fourier domain optical coherence tomography for in vivo measurement of the human eye. *Opt. Express*, 13:1131–1137, 2005.

[57] C. Grashoff, B.D. Hoffman, M.D. Brenner, R. Zhou, M. Parsons, M.T. Yang, M.A. McLean, S.G. Sligar, C.S. Chen, T. Ha, and M.A. Schwartz. Measuring mechanical tension across vinculin reveals regulation of focal adhesion dynamics. *Nature*, 466:263–266, 2010.

[58] F. Guilak, D.M. Cohen, B.T. Estes, J.M. Gimble, W. Liedtke, and C.S. Chen. Control of stem cell fate by physical interactions with the extracellular matrix. *Cell Stem Cell*, 5:17–26, 2009.

[59] A. Haeger, M. Krause, K. Wolf, and P. Friedl. Cell jamming: collective invasion of mesenchymal tumor cells imposed by tissue confinement. *Biochim. Biophys. Acta*, 1840:2386–2395, 2014.

[60] K.M. Hakkinen, J.S. Harunaga, A.D. Doyle, and K.M. Yamada. Direct comparisons of the morphology, migration, cell adhesions, and actin cytoskeleton of fibroblasts in four different three-dimensional extracellular matrices. *Tissue Eng. Part A*, 17:713–724, 2011.

[61] M.S. Hall, F. Alisafaei, E. Ban, X. Feng, C.Y. Hui, V.B. Shenoy, and M. Wu. Fibrous nonlinear elasticity enables positive mechanical feedback between cells and ecms. *Proc. Natl. Acad. Sci. U.S.A.*, 113:1404314048, 2016.

[62] M.S. Hall, R. Long, X. Feng, Y. Huang, C.Y. Hui, and M. Wu. Toward single cell traction microscopy within 3d collagen matrices. *Exp. Cell Res.*, 319:2396–2408, 2013.

[63] M.S. Hall, R. Long, C.Y. Hui, and M. Wu. Mapping three-dimensional stress and strain fields within a soft hydrogel using a fluorescence microscope. *Biophys. J.*, 102:2241–2250, 2012.

[64] W. Han, S. Chen, W. Yuan, Q. Fan, J. Tian, X. Wang, L. Chen, X. Zhang,

W. Wei, R. Liu, J. Qu, Y. Jiao, R.H. Austin, and L. Liu. Oriented collagen fibers direct tumor cell intravasation. *Proc. Natl. Acad. Sci. U.S.A.*, 113:1120811213, 2016.

[65] A.K. Harris, P. Wild, and D. Stopak. Silicone rubber substrata: a new wrinkle in the study of cell locomotion. *Science*, 208:177–179, 1980.

[66] D. Hillmann, H. Spahr, C. Hain, H. Sudkamp, G. Franke, C. Pfffle, C. Winter, and G. Httmann. Aberration-free volumetric highspeed imaging of in vivo retina. *Sci. Rep.*, 6, 2016.

[67] C.N. Holenstein, U. Silvan, and J.G. Snedeker. High-resolution traction force microscopy on small focal adhesions - improved accuracy through optimal marker distribution and optical flow tracking. *Sci. Rep.*, 7, 2017.

[68] P.J. Hunter and T.K. Borg. Integration from proteins to organs: the physiome project. *Nat. Rev. Mol. Cell Biol.*, 4:237–243, 2003.

[69] H. Jang, J. Notbohm, B. Gweon, Y. Cho, C.Y. Park, S.-H. Kee, J.J. Fredberg, J.H. Shin, and Y. Park. Homogenizing cellular tension by hepatocyte growth factor in expanding epithelial monolayer. *Sci. Rep.*, 8, 2017.

[70] K.A. Jansen, R.G. Bacabac, I.K. Piechocka, and G.H. Koenderink. Cells actively stiffen fibrin networks by generating contractile stress. *Biophys. J.*, 105:22402251, 2013.

[71] K.A. Jansen, D.M. Donato, H.E. Balcioglu, T. Schmidt, E.H. Danen, and G.H. Koenderink. A guide to mechanobiology: Where biology and physics meet. *Biochim Biophys Acta*, 1853 (11 Pt B):3043–3052, 2015.

[72] B. Karamata, P. Lambelet, M. Laubscher, R.P. Salath, and T. Lasser. Spatially incoherent illumination as a mechanism for cross-talk suppression in wide-field optical coherence tomography. *Opt. Lett.*, 29:736–738, 2004.

[73] B. Karamata, M. Leutenegger, M. Laubscher, S. Bourquin, T. Lasser, and P. Lambelet. Multiple scattering in optical coherence tomography. ii. experimental and theoretical investigation of cross talk in wide-field optical coherence tomography. *J. Opt. Soc. Am. A*, 22:1380–1388, 2005.

[74] M. Keating, A. Kurup, M. Alvarez-Elizondo, A.J. Levine, and E. Botvinick. Spatial distributions of pericellular stiffness in natural extracellular ma-

trices are dependent on cell-mediated proteolysis and contractility. *Acta Biomater.*, 57:304–312, 2017.

[75] B.F. Kennedy, K.M. Kennedy, and D.D. Sampson. A review of optical coherence elastography: fundamentals, techniques and prospects. *IEEE J. Sel. Top. Quantum Electron.*, 20:1–17, 2014.

[76] J. Kim, C.A. Jones, N.S. Groves, and B. Sun. Three-dimensional reflectance traction microscopy. *PLoS One*, 11:e0156797, 2016.

[77] J.H. Kim, X. Serra-Picamal, D.T. Tambe, E.H. Zhou, C.Y. Park, M. Sadati, J.-A. Park, R. Krishnan, B. Gweon, E. Millet, J.P. Butler, X. Trepat, and J.J. Fredberg. Propulsion and navigation within the advancing monolayer sheet. *Nat. Mater.*, 12:856–863, 2013.

[78] T.M. Koch, S. Mnster, N. Bonakdar, J.P. Butler, and B. Fabry. 3d traction forces in cancer cell invasion. *PLoS One*, 7:e33476, 2012.

[79] M.A. Kotlarchyk, S.G. Shreim, M.B. Alvarez-Elizondo, L.C. Estrada, R. Singh, L. Valdevit, E. Kniazeva, E. Gratton, A.J. Putnam, and E.L. Botvinick. Concentration independent modulation of local micromechanics in a fibrin gel. *PLoS One*, 6:e20201, 2011.

[80] C.M. Kraning-Rush, J.P. Califano, and C.A. Reinhart-King. Cellular traction stresses increase with increasing metastatic potential. *PLoS One*, 7:e32572, 2012.

[81] C.M. Kraning-Rush, S.P. Carey, J.P. Califano, and C.A. Reinhart-King. Quantifying traction stresses in adherent cells. *Methods Cell Biol.*, 110:139–178, 2012.

[82] D. Kroon. Smooth triangulated mesh. Online.

[83] A. Kumar, W. Drexler, and R.A. Leitgeb. Subaperture correlation based digital adaptive optics for full field optical coherence tomography. *Opt. Express*, 21:1085010866, 2013.

[84] A. Kumar, T. Kamali, R. Platzer, A. Unterhuber, W. Drexler, and R.A. Leitgeb. Anisotropic aberration correction using region of interest based digital adaptive optics in fourier domain oct. *Biomed. Opt. Express*, 6:1124–1134, 2015.

[85] M.L. Kutys and C.S. Chen. Forces and mechanotransduction in 3d vascular biology. *Curr. Opin. Cell. Biol.*, 42:73–79, 2016.

[86] A. Labernadie, T. Kato, A. Brugus, X. Serra-Picamal, S. Derzsi, E. Arwert, A. Weston, V. Gonzlez-Tarrag, A. Elosegui-Artola, L. Albertazzi, J. Alcaraz, P. Roca-Cusachs, E. Sahai, and X. Trepat. A mechanically active heterotypic e-cadherin/n-cadherin adhesion enables fibroblasts to drive cancer cell invasion. *Nat. Cell. Biol.*, 19:224–237, 2017.

[87] N. Leartprapun, R.R. Iyer, G.R. Untracht, J.A. Mulligan, and S.G. Adie. Photonic force optical coherence elastsography for three-dimensional mechanical microscopy. *Nat. Commun.*, 9, 2018.

[88] K.-S. Lee and J.P. Rolland. Bessel beam spectral-domain high-resolution optical coherence tomography with micro-optic axicon providing extended focusing range. *Opt. Lett.*, 33:1696–1698, 2008.

[89] W.R. Legant, J.S. Miller, B.L. Blakely, D.M. Cohen, G.M. Genin, and C.S. Chen. Measurement of mechanical tractions exerted by cells in three-dimensional matrices. *Nat. Methods*, 7:969–971, 2010.

[90] R.A. Leitgeb, M. Villiger, A.H. Bachmann, L. Steinmann, and T. Lasser. Extended focus depth for fourier domain optical coherence microscopy. *Opt. Lett.*, 31:2450–2452, 2006.

[91] K.R. Levental, H. Yu, L. Kass, J.N. Lakins, M. Egeblad, J.T. Erler, S.F. Fong, K. Csiszar, A. Giaccia, W. Weninger, M. Yamauchi, D.L. Gasser, and V.M. Weaver. Matrix crosslinking forces tumor progression by enhancing integrin signaling. *Cell*, 139:891–906, 2009.

[92] O. Liba, M.D. Lew, E.D. SoRelle, R. Dutta, D. Sen, D.M. Moshfeghi, S. Chu, and A. de la Zerda. Speckle-modulating optical coherence tomography in living mice and humans. *Nat. Commun.*, 8, 2017.

[93] C.T. Lim, A. Bershadsky, and M.P. Sheetz. Mechanobiology. *J. R. Soc. Interface*, 7:S291–S293, 2010.

[94] L. Ling, J.A. Mulligan, Y. Ouyang, A.A. Shimpi, R.M. Williams, G.F. Beeghly, B.D. Hopkins, J.A. Spector, S.G. Adie, and C. Fischbach. Obesity-associated adipose stromal cells promote breast cancer invasion through direct cell contact and ecm remodeling. *Adv. Funct. Mater*, page 1910650, 2020.

[95] S. Liu, M.R.E. Lamont, J.A. Mulligan, and S.G. Adie. Aberration-diverse optical coherence tomography for suppression of multiple scattering and speckle. *Biomed. Opt. Express*, 9:49194935, 2018.

[96] S. Liu, J.A. Mulligan, and S.G. Adie. Volumetric optical coherence microscopy with a high space-bandwidth-time product enabled by hybrid adaptive optics. *Biomed. Opt. Express*, 9:3137–3152, 2018.

[97] X. Liu and J.U. Kang. Compressive sd-oct: the application of compressed sensing in spectral domain optical coherence tomography. *Opt. Express*, 18:22010–22019, 2010.

[98] Y.-Z. Liu, N.D. Shemonski, S.G. Adie, A. Ahmad, A.J. Bower, P.S. Carney, and S.A. Boppart. Computed optical interferometric tomography for high-speed volumetric cellular imaging. *Biomed. Opt. Express*, 5:2988–3000, 2014.

[99] J.I. Lopez, J.K. Mouw, and V.M. Weaver. Biomechanical regulation of cell orientation and fate. *Oncogene*, 27:6981–6993, 2008.

[100] P. Lu, V.M. Weaver, and Z. Werb. The extracellular matrix: a dynamic niche in cancer progression. *J. Cell Biol.*, 196:395–406, 2012.

[101] T. Mammoto, A. Mammoto, and D.E. Ingber. Mechanobiology and developmental control. *Annu. Rev. Cell Dev. Biol.*, 29:27–61, 2013.

[102] D.L. Marks, A.L. Oldenburg, J.J. Reynolds, and S.A. Boppart. Autofocus algorithm for dispersion correction in optical coherence tomography. *Appl. Opt.*, 42:3038–3046, 2003.

[103] S.A. Maskarinec, C. Franck, D.A. Tirrell, and G. Ravichandran. Quantifying cellular traction forces in three dimensions. *Proc. Natl. Acad. Sci. U.S.A.*, 106:22108–22113, 2009.

[104] B.N. Mason, A. Starchenko, R.M. Williams, L.J. Bonassar, and C.A. Reinhart-King. Tuning 3d collagen matrix stiffness independently of collagen concentration modulates endothelial cell behavior. *Acta Biomater.*, 9:4635–4644, 2013.

[105] A.H. Mekhdjian, F. Kai, M.G. Rubashkin, L.S. Prahl, L.M. Przybyla, A.L. McGregor, E.S. Bell, J.M. Barnes, C.C. DuFort, G. Ou, A.C. Chang,

L. Cassereau, S.J. Tan, M.W. Pickup, J.N. Lakins, X. Ye, M.W. Davidson, J. Lammerding, D.J. Odde, A.R. Dunn, and V.M. Weaver. Integrin-mediated traction force enhances paxillin molecular associations and adhesion dynamics that increase the invasiveness of tumor cells into a three-dimensional extracellular matrix. *Mol. Biol. Cell*, 28:1467–1488, 2017.

[106] R. Merkel, N. Kirchgener, C.M. Cesa, and B. Hoffmann. Cell force microscopy on elastic layers of finite thickness. *Biophys. J.*, 93:3314–3323, 2007.

[107] J.S. Miller, C.J. Shen, W.R. Legant, J.D. Baranski, B.L. Blakely, and C.S. Chen. Bioactive hydrogels made from step-growth derived peg-peptide macromers. *Biomaterials*, 31:3736–3743, 2010.

[108] N. Mohan, I. Stojanovic, W.C. Karl, B.E.A. Saleh, and M.C. Teich. Compressed sensing in optical coherence tomography. *Proc. SPIE*, 7570:75700L, 2010.

[109] I. Muhamed, J. Wu, P. Sehgal, X. Kong, A. Tajik, N. Wang, and D.E. Leckband. E-cadherin-mediated force transduction signals regulate global cell mechanics. *J. Cell Sci.*, 129:1843–1854, 2016.

[110] J.A. Mulligan, F. Bordeleau, C.A. Reinhart-King, and S.G. Adie. Measurement of dynamic cell-induced 3d displacement fields in vitro for traction force optical coherence microscopy. *Biomed. Opt. Express*, 8:1152–1171, 2017.

[111] J.A. Mulligan, F. Bordeleau, C.A. Reinhart-King, and S.G. Adie. *Biomechanics in Oncology*, chapter Traction Force Microscopy for Noninvasive Imaging of Cell Forces. Springer Nature Switzerland AG, 2018.

[112] J.A. Mulligan, X. Feng, and S.G. Adie. Quantitative reconstruction of time-varying 3d cell forces with traction force optical coherence microscopy. *Sci. Rep.*, 9, 2019.

[113] J.A. Mulligan, G.R. Untracht, S.N. Chandrasekaran, C.N Brown, and S.G. Adie. Emerging approaches for high-resolution imaging of tissue biomechanics with optical coherence elastography. *IEEE J. Sel. Top. Quantum Electron.*, 22, 2016.

[114] M. Munter, M. vom Endt, M. Pieper, M. Casper, M. Ahrens, T. Kohlfaerber, R. Rahmanzadeh, P. Konig, G. Httmann, and H. Schulz-Hildebrandt. Dynamic contrast in scanning microscopic oct. *arXiv:2003.00006*, 2020.

[115] S. Nam, K.H. Hu, M.J. Butte, and O. Chaudhuri. Strain-enhanced stress relaxation impacts nonlinear elasticity in collagen gels. *Proc. Natl. Acad. Sci. U.S.A.*, 113:5492–5497, 2016.

[116] J. Notbohm, S. Banerjee, K.J.C. Utuje, B. Gweon, H. Jang, Y. Park, J. Shin, J.P. Butler, J.J. Fredberg, and M.C. Marchetti. Cellular contraction and polarization drive collective cellular motion. *Biophys. J.*, 110:2729–2738, 2016.

[117] F. Pampaloni, E.G. Reynaud, and E.H.K. Stelzer. The third dimension bridges the gap between cell culture and live tissue. *Nat. Rev. Mol. Cell Biol.*, 8:839–845, 2007.

[118] B. Pan, K. Qian, H. Xie, and A. Asundi. Two-dimensional digital image correlation for in-plane displacement and strain measurement: a review. *Meas. Sci. Technol.*, 20:062001, 2009.

[119] C.Y. Park, E.H. Zhou, D. Tambe, B. Chen, T. Lavoie, M. Dowell, A. Simeonov, D.J. Maloney, A. Marinkovic, D.J. Tschumperlin, S. Burger, M. Frykenberg, J.P. Butler, W.D. Stamer, M. Johnson, J. Solway, J.J. Fredberg, and R. Krishnan. High-throughput screening for modulators of cellular contractile force. *Integr. Biol.*, 7:1318–1324, 2015.

[120] J.-A. Park, L. Atia, J.A. Mitchel, J.J. Fredberg, and J.P. Butler. Collective migration and cell jamming in asthma, cancer and development. *J. Cell Sci.*, 129:3375–3383, 2016.

[121] K.K. Parker, A.L. Brock, C. Brangwynne, R.J. Mannix, N. Wang, E. Ostuni, N.A. Geisse, J.C. Adams, G.M. Whitesides, and D.E. Ingber. Directional control of lamellipodia extension by constraining cell shape and orienting cell tractional forces. *FASEB J.*, 16:1195–1204, 2002.

[122] M.J. Paszek, N. Zahir, K.R. Johnson, J.N. Lakins, G.I. Rozenberg, A. Gefen, C.A. Reinhart-King, S.S. Margulies, M. Dembo, D. Boettiger, D.A. Hammer, and V.M. Weaver. Tensional homeostasis and the malignant phenotype. *Cancer Cell*, 8:241–254, 2005.

[123] A.F. Pegoraro, J.J. Fredberg, and J.A. Park. Problems in biology with many scales of length: cell-cell adhesion and cell jamming in collective cellular migration. *Exp. Cell Res.*, 343:54–59, 2016.

[124] R.J. Pelham and Y.L. Wang. Cell locomotion and focal adhesions are regu-

lated by substrate flexibility. *Proc. Natl. Acad. Sci. U.S.A.*, 94:13661–13665, 1997.

[125] X. Pennec, P. Cachier, and N. Ayache. *Medical Image Computing and Computer-Assisted Intervention - MICCAI'99*, chapter Understanding the "Demon's Algorithm": 3D non-rigid registration by gradient descent, pages Lecture Notes in Computer Science, vol 1679. Springer, Berlin, Heidelberg, 1999.

[126] A.S. Piotrowski, V.D. Varner, N. Gjorevski, and C.M. Nelson. *Tissue morphogenesis. Methods in molecular biology (methods and protocols)*, chapter Three-dimensional traction force microscopy of engineered epithelial tissues. Humana Press, 2015.

[127] S.V. Plotnikov, A.M. Pasapera, B. Sabass, and C.M. Waterman. Force fluctuations within focal adhesions mediate ecm-rigidity sensing to guide directed cell migration. *Cell*, 151:1513–1527, 2012.

[128] S.V. Plotnikov, B. Sabass, U.S. Schwarz, and C.M. Waterman. High-resolution traction force microscopy. *Methods Cell Biol.*, 123:367–394, 2014.

[129] C. Plutoni, E. Bazellieres, M. Le Borgne-Rochet, F. Comunale, A. Brugues, M. Sveno, D. Planchon, S. Thuault, N. Morin, S. Bodin, X. Trepat, and C. Gauthier-Rouvire. P-cadherin promotes collective cell migration via a cdc42-mediated increase in mechanical forces. *J. Cell Biol.*, 212:199–217, 2016.

[130] W.J. Polacheck and C.S. Chen. Measuring cell-generated forces: a guide to the available tools. *Nat. Methods*, 13:415423, 2016.

[131] S.R. Polio, H. Parameswaran, E.P. Canovi, C.M. Gaut, D. Aksyonova, D. Stamenovi, and M.L. Smith. Topographical control of multiple cell adhesion molecules for traction force microscopy. *Integr. Biol.*, 6:357–365, 2014.

[132] S.R. Polio, K.E. Rothenberg, D. Stamenovi, and M.L. Smith. A micropatterning and image processing approach to simplify measurement of cellular traction forces. *Acta Biomater.*, 8:82–88, 2012.

[133] W.H. Press, S.A. Teukolsky, W.T. Vetterling, and B.P. Flannery. *Numerical recipes: the art of scientific computing (third edition)*, chapter 16, pages 848–850. Cambridge University Press, 2007.

[134] P.P. Provenzano, D.R. Inman, K.W. Eliceiri, J.G. Knittel, L. Yan, C.T. Rueden, J.G. White, and P.J. Keely. Collagen density promotes mammary tumor initiation and progression. *BMC Med.*, 6, 2008.

[135] L. Przybyla, J.N. Lakins, R. Sunyer, X. Trepat, and V.M. Weaver. Monitoring developmental force distributions in reconstituted embryonic epithelia. *Methods*, 94:101–113, 2016.

[136] L. Qi, N. Li, R. Huang, Q. Song, L. Wang, Q. Zhang, R. Su, T. Kong, M. Tang, and G. Cheng. The effects of topographical patterns and sizes on neural stem cell behavior. *PLoS One*, 8:e59022, 2013.

[137] T.S. Ralston, D.L. Marks, P.S. Carney, and S.A. Boppart. Interferometric synthetic aperture microscopy. *Nat. Phys.*, 3:129–134, 2007.

[138] C.A. Reinhart-King, M. Dembo, and D.A. Hammer. Cell-cell mechanical communication through compliant substrates. *Biophys. J.*, 95:6044–6051, 2008.

[139] S.M. Rey, B. Povazay, B. Hofer, A. Unterhuber, B. Hermann, A. Harwood, and W. Drexler. Three- and four-dimensional visualization of cell migration using optical coherence tomography. *J. Biophotonics*, 2:370–379, 2009.

[140] S. Rivet, M. Maria, A. Bradu, T. Feuchter, L. Leick, and A. Podoleanu. Complex master slave interferometry. *Opt. Express*, 24:2885–2904, 2016.

[141] P. Roca-Cusachs, V. Conte, and X. Trepat. Quantifying forces in cell biology. *Nat. Cell. Biol.*, 19:742–751, 2017.

[142] A.M. Rollins and J.A. Izatt. Optimal interferometer designs for optical coherence tomography. *Opt. Letters*, 24:1484–1486, 1999.

[143] P. Ronceray, C.P. Broedersz, and M. Lenz. Fiber networks amplify active stress. *Proc. Natl. Acad. Sci. U.S.A.*, 113:2827–2832, 2016.

[144] B. Sabass, M.L. Gardel, C.M. Waterman, and U.S. Schwarz. High resolution traction force microscopy based on experimental and computational advances. *Biophys. J.*, 94:207–220, 2008.

[145] M. Sadati, N. Taheri Qazvini, R. Krishnan, C.Y. Park, and J.J. Fredberg. Collective migration and cell jamming. *Differentiation*, 86:121–125, 2013.

[146] A. Saez, M. Ghibaudo, A. Buguin, P. Silberzan, and B. Ladoux. Rigidity-driven growth and migration of epithelial cells on microstructured anisotropic substrates. *Proc. Natl. Acad. Sci. U.S.A.*, 104:8281–8286, 2007.

[147] G. Scarcelli, W.J. Polacheck, H.T. Nia, K. Patel, A.J. Grodzinsky, R.D. Kamm, and S.H. Yun. Noncontact three-dimensional mapping of intracellular hydromechanical properties by brillouin microscopy. *Nat. Methods*, 12:1132–1134, 2015.

[148] G. Scarcelli and S.H. Yun. Confocal brillouin microscopy for three-dimensional mechanical imaging. *Nat. Photon.*, 2:39–43, 2007.

[149] M.A. Schwartz and D.W. DeSimone. Cell adhesion receptors in mechanotransduction. *Curr. Opin. Cell Biol.*, 20:551–556, 2008.

[150] U.S. Schwarz, N.Q. Balaban, D. Riveline, A. Bershadsky, B. Geiger, and S.A. Safran. Calculation of forces at focal adhesions from elastic substrate data: the effect of localized force and the need for regularization. *Biophys. J.*, 83:1380–1394, 2002.

[151] U.S. Schwarz and S.A. Safran. Physics of adherent cells. *Rev. Mod. Phys.*, 85:1327–1381, 2013.

[152] U.S. Schwarz and J.R. Soin. Traction force microscopy on soft elastic substrates: A guide to recent computational advances. *Biochim. Biophys. Acta*, 1853:30953104, 2015.

[153] B.R. Seo, P. Bhardwaj, S. Choi, J. Gonzalez, R.C. Andresen Eguiluz, K. Wang, S. Mohanan, P.G. Morris, B. Du, X.K. Zhou, L.T. Vahdat, A. Verma, O. Elemento, C.A. Hudis, R.M. Williams, D. Gourdon, A.J. Dannenberg, and C. Fischbach. Obesity-dependent changes in interstitial ecm mechanics promote breast tumorigenesis. *Sci. Transl. Med.*, 7:301ra130, 2015.

[154] X. Serra-Picamal, V. Conte, R. Vincent, E. Anon, D.T. Tambe, E. Bazellieres, J.P. Butler, J.J. Fredberg, and X. Trepat. Mechanical waves during tissue expansion. *Nat. Phys.*, 8:628–634, 2012.

[155] N.D. Shemonski, S.G. Adie, Y. Liu, F.A. South, P.S. Carney, and S.A. Boppart. Stability in computed optical interferometric tomography (part i): stability requirements. *Opt. Express*, 22:1918319197, 2014.

[156] N.D. Shemonski, A. Ahmad, S.G. Adie, Y. Liu, F.A. South, P.S. Carney, and S.A. Boppart. Stability in computed optical interferometric tomography (part ii): in vivo stability assessment. *Opt. Express*, 22:1931419326, 2014.

[157] M.J. Siedlik, V.D. Varner, and C.M. Nelson. Pushing, pulling, and squeezing our way to understanding mechanotransduction. *Methods*, 94:4–12, 2016.

[158] J.R. Soin, C.A. Brand, J. Stricker, P.W. Oakes, M.L. Gardel, and U.S. Schwarz. Model-based traction force microscopy reveals differential tension in cellular actin bundles. *PLoS Comput. Biol.*, 11:e1004076, 2015.

[159] J.R. Soin, N. Hersch, G. Dreissen, N. Hampe, B. Hoffmann, R. Merkel, and U.S. Schwarz. Measuring cellular traction forces on non-planar substrates. *Interface Focus*, 6, 2016.

[160] W. Song, C.K. Tung, Y.C. Lu, Y. Pardo, M. Wu, M. Das, D.I. Kao, S. Chen, and M. Ma. Dynamic self-organization of microwell-aggregated cellular mixtures. *Soft Matter*, 12:57395746, 2016.

[161] J. Steinwachs, C. Metzner, K. Skodzek, N. Lang, I. Thievessen, C. Mark, S. Mnster, K.E. Aifantis, and B. Fabry. Three-dimensional force microscopy of cells in biopolymer networks. *Nat. Methods*, 13:171–176, 2016.

[162] D.A. Stout, E. Bar-Kochba, J.B. Estrada, J. Toyjanova, H. Kesari, J.S. Reichner, and C. Franck. Mean deformation metrics for quantifying 3d cell-matrix interactions without requiring information about matrix material properties. *Proc. Natl. Acad. Sci. U.S.A.*, 113:2898–2903, 2016.

[163] J. Stricker, B. Sabass, U.S. Schwarz, and M.L. Gardel. Optimization of traction force microscopy for micron-sized focal adhesions. *J. Phys. Condens. Matter*, 22, 2010.

[164] C. Sun, B. Standish, B. Vuong, X.-Y. Wen, and V. Yang. Digital image correlation-based optical coherence elastography. *J. Biomed. Opt.*, 18:121515, 2013.

[165] R. Sunyer, V. Conte, J. Escribano, A. Elosegui-Artola, A. Labernadie, L. Valon, and D. Navajas. Collective cell durotaxis emerges from long-range intercellular force transmission. *Science*, 353:1157–1161, 2016.

[166] A. Su-Aun, A. Jorge-Peas, R. Aguilar-Cuenca, M. Vicente-Manzanares,

H. Van Oosterwyck, and A. Muoz-Barrutia. Full l1-regularized traction force microscopy over whole cells. *BMC Bioinformatics*, 18, 2017.

[167] R. Szeliski. *Texts in computer science*, chapter Computer vision: algorithms and applications. Springer-Verlag, 2011.

[168] D.T. Tambe, C.C. Hardin, T.E. Angelini, K. Rajendran, C.Y. Park, X. Serra-Picamal, E.H. Zhou, M.H. Zaman, J.P Butler, D.A. Weitz, J.J. Fredberg, and X. Trepat. Collective cell guidance by cooperative intercellular forces. *Nat. Mater.*, 10:469–475, 2011.

[169] J.L. Tan, J. Tien, D.M. Pirone, D.S. Gray, K. Bhadriraju, and C.S. Chen. Cells lying on a bed of microneedles: an approach to isolate mechanical force. *Proc. Natl. Acad. Sci. U.S.A.*, 100:1484–1489, 2003.

[170] W. Tan, A.L. Oldenburg, J.J. Norman, T.A. Desai, and S.A. Boppart. Optical coherence tomography of cell dynamics in three-dimensional tissue models. *Opt. Express*, 14:7159–7171, 2006.

[171] H. Tang, J.A. Mulligan, G.R. Untracht, X. Zhang, and S.G. Adie. Gpu-based computational adaptive optics for volumetric optical coherence microscopy. *Proc. SPIE*, 9720:97200O, 2016.

[172] J. Toyjanova, E. Bar-Kochba, C. Lpez-Fagundo, J. Reichner, D. Hoffman-Kim, and C. Franck. High resolution, large deformation 3d traction force microscopy. *PLoS One*, 9:e90976, 2014.

[173] J. Toyjanova, E. Hannen, E. Bar-Kochba, E.M. Darling, D.L. Henann, and C. Franck. 3d viscoelastic traction force microscopy. *Soft Matter*, 10:8095–8106, 2014.

[174] X. Trepat and J.J. Fredberg. Plithotaxis and emergent dynamics in collective cellular migration. *Trends Cell Biol.*, 21:638–646, 2011.

[175] X. Trepat, M.R. Wasserman, T.E. Angelini, E. Millet, D.A. Weitz, J.P. Butler, and J.J. Fredberg. Physical forces during collective cell migration. *Nat. Phys.*, 5:426–430, 2009.

[176] L. Valon, A. Marn-Llaurad, T. Wyatt, G. Charras, and X. Trepat. Optogenetic control of cellular forces and mechanotransduction. *Nat. Commun.*, 8, 2017.

[177] R.F. van Oers, E.G. Rens, D.J. LaValley, C.A. Reinhart-King, and R.M. Merks. Mechanical cell-matrix feedback explains pairwise and collective endothelial cell behavior in vitro. *PLoS Comput. Biol.*, 10:e100377, 2014.

[178] T. Vercauteren, X. Pennec, A. Perchant, and N. Ayache. Diffeomorphic demons: efficient non-parametric image registration. *Neuroimage*, 45:S61–S72, 2009.

[179] L.G. Vincent, Y.S. Choi, B. Alonso-Latorre, J.C. del lamo, and A.J. Engler. Mesenchymal stem cell durotaxis depends on substrate stiffness gradient strength. *Biotechnol. J.*, 8:472–484, 2013.

[180] V. Vogel and M. Sheetz. Local force and geometry sensing regulate cell functions. *Nat. Rev. Mol. Cell Biol.*, 7:265–275, 2006.

[181] T. Wakatsuki, B. Schwab, N.C. Thompson, and E.L. Elson. Effects of cytochalasin d and latrunculin b on mechanical properties of cells. *J. Cell Sci.*, 114:1025–1036, 2001.

[182] H. Wang, A.S. Abhilash, C.S. Chen, R.G. Wells, and V.B. Shenoy. Long-range force transmission in fibrous matrices enabled by tension-driven alignment of fibers. *Biophys. J.*, 107:2592–2603, 2014.

[183] J.P. Wang and A. Hielscher. Fibronectin: how its aberrant expression in tumors may improve therapeutic targeting. *J. Cancer*, 8:674–682, 2017.

[184] S. Wang and K.V. Larin. Optical coherence elastography for tissue characterization: a review. *J. Biophotonics*, 8:279–302, 2015.

[185] J.P. Winer, S. Oake, and P.A. Janmey. Non-linear elasticity of extracellular matrices enables contractile cells to communicate local position and orientation. *PLoS One*, 4:e6382, 2009.

[186] D. Wirtz, K. Konstantopoulos, and P.C. Searson. The physics of cancer: the role of physical interactions and mechanical forces in metastasis. *Nat. Rev. Cancer*, 11:512–522, 2011.

[187] V.W. Wong, S. Akaishi, M.T. Longaker, and G.C. Gurtner. Pushing back: wound mechanotransduction in repair and regeneration. *J. Investig. Dermatol.*, 131:2186–2196, 2011.

[188] W.R., Legant, C.K. Choi, J.S. Miller, L. Shao, L. Gao, E. Betzig, and C.S.

Chen. Multidimensional traction force microscopy reveals out-of-plane rotational moments about focal adhesions. *Proc. Natl. Acad. Sci. U.S.A.*, 110:881–886, 2013.

[189] M. Wu, D.M. Small, N. Nishimura, and S.G. Adie. Computed optical coherence microscopy of mouse brain ex vivo. *J. Biomed. Opt.*, 24:116002, 2019.

[190] J. Zhang, A. Fiore, S.-H. Yun, H. Kim, and G. Scarcelli. Line-scanning brillouin microscopy for rapid non-invasive mechanical imaging. *Sci. Rep.*, 6, 2016.

[191] P. Zhang, E.B. Miller, S.K. Manna, R.K. Meleppat, E.N. Pugh, and R. Zawadzki. Temporal speckle-averaging of optical coherence tomography volumes for in-vivo cellular resolution neuronal and vascular retinal imaging. *Neurophoton.*, 6:041105, 2019.

[192] R. Zhao, T. Boudou, W.-G. Wang, C.S. Chen, and D.H. Reich. Magnetic approaches to study collective three-dimensional cell mechanics in long-term cultures. *J. Appl. Phys.*, 115, 2014.

[193] J. Zhou, S. Pal, S. Maiti, and L.A. Davidson. Force production and mechanical accommodation during convergent extension. *Development*, 142:692–701, 2015.